Guiding treatment selection for advanced prostate cancer with biogenic silver nanoparticles

by

Sunil Rajput

A thesis submitted in partial fulfillment of the requirements for the degree of

Doctor of Philosophy

Department of Chemistry
University of Alberta

Abstract

Prostate cancer (PCa) is the second most common cancer in men worldwide. Men with advanced PCa often face poor prognosis and are at high risk for mortality. To improve prognosis in this high risk population, targeting a reliable biological factor or marker that predicts a patient's response (sensitivity or resistance) to a specific treatment offers therapeutic guidance and clinical benefit. Two major hormonal treatments for advanced PCa are enzalutamide and abiraterone; which either block the binding of a steroid (androgen) to its protein receptor (androgen receptor, AR) or decrease androgen synthesis. Recently, presence of an AR variant (AR-V7) has been linked to resistance of these hormonal treatments. Thus, triaging PCa patients that are AR-V7 positive to other systemic treatments (e.g., taxane-based chemotherapy) can improve progression-free survival and overall survival. However, optimal sequencing available systemic treatments to maximize individual patient benefits remains a critical unmet need in this clinical setting. This work demonstrates a nanomaterial-enhanced antibody sandwich assay for the successful detection of AR-V7 protein in serum of metastatic castration-resistant prostate cancer (mCRPC) patients. Highly sensitive detection is driven by the optical properties of noble metal nanoparticles. Biogenic spherical silver metal nanoparticles, produced by the fungus *Fusarium oxysporum*, were incorporated as plasmonic labels for enhanced spectroscopy. Biogenic silver nanoparticles are stabilized with a surface corona that is unique relative to their chemically-prepared counterparts. This method produces nanoparticles with a native biological scaffold surrounding the nanoparticles that provides

enhanced stability and enables facile antibody attachment. AR-V7 was captured onto a fabricated chip containing specific antibodies immobilized on gold spots and subsequently labelled for detection by antibody coated silver nanoparticles. Measurement of the number of nanoparticles that bind to the chip was accomplished using surface-enhanced Raman scattering (SERS), which provides a unique chemical fingerprint of the label. A prospective pilot scale investigation of clinical utility demonstrated the ability to quantitatively measure AR-V7 in serum of a blinded retrospective cohort of seven advanced PCa patients pre / post treatment with enzalutamide and / or abiraterone. Results presented show distinct separation of PCa patients by AR-V7 status (positive or negative) by a low detection limit established with normal healthy male controls. Presence and amount of AR-V7 in serum offers predictive and prognostic value to inform selection between two classes of systemic treatments (i.e., hormones or taxanes) outlined in the Canadian and American clinical guidelines for managing castration-resistant PCa. Contributions of this work paves the way for a sensitive, rapid, and minimally-invasive SERS-based tool for advanced PCa patients with the aim of better patient outcomes.

Preface

This thesis is an original work by Sunil Rajput (S.R.) under the supervision of Professor Mark T. McDermott (M.T.M). A piece of the research work contained has been published (Chapter 2). Other pieces of work have been done with collaborative efforts. Below are details of each experimental chapter.

Chapter 2 of this thesis has been published as Rajput, S.; Werezuk, R.; Lange, R. M.; McDermott, M. T., Fungal Isolate Optimized for Biogenesis of Silver Nanoparticles with Enhanced Colloidal Stability. *Langmuir* **2016,** *32* (34), 8688-8697. The work was conceived by S.R. Critical inputs were provided by M.T.M. and R.L. S.R. performed most of the experiments and analyzed the data in the manuscript. R.W. assisted with the screening, temperature, pH, DLS, ZP, and UV-visible experiments. Electron microscopy was performed through the electron microscopy facilities at the University of Alberta (Department of Biology) with assistance from Arlene Oatway and Dee-Ann Rollings. The manuscript was written by S.R., M.T.M, and R.L.

Chapter 3 was conducted in collaboration with the Mass Spectrometry Facility (University of Alberta, Chemistry), Nuclear Magnetic Resonance Facility (University of Alberta, Chemistry), Biological Services Facility (University of Alberta, Chemistry) and the National Research Council Nanotechnology Research Centre (Edmonton). The work was

conceived by S.R. Critical inputs were provided by M.T.M. S.R. performed most of the experiments, analyzed the data, and wrote the chapter. Jing Zheng (Mass Spectrometry Facility) performed the MALDI-MS and LC-MS/MS experiments and contributed to data analysis. Bela Reiz and Professor Liang Li also assisted with mass spectrometry experiments and data analysis. Mark Miskolzie (NMR Facility) performed the NMR experiments and contributed to data analysis. Gareth Lambkin (Biological Services) assisted with SDS-PAGE experiments and data analysis. Hui (Julie) Qian and Kai Cui (National Research Council) performed the surface layer TEM experiments. Paul Concepcion (National Research Council) assisted with electron microscopy experiments.

For Chapter 4, the work was conceived by S.R. and M.T.M. Critical inputs were provided by M.T.M. S.R. performed all the experiments except for the XPS experiments performed by nanoFAB (University of Alberta). S.R. analyzed the data and wrote the chapter. Special recognition to Vincent Bizon (University of Alberta) for assisting with biochip mask fabrication.

Chapter 5 was conducted in collaboration with Professor John D. Lewis, Dr. Desmond Pink, Dr. Scott Findlay, and Mrs. Emma Woolner. These collaborators are part of the Department of Oncology at the University of Alberta. This chapter is largely composed as a journal manuscript and is intended to be submitted shortly after final thesis submission. The work was conceived by S.R. Critical inputs were provided by M.T.M, J.D.L, D.P., S.F., and E.W. S.R. performed most the experiments, analyzed the data, and wrote the

manuscript. D.P. contributed to AR-V7 production, assisted with accessing human clinical specimens, as well as providing value insights to the field of PCa. S.F. designed, performed, and analysed the ddPCR experiments. E.W. performed western blotting and contributed to the lysate experiments. The chapter manuscript was critically reviewed by all the authors. Special recognition to: (1) Dr. Lars B. Laurentius (University of Utah) for providing critical inputs in designing and performing the SERS immunoassay experiments; and (2) Catalina Vasquez (University of Alberta) for providing critical inputs in selecting, accessing clinically characterized patient serum and plasma specimens, and collecting control patient blood samples; (3) Dr. Jun Luo (Johns Hopkins University) for generously providing VCaP cells; (4) Dr. Emmanuel Antonarakis (Johns Hopkins University) and (5) Dr. Michael Kolinsky (University of Alberta) for providing clinical relevance (e.g., clinical guidelines) to assist with clinical utility; (6) Dr. Sunita Ghosh (University of Alberta) for contributing to bio-statistical analysis and providing a critical perspective on clinical validation studies; and (7) Dr. Xuesen Dong (Vancouver Prostate Centre) for providing assistance with improving AR-V7 yield in VCaP cells.

Dedication

To my wife, Venita Rajput, and to my daughter, Ellianna Rajput:

Your strong support, encouragement, and cheerfulness has empowered me to pursue my scientific ambitions with the aim of shaping a better future.

To the next generations of scientists:

Challenge status quo. Be bold and creative in the face of opposition when exploring new research fields. Humankind and our planet needs you desperately.

Acknowledgements

The research work described in this thesis would not have been possible without the strong support, encouragement, and good will of several individuals and financial agencies. The body of work expressed in this thesis is the result of many wonderful and exciting interactions. As such, the research work has come to fruition through a team effort and generous financial support.

First, I thank my wife, Venita Rajput, for your understanding, encouragement, and great patience especially over the past five years of my PhD program. Though the time has been challenging, you have helped me persevere and reach this goal. To my daughter, Ellianna Rajput, your cheery playfulness, awe-inspiring curiosity, and amazing abilities has provided me with refreshing new perspectives on life and towards the future. I also thank my extended family for their strong support and understanding in pursuing my ambitions.

At the University of Alberta: I am indebted to Professor Mark McDermott and the McDermott Lab. I am extremely thankful to Mark for accepting me into his group and providing me with wisdom, guidance, support, and allowing me to branch out into a new research area. Mark, I express my heart-filled thanks to you for believing in me and for bestowing me with strength I desperately needed at this stage of my life/career. With your influence, I learned both what constitutes a good scientist and a good supervisor. I have the utmost respect for you as a mentor, colleague, and friend. Big thanks to my fellow group members: Ahmed Mahmoud, Casey Rusin, Kenny Xu, Dr. Rongbing Du, Nicole Jankovic, Thuy Nguyen, Amy Mao, Dr. Abdelhaq Benkaddour, and Taylor Lynk. Special

thanks to a few alumni group members: Drs. Lars Laurentius (now in M. Porter Lab), Greg Kaufman, Shereen Elbayomy, and Albert (Yong) Cao. Collectively, you all have been collaborative, supportive, and very helpful over the years. Being a part of the McDermott Lab has re-sparked my passion for science. To the Lewis Lab, I am thankful to Professor John Lewis, Dr. Desmond Pink, Emma Woolner, Dr. Arun Raturi, and Catalina Vasquez. It has been and continues to be a true honour to work with J. Lewis Lab. With John's stewardship, the Lewis Lab's passion and motivation is inspiring. John, I am very thankful for your collaborative spirit, business acumen, humbleness, support, for introducing me to Desmond, and welcoming me into your research network. Your mix of scientific / business understanding as well as high level presentation has been inspiring to me. Special thanks to Dr. Desmond Pink and Catalina Vasquez for your brilliant friendship and scientific support. Desmond, you are a strong scientist and a trusted friend; I see you as one of my highly respected mentors. Huge Thanks to all the technical and administrative staff in the Department of Chemistry (DC), Faculty of Science (FS), Faculty of Engineering (FE), Faculty of Graduate Studies and Research (FGSR), at the National Resources Council (NRC) NANO, and NanoFAB. Special thanks to Anita Weiler (DC), Jing Zheng (DC), J. Veinot Lab (DC), R. Campbell Lab (DC), J. Buriak Lab (DC), J. Gibbs Lab (DC), M. Serpe Lab (DC), Mass Spectrometry Services (DC), Gareth Lambkin (DC), Mark Miskolzie (DC), the Chemistry Machine Shop folks (DC), Scott Stelck (DC), the Chemistry Awards Committee (DC), Shannon Guenette (DC), Ryan Lewis (DC), Wayne Moffat (DC), Michelle Fuko (FS), Amal Kirkland (FS), Dr. Yaman Boluk (FE), Ekaterina (Katya) Joshi (FGSR), Paul Concepcion (NRC), Mike Xia (NRC), Julie Qian (NRC), Kai Cui (NRC), Brad Haynes (NRC), Dr. Shihong Xu (nanoFAB), and Dr. Anqiang He (nanoFAB). At the Cross Cancer Institute / University of

Alberta, Drs. Michael Kolinsky, Sunita Ghosh, Wei-Feng Dong, and Gilbert Bigras have been tremendously supportive.

At InnoTech / Alberta Innovates: Ralph Lange, Dr. Anthony Anyia, and Richard Wayken for support in helping me establish an unprecedented *PhD Accelerator Program* at Alberta Innovates Technology Futures. These three gentlemen help me pioneer this program and I will never forget this. Dr. Raja Mita for providing critical inputs in orienting me to the field of cancer research and for introducing me to Drs. John Lewis and Roseline Godbout. Dr. Angela Keuling for helping me with my first NSERC application, for assisting with market relevance, and navigating the world of patent. Dr. John Wolodko and Thomas Perras for helping me build business acumen. In my hour of need, I am grateful to Richard Gibson, Kirk Rockwell, and Dr. Marlene Huerta for financial support. I also thank Rod Werezuk, Wendi Dmytriw, Sarah Lee, and Dr. Jan Slaski for their support and encouragement.

Beyond the University of Alberta: Dr. M. Porter Lab, Dr. Nicholas Owen, Dr. Jeremy Driskell, Seth Filbrun for collectively helping me with SERS immunoassays and for introducing me to mercaptobenzonitrile. Dr. Lisa Saccamano (Abcam) for assistance with antibody selections. Dr. Dipti Tankala (Astellas Pharma Canada) for assistance with acquiring Enzalutamide. Dr. Xuesen Dong (BC Prostate Centre) for valuable assistance on boosting AR-V7 production. Dr. Jun Luo (Johns Hopkins University) for providing VCaP cells. Dr. Emmanuel Antonarakis (John Hopkins University) for providing valuable insights to the field of prostate cancer and AR-V7.

Funding sources: I am tremendously grateful and honoured to have received the following Awards and Scholarships – inaugural PhD Accelerator Scholarship (InnoTech Alberta, formerly Alberta Innovates Technology Futures); National Sciences and Engineering Research Council of Canada (NSERC) Alexander Graham Bell Canada Graduate Scholarship - Doctoral (CGSD3 - 460383 - 2014); Alberta Innovates Graduate Student Scholarship Top-Up Award; University of Alberta's President's Doctoral Prize of Distinction scholarship, University of Alberta's Queen Elizabeth II scholarship, University of Alberta Faculty of Graduate Studies and Research Travel Award, University of Alberta Department of Chemistry Robert Swindlehurst book prize. NSERC discovery and Alberta Innovates Nano-programs Grants (awarded to Mark McDermott). All financial support was extremely critical in completing the research work. Progress would not be possible without this financial support.

Table of Contents

List of Figures

Chapter 1

List of Tables

Chapter 2

Chapter 3

List of Abbreviations

Abi (ABI)	abiraterone
Ab(s)	antibody(ies)
ACN	acetonitrile
ADT	androgen deprivation therapy
Ag	silver
$AgNO_3$	silver nitrate
AgNP(s)	silver nanoparticle(s
AR	androgen receptor
AR-V7	androgen receptor splice variant 7
A.U.	arbitrary units
Au	gold
AuNP(s)	gold nanoparticle(s)
B-AgNP(s)	biogenic silver nanoparticle(s)
BB	borate buffer
BBT	borate buffer containing tween
B-ERL(s)	biogenic extrinsic Raman label(s)
BF	bright field
BPI	base peak ion
BSA	bovine serum albumin

CTC(s)	circulating tumour cell(s)
CRPC	castration-resistant prostate cancer
ddPCR	droplet digital polymerase chain reaction
DI	deionized water
DMS	tridecafluoro-1,1,2,2-tetrahydrooctyl dimethylchlorosilane
DMSO	dimethyl sulfoxide
DTSP	dithiobis(succinimidyl propionate)
eCHEM	electrochemical
EDC	N-(3-dimethylaminopropyl)-N'-ethylcarbodiimide hydrochloride
ELISA	enzyme linked immunosorbent assay
Enz (ENZ)	enzalutamide
ERL(s)	extrinsic Raman label(s)
Foxy	*Fusarium oxysporum* isolate 405
FWHM	Full width at half maximum
GMR	giant magnetoresistance
IgG	immunoglobulin G
IR	infra-red
LC	liquid chromatography
LOD	limit of detection
LSPR	localized surface plasmon resonance
mAb(s)	monoclonal antibody(ies)
MALDI	matrix-assisted laser desorption ionization

MBA	4-mercaptobenzoic acid
MBN	4-mercaptobenzonitrile
mCRPC	metastatic castration-resistant prostate cancer
MP	4-mercaptophenol
MS	mass spectrometry
NBT	4-nitrobenzene thiol
NCBI	National Centre for Biotechnology Information
NHS	N-hydroxysuccinimide
NIR	near infra-red
NP(s)	nanoparticle(s)
NRRL	United States agricultural research service culture collection
NT	2-napthalene thiol
pAb(s)	polyclonal antibody(ies)
PBS	phosphate buffer saline
PBST	phosphate buffer saline containing tween
PC3	Human Prostatic Carcinoma cells
PCa	prostate cancer
PDA	potato dextrose agar
ppm	parts per million
SAMs	self-assembled (adsorbed) monolayers
SERS	surface-enhanced Raman scattering
SPR	surface plasmon resonance

ROS	reactive oxygen species
RMS	root mean square
rpm	revolutions per minute
RRM(s)	Raman reporter molecule(s)
%RSD	percent relative standard deviation
TOF	time of flight
UV-vis	ultraviolet visible
QCμB	quartz crystal microbalance
VCaP	Human Vertebral-Cancer of the Prostate cells
YE	yeast extract
YGP	yeast extract, D-glucose and Bacto-peptone medium

List of Symbols

Å	Angstrom
λ_{max}	absorbance band maximum / position
$\Delta\lambda$	wavelength shift
ø	diameter
cm^{-1}	wavenumber
cP	centipoise
Da	Dalton
D_{hyd}	hydrodynamic diameter
g	gravity
d	adsorbed molecules effective thickness (nm)
l_d	electromagnetic field decay length (nm)
m	bulk refractive-index response of the nanoparticle(s)
n	refractive index
ν_s	stretch (symmetric)
δ_s	bend (symmetric)
KDa	Kilo Dalton
kV	kilo Volts
h	hour
min	minute

sec	second
°C	degrees Celsius
µ	micro
σ_{ext}	extinction cross section
σ_{abs}	absorbance cross section
σ_{sca}	scattering cross section
ε_r	real dielectric function
ε_i	imaginary dielectric function
ε_m	real dielectric function of surrounding medium
δ	chemical shift
L : D	light : dark conditions
MΩ-cm	mega ohm centimetre
N	nine
N/m	Newton / meter
M	Molar
S.D.	standard deviation
R^2	correlation coefficient
R^3	particle volume $(4/3\ \pi\ r)^3$
W	Watts
mW	milli Watts
µW	micro Watts
eV	electron volts

V	volts
v	version
X	solution concentration / solution strength / multiplication factor (times)

Chapter 1. Introduction

1.1. Research scope and objectives

Quantitative and qualitative detection of biomolecules is an ever-increasing global need. Results of such assays informs critical decision points ranging from industrial-scale operations (e.g., health, environment, and food) to personal care (e.g., glucose monitoring, pregnancy test). In health, bioassays with high specificity and high sensitivity are constantly in high demand. The scope of this research work demonstrates use of biologically synthesized (biogenic) spherical silver nanoparticles (B-AgNPs) as optical labels for detection of a prostate cancer biomarker, androgen receptor splice variant 7 (AR-V7), in a sandwich immunoassay platform with surface-enhanced Raman spectroscopy. This research work aims to reveal unique properties of biogenic nanoparticles and deliver on an unmet clinical need for prostate cancer, the world's second most commonly diagnosed cancer in men. Currently, an unmet clinical need is how to effectively sequence systemic treatments for men with advanced stages of prostate cancer disease. Recently, AR-V7 has been linked to resistance for two major hormonal therapies, enzalutamide and abiraterone. Detection of AR-V7 enables triaging to other systemic therapies (e.g., chemotherapy).

Experimental research objectives are: (1) Develop and optimize a method to biologically synthesize AgNPs; (2) Identify and characterize unique properties of B-AgNPs

in comparison to chemically synthesized counterparts; (3) Demonstrate feasibility of surface modification of B-AgNPs; and (4) Demonstrate application of B-AgNPs in a surface-enhanced Raman scattering (SERS)–based immunoassay for advanced prostate cancer.

This chapter will introduce pertinent topics that are fundamental to understanding use of nanoparticles as labels for bioanalyses. Topics briefly examined below are: (1) types of nanoparticles for (bio)analyses focusing on noble metal nanoparticles; (2) optical properties of noble metal nanoparticles focusing on silver; (3) noble metal nanoparticles for biosensing applications with emphasis on localized surface plasmon resonance (LSPR) and SERS; (4) biologically synthesis of silver nanoparticles; and (5) importance of the surface layer and its modification. A detailed introduction to prostate cancer and the investigated biomarker, AR-V7, is provided in chapter 5.

1.2. Nanoparticles for (bio) analyses

Nanoparticle (NP) labels are often used in bioassays to enhance selectivity and / or sensitivity in analyte detection. Figure 1–1 summaries the range of NP platforms (i.e., noble metals, silica, quantum dots), various transduction modalities (e.g., colourimetry, luminescence, SERS), and their limits of detection (LOD).[1] In defining a nanoscale particle, the most accepted size is ~ 100 nm in diameter.[1-2] Consequently, the surface area to volume ratio of a nanoparticle is substantially larger than the same material in bulk form. As size diameter of a NP decreases, the atoms at the surface become a larger fractional

component of the material.[1] Thus, the surface plays a stronger role in the physical and chemical properties exhibited. Unique physical and chemical properties displayed by nanoparticles are the heart of transduction modalities employed in biosensing platforms. Herein, I will focus on noble metal nanoparticles and their optical properties for biosensing applications.

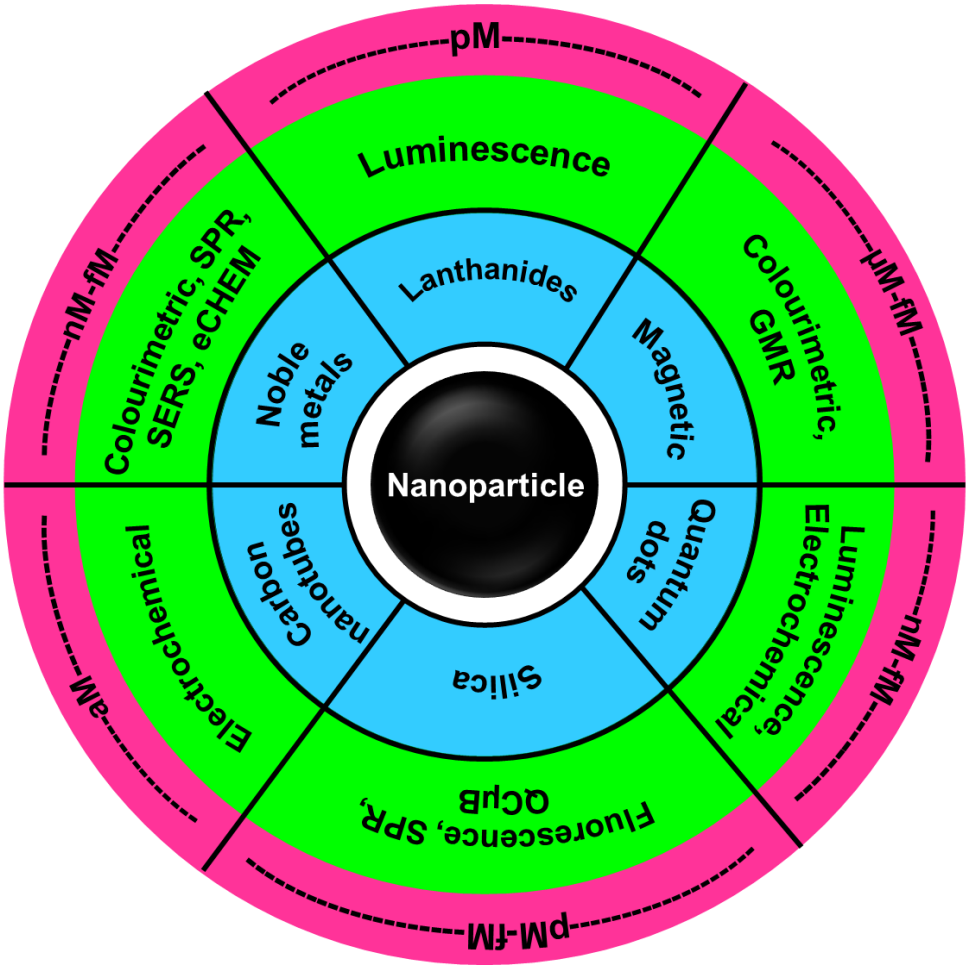

Figure 1–1. Type of nanoparticles (blue) used in detection strategies for signal transduction modalities (green) with reported limits of detection (pink) for each approach. SPR = surface plasmon resonance; SERS = surface-enhanced Raman scattering; eCHEM = electrochemical; QCμB = quartz crystal microbalance; GMR = giant magnetoresistance. Adapted from *Expert Review of Molecular Diagnostics* 2016, *16* (8), 883-395.[1]

1.3. Optical properties of noble metal nanoparticles

Colloidal noble metal nanoparticles, particularly gold and silver, have been of interest for centuries and have been widely used to vividly colour glass and ceramics.[3] The most famous example is the Lycurgus cup, which changes colour depending on the direction of light, was manufactured in the 4th or 5th century.[3-4] Brilliant red and yellow colours of stained glass of cathedrals in Europe are attributed to gold and silver nanoparticles, respectively. In 1857, Faraday reported an initial understanding of gold nanoparticles by investigating optical properties of thin films prepared from dried colloidal solutions.[5] Since Faraday's initial report, there has been continued strong interest in noble metal nanoparticles for their physical and optical properties resulting in broad applicability, particularly in biosensing platforms. The LSPR effects underpin scientific interest and use of NPs as optical labels in biosensing platforms.[6-9] These effects result in extremely high absorption and scattering (i.e., extinction) of light. Molar extinction coefficients of metallic NPs are several orders of magnitude higher than organic dyes and outperform fluorescent molecules as well, thus exhibiting promising application as labelling reagents.[10]

In 1908, Gustav Mie presented a solution derived from Maxwell's equations that describes the influence of electromagnetic radiation on spherical colloids.[6] According to Mie, when light impinges on a particle, the interaction can be summed by the extinction cross section σ_{ext}, which is made up of two terms, namely σ_{abs} (absorbance) and σ_{sca} (scattering) as shown by Equation 1–1.[6, 8]

Equation 1–1

$$\sigma_{ext} = \sigma_{abs} + \sigma_{sca}$$

The extinction cross section can be calculated from equation 1–2.[11]

Equation 1–2

$$\sigma_{ext} = \frac{12\pi R^3 {\varepsilon_m}^{3/2}}{\lambda}\left(\frac{\varepsilon_i}{[\varepsilon_r + 2\varepsilon_m]^2 + {\varepsilon_i}^2}\right)$$

The expression for σ_{ext} in Equation 1–2 reveals that the extinction cross section is dependent on particle volume (R^3), the incident wavelength (λ), the real and imaginary parts of the particle's dielectric function (ε_r and ε_i) and the real dielectric function of the surround medium (ε_m). The LSPR σ_{ext} maximum occurs when the denominator of the term in brackets approaches zero. This condition is satisfied at the wavelength where ε_i is small and $\varepsilon_r = -2\varepsilon_m$. Considering σ_{ext} dependence on the nanoparticle volume term (R^3), implies that larger nanoparticles have a higher extinction cross section and will result in greater absorption/scattering of light.

Figures 1–2 and 1–3 show the size and shape dependent properties, respectively, of colloidal silver nanoparticles. The LSPR absorption band for silver (and gold nanospheres) is found in visible region of the electromagnetic radiation spectrum. For example, in water, it is well known that ~ 20 nm diameter spherical silver particles have their LSPR centred at ~ 420 nm.[12] As particle size increase, the absorption band red-shifts as predicted by the Mie equations (Equations 1–1 and 1–2).[13-16]

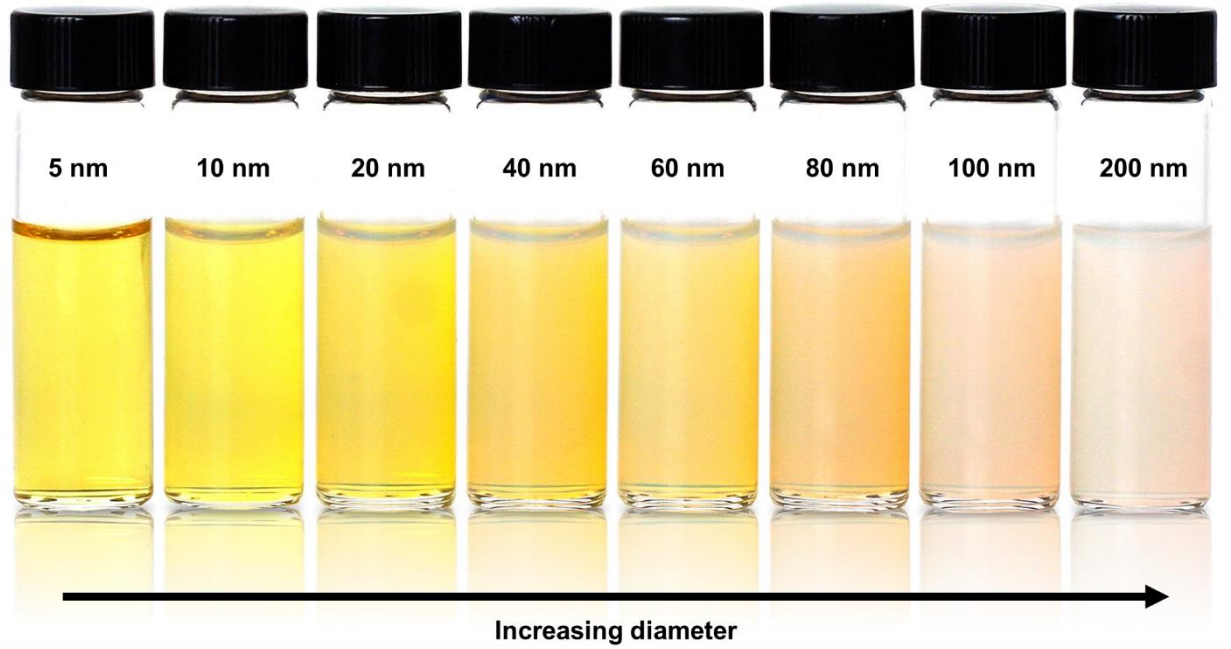

Figure 1–2. Size (diameter) dependent optical property of colloidal silver nanospheres in aqueous solution. Approximate diameters shown. Image obtained and used with permission from nanoComposix.[17] Copyright (2018) nanoComposix.

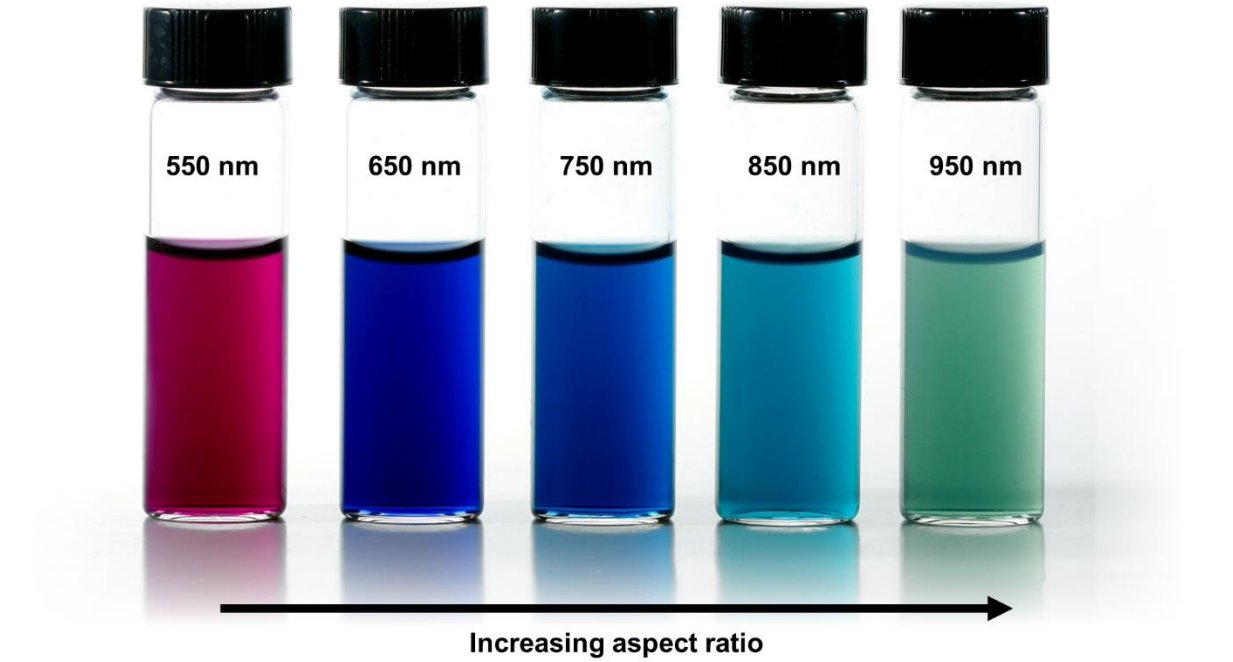

Figure 1–3. Shape (aspect ratio) dependent optical property of colloidal silver triangular nanoplates in aqueous solution. Approximate peak resonant wavelengths shown. Image obtained and used with permission from nanoComposix.[18] Copyright (2018) nanoComposix.

1.4. Noble metal nanoparticles for biosensing applications

Among noble metal NPs, silver and gold nanospheres are the most widely used biosensor labels. As shown in Figure 1–4, an exponential growth in scientific reports over the past 15 years have been dedicated to the use of silver and gold for biosensing applications. Widespread interest is being driven from two major aspects. First, nanoparticles can be produced with tunable sizes, tailorable optoelectronic properties, and straight-forward surface modification.[19-21] Second, such materials have been applied in a broad range of market sectors (e.g., human health diagnostics/imaging and therapeutic monitoring, environmental monitoring, electronics, and energy).[1, 22-25]

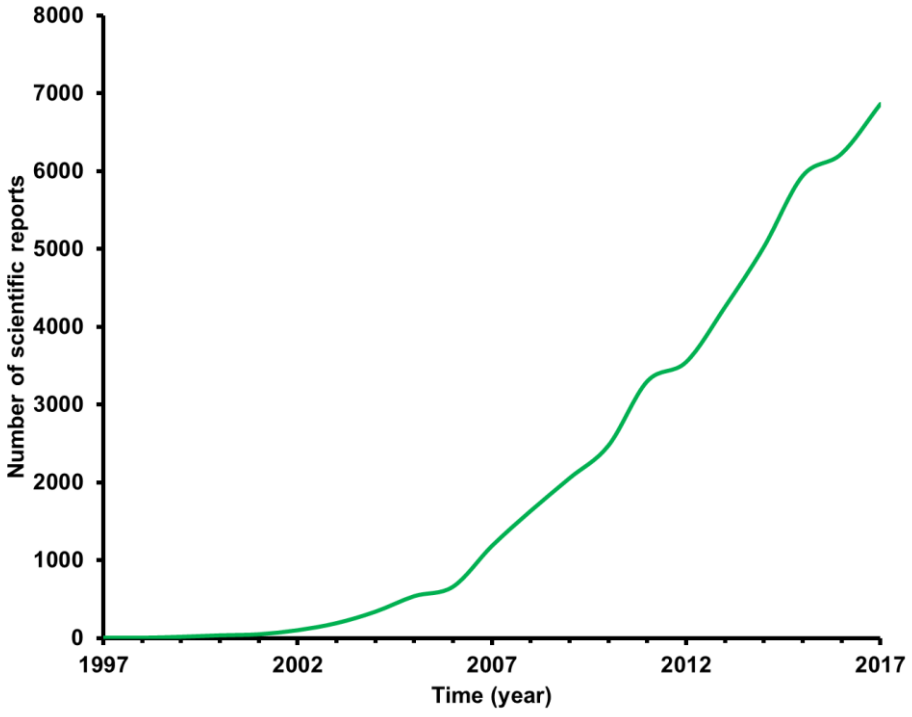

Figure 1–4. Web of Science search results on the use of gold or silver nanoparticles for detection in biosensing platforms. Search performed on 12 May 2018 using the following search parameters: (gold AND nanoparticle*) AND (biosens*); (gold AND nanoparticle*) AND (detection); (silver AND nanoparticle*) AND (biosens*); (silver AND nanoparticle*) AND (detection). Results shown have been aggregated.

Colloidal metallic nanoparticles are the simplest and most accessible substrates for plasmonic (e.g., SERS) applications.[26] However, there are two other major classes of SERS substrates such as planar metallic structures on planer substrates (e.g., glass, silica, metals) and metallic electrodes.[27] As previously stated, silver and gold NPs are most commonly used in the visible to near-infrared range (400 nm – 1000 nm). Gold NPs have received more attention compared to silver NPs for their longer periods of stability, acceptable biocompatibility, and well understood surface chemistry. Thus, there are several reviews and theses dedicated to AuNPs for chemical and biosensing applications.[10, 19, 24, 28-31] Previous reports have shown silver spherical nanoparticles to enhance SERS signals[32] by 10-fold to 100-fold higher than those for similar sized spherical AuNPs.[33] Therefore, I focus on silver NPs for higher electric field enhancements and lower absorptivity (more negative ε_r and lower ε_i) compared to Au for SERS application.[27]

Reproducible preparation and structural stability of SERS substrates is important for the reliability of surface assays.[34] To manage reproducibility and structural stability, the approach in this work uses spherical particle geometry that can be prepared more reproducibly and are structurally stable.[34] As a trade-off, spherically shaped particles do not have large enhancements compared to faceted nanoparticles (e.g., cubes, blocks)[35] and other types of nanostructured materials (e.g., nanocavity arrays, nanostructured metal surfaces, and porous metal films).[34, 36] However, this approach builds on the merits of robust quantitative SERS consistent with other laboratories conducting SERS-based analyses.[32, 34, 37-39]

Spherical silver particles are typically synthesized by reduction of silver nitrate ($AgNO_3$) in the presence of a reducing agent (e.g., $NaBH_4$, ethylene glycol[40]) and a stabilizing agent (e.g., anions, polymers, surfactants) to avoid NP aggregation. A popular method is a Lee-Meisel method published in 1982.[41] In this method, $AgNO_3$ is reduced with $NaBH_4$ and sodium citrate. This simple method allows for control over size distribution and stability. Therefore, paving the way for basic studies or biosensing applications.

A variety of signal transduction mechanisms have been demonstrated in biosensing platforms using silver or gold NPs. Relevant to the work in this thesis, the following sections expand on LSPR and SERS. Other referenced examples are: electrochemical,[42-44] fluorescence quenching,[45] quartz microbalance,[46-47] and surface plasmon resonance.[48-50]

1.4.1. Localized surface plasmon resonance (LSPR)

As depicted in Figure 1–5, the LSPR is a characteristic optical property of noble metal NPs that occurs when incident light is resonant with the collective oscillations of conduction electrons of the NP.[51] This condition occurs when the NP size is much smaller than the impinging wavelength of light ($NP_{radius}\ \lambda^{-1} < 0.1$).[9] The underlying sensing principle is that the extinction spectrum of noble metal NPs is dependent on NP shape, size, inter-particle distance, dielectric properties of the nanomaterial, and dielectric properties of the surrounding medium.[9, 51-53] Sensitivity to these aspects allows for the detection of binding events to the NP ($\Delta\varepsilon_m$; refractive index sensor) or aggregation of NPs (Δ inter-

particle due to surface plasmon coupling; colourimetric sensor) to be monitored by extent of λ_{max} shift.[9, 54] Thus, LSPR based biosensors offer similar merits as SPR based biosensors with added benefits such as higher spatial resolution and faster response time.[39, 51, 55] Formats for such assays involve either suspension of metallic NPs or LSPR sensors on planar substrates (e.g., glass, paper, plastics).[39] Planar formats have received more attention than colloidal formats due to NP stability concerns. Colourimetric sensing involves aggregation of silver NPs of appropriate sizes that typically results in a visible colour change from yellowish to brownish at low (nM) concentrations.[39] In the extinction spectrum, aggregation of metallic NPs is observed as a red-shift in λ_{max} and broadening on the surface plasmon band largely due to inter-particle plasmon coupling.[10, 56] Many LSPR sensors using metal nanospheres have been developed for detection of large biomolecules, such as DNA and proteins.[54, 57-61]

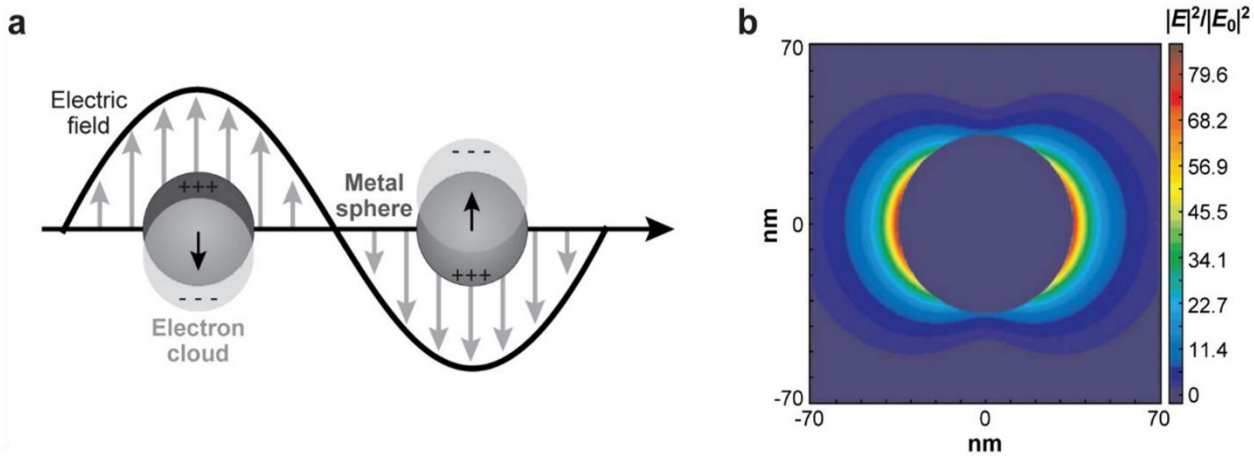

Figure 1–5. Localized surface plasmon resonance effect of a spherical metal nanoparticle. (a) Illustration of the collective oscillations of conduction electrons. (b) Extinction efficiency (ratio of cross section to effective area) of a spherical silver nanoparticle of 35 nm radius in vacuum $|E|^2$ contours for a wavelength corresponding to the plasmon extinction maximum; peak $|E|^2 = 85$. Electric field is perpendicular to the incident light. Reproduced with permission from *Annual Review of Analytical Chemistry* **2008**, *1*, 601–626.[62]

Drawing from the principles of LSPR of spherical metal NPs, this thesis focuses on biogenic silver NPs as an optical label in a sandwich format immunoassay with a SERS readout.

1.4.2. Surface-enhanced Raman scattering (SERS)

In 1928, Raman and Krishnan discovered a new type of weak irradiation known as Raman scattering, which is used as a vibrational spectroscopic technique.[63] The cause of weak Raman signals was later determined to be a result of only 1 in 10^6 – 10^8 inelastically scattered photons.[27, 62-65] In 1974, Fleischmann and co-workers first reported high Raman signal intensities with pyridine adsorbed on a rough silver metal electrode.[66] The authors concluded that an increase in surface coverage led to enhanced signal intensities. In 1977, Van Duyne and Jeanmaire concluded that the enhanced signal intensities is due to an electric field effect.[67] Concurrently, Albrecht and Creighton independently postulated another mechanism for enhancement involving chemical effects.[68] Collectively, these three discoveries established the field of SERS. The SERS effect is observed for molecules on or near the surface of metallic nanostructures that can support localized surface plasmon resonances (i.e., SERS substrate).[64] SERS substrates are typically rough metal substrates, which may be rough electrodes, thin films, or NPs. As previously stated, colloidal NPs are most popular for quantitative assays.[69] SERS signals are several orders of magnitude higher than in conventional Raman scattering, providing high sensitivity required for bioanalytical and biomedical applications.[64] Signal enhancement factors of 10^4 –10^6 compared to conventional Raman have been reported.[62, 70-72] Additional enhancement

(potentially up to $10^{11} - 10^{14}$) can be achieved under localized resonance between the analyte and the excitation wavelength leading to single molecule detection,[69, 71, 73-74] rivalling the performance of fluorescence measurements.[75]

The SERS phenomenon has been attributed to two primary mechanisms; electromagnetic (EM) enhancement and chemical enhancement (CE).[67-68, 76] Electromagnetic process dominates the contribution to the SERS phenomenon. This process arises from collective oscillation of the conduction electrons (i.e., LSPR) that results when a metal is irradiated with light.[75] When an adsorbate interacts with the LSPR, the amplified EM field results in an enhancement of Raman bands. This enhancement has a strong distance dependence between the adsorbate and surface, which varies inversely with the 10^{th} power of the distance from the surface.[62] Electromagnetic theory predicts that molecules on or very close (≤ 10 nm)[77] to the metal surface experience enormous field enhancement.[27, 62] Adsorbate surface coverage and orientation on metal surface are also play important roles in signal enhancement.[65] The EM enhancement mechanism partially explains aspects of the SERS phenomenon. Another contribution to SERS is a chemical effect. This is based on a charge-transfer mechanism between the metal and adsorbed scattering molecule. Consequently, a two-way transfer of electrons from the adsorbate to surface occurs and vice versa.[65] Due to an increase in molecular polarizability, the Raman signal is enhanced by an order or two of magnitude. As described by Goodacre and co-workers, there is still debate on the underlying mechanisms that are responsible for SERS (see papers in Themed Collection: Surface Enhanced Raman Scattering, *Faraday*

Discussions, **2017**, *205*, 1 – 626).[65, 78] However, this has not stopped SERS being used in a vast area of applications.[12, 64, 69, 75, 79-92]

SERS applications have largely been driven by lower Raman instrument costs with different system configurations (e.g., fibre optics), high power lasers, improved detectors, and field-deployable capability. In addition, controllable fabrication of SERS substrate paved the way for sensitive and reproducible measurements. To achieve high signals (i.e., high sensitivity) SERS labels often exploit strong Raman scattering of aromatic molecules called Raman reporters. Preparation of extrinsic SERS labels will be discussed in detail in chapter 4. SERS labels offer four main advantages over other optical probes, such as organic fluorescent dyes and quantum dots (QDs).[64] First, each label is coated with a large number of reporter molecules ($10^3 – 10^5$).[75] Therefore, each individual binding event results in an amplified signal response. Second, Raman vibrational bands exhibit narrow line width (~ 1 nm) compared to fluorescent bands (~ 50 nm). This allows for Raman labels to be multiplexed. Third, extremely short lifetimes of Raman scattering minimizes photo-bleaching, energy transfer, or quenching of Raman reporters in the excited state; rendering high photostability. Fourth, optimal contrast can be achieved using red to near-infrared (NIR) excitation to minimize the disturbing autofluorescence of cells and tissues, enabling SERS labels to be used for non-invasive imaging in living objects.[64]

In applying colloidal nanospheres as a SERS labels, two important factors to consider are: size (diameter) and colloidal stability (i.e., inter-particle distance). To note, there are

other factors to consider, however relevant emphasis is placed on size and colloidal stability. Size of silver nanopheres have been shown to play a crucial role in SERS signal enhancement.[93-94] Abale-Cela and co-workers explain the electromagnetic (EM) field intensity is strongly dependent on the number of electrons excited, which relates to the volume of the nanoparticle.[33] The upper size limit is influenced by radiative damping effects,[33] which become increasing significant as particle size is increased (> ø250 nm). The optimal size range suggested is ø20 nm – ø100 nm.[95-96] Another important factor to consider is colloidal stability.[97] As discussed above in the LSPR section, inter-particle spacing influences the plasmon coupling. Aggregated NPs can also lead to irreproducibility issues. SERS labels that employ Raman reporter molecules (for signal amplification) and a biorecognition element (e.g., antibodies) for selectivity are required to maintain colloidal stability throughout the modification process. Thus, a hypothesis is that biologically produced silver nanoparticles will have enhanced colloidal stability compared to chemical counterparts due an intrinsic biomolecular surface layer (corona) deposited at the time of synthesis.

1.5. Biogenic silver nanoparticles (B-AgNPs)

The interest here in biogenic nanoparticles is to explore the possibility of using these materials for SERS-based bioanalyses. Currently, there are only a few reports in the literature that have explored biogenic nanoparticles as SERS labels.[98] This relatively unexplored field presents an exciting opportunity. Guiding the approach towards SERS bioanalyses is a large body of knowledge and applications amassed with chemically

synthesized nanoparticles. As mentioned in the previous section, a putative advantage of biogenic nanoparticles over chemical counterparts is the inherent surface layer (corona). This surface layer is believed to play a role in colloidal stability and is viewed as a modification scaffold. Details on the surface layer of nanoparticles and modification are presented in sections below. Prior to this, it is important to establish a foundation in the biosynthetic process of producing nanoparticles. Figure 1–6 presents a visual overview of the major steps involved to produce biogenic silver nanoparticles. The final product showing a colloidally stable dispersion of nanoparticles with a characteristic yellowish brown colour consistent with silver is shown in the lower panel of Figure 1–6d.

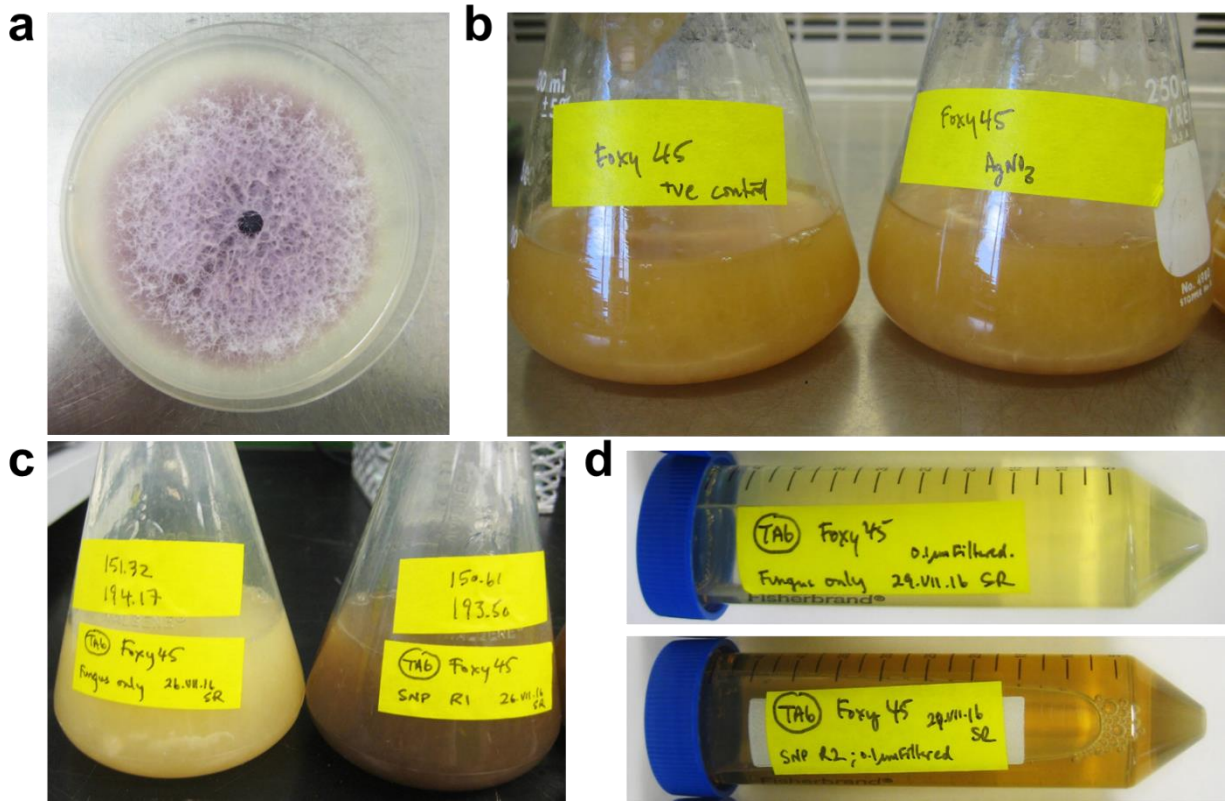

Figure 1–6. Representative images of major steps involved in the production of ~ ø30 nm silver nanoparticles using *Fusarium oxysporum*. (a) Top down image of a seven day old *F. oxysporum* culture on potato dextrose agar. This culture stage is used to start liquid cultures shown in (b). Inoculum plug is located at the centre. (b) Liquid cultures of *F. oxysporum* after four days incubation without $AgNO_3$. This step is required to produce fungal biomass that can be separated from growth media prior to $AgNO_3$ incubation. (c) Liquid culture of *F. oxysporum* with and without $AgNO_3$ after exposure to heat (~ 45°C) for three days. Fungus control flask (left) does not contain $AgNO_3$. Right side flask contains $AgNO_3$. (d) Final product after fungal filtration. Colloidal silver nanoparticle dispersion shown in lower image.

Microorganisms are widely viewed as self-organized systems that are capable of autonomously synthesizing molecules on a nano- and micro-scale in a highly selective manner. Various microorganisms, such as fungi and bacteria, have evolved resistance mechanisms against metallic ions that involve oxidation-reduction reactions.[99-103] As such, they are becoming increasingly popular candidates for metal nanoparticle synthesis.[101-103]

A primary advantage fungi have over other planktonic microorganisms and plants is their ability to tolerate high concentrations of metal ions.[104] This is a result of their inherent ability to produce higher protein titers that function to reduce metal ions to less toxic forms.[102, 104] This reductive process is facilitated by enzymes (i.e., reductases) and perhaps cytochromes or other electron transporters present in the cell wall, cytoplasmic membrane, or within the cytoplasm.[102-103, 105-106] Thus, fungal organisms can be selected on the basis of highest nanoparticle localization, either intracellular or extracellular.

Production of nanoparticles by a variety of fungal organisms has been explored. Due to their antimicrobial activity as well as their optical properties, AgNPs have been the target of many of these investigations. Fungal organisms such as *Aspergillus fumigatus*, *Aspergillus flavus*, *Fusarium semitectum* and *Penicillium fellutanum* have all shown the ability to produce AgNPs with somewhat controllable shape and size.[107-110] The fungus *Fusarium oxysporum* has also been shown to produce Ag as well as Au and CdS nanoparticles.[111-113] Relevant to the present work, Sastry and co-workers were first to show that AgNPs are produced extracellularly by *F. oxysporum*.[113] Duran et al. proposed a mechanism for AgNP production by *F. oxysporum* that involves a nitrate–dependent reductase and a quinone-based redox shuttle.[105] Recently, AgNPs from *F. oxysporum* have been employed as antifungal agents[114] and as labels for cellular imaging.[98] These previous reports indicate that *F. oxysporum* is able to produce stable AgNPs that can be valuable for a variety of applications.

1.5.1. Surface layer or corona of nanoparticles

The surface layer is believed to be a unique difference between biologically synthesized NPs and chemically synthesized NPs. Chemically synthesized NPs are typically capped with citrate ions or a surfactant species that affords colloidal stability. Whereas, the surface chemistry of biogenic NPs is complex with biomolecules and can be exploited for specialized applications.[98] Currently, our understanding of the surface layer of biogenic NPs is limited.

Over the past decade, there has been tremendous interest within the scientific community on understanding the influence of adsorbed biomolecules on nanoparticles.[115-125] Cedervall and co-workers first described a "protein corona," which later became "biocorona" of nanoparticles; and suggested it to define the biological identity of nanoparticles.[115, 120, 126-127] Consequently, impact of the surface layer with the surrounding environment can be beneficial or detrimental.[128-130] Understanding the chemical and physical makeup of the surface corona enables researchers to predict interactions within an environmental matrix.[131-132] There are several reports in the literature that discuss chemically synthesized nanoparticles that are deliberately exposed to a variety of protein matrices, such as the use of cationic gold nanoparticles exposed to serum.[132] In this thesis, attention is focused on the inherent surface layer of biologically synthesized nanoparticles. Within this context, many researchers have previously purported that the surface layer of biogenic nanoparticles consists of proteins.[104-105, 133-134] Though several techniques have been used to probe the surface layer, the current body of evidence is inconclusive in

providing structural and compositional details. Currently, there are no reports describing the surface layer of biogenic AgNPs providing both direct and indirect structural and compositional evidence. To this end, chapter 3 provides systematic evidence of the surface chemistry of biogenic AgNPs produced by *F. oxysporum.* Understanding the surface chemistry enables modification to further advance towards a SERS-based biosensing platform.

1.5.1.1. Surface modification

Though bare (unmodified) nanoparticles can be used for direct SERS measurements, [135-136] typically SERS substrates are modified for indirect (extrinsic) measurements. Schlücker summarizes two important components of an extrinsic SERS label, albeit Raman reporter molecules (Raman labels) and a biorecognition agent.[64] Raman reporter molecules allow for enhanced sensitivity and simple identification. Biorecognition agents such as oligonucleotides (DNA / RNA) or antibodies (protein) are used for target specificity.[64, 69]

Modification strategies are typically derived from modification schemes for planar substrates and applied to surface modification of nanoparticles. Through this approach, well understood systems can be applied and extended to a new substrate. Thus, established techniques for modifying planar gold will be extended to biogenic silver nanoparticles.

A popular method to modify gold is through thiol self-assembled monolayers (SAMs).[137] In this system, a sulfur head group of a thiol molecule binds to gold while the other end of the molecule, the terminal group, can be tailored to meet a specific surface functionality. In 1983, Nuzzo and Allara first demonstrated spontaneous formation (self-assembly) of thiol monolayers by adsorption of disulfides on gold.[138] Since this initial demonstration, a broad range of commercially available aryl and alkyl thiols with numerous terminal functional groups have enabled applications ranging from molecular electronics[139-140] to biomolecule immobilization.[141-142] Beyond gold, thiols have also been used to coat a variety of other substrates such as silver, platinum, and copper.[137, 141, 143-144]

Major benefits of using thiols to modify gold and silver surfaces include ease of use, reproducible film formation, and flexibility of the terminal group allowing for expanded capabilities.[141] Figure 1–7 shows a scheme of an aryl thiolate monolayer formation on gold. Thiolate film formation consists of several steps including diffusion to the surface and re-arrangement into a crystalline film.[141] Generally, thiols and disulfides are understood to adsorb to gold surfaces as thiolates.[141] This understanding is due to the strength of the sulfur-gold interaction reported to be ~ 50 kcal mol^{-1}, which is stronger than physisorbed interaction.[141] Thiolate films have been documented on gold nanoparticles during synthesis as capping agents and in the modification of preformed AuNPs.[145-146]

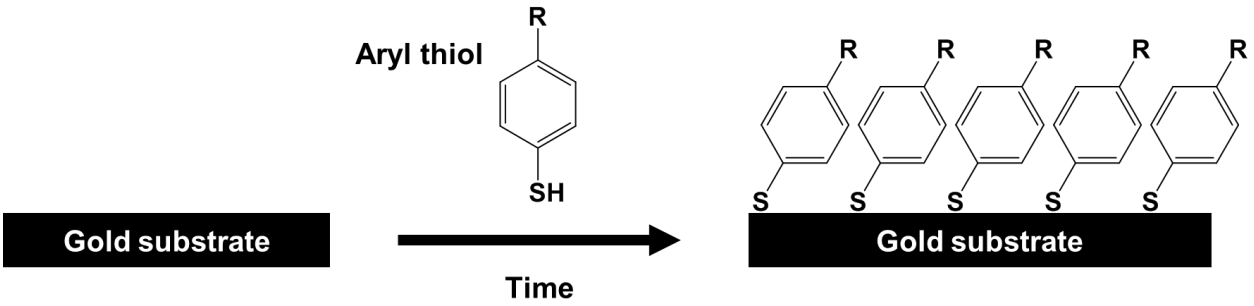

Figure 1–7. Spontaneous self-assembly of aryl thiols on gold forming a well-ordered monolayer.

Type of thiol used for modification plays a role in crystallinity. Long alkanethiols (C ≥ 9) produce more densely packed, organised structures stabilised by van der Waals interactions between the alkyl chains.[147] Monolayers on silver are structurally related to those formed by adsorption on gold, but differ in orientation.[137, 143-144] Depending on the chain length, *n*-alkanethiol molecules typically orient themselves tilted with respect to the surface normal on gold (20° – 30°) and silver (10° – 15°) to maximize intermolecular forces.[137, 144, 147-148] Collectively, thiol chemistry provides a robust foundation to approach modifying the surface of biogenic nanoparticles with thiol-based Raman reporter molecules.

For target specificity, antibodies are used in this work. Two common strategies for antibody conjugation to SERS substrates are: (1) covalent attachment via, for example, a bifunctional cross linker with N-(3-dimethylaminopropyl)-N'-ethylcarbodiimide hydrochloride (EDC) / N-hydroxysuccinimide (NHS) ester coupling via lysine residues[149-

[150] or (2) electrostatic attachment.[75, 151-152] Detailed preparation of extrinsic biogenic SERS labels is presented in chapter 4.

1.6. Thesis outline

This thesis contributes in two major fields. First, the field of biogenic nanoparticles by detailed investigations of the inherent surface layer (corona). Second, the field of prostate cancer by advancing a prognostic and predictive immunoassay that uses AgNP-labels and surface-enhanced Raman spectroscopy for the detection of AR-V7.

Chapter 2 explores biological synthesis of AgNPs from several isolates of *F. oxysporum* representing different collection parameters; notably host/substrate, life history, and geographic origin. Such information is considered pertinent when using microorganisms for reliable nanoparticle synthesis and optimization. Control of final product characteristics is gained through isolate selection and culture conditions such as temperature and pH. A direct comparison between biologically synthesized AgNPs (B-AgNPs) and commercially available, chemically synthesized AgNPs is presented. Highlighted is a potential advantage of the organic surface layer inherent to B-AgNPs in terms of colloidal stability and application development.

Chapter 3 characterizes the surface corona of silver nanoparticles produced by *F. oxysporum*. Examination the surface corona of biogenic silver nanoparticles is valuable

towards application development and understanding *in vivo* interactions. The approaches involves both *in situ* analyses of silver nanoparticle dispersions (indirect) and desorption of the surface corona (direct). Results presented show evidence for the surface corona thickness, chemical composition, and relative chemical abundance. Highlighted is the differences between our approaches and discuss the implications of each. Also highlighted is contrasting results of the surface layer and discuss implications from an ecological perspective. This may benefit a mechanistic understanding.

Chapter 4 advances the functionality of B-AgNPs towards a surface-enhanced Raman scattering (SERS) sandwich immunoassay. Contained within this chapter is a collection of experiments to demonstrate controlled surface modification of B-AgNPs by adding Raman reporter molecules and antibodies. In parallel, efforts to optimize a capture substrate that will be used in a SERS immunoassay will be presented. Evidence of modifying ø10 nm, ø20 nm, and ø30 nm B-AgNPs with five different Raman reporter molecules in turn with control is demonstrated. Subsequent addition of IgG antibodies (anti-androgen receptor full length, anti-AR-FL) is demonstrated to add selectivity to the Raman labels. This paves the way for selective detection of protein biomolecules. Successful modification is evidenced by UV-visible extinction and Raman spectroscopy results. With each modification step, B-AgNPs were generally stable with few exceptions that are discussed. Optimization of substrate was performed through plasmonic coupling experiments to determine if 300 nm thick Au or 300 nm thick Ag films provide higher Raman signal intensities. Based on these experiments, a biochip consisting of multiple

metal film spots deposited onto a standard microscope slides were fabricated with the aim of clinical use.

Chapter 5 reports the successful detection of AR-V7 protein at low levels in cultured prostate cancer cells and in human serum using a SERS-based sandwich immunoassay. Calibration results comparing AR-V7 protein and AR-V7 mRNA expression levels are reported. This work uses enhanced expression of AR-V7 in cultured prostate cancer cells to verify presence of AR-V7 protein. To establish a calibration curve and a linear range, detection of AR-V7 protein is evidenced and compared with AR-V7 mRNA results from cultured prostate cancer cells. To this end, a prospective pilot scale study to investigate the clinical utility of a SERS-based immunoassay by using a blinded retrospective cohort of seven mCRPC patients pre / post treatment with enzalutamide and / or abiraterone. The results demonstrate the ability to identify AR-V7 status (positive or negative) in mCRPC patients and provide quantitative measurements to enhance prognostic and predictive value. Furthermore, the results begin to demonstrate the potential of a SERS-based immunoassay to serve in an AR-V7 prognostic/predictive toolkit. Advancing this approach to the clinic and further enhancing the prognostic and predictive potential is also briefly discussed.

Chapter 2. Fungal isolate optimized for biogenesis of silver nanoparticles for enhanced colloidal stability

2.1. Introduction

Noble metal nanoparticles are widely featured in scientific literature and are the basis of a number of commercial products.[24, 153] Unique optical properties and high surface to volume ratio of metallic nanoparticles, such as gold and silver, are the impetus for many applications. In addition, the ability to synthesize metallic nanoparticles with controlled size and shape via straight forward chemical approaches allows researchers to obtain, either commercially or via in-house synthesis, sufficient quantities of these materials to apply in a wide range of experiments. While methods to chemically synthesize metallic nanoparticles have been finely tuned and widely applied,[154-158] there has recently been increased attention toward biologically produced nanoparticles.[159-160] Such particles are produced in aqueous media (often metal salts dissolved in water) with generally low toxicity and may possess chemical and physical properties that can be exploited in new or improved ways. In terms of surface chemistry, chemically synthesized nanoparticles are typically capped with citrate ions or some surfactant species that afford colloidal stability. The chemical makeup of the surface layer of biologically produced nanoparticles is more complex and can be targeted for specialized applications.[98]

Microorganisms are widely viewed as self-organized systems that are capable of autonomously synthesizing molecules on a nano- and micro-scale in a highly selective manner. Various microorganisms, such as fungi and bacteria, have evolved detoxification mechanisms against metals that involve oxidation-reduction reactions.[101-103] As such, they are becoming increasingly popular candidates for metal nanoparticle synthesis.[101-103] A primary advantage fungi have over other planktonic microorganisms and plants is their ability to tolerate high concentrations of metal ions.[104] This is a result of their inherent ability to produce higher protein titers that function to reduce metal ions to less toxic forms.[102, 104] This reductive process is facilitated by enzymes (reductases) present in the cell wall, in the cytoplasmic membrane, or within the cytoplasm.[102-103, 105] As such, fungal organisms can be selected on the basis of highest nanoparticle localization, either intracellular or extracellular.

Production of nanoparticles by a variety of fungal organisms has been explored. Due to their antimicrobial activity as well as their optical properties, silver nanoparticles (AgNPs) have been the target of many of these investigations. Fungal organisms such as *Aspergillus fumigatus*, *Aspergillus flavus*, *Fusarium semitectum* and *Penicillium fellutanum* have all shown the ability to produce AgNPs with somewhat controllable shape and size.[107-110] The fungus *Fusarium oxysporum* has also been shown to produce Ag as well as Au and CdS nanoparticles.[111-113] Relevant to the present work, Sastry and co-workers were first to show that AgNPs are produced extracellularly by *F. oxysporum*.[113] Duran et al. proposed a mechanism for AgNP production by *F. oxysporum* that involves a nitrate–dependent

reductase and a quinone-based redox shuttle.[105] Recently, AgNPs from *F. oxysporum* have been employed as antifungal agents[114] and as labels for cellular imaging.[98] These previous reports indicate that *F. oxysporum* is able to produce stable AgNPs that can be valuable for a variety of applications. However, thorough optimization of AgNP synthesis by *F. oxysporum* in terms of fungal isolate type as well as physical parameters such as temperature and pH has not been undertaken. In addition, a direct comparison between fungal produced AgNPs and commercial, chemically synthesized AgNPs has not been reported.

In this study, we explore biological synthesis of AgNPs from several isolates of *F. oxysporum* representing different collection parameters; notably host/substrate, life history, and geographic origin. We consider such information pertinent when using microorganisms for reliable nanoparticle synthesis and optimization. Control of final product characteristics is gained through isolate selection and culture conditions such as temperature and pH. We present a direct comparison between biologically synthesized AgNPs (B-AgNPs) and commercially available, chemically synthesized AgNPs. We highlight a potential advantage of the organic surface layer inherent to B-AgNPs in terms of colloidal stability and briefly discuss application development.

2.2. Experimental

2.2.1. Reagents and materials

All reagents and media used were analytical grade. Silver nitrate, ACS reagent, ≥ 99% was purchased from Sigma-Aldrich (lot# MKBD7719 V). Sodium chloride, ACS reagent, ≥ 99% was purchased from EMD (lot# TCO9C2EMS). Citrate-capped silver nanoparticle dispersions were purchased from Sigma-Aldrich (Oakville, Ontario, Canada, 10 nm lot# MKBR4545 V and 20 nm lot# MKBJ6307 V) and Nanocomposix (San Diego, California, USA, lot# DAG1159); each at a concentration of 0.02 mg/L. Particle size specifications ranged from 10 nm to 20 nm in diameter. Deionized (DI) water with a resistivity of 18 MΩ-cm was used for all aqueous preparations.

2.2.2. Screening fungal isolates

Twelve *F. oxysporum* isolates were evaluated for extracellular AgNP production (Table 2–1). Isolates were selected based on differences in host, life history, and geographic region. Each isolate was initially cultured on potato dextrose agar (PDA) under light ((16 : 8 h (h), light : dark (L : D)) at 23°C ± 2°C. As an intermediate step prior to incubating in silver nitrate solution, liquid medium was inoculated by removing a single 1 cm^2 solid PDA growth medium piece containing mycelium and conidia from a six day old culture of each isolate and transferring to a sterile 500 mL Erlenmeyer flask containing 100 mL of sterile 0.5% yeast extract (YE) broth. All inoculated flasks were incubated at 25°C ± 1°C under dark conditions with no shaking for 10 days.

After 10 days incubation, fungal biomass was separated from the culture broth by using sterile 50 mL centrifuge tubes and centrifuging at 9600 x *g* at 23°C for 20 min in an Eppendorf 5810R centrifuge. Settled biomass was washed twice with one volume of sterile deionized water, centrifuged for another 10 min and then weighed.

Harvested washed fungal biomass was added to 100 mL of sterile 1 mM aqueous silver nitrate solution in Nalgene polymethylpentene (PMP) conical flasks with screw caps at room temperature (23°C ± 2°C). After inoculating, all flasks were incubated at 25°C ± 1°C under dark conditions with no shaking for 14 days. A negative control containing only silver nitrate solution was maintained simultaneously under identical conditions.

Table 2–1. Description of *Fusarium oxysporum* isolates screened for biosynthesis of silver nanoparticles

Fungal identity	Host/substrate	Life history	Geographic origin	Internal accession #
Fusarium oxysporum	Cabbage	Plant pathogen	USA	112[a]
Fusarium oxysporum	Wheat	Saprophyte	Canada	180
Fusarium oxysporum	Barley	Saprophyte	Canada	181
Fusarium oxysporum	Canola	Plant pathogen	Canada	191[b]
Fusarium oxysporum	Banana	Plant pathogen	Australia	404[c]
Fusarium oxysporum	Pea	Saprophyte	Denmark	405[d]
Fusarium oxysporum	Canola	Plant pathogen	Chile	410[e]
Fusarium oxysporum	Canola	Plant pathogen	Canada	521
Fusarium oxysporum	Canola	Plant pathogen	Canada	522
Fusarium oxysporum	Cabbage	Plant pathogen	Canada	535[f]
Fusarium oxysporum	Canola	Plant pathogen	Canada	571
Fusarium oxysporum	Canola	Plant pathogen	Canada	840

[a]Originally obtained from American Type Culture Collection (identification #16600).
[b]Originally obtained from Agriculture and Agr-Food Canada (identification # 9A).
[c]Originally obtained from American Research Service/NRRL (identification #25603).
[d]Originally obtained from American Research Service/NRRL (identification #31074).
[e]Originally obtained from 20/20 Seeds (Alberta, Canada) (identification #346857).
[f]Originally obtained from Crop Diversification Centre (Manitoba, Canada) (identification #471).

2.2.3. Effect of temperature

Based on results of our screening trails (*vide infra*), we selected *Fusarium oxysporum* isolate 405 to move forward. Similar to our screening trials, *F. oxysporum* 405 was initially cultured on PDA in the dark for seven days at 23°C ± 2°C. As an intermediate step prior to incubating in silver nitrate solution, the liquid medium was inoculated by removing two 1 cm^2 solid PDA growth medium pieces containing mycelium and conidia from a seven day old culture of each isolate and transferring to a sterile 500 mL Erlenmeyer flask containing 100 mL of sterile 1% yeast extract, 1% D-glucose and 1% Bacto-peptone (YGP). Through experience gained in our screening trials, additional inoculum and medium design for our size control trials were selected to increase nanoparticle production by increasing fungal biomass. All inoculated plus control flasks were incubated in the dark at 23°C ± 2°C shaking at 150 rpm. After six days, fungal biomass was separated from the culture broth by centrifuging at 4000 rpm in sterile 250 mL bottles at 23°C for 10 min in an Eppendorf 5810R centrifuge. Settled biomass was washed once with sterile DI water, centrifuged, and weighed.

Harvested washed fungal biomass was added to 100 mL of sterile 1 mM aqueous silver nitrate solution in sterile Nalgene PMP conical flasks with screw cap lids at 23°C ± 2°C. After inoculating, all flasks were incubated either at: a) 25°C ± 1°C, b) 50°C ± 1°C or c) 75°C ± 1°C under dark conditions with shaking at 100 rpm for four days. In our screening trails, we noticed that the fungal mycelium would generally be localized to the medium surface unless cultures were shaken, which limited exposure of mycelium to silver nitrate to the

relatively small submerged portion of mycelium. Shaking allows for complete surface area exposure; however the revolutions per minute were purposefully maintained at a low rate to prevent possible intracellular nanoparticle formation.[161] Simultaneously, a negative control containing only silver nitrate solution and a positive control containing only fungus was maintained under identical experimental conditions. Trials were conducted three times.

2.2.4. Enrichment of nanoparticles

To separate and recover AgNPs, aqueous dispersions of AgNPs with fungi were transferred to sterile 50 mL centrifuge tubes and sonicated for 20 min at 23°C ± 2°C using a Branson 5510 ultrasonicator to separate nanoparticles from fungal mycelia post synthesis. After sonicating, aqueous dispersions with fungal mycelia were briefly vortexed and filtered using a sterile Millipore 0.45 µm Durapore polyvinylidene difluoride 250 mL vacuum filtration unit. Samples were stored in the dark at 4°C.

2.2.5. Effect of pH

Fusarium oxysporum 405 cultures were prepared as described above for size control trials. Six-day-old harvested washed fungal biomass was added to 100 mL of sterile 1 mM aqueous silver nitrate solution previously adjusted to either: a) pH 3, b) pH 5, c) pH 7 or d) pH 9 using either 0.2 M NaOH or 0.2 M HCl in sterile Nalgene PMP conical flasks with screw caps at 23°C ± 2°C. After inoculating, all flasks were incubated at 75°C ± 1°C under dark

conditions with shaking at 100 rpm for 24 h. AgNPs were separated from the biomass as described above.

2.2.6. Extinction spectroscopy

For screening experiments, bioreduction of Ag^+ in aqueous solution was monitored at room temperature using a Bio-Rad Microplate Manager, Version 5.2. Aliquots (0.2 mL) of suspension were periodically sampled and the absorbance measured at 405 nm, 450 nm, 490 nm and 540 nm. The maximum absorbance for AgNP solutions was at 405 nm. Aliquots of fungal cultures were briefly centrifuged (i.e., pulsed) to avoid spectrophotometric interference from the fungal biomass. Deionized water was used as the blank. Prior to the measurement, the plate was shaken for 5 sec.

For temperature experiments, all nanoparticle dispersions were diluted by a factor of 4 with deionized water before analysis. Extinction spectra were collected in absorbance mode on a double-beam Perkin Elmer Lambda 35 spectrophotometer. Spectra were scanned from 900 – 200 nm with a scan rate of 240 nm/min. Deionized water was used as the blank. Measurements were done at room temperature.

2.2.7. Scanning electron microscopy (SEM)

Samples of fungal mycelium were air-dried, mounted on specimen stubs with double-sided adhesive tape, sputter coated with gold/palladium and examined under Philips/FEI XL 30 SEM at 20 kV.

2.2.8. Energy dispersive spectroscopy (EDS)

A sample of fungal mycelium was air-dried prior to mounting on specimen stubs with double-sided adhesive tape and sputter coated with carbon and examined under a Zeiss EVO MA 15 LaB6 filament SEM. Backscattered images were taken using a silicon diode detector. Energy dispersive analysis was performed with a Peltier-cooled 10 mm^2 Bruker Quantax 200 Silicon drift detector with 123 eV resolution. Secondary electron images were obtained using an Everhart-Thornley detector. Working distance was 6.5 mm with an accelerating voltage of 10 kV.

2.2.9. Transmission electron microscopy (TEM)

A droplet of aqueous sample was deposited onto a Formvar 300 micron copper-coated mesh grid. After approximately one minute, excess suspension was wicked-off using Whatman filter paper and then the grid was air-dried at room temperature before analysis. All sample grids were examined under a Philips FEI Morgagni 268 TEM at 80 kV. Images were collected using a Gatan Orius charge-coupled device camera. High-resolution images

were collected by examining sample grids under a 200 kV JEOL 2200 FS field emission TEM equipped with an in-column omega type energy filter.

2.2.10. Dynamic light scattering (DLS)

Hydrodynamic diameter of AgNPs was determined by DLS or photon correlation spectrometry with a Malvern Zetasizer Nano-ZS. Results were collected with a 4 mW He-Ne laser set at 633 nm with a 173° back scattering angle and an avalanche photodiode detector. Measurements were performed under the following conditions: particle refractive index 1.590; particle absorption coefficient 0.013 for Sigma products and 0.118 for B-AgNPs (based on absorbance values recorded at 633nm); water refractive index 1.33; viscosity 0.8872 cP; and temperature 25°C; equilibrated for 120 sec.; 15 runs; n = 3 measurements.

The size distribution is calculated using an inverse Laplace transform algorithm and the hydrodynamic radii is calculated using Stokes-Einstein equation. Hydrodynamic diameter (D_{hyd}) reported represents the mean diameter based on intensity of scattered light. Values reported are an average of three measurements ± standard deviation.

2.2.11. Zeta potential (ZP)

Zeta potentials of AgNPs were determined by Malvern Zetasizer Nano-ZS based on electrophoretic light scattering. A 4 mW HeNe laser with 633 nm wavelength was used as the light source. All measurements were performed under the following conditions: temperature 25°C; equilibrated for 120 sec.; 20 runs; n = 3 measurements; Smoluchowski model.

2.2.12. Colloidal stability

Biologically produced and chemically produced silver nanoparticles with average size diameters of 10 nm and 20 nm were each mixed with aqueous 0.6 M sodium chloride to yield the following final sodium chloride concentrations: 0 mM (AgNPs 'as is'), 120 mM, 200 mM, 300 mM, 400 mM, 480 mM. Immediately after mixing, samples were inverted three times and measured in absorbance mode on a double-beam Perkin Elmer Lambda 35 spectrophotometer. Spectra were scanned from 800 – 300 nm with a scan rate of 240 nm/min. Deionized water was used as the blank. Measurements were done at room temperature and trials were conducted three times.

2.3. Results and discussion

2.3.1. Screening fungal isolates for production of silver nanoparticles

Although there have been previous reports on the generation of AgNPs by fungi,[107-110] including *F. oxysporum*,[113] an examination of a wide range of isolates has not been reported. One previous study reported AgNP production from several strains of *F. oxysporum*, however the strains were not compared with respect to the quantity, shape or size of the AgNPs produced.[105] Another report has documented an optimal set of culture conditions for AgNP production of a single isolate of *F. oxysporum*.[104] This later study is a useful point of reference. We believe a careful understanding of the organism, incubation conditions, and synthesized products are important for providing a path forward towards application development. Our results show that fungal organisms exhibit variability among isolates. We present our inter-isolate screening results and characterize AgNPs that were obtained from our highest yielding isolate.

Twelve *Fusarium oxysporum* isolates were evaluated that exhibited differences in substrate/host, life history, and geographic region. Screening these isolates involved probing the synthesis of extracellular elemental silver nanoparticles production at 25°C ± 1°C under dark conditions with no shaking for 14 days (Table 2–1). Figure 2–1 contains the results of the screening 12 *Fusarium oxysporum* isolates after exposure to $AgNO_3$ *in vitro* over 14 days for AgNP production. The inset of Figure 2–1 is a photograph showing the characteristic colour change of the solution from colourless to yellowish-brown that

can be detected as early as a few hours. It is well established that the yellow colour is due to the localized surface plasmon resonance (LSPR) of AgNPs.[108] All isolates studied induced a colour change when exposed to silver nitrate. Such colour change is consistent with previous reports.[105, 113, 162]

As the extinction (absorbance) peak widths were similar, magnitude of the extinction LSPR band of AgNPs at 405 nm was used to compare the output from the different isolates. Figure 2–1 contains a plot of the extinction as a function of incubation time. A negligible absorbance signal was recorded for 1 mM silver nitrate solution without fungal inoculum (i.e., negative control) throughout a 14 day period. All solutions that contained fungal isolates exhibited absorbance at 405 nm higher than the background, indicating production of AgNPs. No decrease in absorbance was observed implying that the nanoparticles were stable with no evidence of flocculation several weeks post reaction. However, Figure 2–1 shows that production over time varies considerably from isolate-to-isolate, despite all isolates belonging to the same fungal species. Of the isolates included in this study, *F. oxysporum* 405 synthesized the highest quantity of silver nanoparticles more rapidly over time compared to other *F. oxysporum* isolates. Based on our observations with *F. oxysporum* and other fungal organisms (i.e., *F. commune, Aspergillus flavus*, and *Beauveria bassiana*) that we tested (data not shown), we hypothesize saprophytic organisms are more effective at reducing aqueous metals than pathogenic organisms. We speculate saprophytes may be more often exposed to aqueous metals in the environment, thus rely on efficient detoxification mechanisms for survival; whereas pathogens commonly

associated with host disease may be less efficient at detoxification. We recognize that this hypothesis needs further testing, however, in moving forward in this work, we selected *F. oxysporum* 405, a saprophyte, for further evaluation based on its enhanced AgNP production.

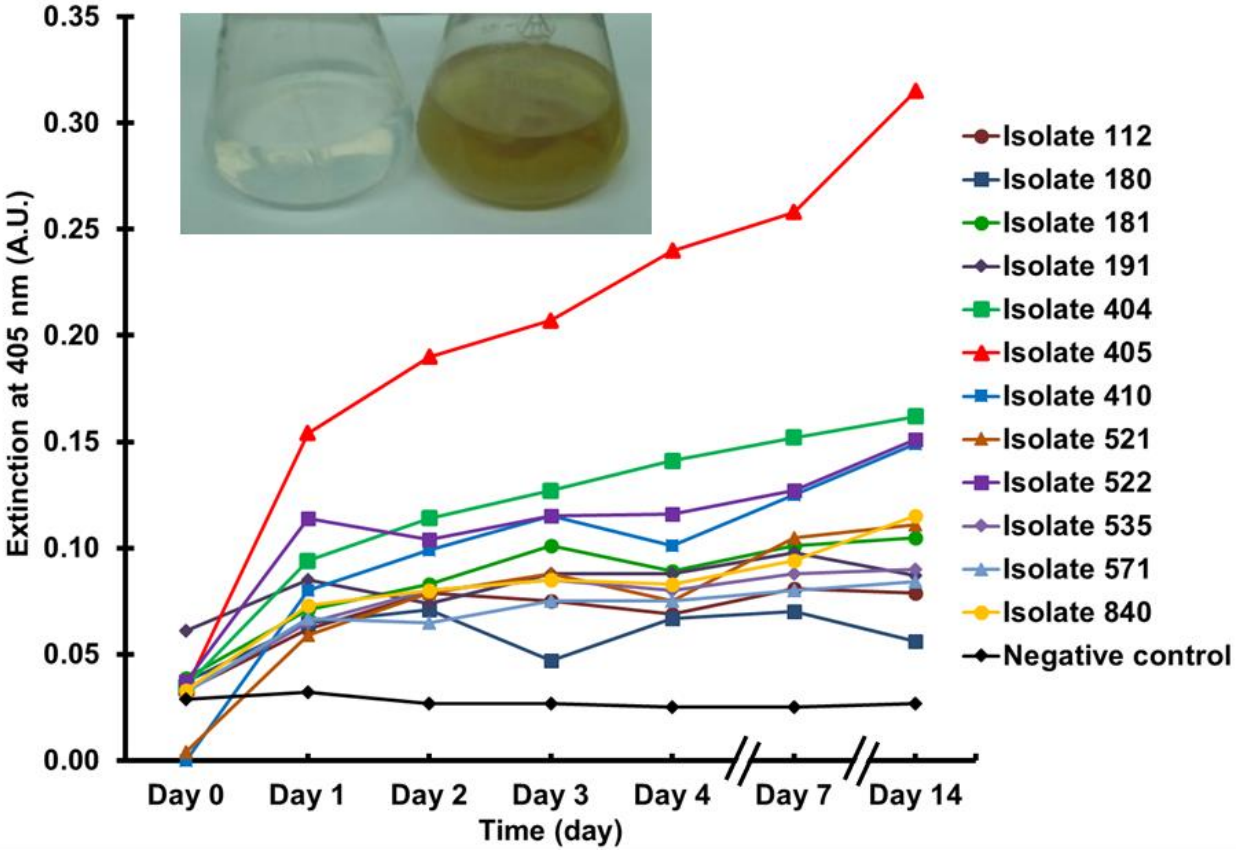

Figure 2–1. Extinction at 405 nm (λmax) as a function reaction time of 1 mM $AgNO_3$ solution with *Fusarium oxysporum* isolates cultured at 25°C in the dark with no shaking for 14 days. Inset shows visual production of silver nanoparticles. Flask with colourless solution (left) is 1 mM silver nitrate solution without fungal inoculum (negative control). The yellowish-brown colour (right) is primarily due to characteristic surface plasmon resonance of silver nanoparticles.

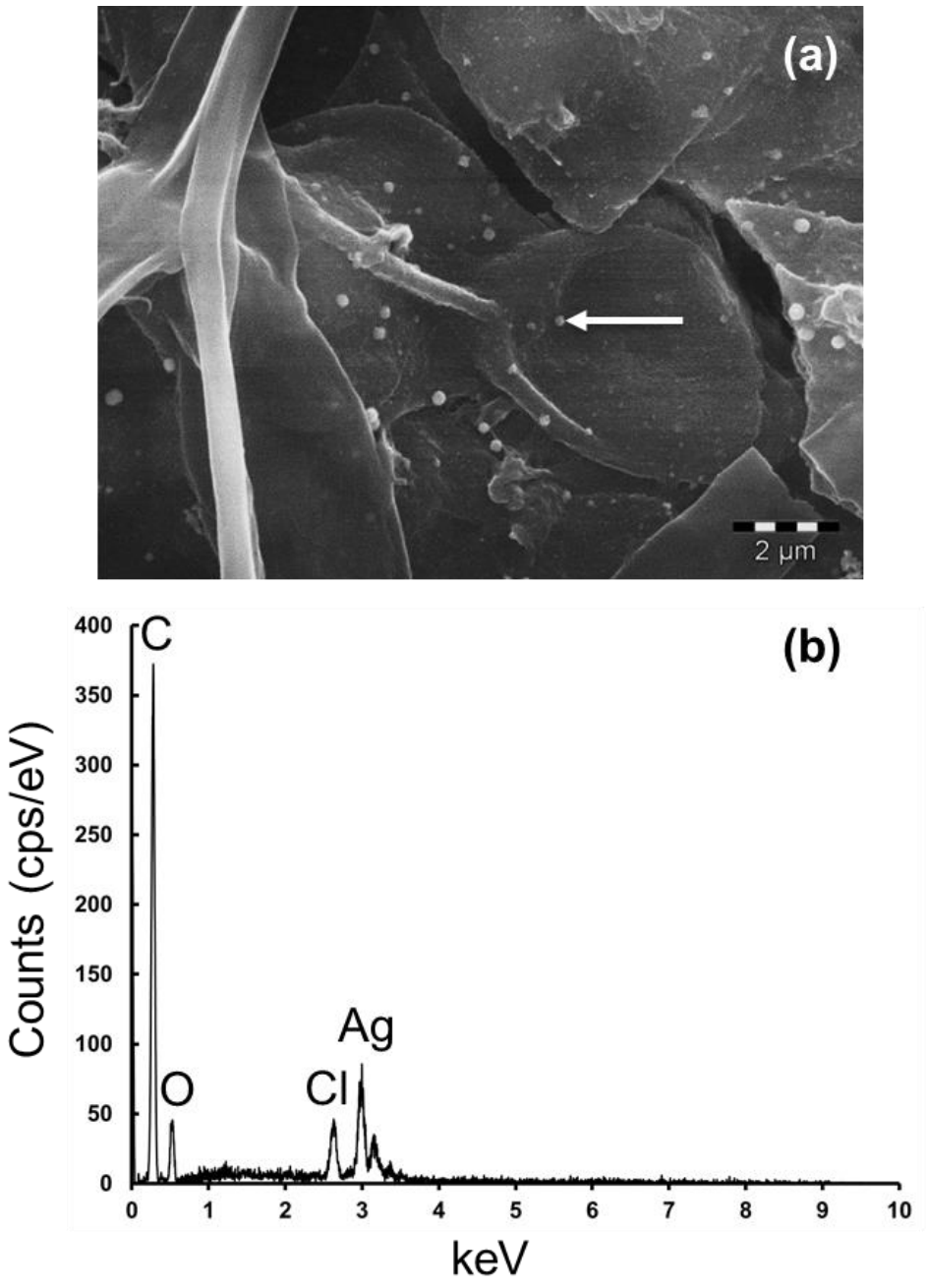

Figure 2–2. Scanning electron micrograph of *Fusarium oxysporum* 405 mycelia incubated in 1 mM silver nitrate solution at 25°C in the dark with no shaking for 14 days. (a) Individual silver nanoparticles deposited on the surface of fungal mycelia (arrow). Note: Fungal mycelia has collapsed due to air-drying. (b) Energy dispersive X-ray spectrum of silver nanoparticles from spot profiles to confirm elemental silver.

Figure 2–2 shows the morphology of nanoparticles synthesized by *F. oxysporum* 405 and confirms elemental silver composition. Figure 2–2a is an SEM image showing AgNPs on the surface of the fungal mycelium. The particles appear spherical and uniform in morphology (see discussion of Figure 2–4). This is in contrast to initial work with *F. oxysporum* wherein the morphology of AgNPs was highly variable and featured spheres and triangles.[105, 113] A more recent study shows predominantly spherical AgNPs produced by *F. oxysporum*[98] and AgNPs produced from other fungal species are primarily spherical.[107-110] The particles observed in Figure 2–2a are well separated on the surface of the fungus with no apparent aggregation. Figure 2–2b is an energy dispersive X-ray spectrum containing strong emission signals from silver in biogenic AgNPs. Weaker X-ray emission signals from sulfur (S), chlorine (Cl), oxygen (O) and phosphorus (P) may originate from biomolecules (e.g., proteins or glycans) that are bound to the surface of silver nanoparticles[163] or from organic fungal tissue. Strong carbon signals are due to a combination of organic fungal tissue and the carbon coating of sample prior to analysis. These results confirm production of spherical AgNPs by *F. oxysporum* 405.

2.3.2. Effect of temperature on the production of silver nanoparticles

A limited number of reports have examined the effect of temperature on fungal produced nanoparticles. Our interest is controlling quantity and size (*vide infra*) of AgNPs produced. Gericke and Pinches demonstrated that size of gold nanoparticles produced by two different fungi could be controlled by temperature.[164] A study by Kathiresan et al. showed a decrease in quantity of AgNPs produced by *Penicillium fellutanum* with

increasing temperature based on optical density measurements.[110] Birla et al. report a maximum production of AgNPs at elevated temperatures (80°C – 100°C) using the filtrate of *F. oxysporum* isolated from banana fruit.[104]

Figure 2–3 presents extinction spectra of filtered aliquots of the incubation solution consisting of 1 mM $AgNO_3$ with *F. oxysporum* 405 at three different temperatures after incubation for 3 days. The spectra for 75°C and 50°C contain a single LSPR band with maximum absorbances at 411 nm and 402 nm, respectively. These spectra show no evidence of aggregation. The spectrum for the 25°C solution does not exhibit a discernible band due to a low quantity of nanoparticles produced at that temperature and time. Although the width of the bands of the B-AgNPs (FWHM ~ 98 nm, ø20 nm) are greater than those of commercial, chemically produced AgNPs (FWHM ~ 68 nm, ø20 nm), electron microscopy analysis discussed below (Table 2–2) indicates that the polydispersity of biogenic AgNPs is similar to commercial AgNPs. A discussion of the LSPR band widths and positions is included below.

We can use the LSPR extinction magnitudes in Figure 2–3 to estimate quantity of AgNPs produced at different temperatures by considering nanoparticle size and corresponding extinction coefficient. As shown below, AgNPs produced at 25°C are significantly larger (diameter > 50 nm) than those produced at higher temperatures, with AgNPs produced at 75˚C exhibiting the smallest diameter (10 nm). Though extinction coefficients for AgNPs produced by *F. oxysporum* 405 have not been determined at this

time, extinction coefficients for citrate-capped AgNPs have been reported.[165] Larger nanoparticles exhibit higher extinction coefficients and the value for 50 nm particles is roughly 100 times that of 10 nm particles. Thus, it is reasonable to conclude that higher concentrations of AgNPs are produced at higher temperature. Based on extinction values for citrate-capped AgNPs, we estimate *F. oxysporum* 405 produces a concentration of 6×10^{12} particles/mL at 75°C and 3×10^{11} particles/mL at 50°C. We have also estimated B-AgNP concentration using ICP-MS to measure the total amount of silver (data not shown). This analysis yielded concentrations of 5×10^{13} particles/mL at 75°C and 4×10^{12} particles/mL produced at 50°C. Both analyses indicate that incubation at 75°C produces 10-fold higher concentration of B-AgNPs than at 50°C. These results are also consistent with those of Birla et al.,[104] who concluded that 40°C and 60°C are optimal temperatures based on amount and rate of AgNP production.

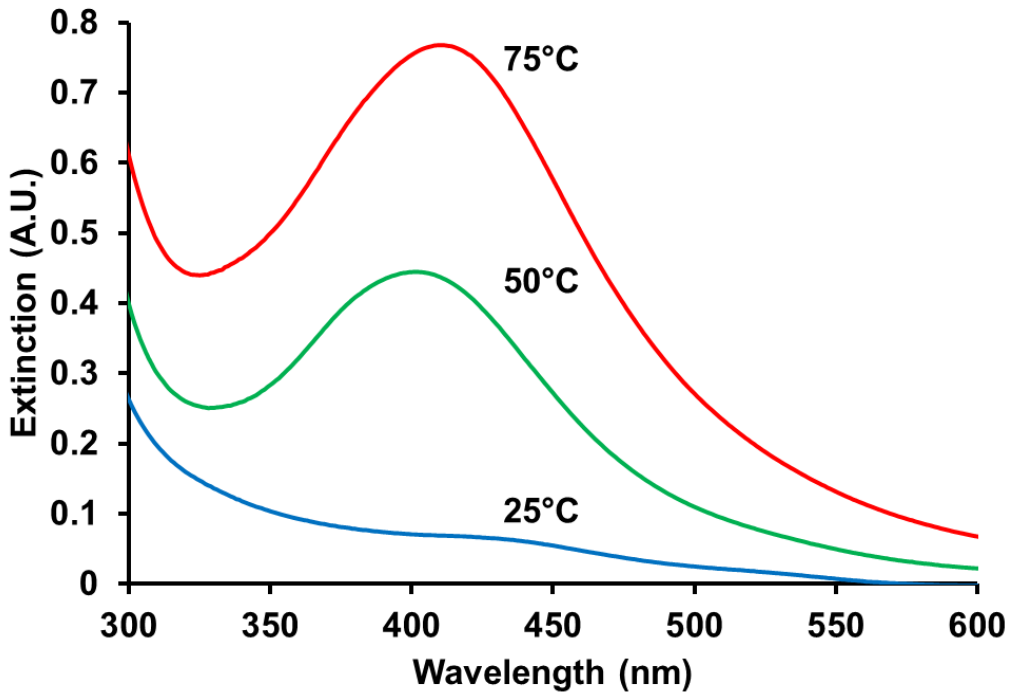

Figure 2–3. Extinction plot demonstrating the effect of temperature on silver nanoparticle biosynthesis. In all cases, 1 mM $AgNO_3$ solution was added to *Fusarium oxysporum* 405 incubated in the dark with shaking at 100 rpm for 3 days.

A method to separate and recover AgNPs from fungal biomass involving ultrasonic treatment and filtration was used to obtain solutions of dispersed particles for further analysis of size and for comparison with chemically synthesized AgNPs. Isolation of B-AgNPs is also important for future applications. A working method employing 20 min ultrasonic treatment (S) and 0.45 μm filtration (F) was used. We rationalize that ultrasonic treatment would dislodge AgNPs from the fungal surface and filtration would remove the biomass. As shown in Figure 2–4, we used extinction spectroscopy to examine AgNPs produced at either 25°C, 50°C, or 75°C and measured aliquots pre and post ultrasonic treatment and filtration. There appears to be no significant difference in the amount of

dispersed AgNPs produced at 75°C pre and post ultrasonic treatment and filtration. However, at 25°C and 50°C, a higher extinction is observed following ultrasonic treatment and filtration. We believe more AgNPs are dislodged from *F. oxysporum* mycelia for these samples. We surmise that the differences in recovery observed (Figure 2–4) are due to variations in the surface composition of the AgNPs produced at different temperatures and their interactions with mycelia. However, it is clear that AgNPs are not lost in the purification treatment based on extinction measurements.

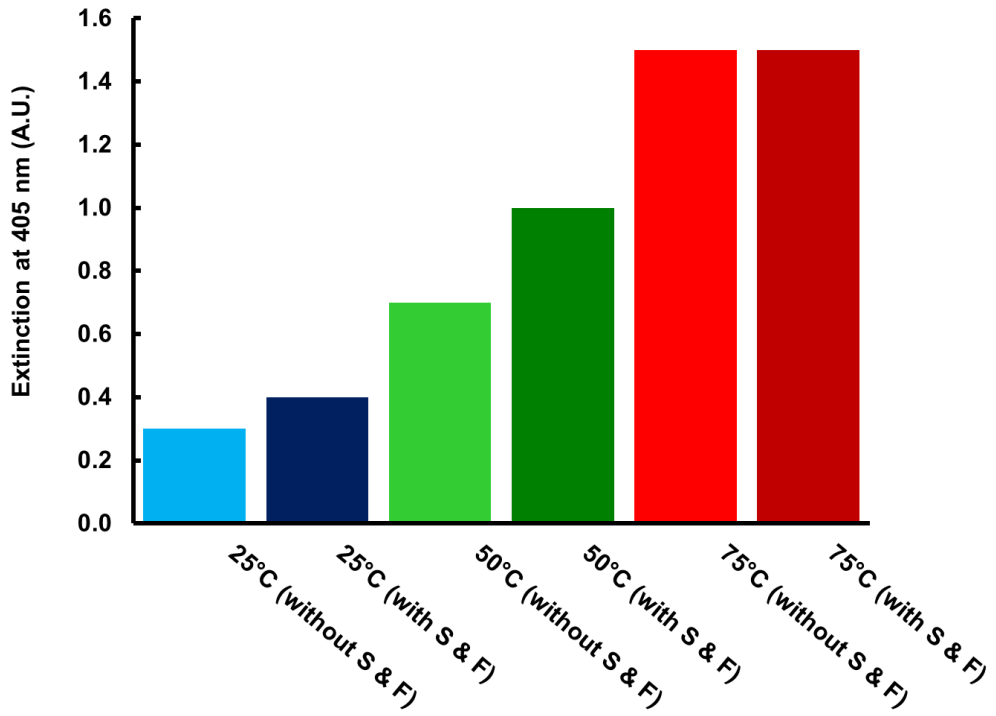

Figure 2–4. Extinction spectra at 405 nm (λ_{max}) demonstrating the effect of ultrasonication (S) and ultrafiltration (F) on the recovery of silver nanoparticles produced by *Fusarium oxysporum* 405 incubated for 4 days at three different temperatures.

The effect of temperature on size, shape, and polydispersity of AgNPs isolated from *F. oxysporum* biomass using the method described above was examined by TEM. Figure 2–5 contains TEM images of AgNPs produced at 25°C, 50°C and 75°C. The particles are spherical for all three temperatures; however, culture temperature significantly affects the size and size distribution of resulting particles. AgNPs produced 25°C are larger (TEM average diameter 39 ± 30 nm) with a visibly larger size distribution. The particles produced at 50°C exhibit an average diameter of 17 ± 3 nm and those produced at 75°C are 9 ± 4 nm in diameter. Higher temperatures also result in a narrower size distribution relative to 25°C. Narrower size distribution can be further improved by decreasing the temperature fluctuations by more stringent upper and lower temperature limits. The control of AgNP diameter by temperature is consistent with previous reports.[104, 164] Due to the influence of temperature on size, polydispersity, and quantity, we chose to use AgNPs produced at 50°C and 75°C in our further studies described below.

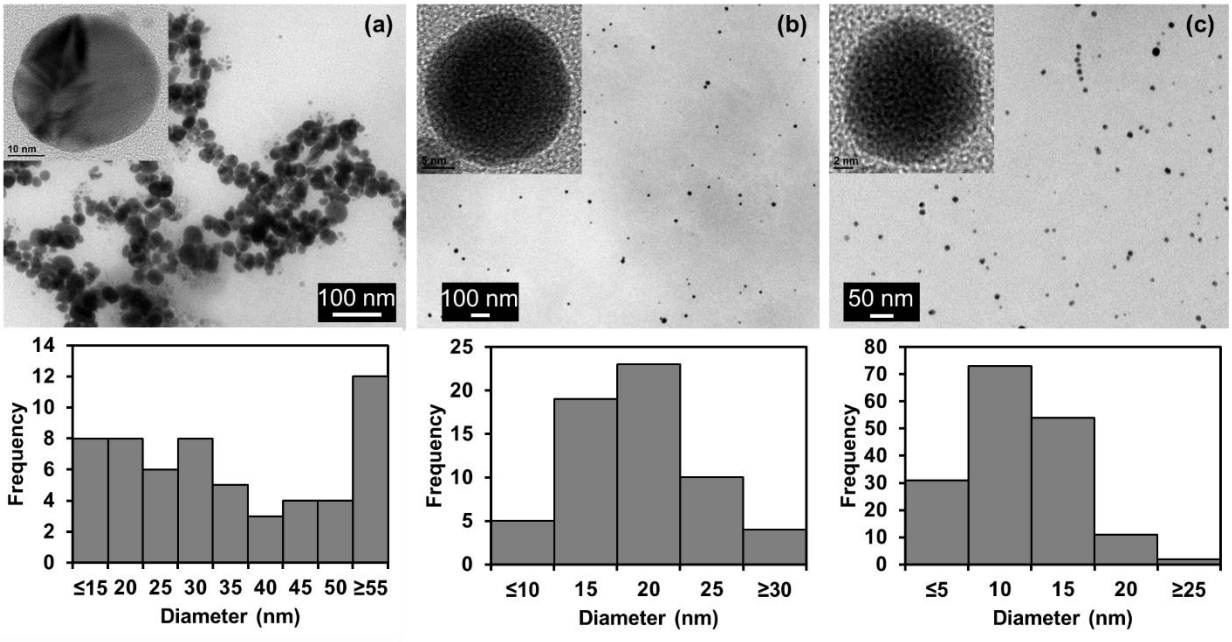

Figure 2–5. Transmission electron micrographs of silver nanoparticles produced by *Fusarium oxysporum* 405 in 1 mM $AgNO_3$ solution at three different temperatures in the dark with shaking at 100 rpm for 4 days (a) 25°C; diameter ≥50 nm (b) 50°C; diameter ~ 20 nm (c) 75°C; diameter ~ 10 nm. Insets in each image are higher resolution images of a single particle. Scale bar sizes of the insets are (a) 10 nm, (b) 5 nm and (c) 2 nm. Particle size distributions shown below each corresponding TEM image. Images were analyzed with ImageJ 1.48v[166]

2.3.3. Effect of pH on the morphology of silver nanoparticles

Consistent with previous studies[104, 164], varying pH affected shape and quantity of AgNPs. Figure 2–6 contains TEM images examining AgNPs produced at pH 3, 5, 7 and 9. At all pH values tested, *F. oxysporum* 405 is able to produce AgNPs. However, pH of the solution did influence size, shape, and polydispersity of the resultant AgNPs. Nanoparticles formed at pH 3 are variable in morphology consisting of rods, triangles, spheres, and other irregular shapes. Nanoparticles produced at pH 5 and 7 are predominantly spherical with relatively uniform size distribution. A pH of 9 produces a mixture of spherical and oblong

shaped nanoparticles. Similar observations have been reported by Gericke and Pinches[164] for gold NP synthesis by *Verticillium luteoalbum.* Considering our results and Gericke and Pinches report, we speculate that varying pH would affect the protonation states of acidic or basic amino acids that are likely involved in forming or stabilizing the nascent nanoparticles. Changes to the protonation states may also change the overall peptide or protein conformation resulting in variations in shape of shape. Similarly, Nayak et al.[167] hypothesized that pH affects conformational changes in nitrate reducing enzymes, which may change the morphology and size of silver nanoparticles. Furthermore, it is known that pH can affect the chelation of ionic silver and the redox potential of chelated silver ion.[168] These effects may also lead to variations in shape / size. Our observations lead us to conclude that the optimal pH range to produce uniform spherical nanoparticles is from 5 to 7.

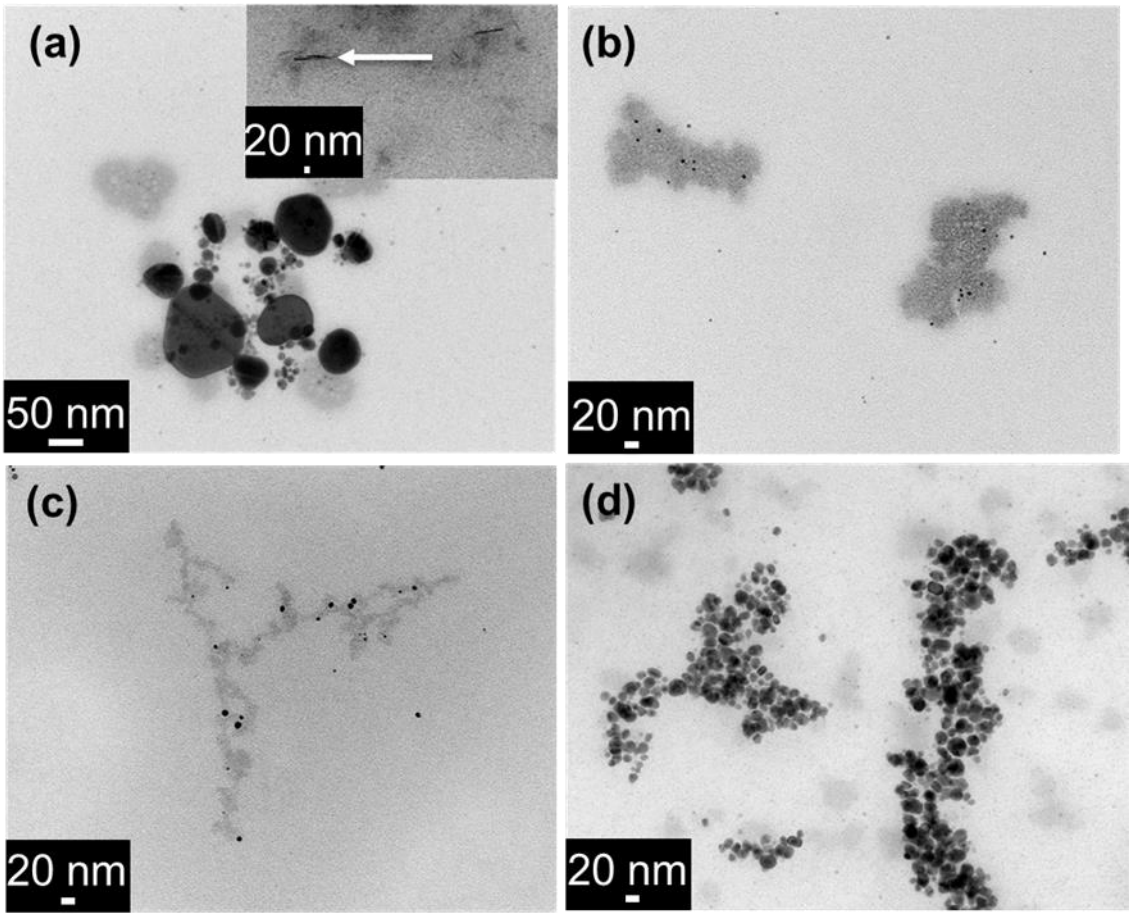

Figure 2–6. Transmission electron micrographs of silver nanoparticles produced by *Fusarium oxysporum* 405 in 1 mM $AgNO_3$ solution at 75°C in the dark with shaking at 100 rpm for 24 hours (a) pH 3. Inset shows a different field of view showing rod nanostructures (arrow) (b) pH 5 (c) pH 7 (d) pH 9. Nanoparticles formed at pH 3 were variable in morphology such as rods, spherical, triangular and irregular, undefined shapes ranging in diameter. Nanoparticles synthesized at pH 5 and at pH 7 were predominately spherical in morphology and relatively similar in diameter. Nanoparticles synthesized at pH 9 were predominately spherical or oblong.

2.3.4. Comparisons between biologically produced versus chemically produced silver nanoparticles

As chemically synthesized, citrate-capped silver nanoparticles are primarily considered for applications, we felt that a direct comparison between biologically produced

AgNPs (B-AgNPs) and commercial products will uncover potential benefits of B-AgNPs. Figure 2–7 contains TEM images of 10 nm and 20 nm Sigma products and *F. oxysporum* 405 50°C and 75°C products. As noted above, B-AgNPs produced at 50°C and 75°C possess uniform characteristics (i.e., size and shape) and aggregate to a lesser extent. Thus, we chose to exclude B-AgNPs produced at 25°C from further analyses. Dynamic light scattering (DLS) and zeta potential (ZP) measurements were also used to further characterize the physical and chemical properties of AgNPs. Table 2–2 contains physical characterization results of particle size, polydispersity indices, surface potential, and relative colloidal stability.

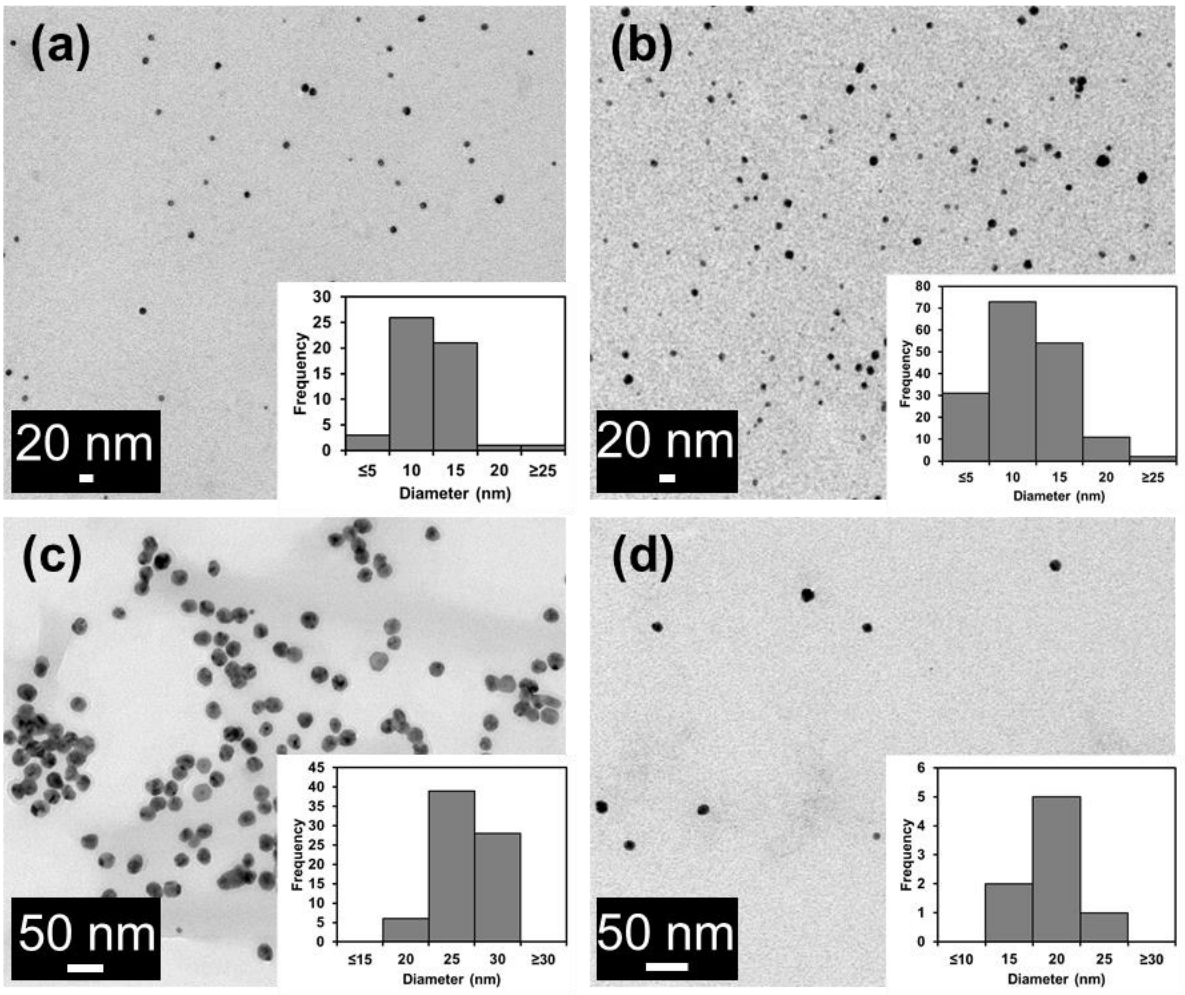

Figure 2–7. Transmission electron micrographs comparing commercially-available, chemically-produced, silver nanoparticles from Sigma-Aldrich with biologically produced silver nanoparticles of comparable size diameters. (a) 10 nm aqueous dispersion from Sigma-Aldrich (b) *Fusarium oxysporum* 405 at in 1 mM $AgNO_3$ solution at 75°C in the dark with shaking at 100 rpm for 4 days; Diameter ~ 10 nm (c) 20 nm aqueous dispersion from Sigma-Aldrich. Contrast region due to air-drying preparation of citrate buffer (d) *Fusarium oxysporum* 405 in 1 mM $AgNO_3$ solution at 50°C in the dark with shaking at 100 rpm for 4 days; Diameter ~ 20 nm. Insets show size distributions for each corresponding TEM image analyzed by ImageJ 1.48v.[166]

Table 2–2 shows results of all AgNPs possess a negative surface potential ranging from –15 to –43 mV at pH 7.0. The ZP values for B-AgNPs were recorded at a range from –15 to –24 mV, while those of the commercial AgNPs are more negative, 35 to 43 mV. The

distribution of ZP values is similar for the B-AgNPs. The magnitude of the ZPs agrees with measurements of similarly produced B-AgNPs in a recent report.[98] Also, an extrapolated value of approximately –18 mV at pH 7.0 was reported by Birla et al.[104] It is well known that a surface potential ≤ –30 mV and ≥ +30 mV is diagnostic of colloidal stability.[169] We note that the lower observed ZP for B-AgNPs relative to the chemically synthesized, commercial counterparts would indicate a less stable dispersion. However, as discussed below, B-AgNPs show a higher degree of stability towards added salt than commercial AgNPs.

Table 2–2. Characterization of chemically or biologically synthesized aqueous silver nanoparticles by dynamic light scattering and zeta potential measurements

Sample description	TEM diameter (nm)[a]	D_{hyd} (nm)[b]	Polydispersity index[c]	Zeta potential (mV) at pH ~ 7.0[d]	LSPR peak (λ_{max}, nm)
Sigma 10nm	10 ± 3	20 ± 1	0.3 ± 0.1	-43 ± 4	401
Sigma 20nm	24 ± 3	26 ± 1	0.5 ± 0.1	-35 ± 1	404
Foxy 405 50°C	17 ± 3	52 ± 1	0.4 ± 0.1	-24 ± 1	402
Foxy 405 75°C	9 ± 4	26 ± 1	0.3 ± 0.1	-15 ± 1	411

[a]Transmission electron micrographs were analysed with ImageJ 1.48v.[166] Values reported are an average of at least eight particles ± standard deviation, however particle counts were greater in most cases.
[b]Hydrodynamic diameter (Z-average) based on intensity. Values reported are an average of three measurements ± standard deviation.
[c]Values reported are an average of three measurements ± standard deviation.
[d]Values reported in millivolts at 25°C. pH values determined by Whatman pH indicator paper (Type CF, pH 0-14).

Comparison of TEM measured diameters of AgNPs with DLS measured hydrodynamic diameters reveals some interesting differences. Our results show the hydrodynamic diameter for Sigma 20 nm to be similar with TEM data. However, for Sigma 10 nm and both biological products, the measured hydrodynamic size is larger than values obtained from TEM measurements. We believe the factor of 2 discrepancy between TEM and DLS results for the Sigma 10 nm AgNPs is due to low levels of aggregation in this product. This result is corroborated by re-testing a two year old lot of 10 nm AgNPs and measuring a diameter of 204 ± 163 nm (n = 3) due to higher levels of aggregation. The difference between the TEM measured diameter and the DLS results for B-AgNPs is more pronounced. The hydrodynamic diameter of both sets of B-AgNPs are 3–times larger than TEM results. We believe this difference reflects the presence of a unique capping layer formed around B-AgNPs. This layer is comprised of biomolecules (e.g. proteins) generated by the host fungus. Such a biocorona layer has been the subject of recent reports.[127, 170] Given that fungi are known to secrete large quantities of biomolecules, it is reasonable for these capping biomolecules to play a dual role in synthesis and stabilization of AgNPs.[171-172] Several studies examining B-AgNPs by other fungal organisms have documented the use of Fourier Transform infrared (FTIR) vibrational spectroscopy[104, 134, 173] and / or SDS-PAGE analysis[171-172, 174] to partially characterize the surface layer. Such studies have led to conclusions suggesting stability may be conferred by a proteinaceous layer. Potara et al. [98] have recently reported evidence of a stabilizing corona in TEM images.

Given that proteinaceous biomolecules can adsorb to the surface layer and that our ZP results confirm a negative surface potential, we investigated whether electrostatic repulsion, steric effects or a combination of these afforded colloidal stability. Figure 2–8 visually shows the effect of varying the ionic strength of B-AgNPs and chemically produced AgNPs. Furthermore, Figure 2–9 presents visible extinction spectra used to track the aggregation of B-AgNPs with increasing ionic strength. As expected, the two citrate-capped, chemically synthesized AgNPs materials destabilized (aggregated) upon addition of NaCl at all concentrations used (120 – 480 mM). In contrast, B-AgNPs retain some colloidal stability in the presence of added NaCl evidenced by the observed plasmon bands in Figure 2–9a. Such effects are illustrated in Figure 2–9b, which plots extinction maximum as a function of NaCl concentration for both types of AgNPs. Thus, our results lead us to conclude that stability is afforded by a combination of both steric effects and electrostatic repulsion.

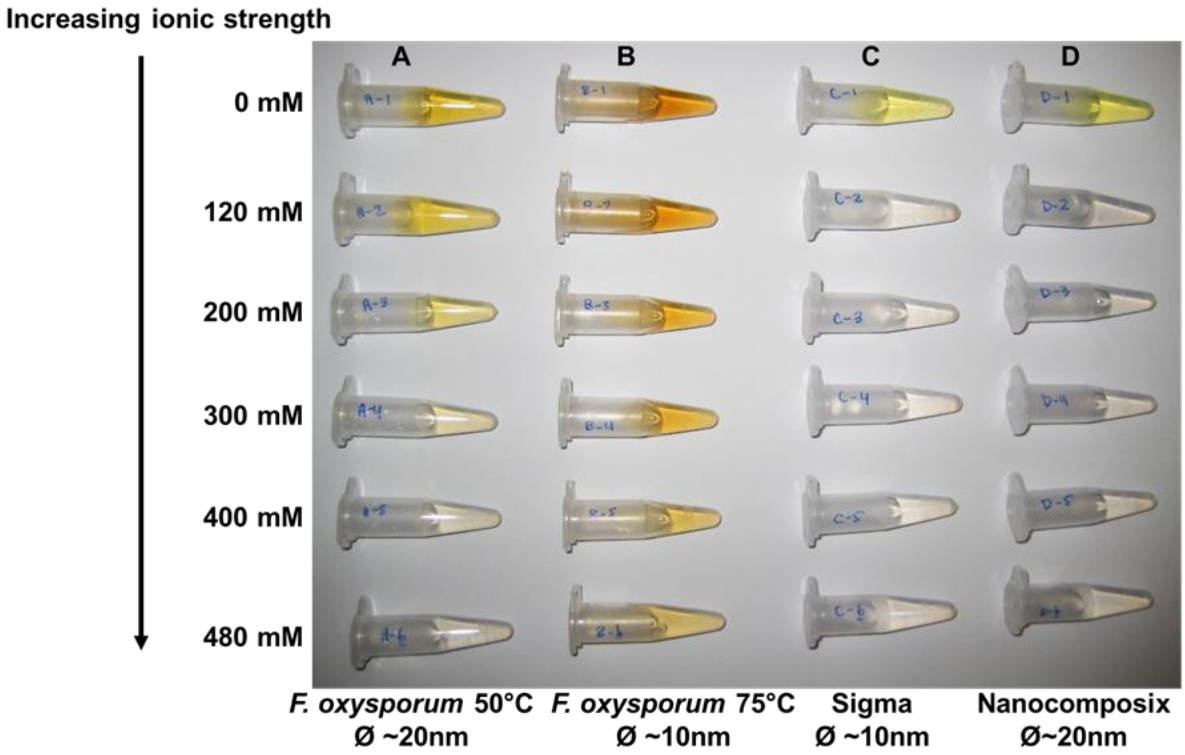

Figure 2–8. Visual demonstration of silver nanoparticles mixed with different concentrations of NaCl ranging from 0 mM to 480 mM. In all cases, nanoparticles destabilize (aggregate) with increasing ionic strength. However chemically synthesized particles destabilize immediately, whereas bio-SNPs destabilize gradually due to both steric and electrostatic effects. Image taken with a Canon PowerShot SD1000 7.1MP digital ELPH camera.

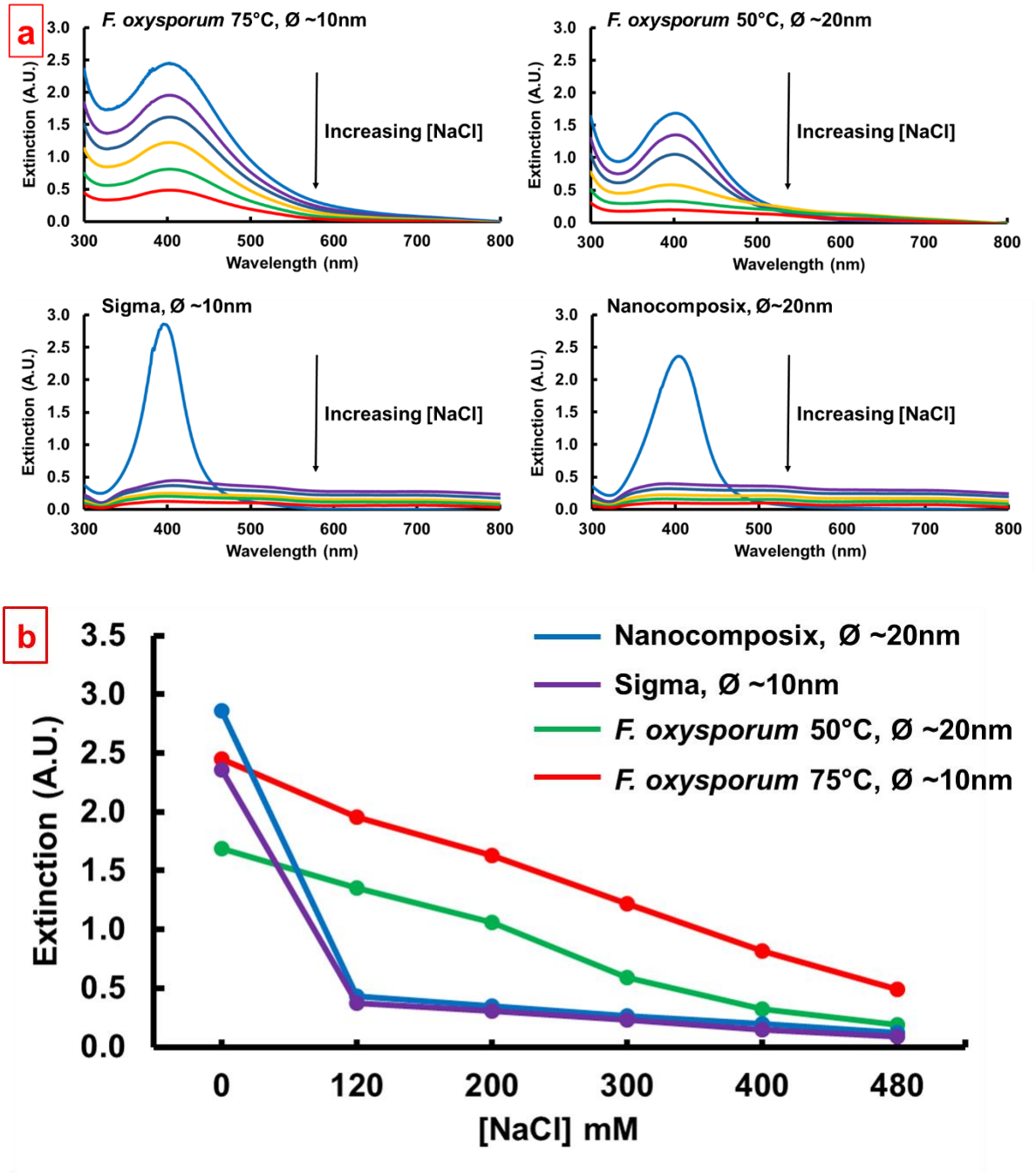

Figure 2–9. Destabilization of biologically synthesized or chemically synthesized silver nanoparticles with increasing ionic strength using NaCl. (a) Extinction spectra recorded for each AgNP product after mixing with different concentrations of NaCl. (b) Extinction plot of plasmon absorbance peaks for each AgNP product with increasing NaCl concentration. Experiments were run in triplicate with a standard deviation of ± 0.01 A.U. Thus, error bars are not shown.

An examination of the UV region of the absorbance spectra of B-AgNPs provides preliminary confirmation of the presence of protein in the filtered solution and, by extension, in the capping layer as seen in Figure 2–10. A distinct band is observed at 260 nm which is typically ascribed to the absorbance of aromatic amino acids (e.g., tryptophan and tyrosine). This band is not observed in the spectra of chemically produced AgNPs. We have used an established method based on the absorbances at 260 nm and 280 nm[175-176] to estimate the amount of protein associated with B-AgNPs (Figure 2–10). The results show that the magnitude of protein content increases with temperature. We speculate that the protein containing capping layer is responsible for some of the observations in the extinction spectra in Figure 2–3 and Figure 2–9. The widths of the B-AgNPs spectra are greater than citrate capped counterparts. Since TEM size results suggest a similar polydispersity, the broader band may be due to a distribution of capping layer compositions, and thus a distribution of the dielectric constant on the B-AgNP surface. As well, a difference in layer composition between particles synthesized at 50˚C vs 75˚C could result in the unexpected trend in LSPR maxima listed in Table 2–2. We are currently conducting a detailed analysis of the surface layer of B-AgNPs and will report on our findings separately.

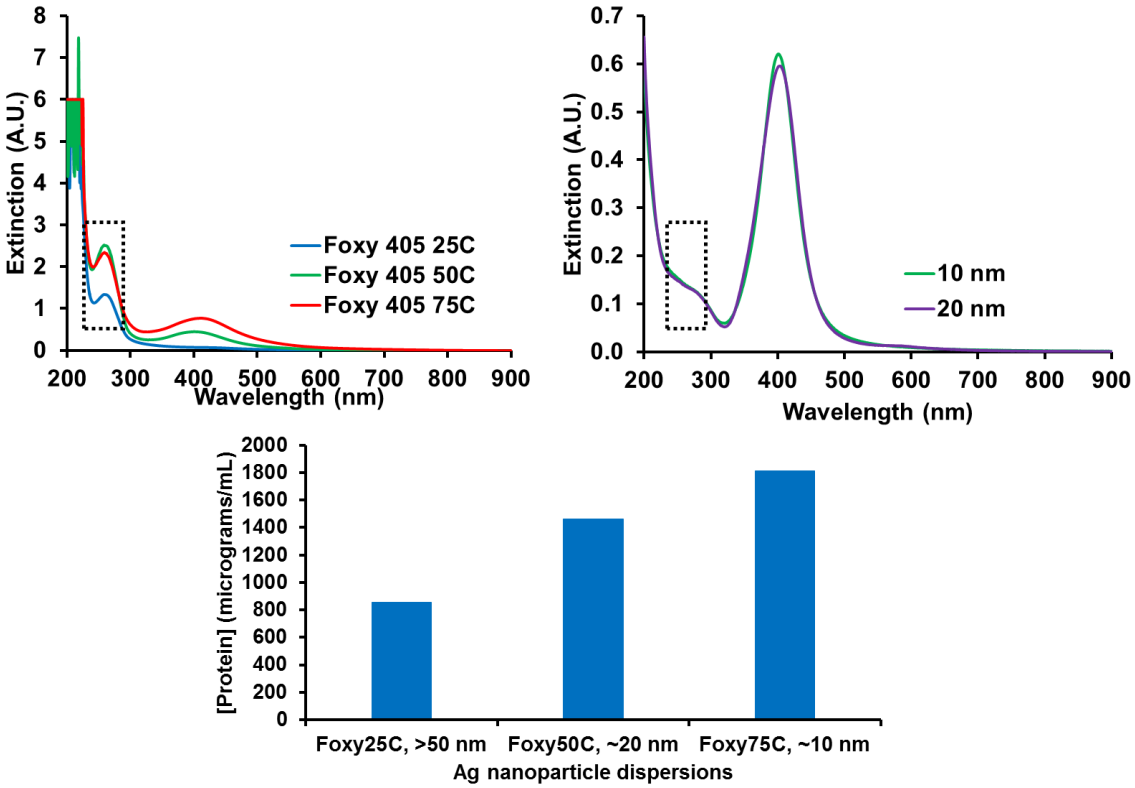

Figure 2–10. Extinction plots of 'as is' (diluted 1:4) B-AgNPs (top-left) and chemically synthesized AgNPs (top-right). Box highlights the spectral region for protein concentration estimation (absorbance at 260 nm and 280 nm). Bottom shows a plot of protein concentration for each of the conditions used for B-AgNPs synthesis. Estimated protein concentration was calculated according to [Protein] mg/mL = $1.55*A_{280}-0.76*A_{260}$.[175-176]

Monopoli et al.[127] refer to the biomolecular layer as a 'corona' that surrounds nanoparticles. The authors[127] describe the high surface energy of nanoscale materials leads to progressive and selective adsorption of biomolecules by weak intermolecular interactions in biological fluids, unless otherwise designed, to effectively lower the surface energy. The corona has been described to be both 'hard' (static) and 'soft' (dynamic) due to the affinity of adsorbed biomolecules and displacement by new biomolecules over a time span associated with the nanoparticle surface.[127] Alarcon et al. have shown that of chemically synthesized silver nanoparticles can be stabilized with biomolecules, such as collagen[177], a peptide / collagen mixture[178], or human serum albumin[179] for improved biocompatibility and anti-bacterial properties. Recently, it has been recently shown that the corona surrounding B-AgNPs can serve as a biocompatible spectroscopic label for cell imaging.[98] We also view the corona as a biomolecular scaffold for bioconjugation strategies. As such, understanding the composition and abundance of biomolecules associated with B-AgNPs will be important for bioconjugation strategies and bioanalytical applications.

2.4. Conclusion

Thorough optimization of AgNP synthesis by *F. oxysporum*, particularly in context of intra-species variability and physical parameters such as temperature and pH has not been previously conducted. In addition, a direct comparison between fungal produced AgNPs and commercial, chemically synthesized AgNPs has not been reported. We studied 12 *Fusarium oxysporum* isolates for production of AgNPs and show intra-species variability

and note the importance of complete records for isolate selection. Based on our isolate screening results, we selected a high AgNP yielding isolate and varied temperature or pH conditions to demonstrate size and shape control, respectively. Separation of AgNPs from fungal mycelium was done by ultrasonication and ultrafiltration. Ultrasonication was found to moderately improve AgNP recovery for nanoparticles > ø10nm. Characterization was performed by UV-Vis spectroscopy, SEM, EDS, TEM, DLS, and ZP measurements. Our results corroborate with increasing incubation temperature increased quantity, yet nanoparticle diameter was inversely related; varying pH predominately influenced nanoparticle morphology. Our results show B-AgNPs can be controllably produced that is physically comparable to commercial, chemically synthesized AgNPs. However, our ionic destabilization results highlight a unique chemical advantage associated with the fungal produced layer (corona) surrounding B-AgNPs. We suggest stabilization is afforded by electrostatic and steric interactions due to charged biomolecules adsorbed on the surface of B-AgNPs. We propose that understanding the composition and relative abundance of such biomolecules will be useful in bioconjugation strategies to link molecular recognition elements (e.g. antibodies or aptamers) for biosensing applications.

Chapter 3. Illuminating the surface corona of biogenic silver nanoparticles

3.1. Introduction

In Chapter 2, the synthesis and optimization of biogenic silver nanoparticles from *Fusarium oxysporum* was described. Biogenic silver nanoparticles were shown to exhibit enhanced colloidal stability with increasing ionic strength compared to chemical counterparts. Enhanced colloidal stability of biogenic silver nanoparticles was attributed to the surface layer affording by both steric and electrostatic interactions due to putatively adsorbed biomolecules. In this chapter, a systematic approach is undertaken to characterize the surface layer for a better understanding of physical structure and chemical composition.

Noble metal nanoparticles are of high interest in the scientific literature due their high value applications in medicine, electronics, agriculture, and energy.[180-182] Widespread interest is principally driven by the optical properties and the high surface to volume ratio of metallic nanoparticles. In addition, ability to synthesize metallic nanoparticles with controlled size and shape via scalable chemical methods enables researchers to obtain adequate quantities of such materials for a wide range of experiments. Though methods to chemically synthesize metallic nanoparticles are well established, there is increasing attention to biological organisms for nanoparticle synthesis. Such nanoparticles are

typically produced in aqueous media with metal salts of interest. Generally, this approach is considered to have lower environmental consequences and the resulting nanoparticles may possess chemical and physical properties that can be exploited in new or improved ways. A unique difference between biologically synthesized nanoparticles and chemically synthesized nanoparticles is the surface chemistry. Chemically synthesized nanoparticles are typically capped with citrate ions or a surfactant species that affords colloidal stability. Whereas, the surface chemistry of biologically synthesized nanoparticles is complex with biomolecules affording enhanced colloidal stability[183] and can be exploited for specialized applications.[98]

The surface layer or corona of nanoparticles is known to define the biological identity of nanoparticles.[115, 120, 126-127, 184] Consequently, the impact of the surface layer with the surrounding environment can be beneficial or detrimental.[128-130] Understanding the chemical and physical makeup of the surface corona enables researchers to predict interactions within an environmental matrix.[131-132, 185] There are several reports in the literature that discuss chemically synthesized nanoparticles that are deliberately exposed to a variety of protein matrices, such as the use of cationic gold nanoparticles exposed to blood serum.[132] In this chapter, we focus our attention to the inherent surface layer of biologically synthesized nanoparticles. Within this context, many researchers have previously purported that the surface layer of biogenic nanoparticles consists of proteins.[104-105, 133-134] Though several techniques have been used to probe the surface layer, the current body of evidence is inconclusive in providing structural and

compositional details. Many of these previous reports principally provide indirect evidence of proteins using methods such as UV-vis spectroscopy[113, 162], vibrational spectroscopy,[133-134] TEM-elemental spectroscopy imaging,[186] SDS-PAGE analysis,[171, 187] and electron microscopy[188] investigating *in situ* AgNP dispersions. Currently, there are no reports describing the surface layer of biogenic AgNPs providing both direct and indirect structural and compositional evidence.

Herein, we characterize the surface corona of silver nanoparticles produced by *F. oxysporum*. Examination the surface corona of biogenic silver nanoparticles is valuable towards application development and understanding *in vivo* interactions. Our approaches involve both *in situ* analyses of silver nanoparticle dispersions (indirect) and desorption of the surface corona (direct). We present our results for the surface corona thickness, chemical composition, and relative chemical abundance. We highlight the differences between our approaches and discuss the implications of each. We also highlight our contrasting results of the surface layer and discuss implications from an ecological perspective. This may benefit a mechanistic understanding.

3.2. Experimental

3.2.1. Reagents and materials

Silver nitrate (ACS reagent grade, ≥ 99%, lot# MKBD7719 V, Sigma-Aldrich). 4-nitrobenzene thiol (NBT, 80%, lot# MKBR2625, Sigma-Aldrich). Acetonitrile (HPLC grade,

Caledon Laboratories and Fisher Scientific). Ethyl alcohol (anhydrous, Commercial Alcohols). BD Bacto yeast extract (product# 212750, lot# 5180630, Fisher), BD Bacto peptone (product# 211677, lot# 2306004, Fisher), dextrose (ACS reagent, product# 73409, lot# 720331, Fisher). Citrate-capped silver nanoparticle dispersion was purchased from Nanocomposix (lot# DAG1159, San Diego, California). Citrate-capped vendor specifications: nanoparticle concentration of 0.02 mg/L; 21 ± 3 nm diameter based on TEM measurements, and 4 x 10^{11} particles/mL. All reagents and materials were used as received unless otherwise specified. Deionized (DI) water with a resistivity of 18 MΩ·cm was used for all aqueous preparations unless otherwise noted.

3.2.2. Production and separation of biogenic silver nanoparticles

A detailed description of silver nanoparticles production has been published[183] and has appeared in the previous chapter. The following is a brief description with changes to further optimize production. *Fusarium oxysporum* isolate 405 was initially cultured on potato dextrose agar (PDA) in the dark for seven days at 23°C ± 2°C. As an intermediate step prior to incubating in aqueous 1 mM $AgNO_3$ solution, *F. oxysporum* was set up as a liquid culture by removing one piece (~ 1 cm x 2 cm) of solid PDA growth medium containing mycelium and conidia and transferring to each sterile 500 mL Erlenmeyer flask containing 100 mL of sterile 1% yeast extract, 1% D-glucose and 1% Bacto-peptone (1% YGP). All inoculated flasks plus control medium flasks (i.e., no fungal inoculum) were incubated in the dark at 23°C ± 2°C shaking at 150 rpm for four days. Next, fungal biomass was separated from the culture broth by centrifuging at 2000 rpm for 5 min in swing out

bucket centrifuge. Settled biomass was washed once with sterile DI water, centrifuged, and weighed after supernatant was decanted. Average fungal fresh (wet) weight and standard deviation was determined to be 42 ± 4 grams (n = 15).

Harvested washed fungal biomass was added to 100 mL of sterile 1 mM aqueous $AgNO_3$ solution (fresh) in sterile Nalgene PMP conical flasks with screw cap lids at 23°C ± 2°C. After inoculating, all flasks were incubated either at: a) 45°C ± 0.3°C, b) 50°C ± 1°C or c) 75°C ± 1°C under dark conditions with shaking at 100 rpm for three days. Simultaneously, a negative control containing only silver nitrate solution and a positive control containing only fungus was maintained under identical experimental conditions. Fungal culture flasks were weighed post incubation. The average mass change and standard deviation in fungal culture was determined to be a loss of 0.2 ± 0.01 grams (n = 6).

3.2.3. Enrichment of biogenic nanoparticles

To separate and recover AgNPs, aqueous dispersions of AgNPs with fungi were sonicated for 20 min at 23°C ± 2°C using a Branson 5510 ultrasonicator to separate nanoparticles from fungal mycelia post synthesis. After sonicating, aqueous dispersions with fungal mycelia were filtered using a sterile 0.1 µm polyethersulfone membrane 250 mL vacuum filtration unit (Millipore, product# SCVPU02RE, Massachusetts, USA). Negative fungal control flasks were treated the same. All samples were stored in the dark at 4°C until use.

3.2.4. Extinction spectroscopy

Biogenic nanoparticle dispersions were diluted by a factor of 2 and the citrate-capped nanoparticle dispersion was diluted by a factor of 4 with deionized water before analysis for similar concentrations. Extinction spectra were collected in absorbance mode on a double-beam Perkin Elmer Lambda 35 spectrophotometer. Spectra were scanned from 900 – 300 nm with a scan rate of 960 nm/min. Deionized water was used as the blank. Measurements were done at room temperature. Both biogenic and citrate-capped nanoparticle dispersions were washed once with DI water prior to analyses.

3.2.5. Dynamic light scattering (DLS) spectrometry

Hydrodynamic diameter of AgNPs was determined using a Malvern Zetasizer Nano-ZS. Results were collected with a 4 mW HeNe laser set at 633 nm with a 173° back scattering angle and an avalanche photodiode detector. Measurements were performed under the following conditions: particle refractive index 1.590; particle absorption coefficient 0.028 for the Nanocomposix product and 0.118 for B-AgNPs (based on absorbance values recorded at 633 nm); water refractive index 1.33; viscosity 0.8872 cP; and temperature 25°C; equilibrated for 120 sec.; 15 runs; n = 3 measurements. Hydrodynamic radii is calculated by the instrument software using the Stokes-Einstein equation for spherical particles. Hydrodynamic diameter (D_{hyd}) reported represents the mean diameter based on intensity of scattered light.

3.2.6. Zeta potential (ZP)

Zeta potential of AgNPs was determined using a Malvern Zetasizer Nano-ZS. A 4 mW HeNe laser with 633 nm wavelength was used as the light source. All measurements were performed under the following conditions: temperature 25°C; equilibrated for 120 sec.; 20 runs; n = 3 measurements; Smoluchowski model.

3.2.7. Transmission/scanning electron microscopy (TEM, S/TEM)

One mL of AgNPs were washed via centrifugation at 10,000 rpm for 10 min in an Eppendorf 5417R microfuge. The supernatant was carefully removed and the AgNP pellet was re-dispersed in 1 mL of DI water.

A droplet of aqueous sample was deposited onto an ultra-thin carbon film coated copper 400 mesh grid (Electron Microscopy Sciences, product# CF400-CU-UL). After one minute, excess suspension was wicked-off using Whatman filter paper and then the grid was air-dried at room temperature before analysis. For adlayer images, sample grids were examined under a 200 kV JEOL 2200 FS field emission TEM equipped with an in-column omega type energy filter. An objective aperture and an energy filter slit were applied to obtain zero-loss bright field (BF)-TEM images, which enhanced the contrast of thin organic layers around the AgNPs. Careful precautions were taken to minimize hydrocarbon artefacts.[189] Thickness measurements were done using the line profile tool (line width =

10), which measures pixel intensity in Gatan Digital Micrograph (v2.31.734.0). For S/TEM, images were collected using a Hitachi S4800 or Hitachi S5500 at 30 kV, 20 μA.

3.2.8. He ion Imaging

Sample grids were prepared as above for TEM and S/TEM. Grids were examined under a Zeiss Orion NanoFab helium-ion microscope.

3.2.9. Raman spectroscopy

Silver nanoparticles were analyzed by surface-enhanced Raman scattering (SERS). A 2 μL volume of AgNPs was deposited on an ethanol rinsed, ozone treated (10 min), gold-coated (300 nm thickness) 25 x 75 x 1 mm plain microscope slide (Fisher Scientific), air dried, and immediately analyzed. SERS spectra were recorded with a Renishaw inVia Raman microscope. Irradiation of 514.5 nm from 30 mW Ar ion, air-cooled laser was used for excitation. SERS spectra was integrated 10 s and the laser power at the sample was 50 ± 3 μW. Laser power at the sample was measured using a handheld laser power meter (Coherent, Laser Check model# 54-018, California, USA). All spectra were collected from the edge of the droplet using a 50X objective (Leica, numerical aperture 0.75; free working distance of 0.37 mm, ~ 0.8 μm laser spot diameter[190]) at three different locations for a signal average. All spectra were background subtracted by applying a single order least squares polynomial fit using Wire (v3.4, Renishaw) for two baseline-definition points. Visual inspections were conducted to deposit equivalent amounts of nanoparticles on the

slide and to focus the laser beam in regions of similar nanoparticle density of each sample. Calibration reference was periodically checked using 520 cm^{-1} vibrational band of silicon.

3.2.10. SDS-PAGE

Proteins were separated using a 12% and 5% discontinuous tris-glycine SDS-PAGE system (30% acrylamide/bis solution; 29:1; 3.3% crosslinker, Bio-Rad, catalog# 161-0156).[191] To remove proteins on the surface of biogenic AgNPs, samples were heated at 87°C for 2 min in loading buffer consisting of 5X SDS sample buffer[192], 33 mM dithiothreitol (DTT), and 50% glycerol. Additional glycerol was added to the reduced sample buffer (buffer plus DTT) to increase viscosity of samples. This allowed for greater loading volume into the gel well. Control samples (i.e. fungus only and media) were treated the same. All samples were loaded (40 µL/well) into a 1.0 mm tris-glycine gel. For reference, Bio-Rad molecular weight standards (Precision Plus Protein Dual Xtra, catalog#161-0377) was run with samples (6 µL/well). Proteins were separated by electrophoresis in 1X tris-glycine-SDS Running Buffer at 50 V (initial 30 min) for the stacking gel and then at 110 V for the resolving gel. After protein separation, gels were briefly rinsed with distilled water and put into a fixation solution[193] consisting of 50% methanol, 10% glacial acetic acid, and 100 mM ammonium acetate for 1 h with gentle agitation. After fixation, gels were again briefly rinsed with distilled water and stained with QC Colloidal Coomassie G-250[194] stain (Bio-Rad, catalog#1610803) overnight (~ 20 h) with gentle agitation. Note: short wash steps between fixation and staining are important for low molecular weight detection. Gels were

destained with distilled water and imaged using ImageQuant RT ECL imager (v1.0.1, General Electric) in trans-illumination mode.

3.2.11. In-gel digestion

Protein bands were excised from gel and digested with 10 ng/μL trypsin (Trypsin Gold, Mass Spectrometry Grade, Promega, catalog# V5280) diluted with DI water and filter-sterilized using a Millex GV 0.22 μm syringe filter according to Shevchenko et al.[195] Digested and extracted peptides were concentrated in 20 μL 0.1% trifluoroacetic acid solution. Extracted peptides were desalted using C18 reversed-phase Zip-Tip pipette tips (Millipore, catalog# ZTC18S008) following manufacturer's guidelines. Improved recovery was achieved by concentrating (Savant SpeedVac) the initial extraction volume by ~ 4X, repeated peptide binding/elution steps thrice, and dried final peptides extraction (Savant SpeedVac) to reconstitute in 0.1% formic acid for LC-MS/MS.

3.2.12. MALDI-MS

α-cyano-4-hydroxycinnamic acid (HCCA) was used as matrix compound for peptide and sinapinic acid was used as matrix compound for proteins. Matrix solution was prepared in 50% acetonitrile with a final concentration of 10 mg/mL. C4 and C18 reversed-phase zip-tipped (Millipore) samples were mixed with the same volume of matrix solution and 0.8 μL were spotted on an 800 μm Bruker's anchorChip MALDI target (Bruker Daltonics) and air-

dried. MALDI-MS was performed on an ultraflexXtreme™ MALDI-TOF/TOF (Bruker Daltonics) mass spectrometer in positive MS mode.

3.2.13. LC-MS/MS

Desalted peptides were subject to LC-MS/MS analysis on a UPLC (Waters Corporation) coupled with Q-TOF premier mass spectrometer (Waters Corporation). 5 µL of the peptides were loaded onto a nanoAcquity UPLC system with peptide trap (180 µm x 20 mm, Symmetry C18 nanoAcquity™ column, Waters Corporation) and a nano-analytical column (75 µm × 150 mm, Atlantis C18 nanoAcquity™ column, Waters Corporation). Desalting on the peptide trap was achieved by flushing trap with 1% acetonitrile, 0.1% formic acid in water at a flow rate of 10 µL/min for 5 min. Peptides were separated with a gradient of 5 – 95% solvent B (acetonitrile, 0.1% formic acid) over 50 min at a flow rate of 350 nL/min. The column was connected to a Q-TOF premier (Waters Corporation) for ESI–MS/MS analysis.

3.2.14. Protein identification

MS/MS data were analyzed using Mascot (v2.3, Matrix science)[196] and searching NCBI non-redundant (nr) protein database (20160529; 88,331,457 sequences; 32,419,248,901 residues) and specifying Fungi taxonomy (5,570,423 sequences). Database search parameters were: parent ion and MS/MS tolerance were set to 0.1 Da and 0.2 Da, respectively; no enzyme was specified and thus 0 missed cleavages were

selected; oxidation on methionine, histidine, and tryptophan were selected as variable modification. Positive identification/extensive homology of protein/peptide were calculated using Mascot's scoring algorithm (http://www.matrixscience.com/help/scoring_help.html) at $P < 0.05$. Manual inspection of the original MS/MS spectra were often performed to ensure major *b* and *y* peaks in the MS/MS spectra were matched and explained. Ion score is calculated by $-10*\text{Log}(P)$, where P is the probability that the observed match is a random event ($P < 0.05$). Protein scores are derived from ions scores as a non-probabilistic basis for ranking protein hits.

3.2.15. NMR analysis

^{1}H NMR spectra were collected on a 700 MHz four channel Agilent VNMRS spectrometer, equipped with a Z-axis gradient HCN cold probe. Samples were dispersed in $H_2O/CH_3CN/10\%$ D_2O mixtures. Solvent suppression was performed using excitation sculpting;[197-198] suppressing both water and acetonitrile (CH_3) resonances. All data were referenced to 4,4-dimethyl-4-silapentane-1-sulfonic acid (DSS) added as 20 µL of a 1% w/v solution in deionized water.[199]

3.3. Results and discussion

3.3.1. Structure and composition of biogenic AgNPs surface corona

The surface of nanoparticles in a biological environment has been described to be capped or covered with an adlayer of biomolecules such as proteins that leads to a

biomolecular interface. This interface is considered to be loosely organized into two components, referred to as the "hard" and "soft" coronas with "long" and "short" typical exchange times.[121, 184] The biological identity of a nanoparticle is typically defined by the surface corona.[121, 127] As Monopoli and co-workers state, the corona may be expressed as a durable, stabilizing coating of the bare surface of NP monomers.[121] Generally, biomolecules in high abundance and lower molecular weight bind first (e.g., albumin), which are later displaced by larger molecular weight biomolecules with higher affinity (e.g., fibrinogen); first described by Vroman using blood serum proteins on surfaces.[200-201]

For biogenic nanoparticles, detailed structural and compositional data is limited. Detailed knowledge of the surface layer will lead to successful applications by providing a rationale for using native or modified biogenic AgNPs, predict possible interactions within a biological milieu, and may provide mechanistic insights on NP synthesis. Previous reports investigating biogenic AgNPs have purported that the surface layer is composed of capping proteins.[104-105, 133-134] Many of these reports principally provide indirect evidence of proteins using methods such as UV-vis spectroscopy,[113, 162] vibrational spectroscopy,[133-134] TEM-elemental spectroscopy imaging,[186] SDS-PAGE analysis,[171, 187] and electron microscopy[188] investigating *in situ* AgNP dispersions. Currently, there are no reports describing the surface layer of biogenic AgNPs providing both direct and indirect structural and compositional evidence.

In this chapter, we report a detailed investigation on the surface layer of biogenic AgNPs produced by *Fusarium oxysporum* isolate 405[183] (Foxy) providing both direct and indirect structural and compositional evidence. Our results are the first to thoroughly describe the composition and propose a model of the surface layer. The work described in this chapter follows our previous chapter and a published report[183] demonstrating enhanced colloidal stability due to both steric and electrostatic effects. Based on our previous work, we suspect that the surface layer is composed of an organic matrix made up of proteineous macromolecules and possibly other biological macromolecules. We indirectly examine the surface layer from *in situ* AgNP dispersions then turn our efforts to desorbing the layer for a direct examination by isolating the NPs from excess biomolecules in the dispersion. Herein, we present our results examining the surface layer and characterize AgNPs that were produced by *F. oxysporum*.

Silver nanoparticles produced by *Fusarium oxysporum* at different culture temperatures were selected on the basis that protein secretion is inversely related to temperature over a finite period.[104, 183] Figure 3–1 contains a scheme of the workflow to investigate B-AgNPs from *F. oxysporum*. The initial set of characterization studies shown in Figure 3–1a involve *in situ* dispersions of nanoparticles. *In situ* dispersions consist of B-AgNPs dispersed in aqueous (DI) medium that were obtained after 20 min sonication and 0.1 μm filtration of fungal biomass after three days incubation in 1 mM $AgNO_3$ at a set temperature condition. Thus, B-AgNPs are coated with a surface layer comprised of biological macromolecules that are in dynamic equilibrium with free macromolecules in

the medium. Our results of *in situ* dispersions is consistent with previous reports that use AgNPs recovered from fungal cultures. As we explain below, the results of our initial characterization studies (Figure 3–1a) led us to enrich B-AgNPs from excess biomolecules in the dispersion medium and use acetonitrile to desorb the surface layer for further analysis as shown in Figure 3–1b. Through this approach, we were able to enrich B-AgNPs and examine the desorbed surface layer using a combination of techniques to reveal a "hard" corona composed of peptides consistent with stress response proteins and show evidence of carbohydrate detection.

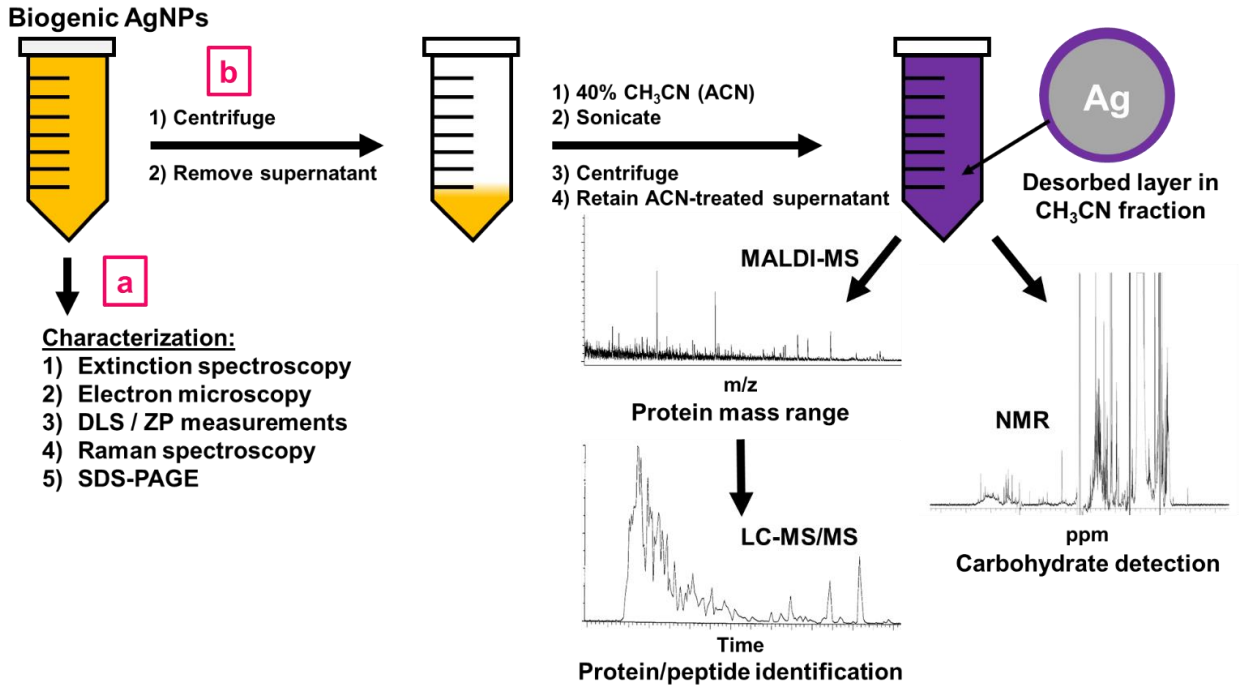

Figure 3–1. Characterization scheme for biogenic silver nanoparticles and the surface corona using indirect and direct methods. (a) *In situ* characterization of biogenic silver nanoparticles post filtration and separation from fungal biomass and indirect characterization of the surface corona. (b) Direct characterization of the surface corona by separation of excess biomolecules in the dispersion, desorption, and analyses of the biomolecules at the nanoparticle surface.

3.3.2. *In situ* surface characterization of silver nanoparticles dispersion

To corroborate presence of a corona or layer on the surface of AgNPs and measure its thickness, we used both electron and helium ion microscopy. Our electron micrographs shown in Figure 3–2 and our He-ion micrographs shown in Figure 3–3 provide visual evidence of a surface layer surrounding biogenic silver nanoparticles produced by *F. oxysporum*. To measure the thickness of the layer, we characterized and compared a series of unmodified (i.e. native) biogenic, thiol modified (i.e., 4-nitrobenzene thiol; NBT) biogenic, and commercial citrate-capped AgNPs with a diameter of ~ 20 nm. The latter two AgNPs provide reference points of different molecular sizes for expected values of thiol and citrate layers. Differences observed in TEM should result from surface layer differences on AgNPs. Modified and unmodified AgNPs were imaged with high-resolution TEM to quantitatively measure the layer thickness. This technique has been previously used to image citrate,[202] aliphatic thiols,[146] and aryl diazonium[30] derived films. Figures 3–4a-c show representative transmission electron micrographs of individual AgNPs and the thickness of the surface film measured using a line profile tool in Gatan Micrograph. Figure 3–4a shows an unmodified AgNP produced by *F. oxysporum*. The layer thickness is measured to be 2.1 ± 0.3 nm. Visible variation in the layer thickness can be seen in Figure 3–4a. Asymmetry in the surface layer can be expected since the surface layer is suspected to be composed of biomolecules (e.g., proteins). To calibrate our measurements, we modified 20 nm AgNPs produced by *F. oxysporum* with NBT to displace the surface layer as seen in Figure 3–4b. This approach allow us to calibrate our measurement to a known

length of a NBT molecule. Also, as acid-base theory suggests, there is a greater propensity of –SH to form a strong interaction with Ag due to –SH soft nucleophilicity. As such, we can expect a symmetrical monolayer coverage as evidenced in Figure 3–4b. Similarly, Figure 3–4c shows a symmetrical film of citrate around chemically produced AgNPs, which is consistent with an expected length of citrate molecule. Fernández-Iglesias and Bettmer exposed citrate-stabilized gold nanoparticles to either bovine serum albumin or human serum and reported TEM results in their supplementary information.[203] The authors conclude that formation of protein layer on 60 nm gold nanoparticles having a thickness of approximately 3 nm indicates monolayer coverage. Thicker regions (7 – 8 nm), as seen with 30 nm gold nanoparticles, indicates multilayer formation. Based on Fernández-Iglesias and Bettmer's report, it is reasonable to infer that our result of 2.1 ± 0.3 nm indicates monolayer coverage.

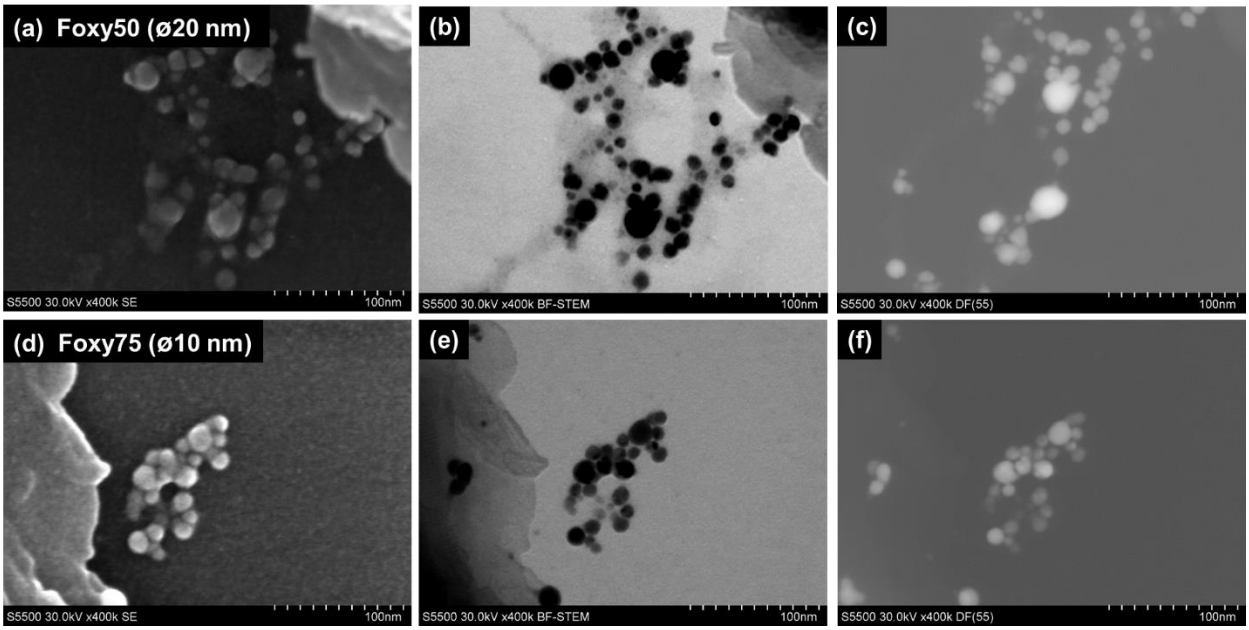

Figure 3–2. Scanning electron micrographs showing spherical nanoparticles with a visible surface film. (a–c) ~ ø20 nm silver nanoparticles produced by *Fusarium oxysporum* at 50°C (Foxy50). (d–f) ~ ø10 nm silver nanoparticles produced by *Fusarium oxysporum* at 75°C (Foxy75). Left panels show secondary emission, middle panels show bright field images in transmission mode, right panels show dark field. Scale bar = 100 nm.

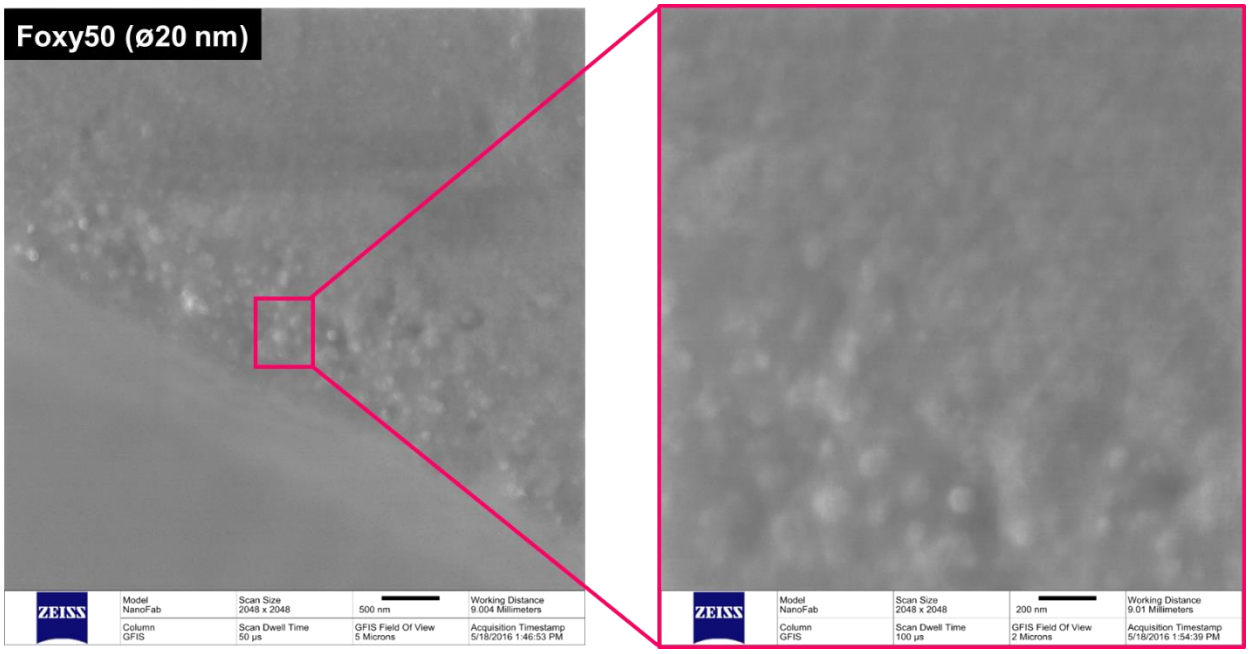

Figure 3–3. Helium ion micrographs showing ~ ø20 nm spherical nanoparticles with a visible surface film produced by *Fusarium oxysporum* at 50°C (Foxy50). Left panel scale bar = 500 nm. Right panel scale bar = 200 nm.

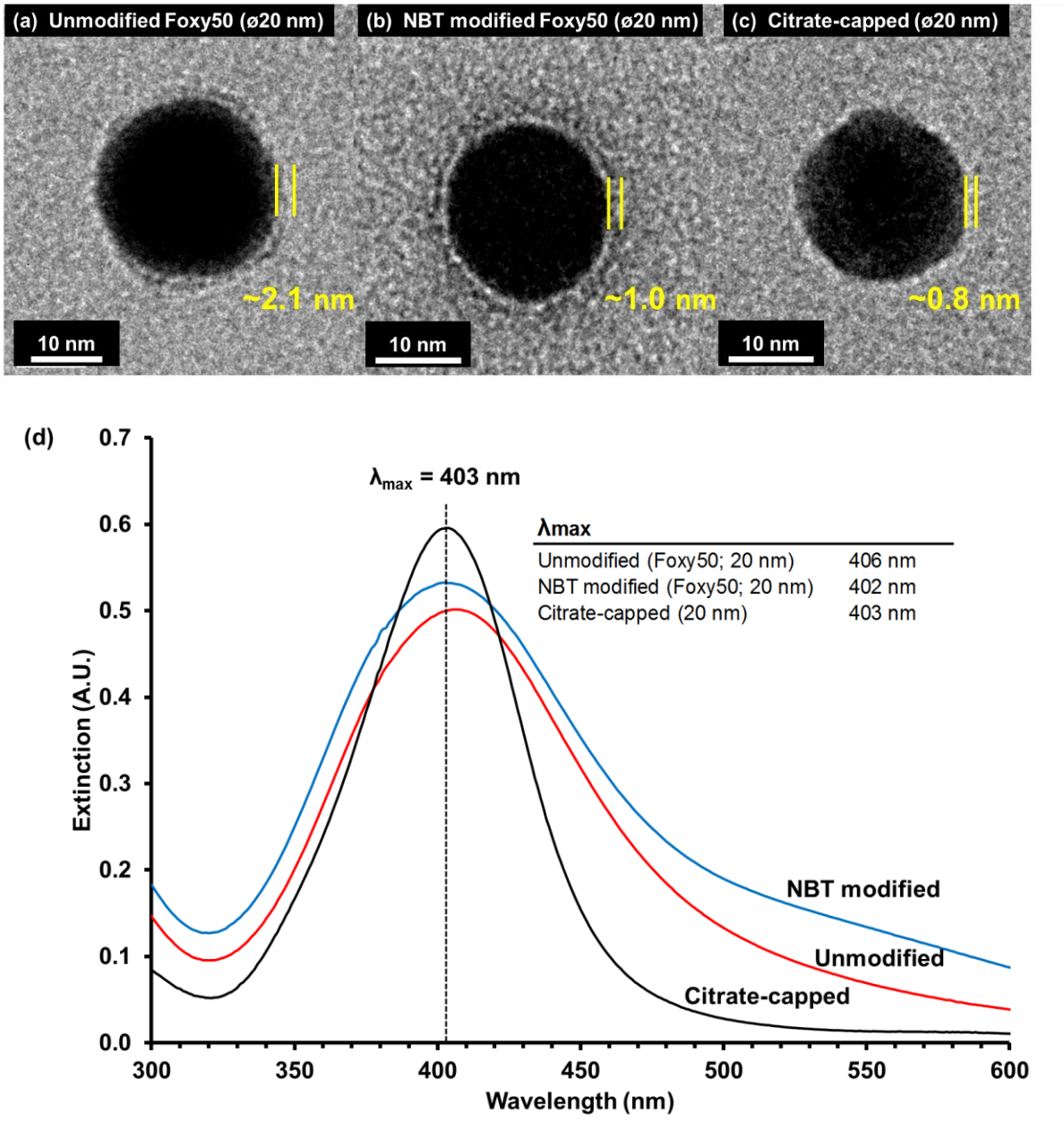

Figure 3–4. Characterization of biogenic silver nanoparticles (~ ø20 nm) produced by *Fusarium oxysporum* 405 at 50°C (Foxy50) and commercial citrate-capped (~ ø20 nm) silver nanoparticles. (a-c) Bright field transmission electron micrographs show the differences in surface layer thickness of unmodified biogenic silver nanoparticles, modified biogenic silver nanoparticles with 5 mM nitrobenzene thiol (NBT), and commercial citrate-capped silver nanoparticles. (d) Extinction plot demonstrating the relative localized surface plasmon resonance (SPR) peak position of the two biogenic nanoparticle preparations (unmodified and modified with NBT) in comparison to commercial citrate-capped nanoparticles. For biogenic silver nanoparticles, a 1 mM $AgNO_3$ solution was added to *Fusarium oxysporum* 405 and incubated in the dark with shaking at 100 rpm for 3 days. The extinction maximum (λ_{max}) for each spectrum is listed on the right.

Effect of the layer structure and thickness on the extinction spectra is shown in Figure 3–4d corresponding to the TEM measurements is discussed below for ~ ø20 nm nanoparticles. All three spectra contain a single LSPR band with maximum absorbances at 406, 402, and 403 nm, respectively. These spectra show no evidence of aggregation. Although the width of the bands of both unmodified B-AgNPs (FWHM ~ 106 nm) and NBT modified B-AgNPs (FWHM ~ 118 nm) are greater than those of commercial, chemically produced AgNPs (FWHM ~ 68 nm); analyses discussed below (Table 3–1) indicates that the polydispersity of biogenic AgNPs is consistent with commercial AgNPs. Thus, we attribute the breadth of the extinction band more to the surface layer and less to polydispersity. In the case of NBT modified B-AgNPs, the width of the band is greater than the unmodified B-AgNPs (FWHM Δ ~ 12 nm). We suspect an increase in bandwidth of ~ 12 nm is due to displacement of native layer with NBT and subsequent adsorption of free biomolecules in in a competitive manner for the NP surface, which may also explain the shift in peak position. According to Mie theory,[6, 204] modification of the nanoparticle surface with organic molecules will change the dielectric constant of the medium affecting the LSPR band position. As seen in Figure 3–4d, LSPR peak position of NBT modified B-AgNPs is blue shifted by 4 nm. This indicates a change in the dielectric environment immediately surrounding the B-AgNPs, which is likely due to desorption of the protein corona. Jain and co-workers reported a similar blue shift observation when they desorbed the protein corona of AgNPs produced by *Aspergillus* species NJPO2 by SDS boiling.[205]

The absolute magnitudes of the extinction bands are not consistent. This likely due to a higher starting concentration of commercial citrate capped nanoparticles compared to biogenic nanoparticles. We attempted to achieve similar concentrations by diluting citrate nanoparticles by four-fold and biogenic nanoparticles two-fold.

Table 3–1. Summary of calculated surface layer thicknesses and experimental measurements taken from extinction spectroscopy, TEM images, dynamic light scattering, polydispersity, and ζ potential for ~ ø20 nm silver nanoparticles: unmodified biogenic (unmodified Foxy50), nitrobenzene thiol modified biogenic (NBT modified Foxy50), and commercial citrate-capped.

	LSPR peak (λ_{max}, nm)	Calculated monolayer film thickness (nm)	TEM film thickness (nm)[b]	TEM diameter (nm)	D_{hyd} (nm)[e]	Polydispersity index[f]	ζ potential (mV)[g]
Unmodified Foxy50 (20 nm)	406	Unknown	2.1 ± 0.3	17 ± 3[c]	52 ± 1	0.4 ± 1	-24 ± 1
NBT modified Foxy50 (20 nm)	402	0.6-0.9[a]	1.0 ± 0.1	21 ± 5[c]	57 ± 2	0.4 ± 1	-2 ± 1
Citrate-capped (20 nm)	403	0.8[a]	0.8 ± 0.1	21 ± 3[d]	21 ± 1	0.4 ± 1	-33 ± 3

[a] Theoretical values for a monolayer thickness are based on reported values on Au substrates.
[b] Values reported are average based on three individual nanoparticles with six measurements per nanoparticle ± standard deviation.
[c] Transmission electron micrographs were analyzed with Gatan Digital Micrograph v2.31.734.0 or ImageJ 1.51t.[166] Values reported are an average ± standard deviation.
[d] According to manufacturer's specifications.
[e] Hydrodynamic diameter (Z-average) based on intensity. Values reported are an average of three measurements ± standard deviation.
[f] Values reported are the mean of three measurements ± standard deviation.
[g] Values reported are an average of three measurements ± standard deviation at 25°C. Measurement were conducted at neutral pH (~ 7). pH values determined by Whatman pH indicator paper (Type CF, pH 0-14).

Table 3–1 summarizes theoretical monolayer thickness calculations along with our measurements obtained from extinction spectroscopy, TEM images, dynamic light scattering, polydispersity indices, and surface potential for the series of three ~ ø20 nm AgNPs described above. In terms of calculated thickness values, we chose to make an indirect correlation to Au substrates since values for Ag substrates have not been reported. Our measured thicknesses for NBT modified B-AgNPs and citrate-capped AgNPs are consistent with values previously reported for Au substrates. For native B-AgNPs, we are unable to accurately report a calculated film layer thickness. This may vary considering the biological matrix that the nanoparticles are within, size of the nanoparticles, surface potential, the evolution of the biomolecular films, and the thickness calibration.

Our measurement of the film thickness is 2.1 ± 0.3 nm. The standard deviation provides an indication on the variability in layer thickness seen in Figure 3–4a. Less variability is observed in the thiol modified layer and citrate-capped AgNPs. Dynamic light scattering and zeta potential measurements were also used to further characterize the physical and chemical properties of AgNPs. Table 3–1 contains physical characterization results of particle size, polydispersity indices, surface potential, and relative colloidal stability.

Examining the DLS-measured hydrodynamic diameters, our results are consistent our previous report[183] stating that the hydrodynamic diameter for both B-AgNPs is ~ 3 times larger than the TEM results (17 ± 3 nm for unmodified) compared to citrate-capped

AgNPs. As we stated in our earlier report, we believe this difference reflects the presence of a unique capping layer formed around B-AgNPs. Table 3−1 also shows the results of all AgNPs possessing a native surface potential ranging from approximately −2 to −33 mV at neutral pH. Consistent with previous results,[183] the ZP values recorded for B-AgNPs were less negative than commercial AgNPs. A low ZP value of −2 mV recorded for NBT modified B-AgNPs can be explained by displacement of ionized biomolecules by neutral NBT molecules; thus increasing the surface potential. Increase in ZP also suggests that the biomolecular layer is largely contributing to the surface potential. Despite a lower ZP value, NBT modified B-AgNPs were highly stable. We suspect that a fraction of biomolecules re-adsorbed to the NP surface after being initially displaced by NBT. We note NPs with Raman active molecules such as NBT that exhibit colloidal stability would be beneficial for studies involving Raman active NP-labels.

Vibrational spectroscopy (e.g., Fourier transform infrared, Raman) is well known for providing information on molecular structure. Previous studies have documented the FTIR[104, 134, 173] and Raman[98, 133] spectroscopy to examine the surface layer of B-AgNPs from fungi and have concluded that the NP surface is capped with proteins. Though vibrational data is informative in providing molecular specificity, defining the surface layer with this technique leads to uncertainty. Also, studies that report infrared frequency assignments alone without showing spectra data require additional validation.[134] Since we are investigating the surface layer around AgNPs, we chose Raman scattering to corroborate previous reports examining *F. oxysporum*[98] and other fungi.[133] The advantage of using

Raman and noble metal nanostructures is that this technique is able to provide large signal enhancements of $10^4 - 10^6$ when molecules are located at or within a few nanometers from the surface of nanostructures commonly referred to as surface-enhanced Raman scattering or SERS.[62, 71, 206-207] The primary mechanism of this surface enhancement is an increased electric field generated by the excitation of the surface plasmon of the metal NP. Thus, we used Raman scattering to examine the possibility of proteins on the surface by interrogating unmodified ~ ø10 nm biogenic NPs along with ~ ø20 nm citrate-capped NPs for comparison shown in Figure 3–5. We do not show the spectrum for ~ ø20 nm in Figure 3–5 because the signal to noise is lower than that of ~ ø10 nm. The SERS spectra for both unmodified biogenic and citrate AgNPs shown in Figure 3–5 exhibit typical vibrational bands for the respective molecules. Proteineous and citrate molecules are poor Raman scatterers, which are represented by weak Raman band intensities observed. However, the major bands appear to be consistent with proteins and citrate molecules. For B-AgNPs, 1624 cm^{-1} is assigned to Amide II band; 1577 cm^{-1} is assigned to the asymmetric COO- stretching mode; and 1378 cm^{-1} for the symmetric COO- stretching mode. For citrate-capped NPs, 1571 cm^{-1} is assigned to the asymmetric COO- stretching mode, 1378 cm^{-1} is assigned to the symmetric COO- stretching mode, and 930 cm^{-1} band is assigned to C-OH deformation. Considering our measurements were collected from a drop-cast of aggregated nanoparticles, other carbonaceous species resulting from photo-damage may have also contributed to the spectra collected (Figure 3–5). Though our spectral richness contrast the works of Mukherjee et al.[133] and Potara et al.,[98] possibly due to differences in experimental configuration, sample material, or sample preparation; our results are

consistent with these works suggesting proteineous molecules are associated with biogenic AgNPs.

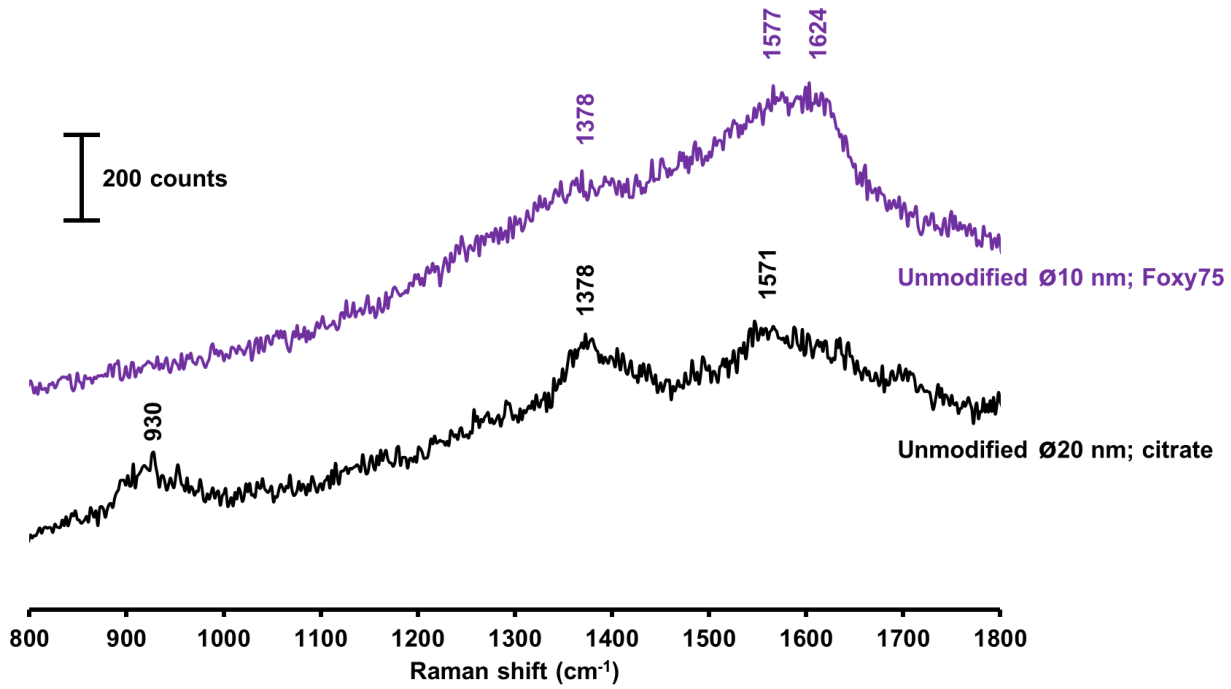

Figure 3–5. Raman spectra collected from unmodified biogenic silver nanoparticles (ø10 nm) to show intrinsic signals compared to commercial citrate-capped silver nanoparticles (ø20 nm). Raman signals collected from drop-casted nanoparticle on a planar gold substrate using a 514.5 nm laser at 50 ± 3 μW at the source and an integration time of 10 s. Spectra offset for clarity.

To identity putative proteins associated with AgNPs produced by *F. oxysporum* and estimate protein attributes of molecular weight and abundance; a standard technique of discontinuous sodium dodecyl sulfate polyacrylamide gel electrophoresis (SDS-PAGE)[208] was employed. This established technique is based on the principle that proteins are separated by electrophoresis according to the protein's molecular weight (size) with larger proteins migrating slower and smaller proteins migrating faster. The result is typically a discrete band that can then be correlated to molecular weight standards to provide an estimate of protein size.[209] There are a few reports that document the use of SDS-PAGE for the analysis of biogenic AgNPs from fungi,[171, 187] including *F. oxysporum*.[172] However no reports have systematically examined B-AgNPs ranging in sizes produced over a range of temperatures by *F. oxysporum*. We examined three sets of samples produced from *F. oxysporum* corresponding to three different temperature conditions (i.e., 45°C, 50°C, and 75°C). Temperature conditions inversely correlate to nanoparticle diameters (i.e., ~ ø30 nm, ~ ø20 nm, and ~ ø10 nm, respectively) and directly correlate to protein synthesis levels (i.e., generally higher abundance of proteins at higher temperatures). Each sample set included two controls, 1% YPG media and fungal filtrate (fungal culture without $AgNO_3$). Figure 3–6 shows a representative image of a 12% SDS-PAGE gel showing the most abundant proteins/peptides resolved by analyzing a set of samples corresponding to three different incubation condition and NP size. The 1% YPG media control lanes in all three cases principally shows a single band ~ 10 kDa in Figures 3–6A, 3–6D, and 3–6G. This result can be explained by ~ 12% of peptone, the major protein source in YPG medium, consists of 5-10 kDa peptides with the remaining ~ 88% consisting of smaller peptides.[210] Figures 3–6B, 3–6E, and 3–6H show fungal filtrate in the absence of $AgNO_3$.

Three bands at ~ 100 kDa, ~ 24 kDa, and ~ 9 kDa are evident for both Foxy45 and Foxy50; however Foxy75 (Figure 3–6H) has a single band at ~ 9 kDa. Given the temperature condition of 75°C, it is likely that larger proteins have degraded to short chain polypeptides as evidenced by the polypeptide staining pattern (i.e., smear) seen in Figure 3–6. In the case of Foxy45 and Foxy50, we note the possibility of two starred bands at ~ 47 kDa (Figure 3–6B) and ~ 35 kDa (Figures 3–6C and 3–6E) in low abundance. Although these bands are faint, they may be consistent with a ~ 44 kDa nitrate reductase reported by Kumar et al. working with *F. oxysporum*[211] and a ~ 25 kDa (~ 36 kDa molecular weight resolved by LC-MS/MS) glyceraldehyde-3-phosphate reported by Zhang et al. also working with *F. oxysporum*.[172] For samples containing AgNPs, the most notable result is the enriched band between ~ 2 kDa and ~ 5 kDa seen in Figures 3–6C and 3–6F for Foxy45 and Foxy50, respectively. This band for Foxy75 is less pronounced (Figure 3–6I). Our results show that this enriched band is specific to the production of AgNPs. In comparing fungal cultures with and without $AgNO_3$ exposure there are two important results. First, a ~ 24 kDa band consistent between filtrate (Figures 3–6B and 3–6E) and the AgNPs (Figures 6C and 6F), suggesting constitutive expression. Second, is a ~ 100 kDa band that appears to be in less abundance for the AgNPs (Figures 3–6C and 3–6F) compared to the filtrate (Figures 3–6B and 3–6E), suggesting down-regulation or inhibition. With Foxy75 it is difficult to draw conclusions since the temperature condition (75°C) is not ideal for protein stability. However, the stronger band intensity seen in Figures 3–6H and 3–6I for ~ 9 kDa supports the notion of increased protein abundance at higher temperatures based on higher staining intensity with increasing protein/peptide abundance. Though Foxy50 and Foxy75 are the predominantly investigated in this chapter, we report results for

Foxy45 as we plan to use NPs from this temperature condition for our future surface-enhanced Raman spectroscopy (SERS) based immunoassay studies. Subsequent chapters will report further details on AgNP modification and application.

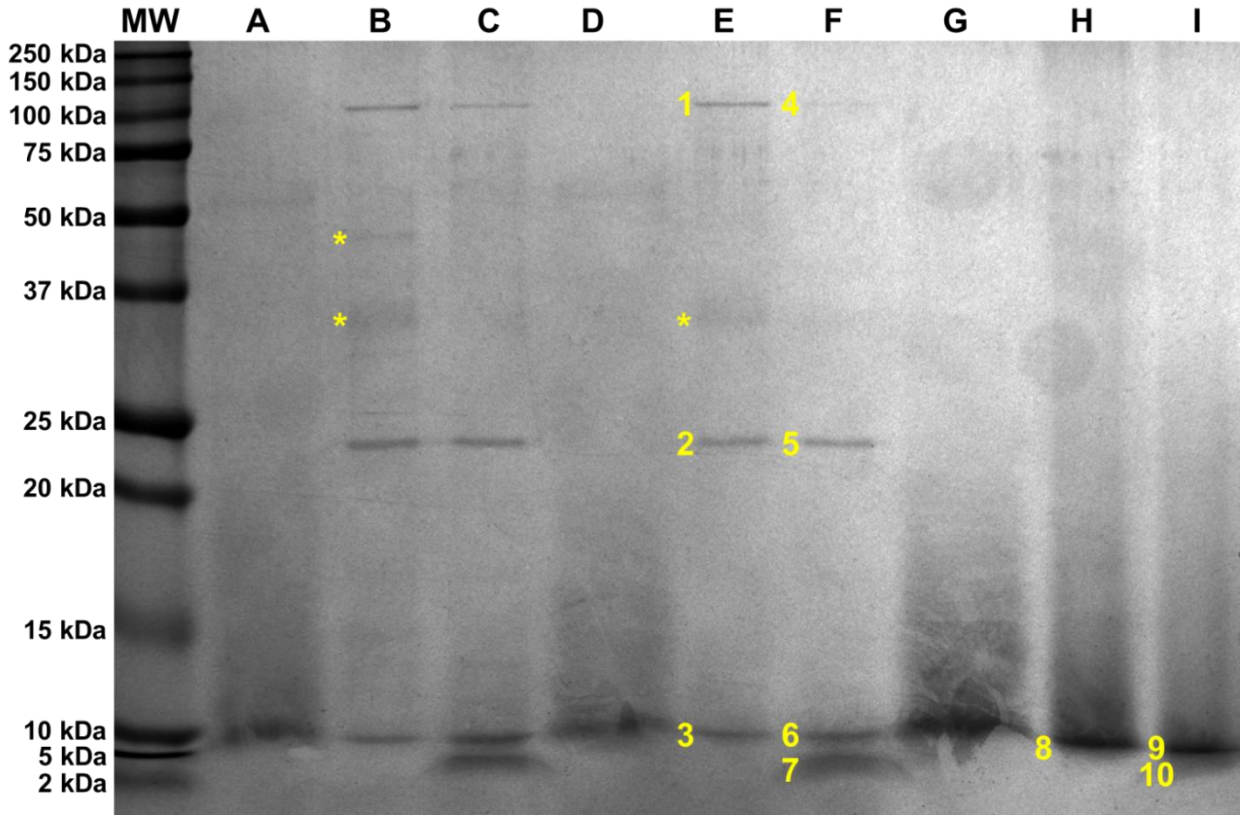

Figure 3–6. Representative grayscale image of a 1-D 12% sodium dodecyl sulfate polyacrylamide gel with proteins/peptides profiles associated with the production of silver nanoparticles by *Fusarium oxysporum* (Foxy) at 45°C, 50°C, and 75°C. Lane (A) Foxy45 1% yeast-peptone-glucose media control. Lane (B) Foxy45 fungal filtrate without 1 mM $AgNO_3$. Lane (C) Foxy45 with 1 mM $AgNO_3$ exposure resulting in silver nanoparticles (ø30 nm). Lane (D) Foxy50 1% yeast-peptone-glucose media control. Lane (E) Foxy50 fungal filtrate without 1 mM $AgNO_3$. Lane (F) Foxy45 with 1 mM AgNO3 exposure resulting in silver nanoparticles (ø20 nm). Lane (G) Foxy75 1% yeast-peptone-glucose media control. Lane (H) Foxy75 fungal filtrate without 1 mM $AgNO_3$. Lane (I) Foxy75 with 1 mM $AgNO_3$ exposure resulting in silver nanoparticles (ø10 nm). MW represents molecular weight standards. The numbered bands correspond to excised bands that were further analyzed using ESI-LC-MS/MS. Stars (*) indicate possible bands in low abundance.

For protein identification, the numbered bands shown in Figure 3–6 were excised, trypsin-digested, and analyzed by LC-MS/MS. Table 3–2 lists the most abundant proteins identified based on extensive homology from the gel-extracted bands. Figure 3–7 contains the tandem mass spectra of the highest Mascot peptide scores for the corresponding gel-extracted bands. Peptide sequences were confirmed by tandem mass spectra providing evidence of high signal intensities and consistent peptide fragments (a and b ions) shown in Figure 3–7. Discrepancy between the estimated molecular weights seen in Figure 3–6 compared to the molecular weights obtained from the NCBI database noted in Table 3–2 may be attributed to either post-translational modification (e.g., glycosylation or phosphorylation), post-translational cleavage, or splice variants by *F. oxysporum*. In analyzing the results contained in Table 3–2, bands 1 and 4 (~ 100 kDa) were both identified as a catalase-peroxidase 2 protein from *F. oxysporum*. Identification of a catalase-peroxidase enzyme result supports previous reports purporting the involvement of a reductase enzyme in *F. oxysporum*.[105, 113] We also suspect catalase-peroxidase enzyme(s) play a major role in studies that demonstrate AgNPs production using fungal culture filtrate. Catalase-peroxidase is an enzyme commonly found in virtually all aerobic organisms and functions to decompose H_2O_2 to water and molecular oxygen.[212] This enzyme is among a class of antioxidants that are involved in counterbalancing reactive oxygen species (ROS) and defend the organism from exceeding oxidative stress.[212] Sun et al. confirm catalase-peroxidase enzymes are involved in ion transport and metabolism and respond to oxidative stress in *F. oxysporum*; which may contribute to higher virulence in banana wilt disease.[213] Reactive oxygen species such as hydrogen peroxide (H_2O_2) and superoxide anion ($O_2^{\bullet -}$) are a group of free radicals, reactive molecules, and ions that are

byproducts of normal metabolism produced by partial reduction of oxygen during respiration.[214-215]

Table 3–2. Identification of the most abundant proteins from excised bands separated by sodium dodecyl sulphate polyacrylamide gel electrophoresis

Gel band #; Molecular weight	Description	Mascot protein score[a]	Mascot threshold[b]	Protein identification[c]	Molecular weight (Da)	NCBI accession number[d]
1; ~ 100 KDa	**Fungus control,** Foxy50	290	>54	Catalase-peroxidase 2 [*Fusarium oxysporum* forma *specialis cubense*]	85264	477517042
2; ~ 24 KDa	**Fungus control,** Foxy50	---	---	Low mass peptides resulted in no protein matches	---	---
3; ~ 9 KDa	**Fungus control,** Foxy50	57	>54	Hypothetical protein FOXB_11747 [*Fusarium oxysporum* Fo5176]	19699	342876063
4; ~ 100 KDa	**~ ø20 nm AgNPs,** Foxy50	58	>52	Catalase-peroxidase 2 [*Fusarium oxysporum* forma specialis *cubense*]	86036	477514144
5; ~ 24 KDa	**~ ø20 nm AgNPs,** Foxy50	95	>54	Superoxide dismutase, [*Fusarium oxysporum* forma specialis *cubense*]	23229	475668421
6; ~ 9 KDa	**~ ø20 nm AgNPs,** Foxy50	136	>53	Ubiquitin C [*Fusarium oxysporum* Fo47]	25731	587693765
7; ~ 3 KDa	**~ ø20 nm AgNPs,** Foxy50	---	---	Low mass peptides resulted in no protein matches	---	---
8; ~ 9 KDa	**Fungus control,** Foxy75	---	---	Low mass peptides resulted in no protein matches	---	---
9; ~ 9 KDa	**~ ø10 nm AgNPs,** Foxy75	126	>53	Ubiquitin C [*Fusarium oxysporum* Fo47]	25731	587693765
10; ~ 3 KDa	**~ ø10 nm AgNPs,** Foxy75	---	---	Low mass peptides resulted in no protein matches	---	---

[a] Protein ion score is -10*Log(P), where P is the probability that the observed match is a random event

[b] Individual ion scores above threshold indicate identity or extensive homology at $P < 0.05$

[c] Identification based on most extensive homology to abundant protein

[d] National Center for Biotechnology Information (NCBI) Protein database

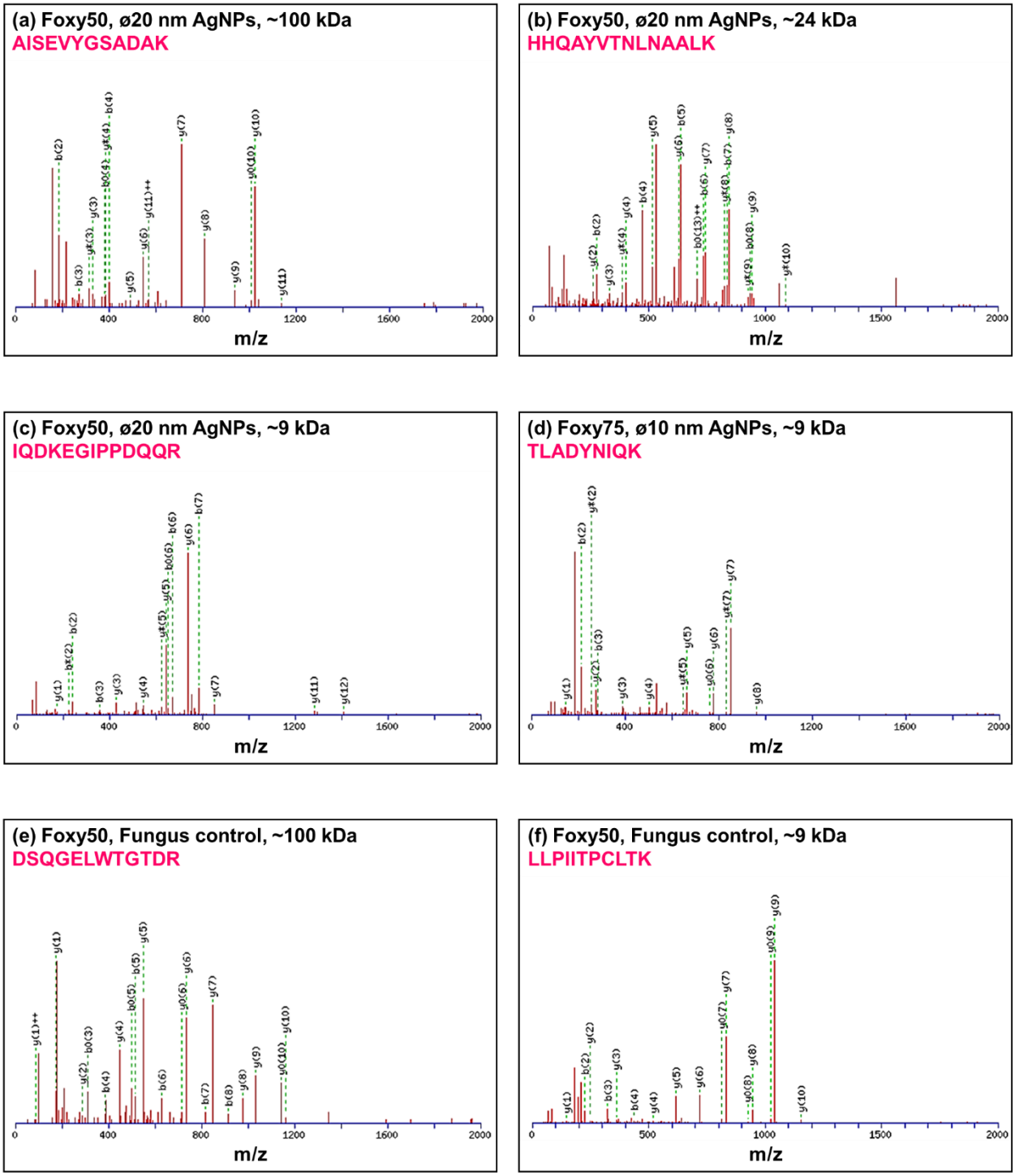

Figure 3–7. Tandem mass spectra of highest peptide scores for gel extracted bands. Plots of intensity as a function of mass to charge (m/z) ratio. (a-c) *Fusarium oxysporum* exposed to 1 mM $AgNO_3$ at 50°C resulting in ~ ø20 nm silver nanoparticles. (d) *Fusarium oxysporum* exposed to 1 mM $AgNO_3$ at 75°C resulting in ~ ø10 nm silver nanoparticles. (e-f) Control fungal filtrate at 50°C without exposure to 1 mM $AgNO_3$.

Aguirre et al. explain in the presence of trace metal ions, $O_2^{\bullet -}$ can react with H_2O_2 and generate a more reactive singlet oxygen species ($^1O_2$). In addition to reactive metal ions, ROS production can increase in fungi due to various stress factors such as starvation, ionizing irradiation, ultra-violet irradiation, visible light, temperature extremes, pH extremes, medium osmolality, mechanical damage, and interactions with other living organisms.[212] Hydrogen peroxide, a major ROS and signaling molecule,[216] leads to the production of hydroxyl radical ($HO^{\bullet}$), which can oxidase virtually any cellular molecule; causing DNA damage, protein inactivation, protein cross-linking and fragmentation, and lipid peroxidation.[214] Thus, at high concentrations of ROS, damage to biomolecules occurs, which may serve to be protective against interspecies competition; whereas, low/moderate concentrations of ROS serve as intracellular signaling molecules regulating physiological responses and developmental processes in fungi[212] and plants.[215] As *F. oxysporum* is commonly considered to be a plant pathogen, hence mechanisms for regulating ROS concentrations within fungi and plants may have co-evolved, since plants are known to produce an oxidative burst[217] in response to fungal structures or activity.[218] Redundancy in ROS proteins may also explain relative abundance of ROS proteins detected in Figure 3–6. As noted above, qualitative comparison between bands 1 and 4 (Figure 3–6) suggests a decrease in abundance in fungal cultures exposed to $AgNO_3$ (Figures 3–6E and 3–6F). Gavanji and co-workers report that catalase enzymes may be inhibited by high concentrations of hydrogen peroxide in context of elevated reactive oxygen species (ROS).[219] Band 2 (~ 24 kDa) and Band 3 (~ 9 kDa) shown in Table 3–2 provide little information with low mass peptides (Table 3–2, Band 2) and a hypothetical protein from *F. oxysporum* (Table 3–2, Band 3). However, in examining the record contained within the

NCBI database for the ~ 9 kDa hypothetical protein (Band 3), this protein is phylogenetically clustered with other mitogen-activated protein (MAP) kinase kinase proteins from fungi, including *F. oxysporum*.[220] Mitogen-activated protein kinase cascades are evolutionarily conserved proteins in eukaryotic cells that are involved in transducing a variety of extracellular signals and regulating growth and differentiation processes.[221] We provide further discussion on MAP kinase cascades below. Band 5 (~ 24 kDa) shown in Table 3–2 is identified to be consistent with superoxide dismutase (SOD) from *F. oxysporum*. Though we did not identify the adjacent band in the fungus control (Table 3–2, Band 2), we suspect a similar protein with SOD activity. Like catalase-peroxidase enzymes, SOD proteins have antioxidant activity in regulating oxidative stress.[212] SOD enzymes catalyzes dismutation of superoxide anion ($O_2^{\bullet -}$) producing H_2O_2 and O_2. As Gessler et al. report, $O_2^{\bullet -}$ can be produced by O_2 reduction with an NADPH catalyzed oxidase.[212] This would be consistent with Durán et al. mechanistic proposal of B-AgNPs production involving the reduction of NADP+ to NADPH and oxidization of NO_3^- to NO_2^-.[105] SOD enzymes believed to be the first line of defense against oxidative stress in eukaryotic cells,[212] which would explain expression in both fungal cultures exposed (Figure 3–6E; Table 3–2) and not exposed to $AgNO_3$ (Figure 3–6F; Table 3–2). From an ecological perspective, an abundance of SOD enzymes can serve to be protective during saprobic growth or can serve to be a competitive (i.e., virulence) factor in colonizing a plant host. For example, a 24 kDa protein from *Fusarium oxysporum* culture filtrates has been reported by Bailey and co-workers. Activity of this protein has been ascribed to eliciting ethylene production and necrosis in coca leaves.[222] We speculate that this 24 kDa protein is involved in the ROS, possibly having SOD activity resulting H_2O_2 production; which would

be consistent with our conclusions. Thus, it would be reasonable to infer *F. oxysporum* exposure to a solution of $AgNO_3$ for the production of AgNPs would lead to increased concentrations of ROS. This notion would be consistent with the observed protein profiles (Figure 3–6) and identification of highly abundant proteins (Table 3–2). Aguirre et al. comment that filamentous fungi [such as *F. oxysporum*] have additional mechanisms to handle ROS, such as the presence of a larger number of phosphorelay sensor kinases, antioxidant enzymes, and secondary metabolites with antioxidant properties.[214] Bands 6 and 9 (~ 9 kDa) was consistently identified as ubiquitin (likely from the ubiquitin c gene, UBC[223]) from *F. oxysporum*. Ubiquitin is a highly conserved regulatory protein[224] that is widely expressed in eukaryotes and has a molecular weight of 8500.[225] Effects of ubiquitinylation include protein degradation, protein trafficking, cell-cycle regulation, DNA repair, apoptosis, and signal transduction.[223] For more details on ubiquitin function, please refer to Hershko and Ciechanover review on the ubiquitin system.[224] Ubiquitin has been reported to be one of the most abundant proteins in eukaryotic cells, however ubiquitin does not seem to be in excess, but rather regulated as a free pool of adequate levels contingent on cell conditions.[223] Ubiquitin C has been ascribed to the UBC gene in mammals that is responsive to UV irradiation, heat shock, oxidative stress, and translational impairment.[223] Also, site-specific interactions between ubiquitin and gold nanoparticles have been reported.[226] Collectively, these pieces of evidence support our inference of adaptive or stress responsive proteins are involved with silver ion exposure by *F. oxysporum*. For enriched bands seen in Figure 3–6 for Foxy50 (band 7) and Foxy 75 (band 10), mass spectrometric results yielded low mass peptides with no protein matched (Table 3–2).

Thus, to identify enriched bands associated with B-AgNPs, we took a unique approach to desorb the surface corona using acetonitrile (Figure 3–1b) and analyzed the desorbed fraction using both MALDI-MS and LC-MS/MS. Prior to mass spectrometric analyses, we sought to confirm the effectiveness of acetonitrile in desorbing the surface corona by extinction spectroscopy and DLS. Figure 3–8 contains an extinction plot showing ~ ø20 nm AgNPs with a single extinction band with a surface plasmon peak centred at 402 nm. After these NPs were treated with 40% acetonitrile, centrifuged, and resuspended in DI H_2O, the AgNPs destabilized as evidenced by the loss in the extinction band in Figure 3–8. We also used extinction spectroscopy to estimate the total protein at each step for an approximate protein recovery by recording the absorbance at 260 nm and 280 nm. Tables 3–3 and 3–4 contain our estimated protein concentrations for both ~ ø20 nm and ~ ø10 nm treated with either 40% acetonitrile (more polar) or 80% acetonitrile (less polar), respectively.

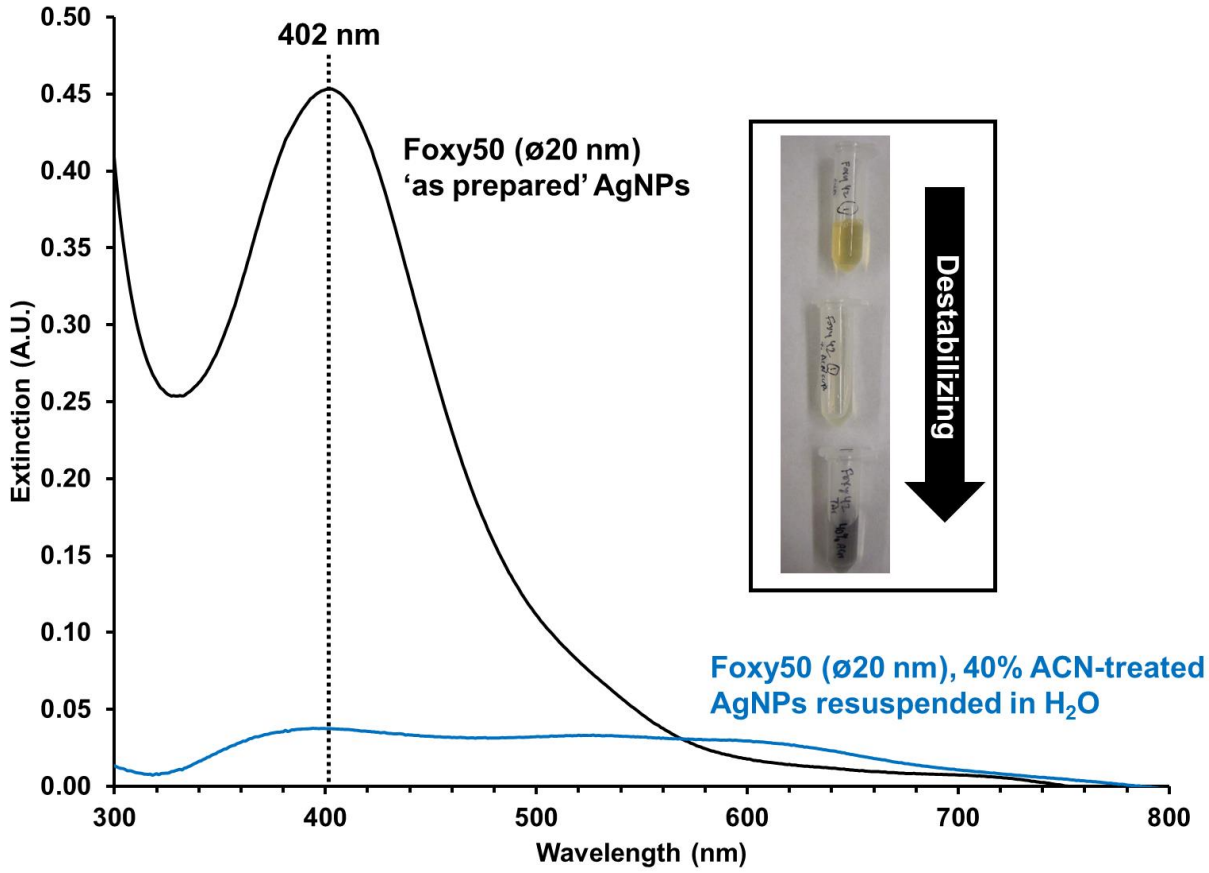

Figure 3–8. Extinction plot of ~ ø20 nm silver nanoparticles produced by *Fusarium oxysporum* with and without acetonitrile treatment to desorb the surface corona. The black spectra shows the extinction band of 'as prepared' nanoparticles with a surface plasmon peak at 402 nm. The blue spectra shows the extinction of the ~ ø20 nm treated with 40% acetonitrile, centrifuged, and resuspended in deionized water. Inset shows the 'as prepared' nanoparticles with characteristic yellow colour indicting of plasmonic AgNPs (top), the middle tube is the acetonitrile supernatant removed after centrifugation, the bottom tube show AgNPs resuspended in water after acetonitrile treatment. Grayish coloured solution is characteristic of destabilized (aggregated) nanoparticles, suggesting removal of the surface corona.

Consistent with our previous work,[183] ~ ø10 nm AgNPs have a higher abundance of proteins compared to ~ ø20 nm AgNPs. In all cases, most proteins are removed (~ 80-94%) in the supernatant after centrifugation (Tables 3–3 and 3–4). It is important to note that *in situ* characterization of capping proteins would contain more abundance of these proteins, resulting in higher levels of excess or background protein. For ~ ø20 nm AgNPs, 2–7% of proteins are recovered within the acetonitrile fractions with more recovered using 40% rather than 80% (Tables 3–3 and 3–4). For ~ ø10 nm AgNPs, 5–15% of proteins are recovered in the acetonitrile fractions with a more pronounced improvement using 40% acetonitrile (Tables 3–3 and 3–4). The residual protein fraction recovered after the removal of the surface corona and resuspension in DI H_20 is < 5%, except for ~ ø10 nm treated with 80% acetonitrile (Tables 3–3 and 3–4). Though most protein fraction can be displaced with a single wash step, a small fraction of proteins will likely remain chemically bonded to the nanoparticle surface (e.g., cysteine or amine linkages). Based on our estimated protein analyses, we selected 40% acetonitrile to be our choice for desorbing the surface corona. To track destabilization of the AgNPs after removal of the surface corona, we used DLS to monitor the change in hydrodynamic diameter. We expect that the AgNPs will destabilize (aggregate) by removing the surface corona. Table 3–5 contains our results confirming an increase in hydrodynamic diameter with acetonitrile treatments. For ~ ø20 nm AgNPs, the hydrodynamic diameter increases from 57 ± 1 nm to 687 ± 351 nm after two treatments of 40% acetonitrile. We also tried 80% acetonitrile and a similar, yet less pronounced increase in hydrodynamic diameter is recorded for ~ ø20 nm AgNPs. Our results for ~ ø20 nm AgNPs were consistent with our ~ ø10 nm AgNPs. Thus, our DLS study confirms that the NPs destabilize (aggregate) with the removal of the surface corona

and 40% acetonitrile was more efficient than 80% in desorbing the surface corona. Thus, we proceeded to determine the surface corona composition of B-AgNPs by removal of excess free proteins, 40% treatment of the AgNPs, followed by mass spectrometry and nuclear magnetic resonance.

Table 3–3. Protein concentration of biogenic silver nanoparticles *in situ* and desorbing of the surface layer using 40% acetonitrile.

Biogenic nanoparticle diameter	Sample description	Total protein[a] (mcg/mL)	Normalized percent recovery[b]
~ Ø20 nm	'As prepared' AgNP dispersion[c]	1439 ± 23	100%
	Supernatant fraction	1279 ± 10	87 – 91%
	Supernatant from 40% acetonitrile treated AgNPs	73 ± 7	5 – 7%
	40% acetonitrile treated AgNPs pellet and resuspended in water (2nd treatment)[d]	29 ± 19	1 – 3%
~ Ø10 nm	'As prepared' AgNP dispersion[c]	1883 ± 11	100%
	Supernatant fraction	1537 ± 36	80 – 83%
	Supernatant from 40% acetonitrile treated AgNPs	251 ± 25	12 – 15%
	40% acetonitrile treated AgNPs pellet and resuspended in water (2nd treatment)[d]	45 ± 36	1 – 4%

[a] Estimated protein concentration was calculated according to [Protein] mg/mL = $1.55*A_{280}$-$0.76*A_{260}$.[175-176] Values reported in micrograms/millilitre. Error is reported as standard deviation of three measurements.

[b] Normalized to 'as-prepared' sample. Reported values are approximations.

[c] Silver nanoparticles dispersed in aqueous medium recovered post separation from fungal culture (i.e. post filtration).

[d] AgNPs treated with 40% acetonitrile, centrifuged, and resuspended in water (2nd treatment).

Table 3–4. Protein concentration of biogenic silver nanoparticles *in situ* and desorbing of the surface layer using 80% acetonitrile.

Biogenic nanoparticle diameter	Sample description	Total protein[a] (mcg/mL)	Normalized percent recovery[b]
~ Ø20 nm	'As prepared' AgNP dispersion[c]	1439 ± 23	100%
	Supernatant fraction	1352 ± 106	85 – 94%
	Supernatant from 80% acetonitrile treated AgNPs	47 ± 19	2 – 4%
	80% acetonitrile treated AgNPs pellet and resuspended in water (2nd treatment)[d]	16 ± 3	1 – 3%
~ Ø10 nm	'As prepared' AgNP dispersion[c]	1883 ± 11	100%
	Supernatant fraction	1543 ± 33	81 – 83%
	Supernatant from 80% acetonitrile treated AgNPs	111 ± 5	5 – 6%
	80% acetonitrile treated AgNPs pellet and resuspended in water (2nd treatment)[d]	120 ± 63	3 – 10%

[a] Estimated protein concentration was calculated according to [Protein] mg/mL = $1.55*A_{280}$-$0.76*A_{260}$.[175-176] Values reported in micrograms/millilitre. Error is reported as standard deviation of three measurements.

[b] Normalized to 'as-prepared' sample. Reported values are approximations.

[c] Silver nanoparticles dispersed in aqueous medium recovered post separation from fungal culture (i.e. post filtration).

[d] AgNPs treated with 80% acetonitrile, centrifuged, and resuspended in water (2nd treatment).

Table 3–5. Tracking changes in hydrodynamic diameter of biogenic silver nanoparticles *in situ* and desorbing of the surface layer using either 40% or 80% acetonitrile.

Biogenic nanoparticle diameter	Sample description	Hydrodynamic diameter[a] (nm)
~ Ø20 nm	'As prepared' AgNP dispersion[b]	57 ± 1
	40% acetonitrile treated AgNPs pellet and resuspended in water (1st treatment)[c]	69 ± 1
	40% acetonitrile treated AgNPs pellet and resuspended in water (2nd treatment)[c]	687 ± 351
	80% acetonitrile treated AgNPs pellet and resuspended in water (1st treatment)[c]	126 ± 1
	80% acetonitrile treated AgNPs pellet and resuspended in water (2nd treatment)[c]	371 ± 15
~ Ø10 nm	'As prepared' AgNP dispersion[b]	22 ± 1
	40% acetonitrile treated AgNPs pellet and resuspended in water (1st treatment)[c]	64 ± 1
	40% acetonitrile treated AgNPs pellet and resuspended in water (2nd treatment)[c]	779 ± 56
	80% acetonitrile treated AgNPs pellet and resuspended in water (1st treatment)[c]	82 ± 2
	80% acetonitrile treated AgNPs pellet and resuspended in water (2nd treatment)[c]	319 ± 12

[a] Z-Average based on intensity. Error is reported as standard deviation of three measurements.
[b] Silver nanoparticles dispersed in aqueous medium recovered post separation from fungal culture (i.e. post filtration).
[c] Silver nanoparticles treated with acetonitrile, centrifuged, and resuspended in water.

3.3.3. Determination of the surface corona composition

To understand the surface corona in more detail, we removed excess proteins in the dispersion and desorbed the surface layer of biogenic AgNPs using 40% acetonitrile (Figure 3–1). This approach enabled us to interrogate the biomolecules associated with the NPs and provide information on the ≤ 5 kDa enriched SDS-PAGE bands we observed in Figure 3–4. Our three-pronged characterization approach involved (1) MALDI-MS to confirm the molecular size range of all proteins associated with B-AgNPs; (2) LC-MS/MS for identification; and (3) NMR to investigate our suspicion of carbohydrates. Figures 3–9 and 3–10 contain our MALDI-MS and LC-MS/MS results for ~ ø20 nm, ~ ø10 nm, and the corresponding controls, respectively. Based on our MALDI-MS results shown in Figures 3–9a-d and 3–10a-d, we conclude that there are expected spectral differences among the samples and that the highest signals were recorded below 5 kDa. Future work may include tracking the origin the peptides and examining the influence of culture media. In context of m/z signal similarities, the MALDI spectrum recorded from the acetonitrile desorbed layer is more consistent with the fungal control rather than that of the media (Figures 3–9 and 3–10). Our results suggest that the biomolecules associated with the corona primarily originate from *F. oxysporum* and not from the culture media (Figures 3–9 and 3–10). In terms of size ranges for MALDI analysis, we also tested ranges up to 20 kDa and 220 kDa, however the signal to noise ratio was low suggesting low abundance (data not shown). Thus, our MALDI-MS provides evidence that the surface corona is composed largely of peptides. Next, we proceeded to identify the peptides in each sample by LC-MS/MS. Figures 3–9e-h and 3–10e-h contain our base peak ion chromatograms (BPI) for acetonitrile treated ~ ø20 nm AgNPs and ~ ø10 nm AgNPs; supernatants of the 'as

prepared' dispersions, fungus control (without $AgNO_3$), and media control (1% YPG). Consistent with MALDI-MS spectral differences among the samples, our BPI chromatograms show differences among samples. However, most peptides have short retention time (~ 5 min) suggesting that there is a higher ratio of more polar than less polar peptides, which would be reasonable given that the NPs are dispersed in an aqueous medium. Figure 3–11 contains our tandem mass spectra and peptide sequences with the highest Mascot scores. Peptide sequences were confirmed by tandem mass spectra providing evidence of high signal intensities and consistent peptide fragments (a and b ions) shown in Figure 3–11.

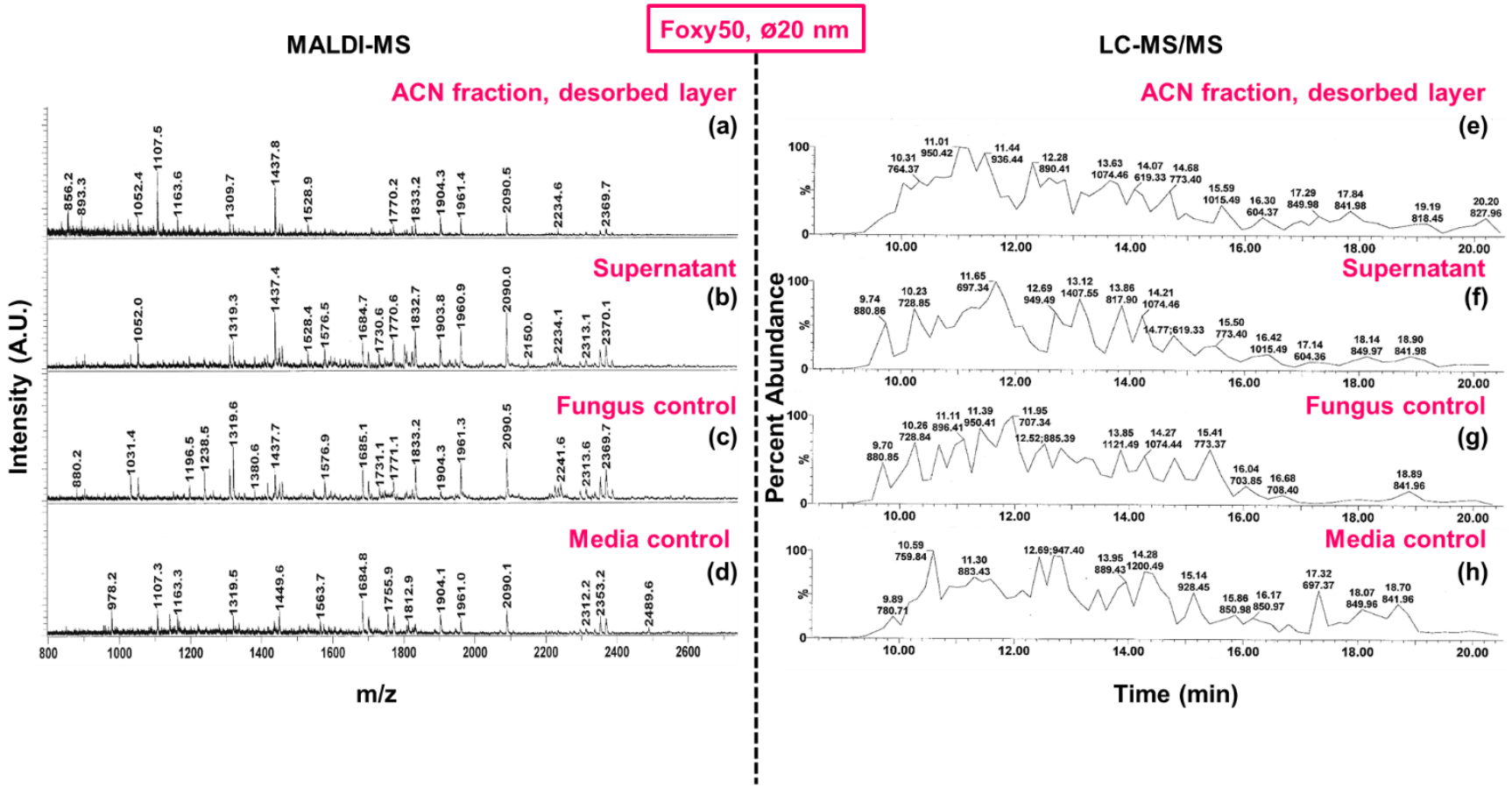

Figure 3–9. Mass spectrometry results from ~ ø20 nm silver nanoparticles produced by *Fusarium oxysporum* at 50°C (Foxy50) compared to controls: fungus only with no silver nitrate exposure and media used to culture fungus. MALDI-MS spectra (a-d) are shown on the left and corresponding LC-MS/MS chromatograms (e-h) are shown on the right. (a and e) Results collected from an acetonitrile fraction containing the desorbed layer. (b and f) Results collected from the supernatant after centrifugation of silver nanoparticles. (c and g) Results collected from *F. oxysporum* culture filtrate in the absence of 1 mM silver nitrate. (d and h) Results collected from 1% yeast-peptone-glucose media incubated at 50°C. This media was used to initially culture F. oxysporum and used as a negative control during nanoparticle production.

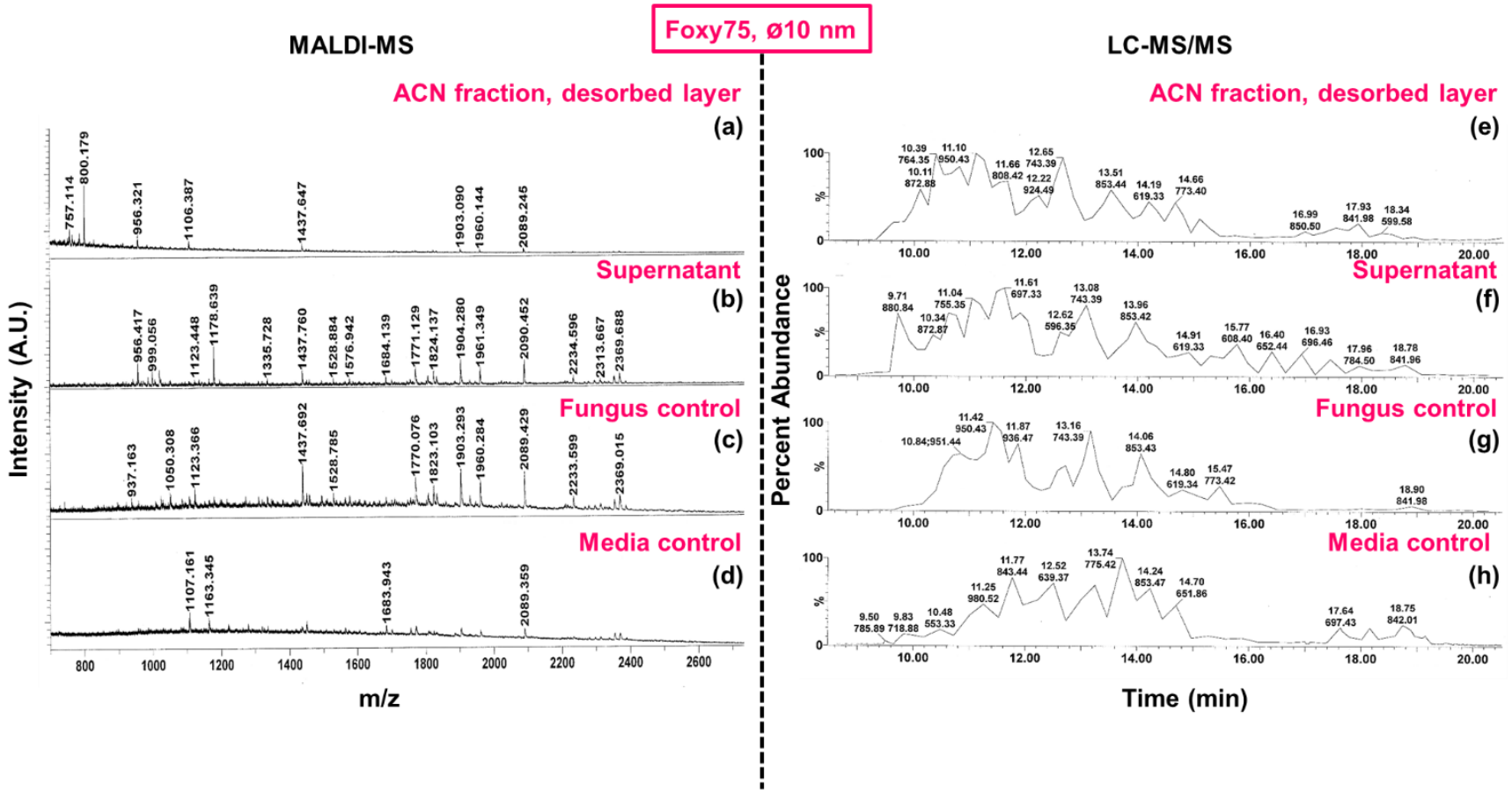

Figure 3–10. Mass spectrometry results from ~ ø10 nm silver nanoparticles produced by *Fusarium oxysporum* at 75°C (Foxy75) compared to controls: fungus only with no silver nitrate exposure and media used to culture fungus. MALDI-MS spectra (a-d) are shown on the left and corresponding LC-MS/MS chromatograms (e-h) are shown on the right. (a and e) Results collected from an acetonitrile fraction containing the desorbed layer. (b and f) Results collected from the supernatant after centrifugation of silver nanoparticles. (c and g) Results collected from *F. oxysporum* culture filtrate in the absence of 1 mM silver nitrate. (d and h) Results collected from 1% yeast-peptone-glucose media incubated at 50°C. This media was used to initially culture F. oxysporum and used as a negative control during nanoparticle production.

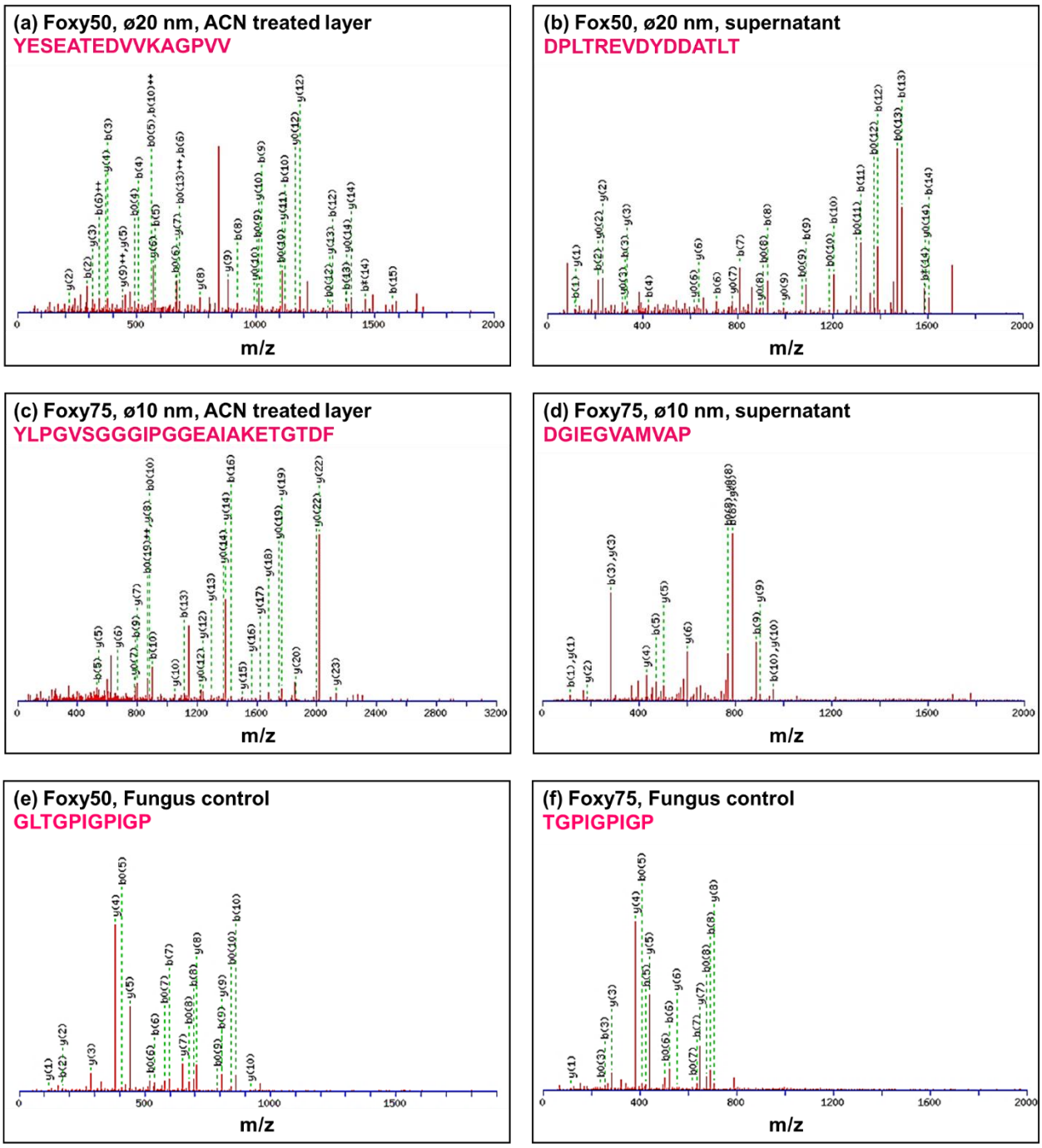

Figure 3–11. Tandem mass spectra of highest peptide scores for desorbed surface layer from ~ ø20 nm and ~ ø10 nm biogenic silver nanoparticles produced by Fusarium oxysporum (Foxy) at either 50°C or 75°C. Plots of intensity as a function of mass to charge (m/z) ratio. (a) Surface layer desorbed from ~ ø20 nm silver nanoparticles with acetonitrile (ACN). (b) supernatant fraction of ~ ø20 nm silver nanoparticles post centrifugation. (c) Surface layer desorbed from ~ ø10 nm silver nanoparticles with ACN. (d) supernatant fraction of ~ ø10 nm silver nanoparticles post centrifugation. (e-f) Control fungal filtrate at 50°C or 75°C without exposure to 1 mM $AgNO_3$.

Tables 3–6 and 3–7 contains the most abundant proteins identified with extensive homology for ~ ø20 nm and ~ ø10 nm AgNPs, respectively, based on tandem mass spectrometry. All proteins identified in the desorbed surface corona of both ~ ø20 nm and ~ ø10 nm AgNPs are homologous to *F. oxysporum* (Tables 3–6 and 3–7). In Table 3–6, phosphoenolpyruvate carboxykinase, glyceraldehyde-3-phosphate dehydrogenase, and malate dehydrogenase enzymes have been reported to be involved in carbohydrate transport and metabolism with co-enzyme nicotinamide adenine dinucleotide.[213, 227] Identification of elongation factor 2 suggests the abundance of a protein involved in protein synthesis (Table 3–6). The supernatant of ~ ø20 nm AgNPs contains phosphoenolpyruvate carboxykinase (Table 3–6). The abundance of phosphoenolpyruvate carboxykinase suggests that *F. oxysporum* is expressing proteins in high abundance involved in the generation of high energy molecules such as adenosine triphosphate (ATP). In comparison with Foxy50 fungal filtrate control, cultures exposed to $AgNO_3$ have upregulated or have higher expression levels consistent with carbohydrate metabolism as evidenced by the hypothetical proteins from other fungal organisms shown in Table 3–3. These results are consistent with the fractions derived ~ ø10 nm AgNPs and the related Foxy75 controls (Table 3–7). Changes in relative protein abundance could be attributed to differences in production temperature (50°C versus 75°C) and protein stability. For our medium control, we identified a peptide with extensive homology to *Saccharomyces cerevisiae*, which is consistent with the yeast extract component (Table 3–6). Low mass peptides resulting in no protein matches were found for the medium control for ~ ø10 nm; likely due to protein degradation at 75°C (Table 3–7).

Table 3–6. Identification of the most abundant proteins based on extensive homology from ~ ø20 nm silver nanoparticles or culture filtrate produced by *Fusarium oxysporum* at 50°C.

Sample description	Mascot protein Score[a]	Mascot threshold[b]	Protein identification[c]	Molecular weight (Da)	NCBI accession number[d]
Desorbed surface corona from ø20 nm AgNPs	302	>73	Phosphoenolpyruvate carboxykinase [*F. oxysporum* forma specialis *lycopersici*]	36980	902727943
	135	>73	Glyceraldehyde-3-phosphate dehydrogenase [*F. oxysporum* forma specialis *cubense*]	36085	475671174
	116	>73	Elongation factor 2 [*F. oxysporum* forma specialis *lycopersici*]	50294	902732414
	82	>73	Malate dehydrogenase, [*F. oxysporum*]	31158	587669178
ø20 nm AgNPs supernatant	113	>73	Phosphoenolpyruvate carboxykinase [*F. oxysporum* forma specialis *lycopersici*]	36980	902727943
Foxy50 fungus control[e]	282	>73	Hypothetical protein TGAM01_01851 [*Trichoderma gamsii*]	89417	969886537
	80	>73	Hypothetical protein, variant [*Magnaporthe oryzae*]	134233	389623189
Medium control[f]	163	>71	YGR192C [*Saccharomyces cerevisiae*]	35666	45269553

[a] Protein ion score is -10*Log(P), where P is the probability that the observed match is a random event.
[b] Individual ion scores above threshold indicate identity or extensive homology at $P < 0.05$
[c] Identification based on most extensive homology to abundant protein
[d] National Center for Biotechnology Information (NCBI) Protein database
[e] Fungus cultured without 1 mM $AgNO_3$
[f] 1% yeast-peptone-glucose broth

Table 3–7. Identification of the most abundant proteins based on extensive homology from ~ ø10 nm silver nanoparticles or culture filtrate produced by *Fusarium oxysporum* at 75°C.

Sample description	Mascot protein Score[a]	Mascot threshold[b]	Protein identification[c]	Molecular weight (Da)	NCBI accession number[d]
Desorbed surface corona from ø10 nm AgNPs	84	>73	Malate dehydrogenase, NAD-dependent [*Fusarium oxysporum*]	34862	587669372
Ø10 nm AgNPs supernatant	90	>73	Hypothetical protein, variant [*Magnaporthe oryzae*]	134233	389623189
	73	>73	Putative serine endopeptidase protein [*Eutypa lata*]	101362	629667903
Foxy75 fungus control[e]	84	>73	Hypothetical protein, variant [*Magnaporthe oryzae*]	134233	389623189
	75	>73	Hypothetical protein TGAM01_01851 [*Trichoderma gamsii*]	89417	969886537
Medium control[f]	---	---	Low mass peptides resulted in no protein matches	---	---

[a] Protein ion score is -10*Log(P), where P is the probability that the observed match is a random event.
[b] Individual ion scores above threshold indicate identity or extensive homology at $P < 0.05$
[c] Identification based on most extensive homology to abundant protein
[d] National Center for Biotechnology Information (NCBI) Protein database
[e] Fungus cultured without 1 mM $AgNO_3$
[f] 1% yeast-peptone-glucose broth

Our results profiling the composition of the surface corona is consistent with a previous report identifying glyceraldhehyde-3-phosphate dehydrogenase from 128 ± 70 nm gold nanoparticles synthesized by *F. oxysporum*.[172] Zhang et al. also identified a 3-glucan binding protein that contrasts our results; however both proteins are consistent with carbohydrate metabolism. Sun et al.[213] reported 99 proteins expressed by mainly two pathotypes (low and high virulence) of *F. oxysporum* that cause banana wilt. Based on the author's cluster analysis of orthologous groups of proteins, the largest functional classification is carbohydrate transport and metabolism (~ 30% of total proteins).[213] Gene ontology analysis revealed that most of 99 proteins were involved in either processes related to carbohydrate metabolism or antioxidation.[213] Thus, the authors conclude that carbohydrate metabolism and ion transport may be important in the pathogenesis of *Fusarium* wilt disease in bananas.[213] In an ecological context, high abundance of proteins involved in carbohydrate metabolism and ion transport for activating antioxidant molecules would be consistent with biotic and abiotic stress response.

Our *in situ* characterization and our direct characterization of the surface corona by acetonitrile desorption suggests that the peptides identified with extensive homology to proteins involved in either carbohydrate metabolism or responding to reactive oxygen species (i.e., anti-oxidation). We hypothesis that higher expression of proteins involved in carbohydrate metabolism or anti-oxidation are ultimately regulated by mitogen-activated protein (MAP) kinase cascades. Segorbe and co-workers[228] describe MAP kinase cascades as a family of evolutionarily conserved three-tiered protein kinase modules composed of a

MAP kinase kinase kinase (MAP3K) that phosphorylates downstream MAP kinase kinase (MAP2K), which activates a MAP kinase for downstream transmission of cellular signals and gene transcription. Phosphorylation occurs at the hydroxyl group of serine, threonine, and tyrosine residues. These evolutionarily conserved pathways in a variety of organisms from fungi,[220-221, 228-229] plants,[218, 230] to mammals[231-232] function as crucial signal transducers of environmental stimulus, stress adaptation, and host recognition to activate gene transcription for cellular responses (e.g., apoptosis, proliferation, differentiation, defense). A previous report indicates that MAP kinases are associated with the regulation of physiological traits and virulence in banana wilt disease caused by *F. oxysporum* forma specialis c*ubense*.[220] Recently, three MAP kinases Fmk1, Mpk1, and Hog1 are involved in the regulation of development (e.g., hyphal growth, fusion, and aggregation), stress response (e.g., cell wall integrity, heat, hyperosmotic, oxidative), and virulence of *F. oxysporum* against plant and animal hosts.[233] Segorbe and co-workers describe Mpk1 and Hog1 regulate cellular adaptation to different types of stress, whereas Fmk1 and Mpk1 jointly contribute to ROS homeostasis. Both processes impact fungal growth and affect virulence towards plants or animal hosts.[228] Thus, our results leads us to conclude that the surface corona of B-AgNPs produced by *F. oxysporum* is composed of peptides from adaptive or protective proteins likely responding to environmental stress. We postulate *F. oxysporum* is predominantly responding to reactive silver ions and to a lesser extent heat stress and upregulating expression of proteins involved in metal detoxification. Given that surface corona is composed of peptides, we suspect that the mechanism of Ag^{+} ions reduction to AgNPs may be consistent with Kracht and co-workers[234] report demonstrating AgNPs synthesis using peptide aggregates in the presence of chloride ions as a medium for

electron transfer. We have previously shown an energy dispersive X-ray spectrum with a strong signal originating from chloride collected from spot profiles of AgNPs on fungal mycelia.[183]

In another study investigating B-AgNPs from using culture filtrate of *Aspergillus tubingensis*, Ballottin and co-workers[235] identified eight proteins *in situ* from ~ ø35 nm AgNPs by mass spectrometry. Based on the enzyme commission (EC) numbers provided in Ballottin et al. paper, three proteins identified were glucan 1,4-alpha-glucosidase (EC 3.2.1.3)[236], acid phosphatase (EC 3.1.3.2)[237], and prolyl oligopeptidase (EC 3.3.21.26).[238] The authors conclude that all proteins were involved in metabolic pathways and are important for carbon, phosphorus, and nitrogen uptake, and for fungal growth. Furthermore, the authors claim identified proteins are involved in the formation and stabilization of B-AgNPs. Though we agree with Ballottin and co-workers that protein/peptides are involved in formation and stabilization of B-AgNPs, our identified proteins from *F. oxysporum* contrasts those of Ballottin's report. Though the studies examine different fungal organisms, we believe it is more important to evaluate the characterization approach for a fair comparison. Thus, we provide an explanation below in examining our characterization approaches of *in situ* versus a more direct investigation of the surface corona.

In examining our two characterization approaches (Figure 3–1), a few key points must be noted. Both approaches led to identifying peptides that have extensive homology

to protective or adaptive proteins. However, the exact proteins identified through each approach were different. The difference can be explained by higher background protein expression levels *in situ*. As discussed above, 80 – 91% of total protein abundance is found in the supernatant after centrifuging AgNPs (Tables 3–3 and 3–4). Higher protein backgrounds affect the overall protein profile and careful interpretations must be made in context of the surface corona. Differences in protein abundance and protein profiles should be interpreted in context of the fungal culture conditions. For example, temperature conditions will influence protein expression levels and stability. Initial culture media may also play a role. Also, organism variability may influence specific proteins expressed, however we believe that most fungal proteins will lead to adaptive or protective proteins in the event of metal ion exposure. Thus, we encourage researchers investigating the surface corona of B-AgNPs to carefully document methods of characterization to enable appropriate treatment of the data for ecological interpretations.

We now turn our attention to our hypothesis of glycosylated proteins on the surface of B-AgNPs. Based on our discussion above related to post-translational modification of proteins in context of our SDS-PAGE results and our experience producing AgNPs, we hypothesized that a fraction of amino acid residues may be glycosylated. Wan and co-workers state that glycosylation is one of the most abundant post-translational protein modifications.[239] As such, we investigated the possibility of carbohydrates associated with the surface layer of B-AgNPs by one dimensional ^{1}H NMR. Figure 3–12 shows our ^{1}H NMR spectrum with signals collected at ~ δ 3.6 and ~ δ 5.2 ppm consistent with carbohydrates,

likely anomeric resonances of glucose.[240] Further investigation using 2D NMR and possibly coupled with liquid chromatography may help identify the carbohydrates more definitely. The broad bands with densely crowded resonance lines seen between ~ δ 1.2, ~ δ 3.8, ~ δ 7.3, and ~ δ 8.0 ppm are consistent with proteins.[241] Currently, there are no reports of the surface corona of B-AgNPs being comprised of carbohydrates. We are the first to provide evidence of surface corona composed of peptides and carbohydrates. The implications for carbohydrates is broader modification strategies, role in colloidal stability,[239] possible effect on nanoparticle size/morphology,[242] use as effective capping agents,[243-245] and influencing nanoparticle-cell interactions either by enhancing cell membrane adhesion and uptake or stimulating the immune system in humans.[239]

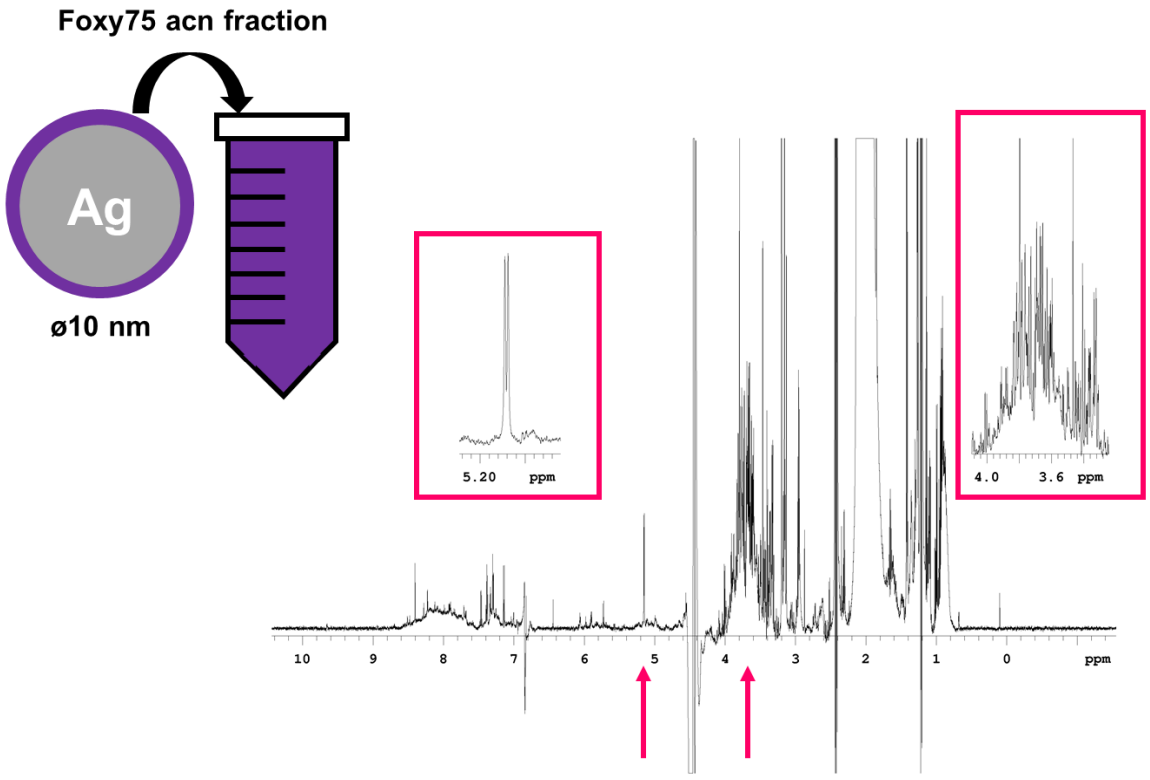

Figure 3–12. ^{1}H Nuclear magnetic resonance spectrum collected from an acetonitrile fraction containing the desorbed surface layer (purple in cartoon) of ~ ø10 nm silver nanoparticles produced by *Fusarium oxysporum* in heavy water (i.e., deuterium oxide). Highlighted regions (pink arrow and boxes) show signals consistent with carbohydrates, likely anomeric resonances of glucose. Signals for deuterium oxide resonance seen at ~ δ 4.4 and acetonitrile resonance seen at ~ δ 2.1 ppm.[246]

We propose the model shown in Figure 3–13 to depict our current understanding of the surface corona of AgNPs produced by *F. oxysporum* based on our results. We believe that the surface corona is a thin mixed layer comprised predominately of peptides originating from adaptive or protective proteins from MAP kinase cascades triggered by environmental stress (e.g., reactive silver metal ions). To lesser extent, other primary or secondary metabolic peptides may be part of the layer. Peptides are presumed to adsorb stochastically around the silver nanoparticle effectively lowering the surface energy.[247-248]

In terms of specific amino acid residues interacting with the AgNP surface, there are reports of proline and hydroxyl-containing residues, along with Cys, Leu, Lys, Arg, Ser, Met, and NH_2 groups are known to interact with Ag ions.[179, 247, 249-250] Collectively, the selection and arrangement of peptides enable nanoparticle stability, establish a reducing environment,[247] and provide a biological identity. Based on Monopoli and co-workers descriptions of a "hard" and "soft" corona,[121] we also believe that such an interface extends to B-AgNPs wherein the mixed corona layer is made up of a "hard" corona with peptides bound to the nanoparticle surface and a "soft" corona that is in equilibrium with the aqueous medium. To this end, we note that other factors such as NP size, shape, surface potential, and biological backgrounds will influence corona formations. Hence, we acknowledge that our assumptions will need to be tested for confirmation.

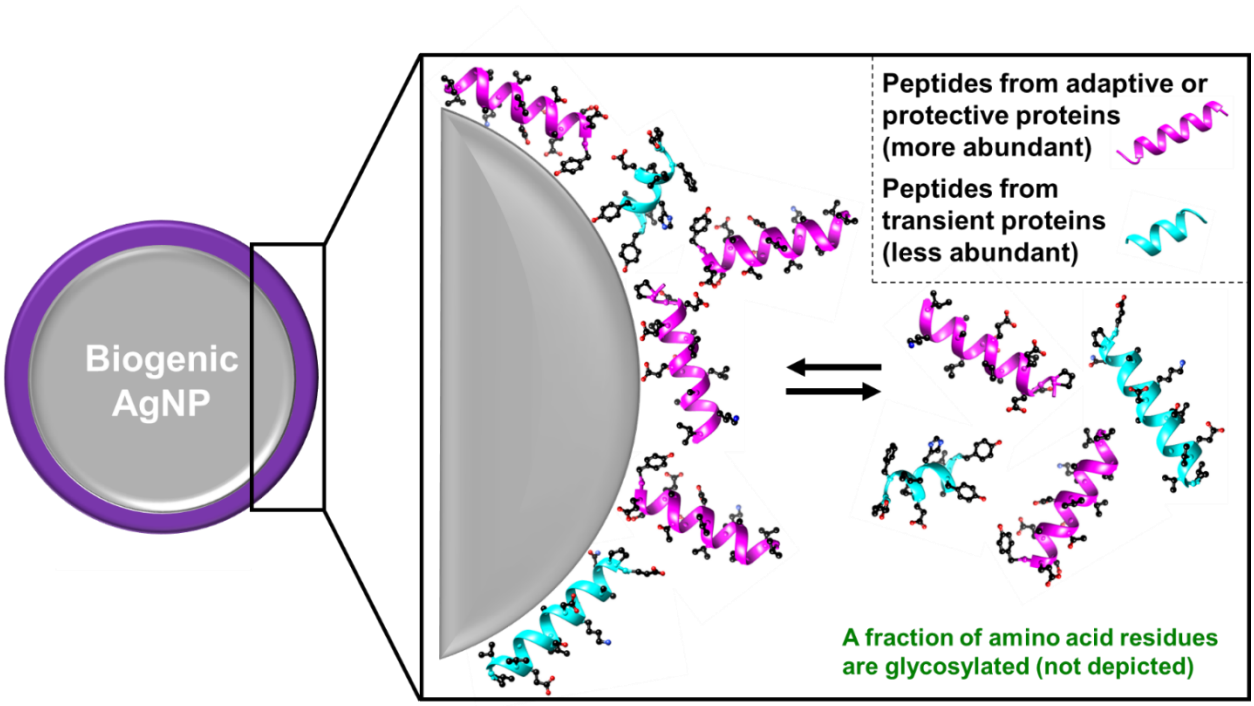

Figure 3–13. Model of the surface corona of biogenic AgNPs produced by *Fusarium oxysporum* based on optical and mass spectrometric results. The mixed layer (purple) is predominately comprised of peptides from adaptive or protective proteins (pink) and peptides from transient proteins (blue) synthesized by *F. oxysporum* in response to environmental stress. A fraction of peptides form a "hard" corona that is bound to the surface and others form a "soft" corona that is in equilibrium with the aqueous medium. Amino acid side chains are shown with black atoms representing carbon, red atoms representing oxygen, and blue atoms representing nitrogen. A fraction of amino acids will be glycosylated, however proportion and N– or O–linked chemistry is unknown.

3.4. Conclusion

The surface corona of nanoparticles is the interface with the environment. As such, a detailed understanding of the surface corona is valuable for application development and understanding *in vivo* interactions. Currently, our understanding the inherent surface corona of biogenic silver nanoparticles is limited. Previous reports investigating biogenic silver nanoparticles have suggested that the surface layer is comprised of capping proteins. However, many of these reports have contributed indirect evidence to substantiate claims and have not clearly addressed excess biomolecules in the dispersion. Currently, there are no reports describing the surface corona of biogenic silver nanoparticles providing both indirect and direct structural and compositional evidence. Using our previously optimized fungal isolate of *Fusarium oxysporum*, we examination involved both *in situ* analyses of silver nanoparticle dispersions (indirect) and desorption of the surface corona (direct). Using a series of orthogonal characterization techniques such as UV-visible spectroscopy, TEM, SEM, DLS, ZP, Raman spectroscopy, SDS-PAGE, MALDI-MS, LC-MS/MS, and NMR; we show evidence the surface corona of biogenic silver nanoparticles produced by *Fusarium oxysporum* is comprised of a thin mixed layer of peptides and carbohydrates. We hypothesize the origin of these peptides is from adaptive or protective proteins from the mitogen activated protein kinase cascades triggered by environmental stress (e.g., reactive silver metal ions). Peptides are presumed to adsorb stochastically around the silver nanoparticle to minimize surface energy; thus conferring nanoparticle stability, a reducing environment, and biological identity. We believe careful documentation of methods used to characterize the inherent surface corona of biogenic silver nanoparticles will allow for

more judicious interpretations. Important implications of the surface corona will impact application develop by defining modification strategies with enhanced colloidal stability for nanoparticle-enhanced bioassays and influence nanoparticle-cell interactions *in vivo*.

Chapter 4. Evidence for controlled modification of biogenic silver nanoparticles

4.1. Introduction

In Chapter 3, the surface corona of biogenic silver nanoparticles produced by a fungus, *Fusarium oxysporum*, was examined in detail. Examination of the corona involved both *in situ* analysis of silver nanoparticle dispersions (indirect) and desorption of the surface corona (direct). Using a series of orthogonal characterization techniques such as UV-visible extinction spectroscopy, TEM, SEM, DLS, ZP, Raman spectroscopy, SDS-PAGE, MALDI-MS, LC-MS/MS, and NMR; we showed evidence of the surface corona is comprised of a thin mixed layer of peptides and carbohydrates. We hypothesize the origin of these peptides is from adaptive or protective proteins that are part of mitogen activated protein kinase cascades triggered by environmental stress (e.g., reactive silver metal ions). Peptides are presumed to adsorb stochastically around the silver nanoparticle to minimize surface energy. This process confers nanoparticle stability, establishes a reducing environment, and provides biological identity. We believe careful documentation of methods used to characterize the inherent surface corona of biogenic silver nanoparticles will allow for more judicious interpretations of composition. Understanding the surface corona of biogenic nanoparticles will impact applications by defining surface modification strategies, enhancing colloidal stability, and allowing prediction for *in vitro* or *in vivo* interactions.

This chapter advances the functionality of biogenic AgNPs (B-AgNPs) towards a surface-enhanced Raman scattering (SERS) sandwich immunoassay. Contained within this chapter is a collection of experiments to demonstrate controlled surface modification of B-AgNPs by adding Raman reporter molecules and antibodies. In parallel, results to optimize a capture substrate that will be used in a SERS immunoassay are presented. Figure 4–1 displays an overview of the modification strategy and preparation of the capture substrate. Step one involves modifying the surface of B-AgNPs with Raman reporter molecules to produce extrinsic Raman active labels (Figure 4–1A). As discussed in chapter 2, B-AgNPs have a weak intrinsic scattering cross section. Thus, it is important to increase the Raman signal intensity by adding Raman reporter molecules. We demonstrate this by modifying ø10 nm, ø20 nm, and ø30 nm B-AgNPs with five different Raman reporter molecules in turn with control. Subsequent addition of IgG antibodies (anti-androgen receptor full length, anti-AR-FL) is demonstrated to add specificity to the Raman labels. Successful modification is evidenced by UV-visible extinction spectroscopy and Raman spectroscopy results. With each modification step, B-AgNPs were stable with few exceptions that are discussed in this chapter. Optimization of substrate was performed through plasmonic coupling experiments to determine if 300 nm thick Au or 300 nm thick Ag films provide higher Raman signal intensities. Based on these experiments, a biochip consisting of multiple metal film spots deposited onto a standard microscope slides were fabricated with the aim of clinical use.

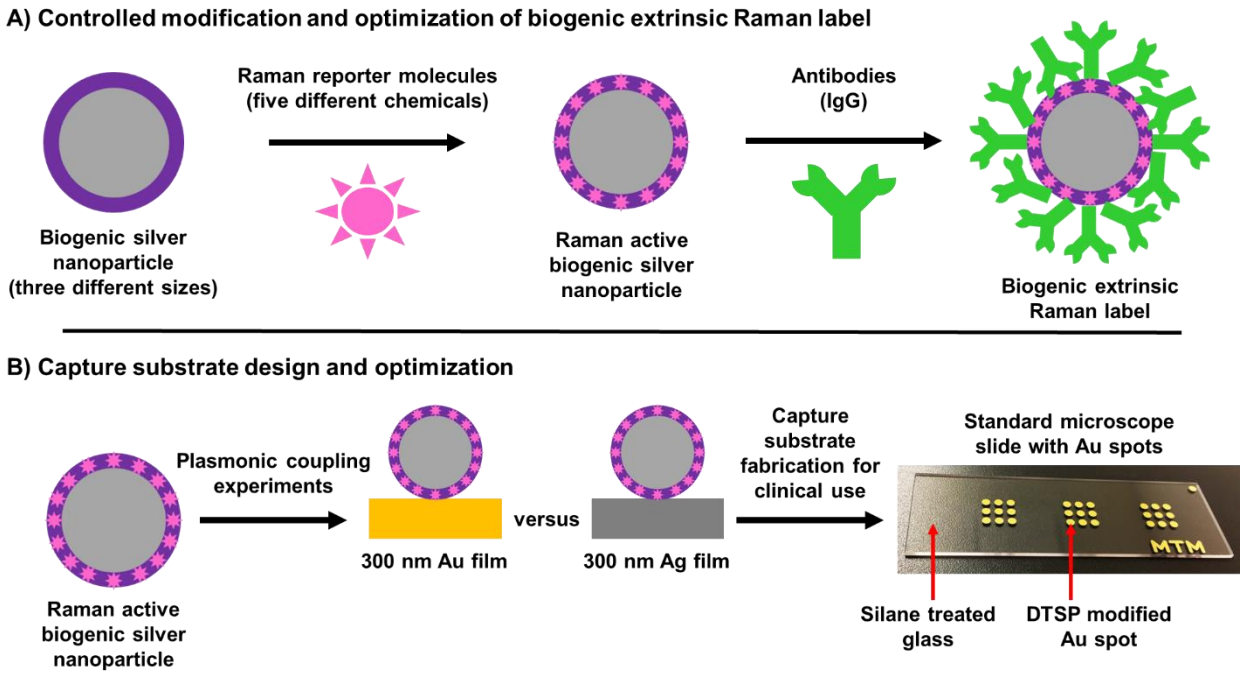

Figure 4–1. Overview scheme to modify the surface of biogenic silver nanoparticles and to optimize a substrate to capture bio-analytes towards biosensing platforms. (A) Three different sizes of biogenic silver nanoparticles were used in modification strategies using five different Raman reporter molecules. After this step, the B-AgNPs were verified to be Raman active. These Raman active AgNPs were further modified with the addition of antibodies for selective targeting of protein biomolecules. (B) To optimize Raman signal intensity, a comparison of two metal films was evaluated for enhanced electronic coupling leading to the design of a substrate aimed for clinical use. The substrate consisted of a standard microscope slide with multiple gold spots. The gold spots were later modified with a bifunctional linker, dithiobis(succinimidyl propionate) (DTSP), for antibody coupling.[152, 251] The glass surface was treated with tridecafluoro-1,1,2,2-tetrahydrooctyl dimethylchlorosilane to provide a hydrophobic background and minimize droplet spreading from the gold spots.

4.2. Experimental

4.2.1. Reagents and materials

The following reagents were used as received: acetonitrile (HPLC grade, Caledon), ethyl alcohol (anhydrous, Commercial Alcohols), H_2SO_4 (95-98%, Caledon), 4-mercaptobenzonitrile (95%, product# SS-7247, Batch# L44964, Combi-Blocks, California, USA), tridecafluoro-1,1,2,2-tetrahydrooctyl dimethylchlorosilane (DMS, product# SIT8170.0, Gelest, USA), anti-androgen receptor-full length antibodies (ab74272, lot# GR315793-3, Abcam, Canada). The following reagents were obtained from Sigma-Aldrich and used as received: 2-naphthalene thiol (99%, product# 270849-5G), 4-mercaptophenol (90%, product# 275395-5G), 4-nitrobenzene thiol (80%, product# N27209-5G), 4-mercaptobenzoic acid (90%, product# 662534-5G), N-(3-dimethylaminopropyl)-N'-ethylcarbodiimide hydrochloride (EDC, ≥ 99%, product# 03449-1G), N-hydroxysuccinimide (NHS, 98%, product# 130672-5G), bovine serum albumin (BSA, ≥ 98%, product# A3059-50G, lot# SLBT8252), H_2O_2 (30%, ACS reagent, product# 216763-500 mL), dithiobis(succinimidyl propionate) (DTSP, product# D3669-500 MG), Sodium chloride (ACS reagent, ≥ 99.0%, catalog# S9888), silver nitrate (≥ 99%, ACS reagent, 209139-25G). The following reagents were obtained from Thermo Fisher Scientific and used as received: BupH borate buffer (BB) packs (catalog# 28384), Pierce 20X phosphate-buffered saline (PBS, catalog# 28348), standard microscope slides (25 mm x 75 mm x 1 mm, Fisher Scientific product# 12-550-A3), BD Bacto yeast extract (product# 212750, lot# 5180630), BD Bacto peptone (product# 211677, lot# 2306004), dextrose (ACS reagent, product# 73409, lot# 720331). Deionized (DI) water with a resistivity of 18 MΩ·cm was

used for all aqueous preparations unless otherwise noted. All buffers were prepared in deionized water.

4.2.2. Production and separation of biogenic silver nanoparticles

A detailed description of silver nanoparticles production has been published[183] and has appeared in the previous two chapters with further optimization in chapter 3. Briefly, *Fusarium oxysporum* isolate 405 was initially cultured on potato dextrose agar (PDA) in the dark for seven days at 23°C ± 2°C. Next, *F. oxysporum* was set up as a liquid culture by removing one piece (~ 1 cm x 2 cm) of solid PDA growth medium containing mycelium and conidia and transferring to each sterile 500 mL Erlenmeyer flask containing 100 mL of sterile 1% yeast extract, 1% D-glucose and 1% Bacto-peptone (1% YGP). All inoculated flasks plus control medium flasks (i.e., no fungal inoculum) were incubated in the dark at 23°C ± 2°C shaking at 150 rpm for four days. Next, fungal biomass was separated from the culture broth by centrifuging at 2000 rpm for 5 min in a swing-out bucket centrifuge. Settled biomass was washed once with sterile DI water, centrifuged, and weighed after supernatant was decanted. Average fungal fresh (wet) weight and standard deviation was determined to be 42 ± 4 grams (n = 15).

Harvested washed fungal biomass was added to 100 mL of sterile 1 mM aqueous $AgNO_3$ solution (fresh) in sterile Nalgene PMP conical flasks with screw cap lids at 23°C ± 2°C. After inoculating, all flasks were incubated either at: a) 45°C ± 0.3°C, b) 50°C ± 1°C or c)

75°C ± 1°C under dark conditions with shaking at 100 rpm for three days. Simultaneously, a negative control containing only silver nitrate solution and a positive control containing only fungus was maintained under identical experimental conditions. Fungal culture flasks were weighed post incubation. The average mass change and standard deviation in fungal culture was determined to be a loss of 0.2 ± 0.01 grams (n = 6).

4.2.3. Enrichment of biogenic nanoparticles

To separate and recover AgNPs, aqueous dispersions of AgNPs with fungi were sonicated for 20 min at 23°C ± 2°C using a Branson 5510 ultrasonicator to separate nanoparticles from fungal mycelia post synthesis. After sonicating, aqueous dispersions with fungal mycelia were filtered using a sterile 0.1 µm polyethersulfone membrane 250 mL vacuum filtration unit (Millipore, product# SCVPU02RE, Massachusetts, USA). Negative fungal control flasks were treated the same. All samples were stored in the dark at 4°C until use.

Biogenic nanoparticles produced at 50°C exhibit an average diameter of 17 nm ± 3 nm (~ ø20 nm) and those produced at 75°C are 9 nm ± 4 nm (~ ø10 nm) based on previous TEM measurements.[183] Nanoparticles produced at 45°C exhibit an average diameter of 27 nm ± 5 nm (~ ø30 nm) based on TEM measurements shown below.

4.2.4. Preparation of biogenic extrinsic Raman labels

4.2.4.1. Post synthesis modification

Biogenic ERLs were prepared in batches using a 1 mL aqueous suspension of AgNPs and adding 10 µL of selected Raman reporter regent in 100% acetonitrile (fresh) and incubating in the dark at room temperature (22°C). For modification with antibodies, 20 µL of anti-human AR-FL pAb (1 mg mL^{-1} stock solution) was added after 1 h incubation with Raman reporter reagent and further incubated overnight (~ 18 h) at room temperature (22°C) in the dark. Excess reactants were removed by centrifugation (Eppendorf 5417R microcentrifuge) at 5000 rpm for 10 min. The resulting supernatant was carefully removed and the ERL pellet was resuspended in 1 mL of DI water or 1% BSA in 2.0 mM BB.

4.2.4.2. *In situ* modification

At the time of silver nanoparticle production (i.e., introduction of 1 mM $AgNO_3$ in culture), 1010 µL of sterile 5 mM solution of MBN (fresh) in anhydrous ethanol was immediately added to designated PMP flasks after $AgNO_3$ addition. Final *in situ* concentration of MBN was 0.05 mM. The 5 mM stock solution was sterilized using a 0.22 µm syringe filter to maintain aseptic technique through the production process. Ethanol was selected as the carrier for MBN due to its lower toxic effects on biological organisms (e.g., fungi) compared to acetonitrile and for its comparable solubility of MBN.

4.2.5. Fabrication of SERS capture substrates with Au or Ag films

Standard microscope slides (25 mm x 75 mm x 1 mm) was purchased from Fisher Scientific and used as the substrate base. The substrates were cleaned using hot piranha solution (4:1, H_2SO_4: 30% H_2O_2) for 30 min followed by thorough rinsing with DI water and blown dry using Ar gas. [*Warning: Piranha solution should be handled with extreme care; it is a strong oxidant and reacts violently with many organic materials. When mixed with incompatible chemicals, this solution presents an explosion hazard. All work should be performed in an appropriate chemical fume hood with appropriate personal protective equipment.*] The cleaned and dried substrates were mounted on a custom holder designed for whole slide coverage or mounted on a mask that exposed twenty-eight 2 mm diameter round spots (three by three arrays and one spot for slide orientation) as seen in Figure 4–1B and placed into the chamber of a thermal evaporator (Torr International Incorporated, New York). Metal films of 10 nm chromium (5N purity) and 300 nm gold (4N purity) or 300 nm silver (5N purity) were sequentially coated on the glass substrate through the holder or the mask under vacuum (≤ 10^{-6} mbar). After removal from the evaporator, the substrates were then either stored in anhydrous ethanol at room temperature (whole slides covered with metal film) or exposed to a vapour of DMS under reduced pressure (dynamic, i.e., continuous) at room temperature (22°C) for ~ 18 h overnight. DMS treatment of the glass substrate with spotted metal films created a hydrophobic background on the glass surface. To modify the glass surface with DMS, a glass vial containing 1 mL of neat DMS was placed in the centre of the desiccator base. Substrates were placed as a single layer in stacked square petri dishes with radially offset ajar lids (3 slides/dish) on top of a vented ceramic platform directly above the glass vial containing

neat DMS. Selection of DMS silane reagent was based on one hydrolyzable Cl group offering monolayer coverage on the glass and minimizing modification of the Au surface.[252] We found that it is important to consider the number of hydrolyzable functional group when using silane reagents. In our experience, we observed silane reagents with three hydrolyzable Cl groups (e.g., tridecafluoro-1,1,2,2-tetrahydrooctyl trichlorosilane) will lead to multilayer surface coverage (IRRAS data not shown). Also, higher number of hydrochloric acid leaving groups will etch the Au surface and foster modification.[253] Also, when using silane reagents with >1 hydrolyzable groups, vacuum condition (i.e., dynamic versus static) is important. Under dynamic vacuum, we have visually observed a modification gradient when using tridecafluoro-1,1,2,2-tetrahydrooctyl trichlorosilane. After silanization, the prepared SERS substrates were stored in a desiccator under dynamic (continuous) vacuum at room temperature until use.

4.2.6. Extinction spectroscopy

UV-visible extinction spectra were collected in absorbance mode with a double-beam PerkinElmer Lamda 35 spectrometer equipped with a photodiode detector. The UV-visible spectrum was scanned from 300 nm to 900 nm with a scan rate of 960 nm min^{-1}. Deionized water was used as a reference for each measurement. Measurements were conducted at room temperature and replicated thrice.

4.2.7. Raman spectroscopy

Biogenic silver nanoparticles were analyzed by surface-enhanced Raman scattering (SERS). A 2 µL volume of AgNPs was deposited on an ethanol rinsed, high purity nitrogen dried, ozone-treated (10 min), gold-coated (300 nm thickness) 25 x 75 x 1 mm plain microscope slide, air dried, and immediately analyzed. For silver films, ozone-treatment was omitted due to film degradation. Raman reporter reagent powder was deposited as a thin uniform layer on an ethanol rinsed, high purity nitrogen dried, ozone-treated, 300 nm gold-coated microscope slide. Raman spectra were recorded with a Renishaw inVia Raman microscope equipped with a 1200 lines/mm grating and a charged coupled device (CCD) detector. Irradiation sources for excitation were a 514.5 air-cooled Ar ion laser and a 633 nm air-cooled He-Ne laser. Power densities for each experiment are provided within the Figure captions. A power meter (Coherent, Laser Check model# 54-018, California, USA) was used to measure laser power at the sample. The microscope attachment was a Leica system. A 5X objective was used to first focus the light path and a 50X objective (Leica, numerical aperture 0.75, ~ 0.8 µm laser spot diameter[254]) or a 20X objective (Leica, numerical aperture 0.4, ~ 2 µm laser spot diameter[255]) was used to collect spectra. All reported spectra are an average of three to five point locations each with either five to ten second integration time. Visual inspections were conducted to deposit equivalent amounts of nanoparticles on the slide substrate and to focus the laser beam in regions of similar nanoparticle density of each sample.

4.2.8. Raman data analysis

All Raman spectra were imported into Spectragryph v1.2.5[256] for baseline correction and data extraction. For baseline correction, spectra were treated twice with individual baseline correction using the "adaptive" curve function (coarseness 10, offset 0).

4.2.9. Dynamic light scattering (DLS) spectrometry

Hydrodynamic diameter of AgNPs was determined using a Malvern Zetasizer Nano-ZS. Results were collected with a 4 mW He-Ne laser set at 633 nm with a 173° back scattering angle and an avalanche photodiode detector. Measurements were performed under the following conditions: particle refractive index 1.590; particle absorption coefficient 0.118 for B-AgNPs (based on absorbance values recorded at 633 nm); water refractive index 1.33; viscosity 0.8872 cP; and temperature 25°C; equilibrated for 120 sec; 15 runs; n = 3 measurements. Hydrodynamic radii is calculated by the instrument software using the Stokes-Einstein equation for spherical particles. Hydrodynamic diameter (d_{hyd}) reported represents the mean diameter based on intensity of scattered light.

4.2.10. Zeta potential (ZP)

Zeta potential of AgNPs was determined using a Malvern Zetasizer Nano-ZS. A 4 mW HeNe laser with 633 nm wavelength was used as light source. All measurements were performed under the following conditions: temperature 25°C; equilibrated for 120 sec; 20 runs; n = 3 measurements; Smoluchowski model.

4.2.11. Electron microscopy

A droplet of aqueous nanoparticle sample (1X washed with DI water) was deposited onto an ultra-thin carbon film coated copper 400 mesh grid (Electron Microscopy Sciences, product# CF400-CU-UL). After one minute, excess suspension was wicked-off using Whatman filter paper and then the grid was air-dried at room temperature before analysis. Electron micrographs were collected on a Hitachi S4800 field emission electron microscope in transmission mode. Image acquisition was conducted with a 20 – 30 kV accelerating voltage, 20 μA emission current, and a working distance of approximately 8 mm. Images were analysed with Gatan Digital Micrograph (version 2.31.734.0) and ImageJ 1.51t.[166]

4.2.12. Energy dispersive X-ray spectroscopy (EDX)

EDX spectra were collected with a Hitachi S5500 field emission electron microscope equipped with a Bruker EDX detector at a 15 kV accelerating voltage for Au and 10 kV accelerating voltage for glass; a working distance of ~ 1.1 mm, and an acquisition time of ~ 5 min. Beam spot size ~ ø50 μm.[257]

4.2.13. Atomic force microscopy (AFM)

Slide substrates with either 300 nm Au or 300 nm Ag films stored previously in anhydrous ethanol were dried with a gentle stream of high purity nitrogen, cut, rinsed with ethanol, and dried again with nitrogen prior to AFM measurements. Measurements were performed in tapping mode using a Digital Instruments Nanoscope III Multimode

microscope using super sharp silicon cantilevers (Nanosensors, product# SSS-NCHR-50) with a spring constant of 50 N/m. Experiments were conducted with a resonant frequency was 274 ± 3 kHz. Images were collected with an amplitude setpoint range of 0.7 – 1.7 V, scan rate of ~ 4 Hz, and a tip velocity of ~ 16 μm sec^{-1}. AFM micrographs were analysed using Gwyddion (version 2.45) open source software[258] to generate height profiles.

4.2.14. X-ray photoelectron spectroscopy (XPS)

XPS analysis was performed using an AXIS Ultra Spectrometer (Kratos Analytical) and a monochromatic Al Kα source ($h\nu$ = 1486.6 eV) at 210 W. The base pressure of the analysis chamber during experiments ≤ 5 x 10^{-10} Torr. A hemispherical electron-energy analyzer with a beam spot size of approximately 400 μm x 700 μm was used to collect spectra. High-resolution spectra were collected for C 1s, O 1s, N 1s, Si 2p, and F 1s with pass energy of 20 eV and a step size of 0.1 eV. Charging effects were corrected by calibrating to the C 1s line at 284.8 eV. XPS data was analysed with CasaXPS version 2.3.16.

4.3. Results and discussion

Towards a SERS-based bioassay platform using B-AgNPs, this chapter provides evidence for controlled modification with Raman active molecules for signal amplification and antibodies for specific biomolecular recognition. This chapter also provides details on substrate design and optimization to be used in a planar surface immunoassay format. Figure 4–1 presents an overview scheme to outline the approach and major experiments

contained within this chapter. As depicted in Figure 4–1, three different sizes of silver nanoparticles were sequentially tested with five different Raman reporter molecules and then further modified with IgG antibodies to produce biogenic extrinsic Raman labels (B-ERLs). We show below UV-visible extinction and Raman spectroscopy data to verify each modification step. To optimize the substrate that will be used to capture the bio-analyte of interest, initial experiments focused on a comparison of 300 nm thick Au and 300 nm thick Ag films for enhanced electronic coupling to maximize Raman scattering signal intensity. These experiments led to designing a substrate that employs a standard glass microscope slide with metal spots aimed at clinical deployment. Presented below is a collection of experiments that led to the design and optimization of both the B-ERLs and the substrate for SERS-based bioassay platforms. As most experiments presented are based on UV-visible extinction spectroscopy and Raman spectroscopy, it is important to establish a brief theoretical basis of each to interpret the results. Thus, the results are treated in this context.

Extinction spectroscopy is a common technique to monitor nanoparticle modification.[9, 51, 259] The position of the extinction band is influenced by nanoparticle size,[260-261] shape,[260-261] flocculation,[55, 146] and the dielectric constant of the particle and the medium.[55, 146, 261] Modification of the nanoparticle surface with organic molecules will affect the dielectric constant of the surrounding medium and in turn affect the localized surface plasmon resonance (LSPR) band position. The sensitivity towards changes in the dielectric constant of the surrounding medium with addition of organic molecules to the

nanoparticle surface can be used as a diagnostic tool to confirm successful surface modification. Equation 4–1 demonstrates the effect of adsorbed molecules on the surface by shift in λ_{max} caused by changes in refractive index.[9, 259]

Equation 4–1

$$\Delta\lambda_{max} \approx \mathrm{m}\,(n_{adsorbate} - n_{medium})\left(1 - e^{-\frac{2d}{l_d}}\right)$$

In Equation 4–1, $\Delta\lambda_{max}$ is the LSPR spectral shift in response to changes in refractive index, *m* is the bulk refractive-index response of the nanoparticle(s) (nm per refractive index units), *n* refers to the refractive index of either the adsorbate or the surrounding medium, *d* is the adsorbed molecules effective thickness (nm), and l_d is the electromagnetic field decay length (nm).[9, 259] Typically, the refractive index of an organic monolayer (1.5 – 1.6)[147, 262] is higher than the refractive index of a solvent (n_{water} = 1.33)[51] resulting in a red shift of the LSPR band.

Extinction spectroscopic results provide evidence for successful surface modification of biogenic AgNPs with a mixed layer consisting of thiolate Raman reporter molecules and native biomolecules. Extinction spectroscopy also provides an indication of colloidal stability of the modified AgNPs. Figure 4–2 contains extinction spectra of ø10 nm and ø20 nm B-AgNPs modified with different solution concentrations of 4-nitrobenzene thiol (NBT) ranging from 1 mM to 20 mM. For both size diameters, the LSPR peak position initially decreases (blue-shifts) with the addition of acetonitrile (ACN) and then increases

(red-shifts) with increasing [NBT]. This is also consistent with the LSPR band width, defined by full width half maximum (FWHM), with the expectation of ø20 nm particles exposed to ACN control solution. Based on our previous results shown in Chapter 3, we suspect ACN is desorbing a fraction of the native biomolecular layer (biocorona). Thus, the shifts in the LSPR band and the LSPR band width indicates variations in the organic coating. However, the exact origin of the shift or band width changes is unclear. We hypothesize that a strong interaction of the thiolate layer[55] and the adsorption of biomolecules results in a film with a slightly higher refractive index. Nanoparticle solution stability can be evaluated by monitoring the extinction spectrum in the region between 500 to 700 nm for the appearance of a second adsorption band that indicates aggregation. As shown in Figure 4–2, there are no additional bands observed in any of the modified AgNPs solutions. Modified AgNPs are stable for at least one month at 4°C.

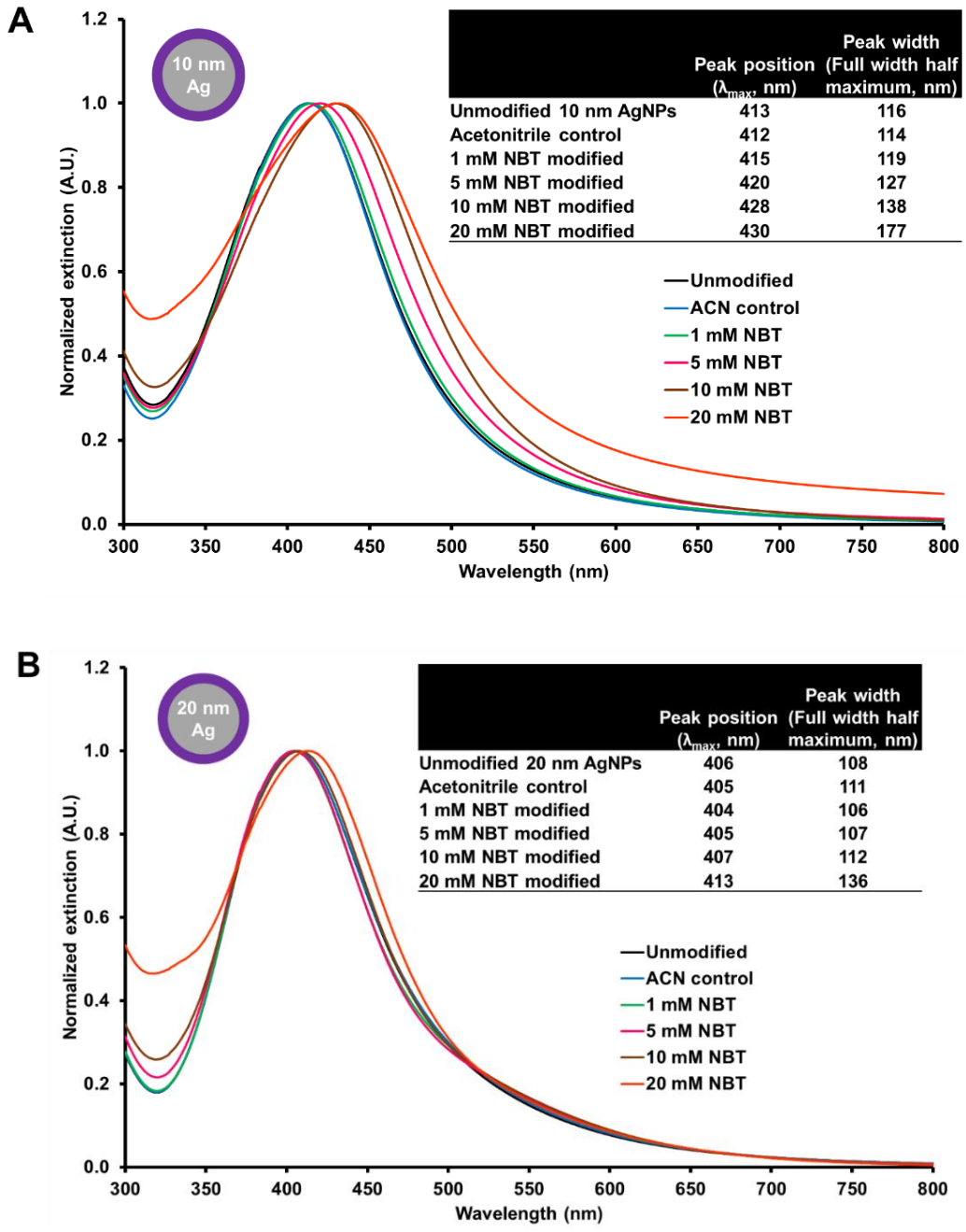

	Peak position (λ_{max}, nm)	Peak width (Full width half maximum, nm)
Unmodified 10 nm AgNPs	413	116
Acetonitrile control	412	114
1 mM NBT modified	415	119
5 mM NBT modified	420	127
10 mM NBT modified	428	138
20 mM NBT modified	430	177

	Peak position (λ_{max}, nm)	Peak width (Full width half maximum, nm)
Unmodified 20 nm AgNPs	406	108
Acetonitrile control	405	111
1 mM NBT modified	404	106
5 mM NBT modified	405	107
10 mM NBT modified	407	112
20 mM NBT modified	413	136

Figure 4–2. Normalized UV-visible extinction spectra collected for biogenic silver nanoparticles before and after modification with 4-nitrobenzene thiol (NBT) dissolved in 100% acetonitrile (ACN) at four different solution concentrations; 1 mM, 5 mM, 10 mM, and 20 mM. Inset shows LSPR peak position, denoted by λ_{max} and peak width, denoted by full width at half maximum. (A) ø10 nm AgNPs. (B) ø20 nm AgNPs.

A detailed discussion of Raman spectroscopy and surface-enhanced Raman scattering (SERS) has appeared in chapter 1. Briefly, Raman spectroscopy is a vibrational technique that provides rich chemical structural information. The technique generally suffers from low signal levels, however molecules located at or very near the surface (~ nm length scales) of noble metal nanostructures provide signal enhancements of $10^4 - 10^6$ or higher depending on conditions.[12, 32, 71] The primary mechanism of this signal enhancement is an increased electric field generated by the excitation of the surface plasmons of the metal nanoparticle.[62, 206-207] We used Raman spectroscopy and SERS to further characterize modified B-AgNPs. SERS spectra were recorded for two sizes of modified B-AgNPs, which were air-dried on 300 nm Au substrates. Initially, we selected NBT as our starting Raman reporter based on the strong symmetric $\nu_s(NO_2)$ feature centred at ~ 1335 cm^{-1} seen in Figure 4–3.

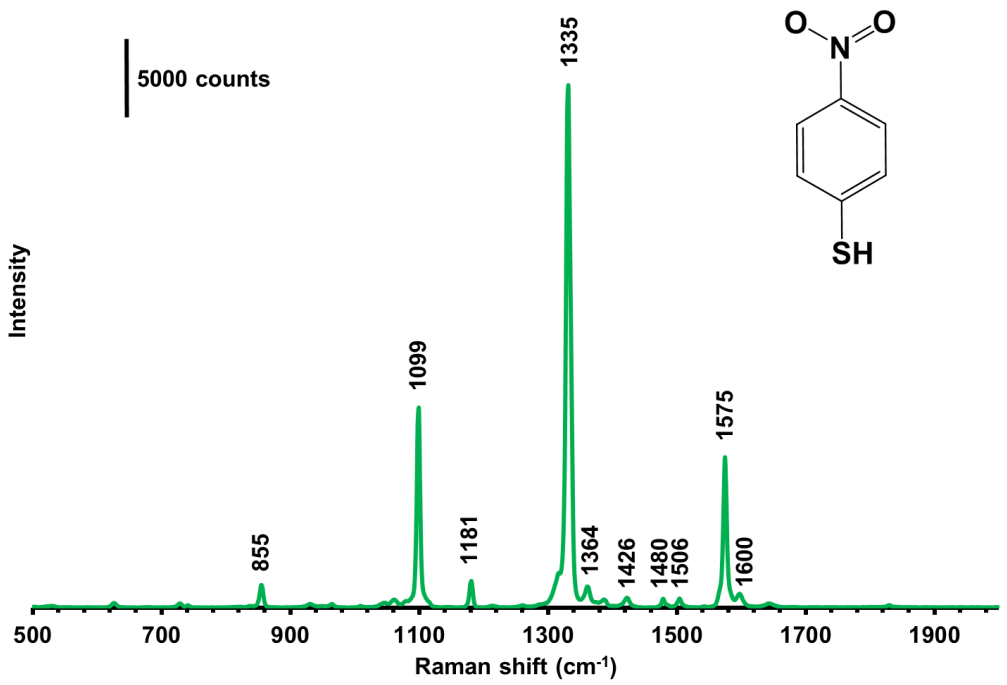

Figure 4–3. Raman spectrum of 4-nitrobenzene thiol (inset) powder on 300 nm Au substrate. A 514.5 nm laser was used to collect the spectrum at 0.17 ± 0.01 mW laser power and an integration time of 10 sec. Spectra averaged from three different locations. Major bands are labelled.

Figure 4–4 presents our SERS results for ø10 nm and ø20 nm B-AgNPs modified with four solution concentrations of NBT incubated overnight (~ 18 h) at room temperature (21°C) in the dark. For both size diameters, we initially observe an expected dose response by tracking the symmetric $\nu_s(NO_2)$ stretch at 1333 cm^{-1} (Figure 4–4). However, with solution concentrations of NBT (≥ 10 mM), a surprising decrease in peak height intensity at 1333 cm^{-1} is observed. In further examining the SERS spectra in Figures 4–4A and 4–4C, we observe a increases in three other peaks; ν_s(C-N) at 1143 cm^{-1}, δ_s(C-H) at 1392 cm^{-1}, and ν_s(N=N) at 1436 cm^{-1}. These frequencies are consistent with photo-reduction of the NO_2 group to dimercaptoazobenzene (DMAB) on Ag surfaces described by

previous reports.[263-265] Previous reports suggest that dimerization is dependent on wavelength, power, and integration time; translating to input energy level. In our experiments, photo-reduction was observed using a low input energy of 28 ± 3 μW for 10 sec from a 514.5 nm laser suggesting sensitive and rapid catalysis. Table 4–1 summarizes the assigned peak frequencies collected from NBT powder and NBT adsorbed on B-AgNPs. The peak frequencies are in agreement with previously published Raman spectra for nitrobenzene.[266-268] The peak frequencies recorded with NBT adsorbed on B-AgNPs are similar with those of NBT powder with the exception of photocatalytic effects[263-265] observed with increases to three peak frequencies at 1192 cm^{-1}, 1392 cm^{-1}, 1436 cm^{-1}, and a striking decrease at 1333 cm^{-1} (Table 4–1). Our results indicate that biogenic AgNPs can be controllably modified with NBT, however photo-reduction occurs with solution concentrations of ≥ 10 mM. Consequently, we proceeded to determine the optimal incubation time for Raman reporter modification with 5 mM because the photo-catalytic effects are less pronounced and $\nu_s(NO_2)$ stretch at 1333 cm^{-1} remains a prominent spectral feature to monitor.

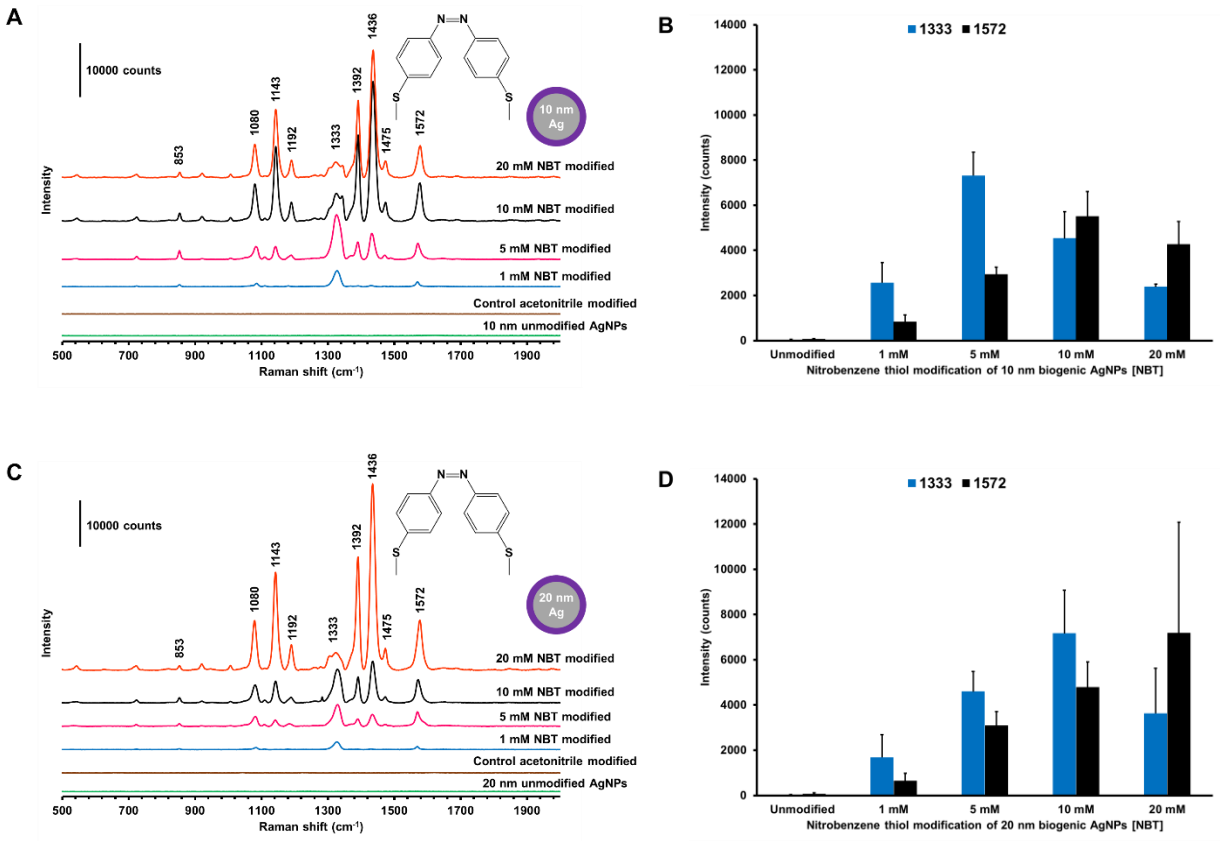

Figure 4–4. Raman spectra of ø10 nm and ø20 nm biogenic AgNPs modified with 4-nitrobenzene thiol (NBT) dissolved in 100% acetonitrile at four different solution concentrations; 1 mM, 5 mM, 10 mM, and 20 mM. A 514.5 nm laser was used to collect each spectrum at 28 ± 3 µW laser power and an integration time of 10 sec. Spectra averaged from three different locations of visually equal amounts of AgNPs and offset for clarity. (A and C) Initial dose response at low [NBT] by tracking $\nu_s(NO_2)$ at 1333 cm^{-1}. At high [NBT], decrease at 1333 cm^{-1} and increases at 1143 cm^{-1}, 1392 cm^{-1} and 1436 cm^{-1}; consistent with NO_2 photo-reduction to dimercaptoazobenzene (inset). (B and D) Bar plot tracking the $\nu_s(NO_2)$ at 1333 cm^{-1} and a ring breathing mode $\nu_s(C=C)$ at 1572 cm^{-1}. Data represent an average and standard deviation of the peak height intensity at the corresponding frequencies from the measurement of three different locations for each sample.

Table 4–1. Peak frequencies and assignments for the Raman spectrum of solid 4-nitrobenzene thiol and the SERS spectrum of nitrobenzene thiol on the surface of 20 nm biogenic silver nanoparticles.[263, 265, 269]

	Raman shift (peak frequency, cm^{-1})	
Assignment	Powder	Adsorbed on B-AgNPs
C-H bend + C-N stretch	855	853 (weak)
C-H bend	1099	1080
C-N stretch	-	1143
C-H bend	1181	1192
Symmetric NO_2 stretch	1335	1333
Symmetric C-H bend + ring stretch	1364 (weak)	-
C-H bend	-	1392
Asymmetric C-H bend + ring stretch	1426 (weak)	-
N=N stretch	-	1436
Asymmetric C-H bend + ring stretch	1480 (weak)	1475
Asymmetric NO_2 stretch	1506 (weak)	-
Ring stretch	1575	1572
Ring stretch	1600 (weak)	-

To determine the optimal incubation time for modification with Raman reporter molecules, we tested ø10 nm and ø20 nm B-AgNPs over time and tracked with UV-visible extinction and Raman spectroscopy. Figure 4–5 presents our extinction data tracking the modification of ø10 nm and ø20 nm B-AgNPs with 5 mM NBT and incubating up to 8 h. The position of the LSPR band seen in Figure 4–5 changes slightly ($\Delta\lambda_{max} \sim 1$ nm) for ø10 nm AgNPs modified with 5 mM, whereas at a higher change is observed for ø20 nm ($\Delta\lambda_{max} \sim 3$ nm at 1440 min). More apparent changes are observed by the peak width, denoted by FWHM. As discussed earlier, the shifts in the LSPR band and the LSPR band width clearly indicates variations in the organic coating over time; thus we can infer that the surface of AgNPs have been modified due to changes in the refractive index. With ø20 nm AgNPs, we

also observe a secondary absorption band between 500 to 700 nm, particularly at longer incubation times of 4 h and 8 h. This indicates that a fraction of AgNPs have destabilized.

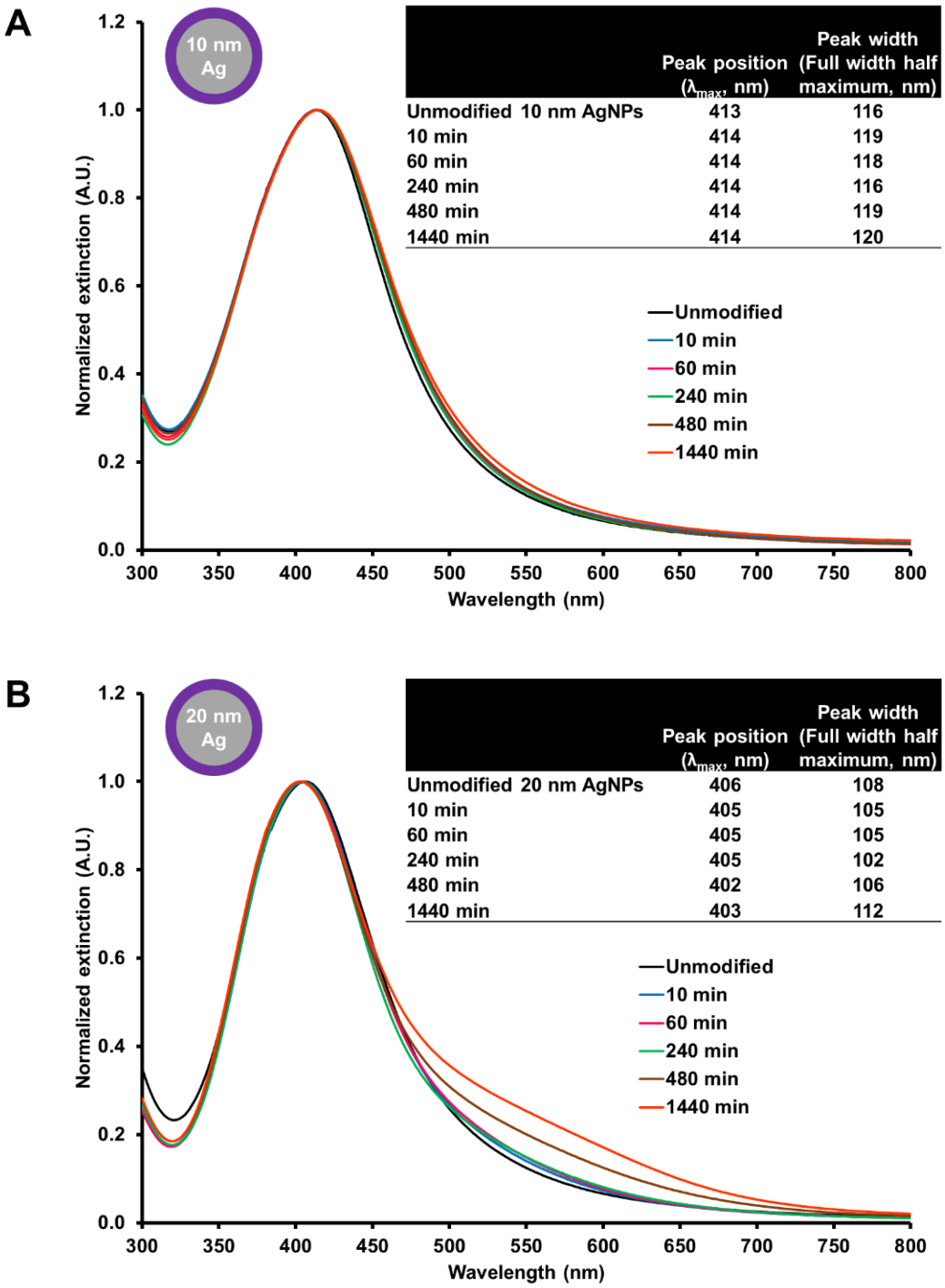

Figure 4–5. Normalized UV-visible extinction spectra collected for biogenic silver nanoparticles before and after modification with 5 mM 4-nitrobenzene thiol (NBT) dissolved in 100% acetonitrile over time. Inset shows LSPR peak position, denoted by λ_{max} and peak width, denoted by full width at half maximum. (A) ø10 nm AgNPs. (B) ø20 nm AgNPs.

Figure 4–6 presents our time-resolved SERS results for ø10 nm and ø20 nm B-AgNPs modified with 5 mM NBT. For both ø10 nm and ø20 nm B-AgNPs, the highest Raman signal intensities are recorded at 60 min incubation. For ø10 nm B-AgNPs, Figure 4–6B shows that the highest signal is recorded at 60 min, followed by variable yet indistinguishable signal intensity at longer measured time points. For ø20 nm B-AgNPs, the results are more defined. Consistent with ø10 nm AgNPs, the highest signal recorded was at 60 min followed by a decline in signal intensity with longer incubation. We hypothesize that the decline in signal intensity beyond 60 min is due to the native biomolecules (biocorona) re-establishing equilibrium after being displaced by the strong interaction of the thiolate layer. Thus, we proceeded with an incubation time of 60 min to maximize the number of adsorbed Raman reporter molecules and minimize the possibility of AgNP destabilization at longer incubation times.

Though the $\nu_s(NO_2)$ stretch is a strong spectral feature in Raman spectroscopy, chemicals with this functional group are not compatible with AgNPs. Therefore, the proceeding set of experiments seek to identify a suitable Raman reporter candidate for AgNPs. We examined four other Raman reporter molecules, namely 2-napthalene thiol, 4-mercaptophenol, 4-mercaptobenzoic acid, and mercaptobenzonitrile. Results and conclusions of our experiments are presented below in turn.

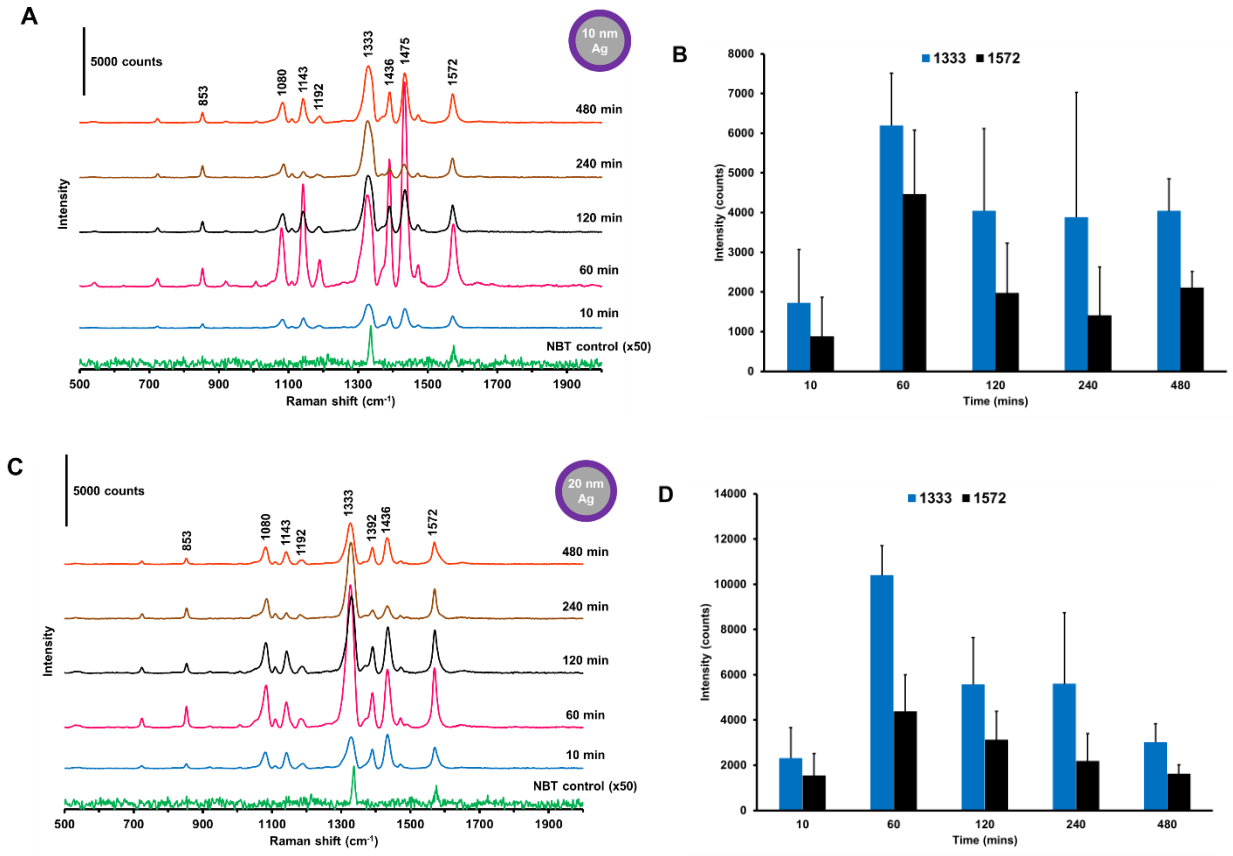

Figure 4–6. Time resolved surface modification of ø10 nm and ø20 nm biogenic AgNPs modified with 5 mM 4-nitrobenzene thiol (NBT) dissolved in 100% acetonitrile at different incubation times. (A and C) Raman spectra collected with a 514.5 nm laser at 28 ± 3 μW laser power and an integration time of 10 sec. Spectra averaged from three different locations of visually equal amounts of AgNPs and offset for clarity. NBT control spectrum has been magnified by a factor of 50. (B and D) Bar plot tracking the $\nu_s(NO_2)$ at 1333 cm^{-1} and a ring breathing mode $\nu_s(C{=}C)$ at 1572 cm^{-1}. Data represent an average and standard deviation of the peak height at the corresponding frequencies from the measurement of three different locations for each sample.

Figure 4–7 shows a Raman spectrum collected from 2-napthalene thiol powder on a 300 nm Au substrate. We selected 2-napthalene thiol for its large Raman cross section, multiple ring breathing vibrational modes, and minimal steric hindrance with the thiol in the ortho (2) position.

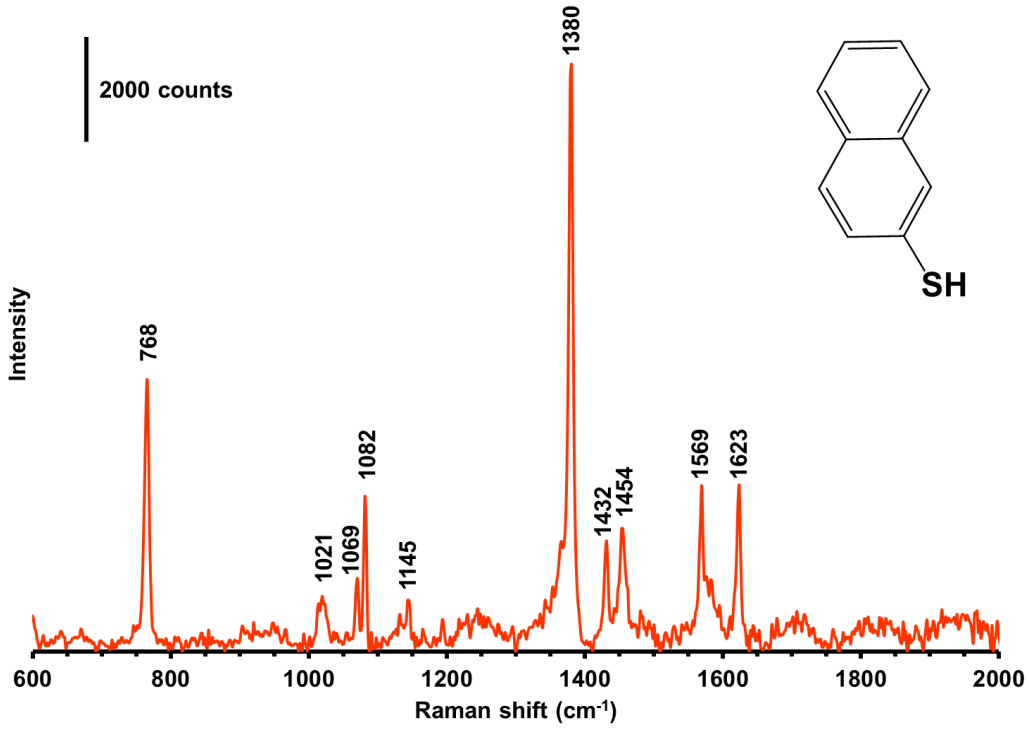

Figure 4–7. Raman spectrum of 2-napthalene thiol (inset) powder on 300 nm Au substrate. A 514.5 nm laser was used to collect the spectrum at 0.17 ± 0.01 mW laser power and an integration time of 10 sec. Spectra averaged from three different locations. Major bands are labelled.

To demonstrate surface modification with 2-napthalene thiol with ø20 nm B-AgNPs, Figure 4–8 presents our Raman spectroscopy data and Figure 4–9 contains our UV-visible extinction data.

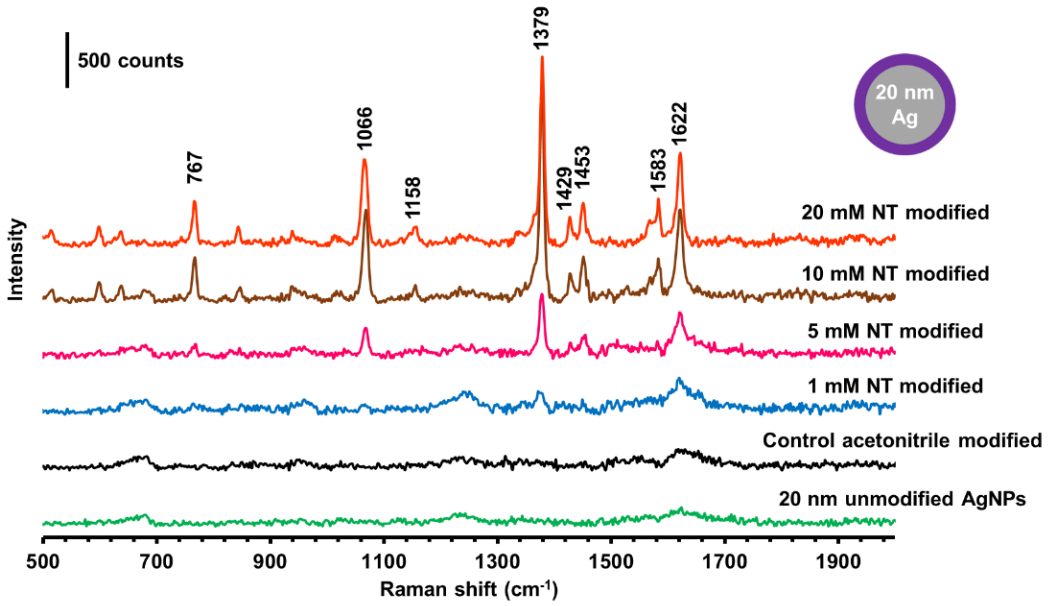

Figure 4–8. Raman spectra for 20 nm biogenic AgNPs before and after modification with 2-napthalene thiol (NT) dissolved in 100% acetonitrile at four different solution concentrations; 1 mM, 5 mM, 10 mM, and 20 mM. A 514.5 nm laser was used to collect each spectrum at 70 ± 3 μW laser power and an integration time of 10 sec. Spectra averaged from three different locations of visually equal amounts of AgNPs and offset for clarity.

Figure 4–8 shows Raman spectra collected from ø20 nm B-AgNPs before and after treatment with different solution concentrations of NT. As evidenced by the labelled bands, a dose response is distinguishable between 5 mM NT to 20 mM NT. The small vibrational features at ~ 682 cm^{-1}, ~ 1236 cm^{-1} (Amide III band, N-H bend), and ~ 1633 cm^{-1} (amide I band, C=0 stretch) seen in the unmodified and control acetonitrile spectra are consistent with protein structural components.[269-270] Table 4–2 summarizes the assigned peak frequencies collected from NT powder and NT adsorbed on ø20 nm B-AgNPs. The peak frequency positions are in agreement with previously published Raman

spectra for 2-napthalene thiol.[271-272] The peak frequencies recorded with NT adsorbed on B-AgNPs are similar with those of NT powder.

Table 4–2. Peak frequencies and assignments for the Raman spectrum of solid 2-napthalene thiol and the SERS spectrum of napthalene on the surface of 20 nm biogenic silver nanoparticles.[269, 271]

	Raman shift (peak frequency, cm^{-1})	
Assignment	Powder	Adsorbed on B-AgNPs
C-H bend + Ring deformation	768	767
C-H bend + Ring deformation	-	846
C-H bend + Ring breathing	1021	-
C-H bend	1069	1066
C-H bend	1082	-
C-H bend	1145	1158 (weak)
Symmetric C-H bend + ring stretch	1380	1379
Asymmetric C-H bend + ring stretch	1432	1429
Asymmetric C-H bend + ring stretch	1454	1453
Ring stretch	1569	1583
Ring stretch	1623	1622

Following our encouraging Raman data, our UV-visible extinction results shown in Figure 4–9 also provided encouragement. Consistent with our previous extinction results using NBT (Figure 4–2), we observe a similar trend with an initial blue shift in band position followed by a red shift (≥ 10 mM). Similarly, we observe an initial narrowing in band width followed by a broadening (10 mM). Figure 4–9B shows a visual representation of colloidal stability. At a solution concentration of 20 mM, a secondary absorption band is evident (Figure 4–9) indicative of destabilized AgNPs. Thus, NT is a compatible candidate for B-AgNPs at a solution concentration of 5 mM consistent with NBT.

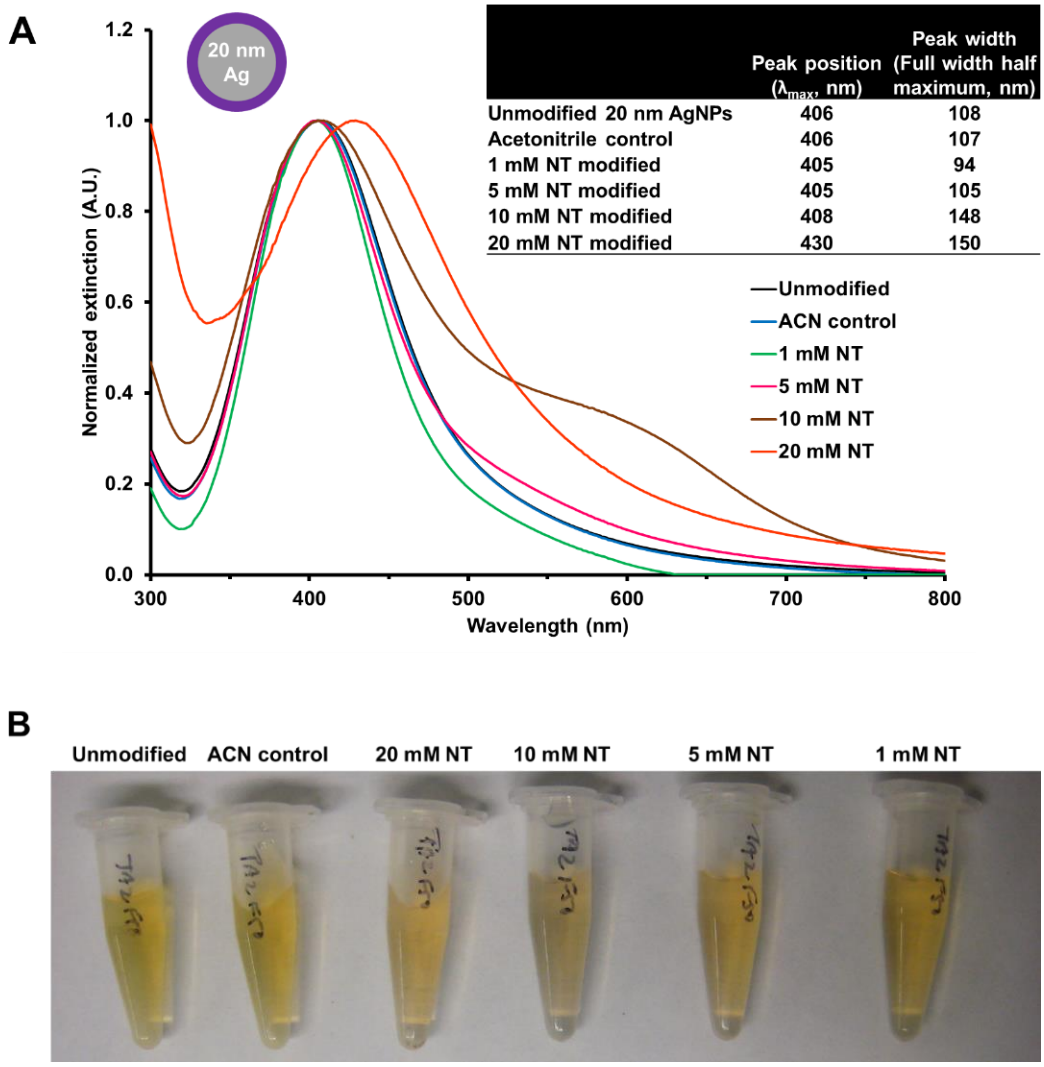

	Peak position (λ_{max}, nm)	Peak width (Full width half maximum, nm)
Unmodified 20 nm AgNPs	406	108
Acetonitrile control	406	107
1 mM NT modified	405	94
5 mM NT modified	405	105
10 mM NT modified	408	148
20 mM NT modified	430	150

Figure 4–9. Normalized UV-visible extinction spectra collected for ø20 nm biogenic silver nanoparticles before and after modification with 2-napthalene thiol (NT) dissolved in 100% acetonitrile at four different solution concentrations: 1 mM, 5 mM, 10 mM, and 20 mM. (A) Inset shows LSPR peak position, denoted by λ_{max} and peak width, denoted by full width at half maximum. (B) Photograph of ø20 nm biogenic silver nanoparticles with no treatment (unmodified), or treated with 100% acetonitrile (ACN) or a solution concentration of NT dissolved in 100% acetonitrile for 60 min.

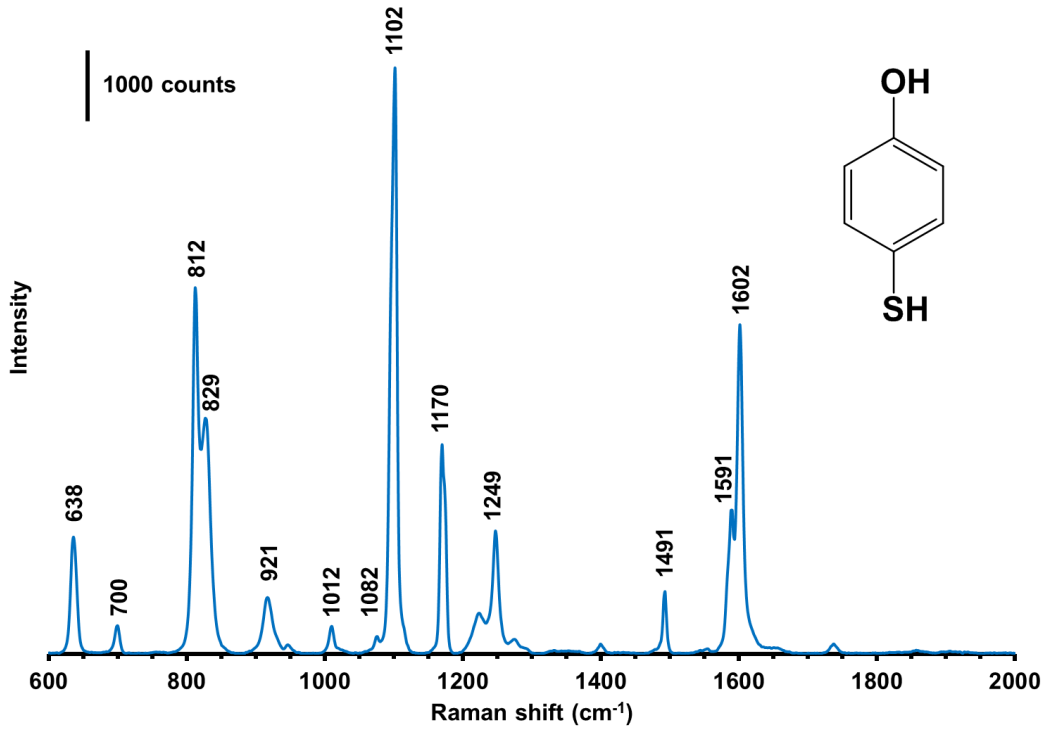

Figure 4–10. Raman spectrum of 4-mercaptophenol (inset) powder on 300 nm Au substrate. A 514.5 nm laser was used to collect the spectrum at 0.17 ± 0.01 mW laser power and an integration time of 10 sec. Spectra averaged from three different locations. Major bands are labelled.

Next, we used 4-mercaptophenol (MP) to modify the surface of ø20 nm B-AgNPs. In following the same approach as previous modification experiments, we began with collecting a Raman spectrum of MP powder to identify prominent spectral features shown in Figure 4–10. Figure 4–11 shows our Raman spectroscopy results and Figure 4–12 shows our UV-visible extinction results in modifying ø20 nm B-AgNPs. Figure 4–11 shows Raman spectra collected from ø20 nm B-AgNPs before and after treatment with different solution concentrations of MP. Consistent with our Raman results for NT, a dose response is distinguishable between 5 mM NT to 20 mM NT as shown by the labelled bands in Figure 4–11. Table 4–3 summarizes the assigned peak frequencies collected from MP powder and

MP adsorbed on ø20 nm B-AgNPs. The peak frequency positions are in agreement with previously published Raman spectra for 4-mercaptophenol.[273] The peak frequencies recorded with MP adsorbed on B-AgNPs are similar with those of MP powder.

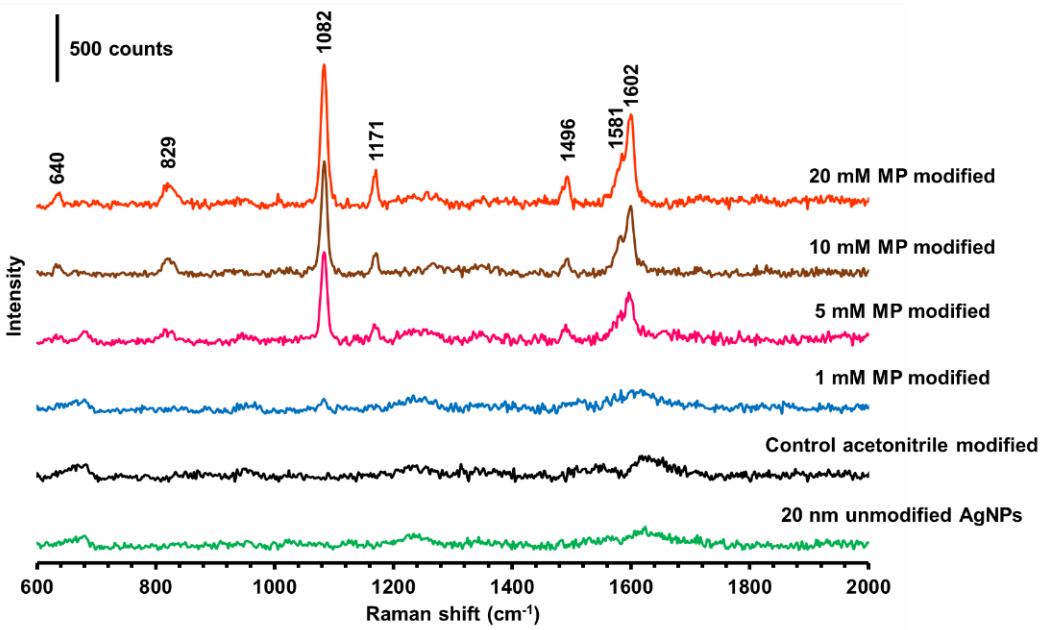

Figure 4–11. Raman spectra for 20 nm biogenic AgNPs before and after modification with 4-mercaptophenol (MP) dissolved in 100% acetonitrile at four different solution concentrations; 1 mM, 5 mM, 10 mM, and 20 mM. A 514.5 nm laser was used to collect each spectrum at 70 ± 3 μW laser power and an integration time of 10 sec. Spectra averaged from three different locations of visually equal amounts of AgNPs and offset for clarity.

Table 4–3. Peak frequencies and assignments for the Raman spectrum of solid 4-mercaptophenol and the SERS spectrum of mercaptophenol on the surface of 20 nm biogenic silver nanoparticles.[269, 273]

	Raman shift (peak frequency, cm^{-1})	
Assignment	Powder	Adsorbed on B-AgNPs
C-S stretch	638	640 (weak)
O-H bend + C-H bend	700	-
C-H bend	812	-
C-H bend	829	829 (weak)
C-H bend	921	-
C-H bend + ring breathing	1012	-
C-H bend	1082	1082
C-H bend	1102	-
C-H bend + C-O bend	1170	1171
C-H bend + C-O stretch	1249	1254 (broad, weak)
Asymmetric C-H bend	1491	1496
Ring stretch	1591	1581
Ring stretch	1602	1602

The UV-visible extinction results shown in Figure 4–12 reveals important considerations in using MP. Consistent with previous extinction results using NBT (Figure 4–2) and NT (Figure 4–9), we observe a similar trend with an initial blue shift in band position followed by a red shift (≥ 10 mM). Similarly, we observe an initial narrowing in band width followed by more pronounced band broadening at a higher solution concentrations (≥ 5 mM) indicative of destabilized AgNPs. Figure 4–9B shows a visual representation of colloidal stability with distinct red-shifted colour changes. Our results led us to conclude that MP is a not a compatible Raman reporter candidate for B-AgNPs. One hypothesis for this remarkable destabilization is due to the disruption of electrostatic interactions at the surface of B-AgNPs. As the pKa of substituted phenols ranges from 7.0–10.3,[274-275] it is likely that most hydroxyl groups will remain protonated and neutral in a AgNPs solution with a pH of 6–7. However, a fraction of hydroxyl groups will be

deprotonated, hence charged. Thus, we suspect that the electrostatic interactions are disrupted due to a combination of (mostly) hydrogen bonding and a fraction of ionic interactions within an aqueous solution of B-AgNPs.

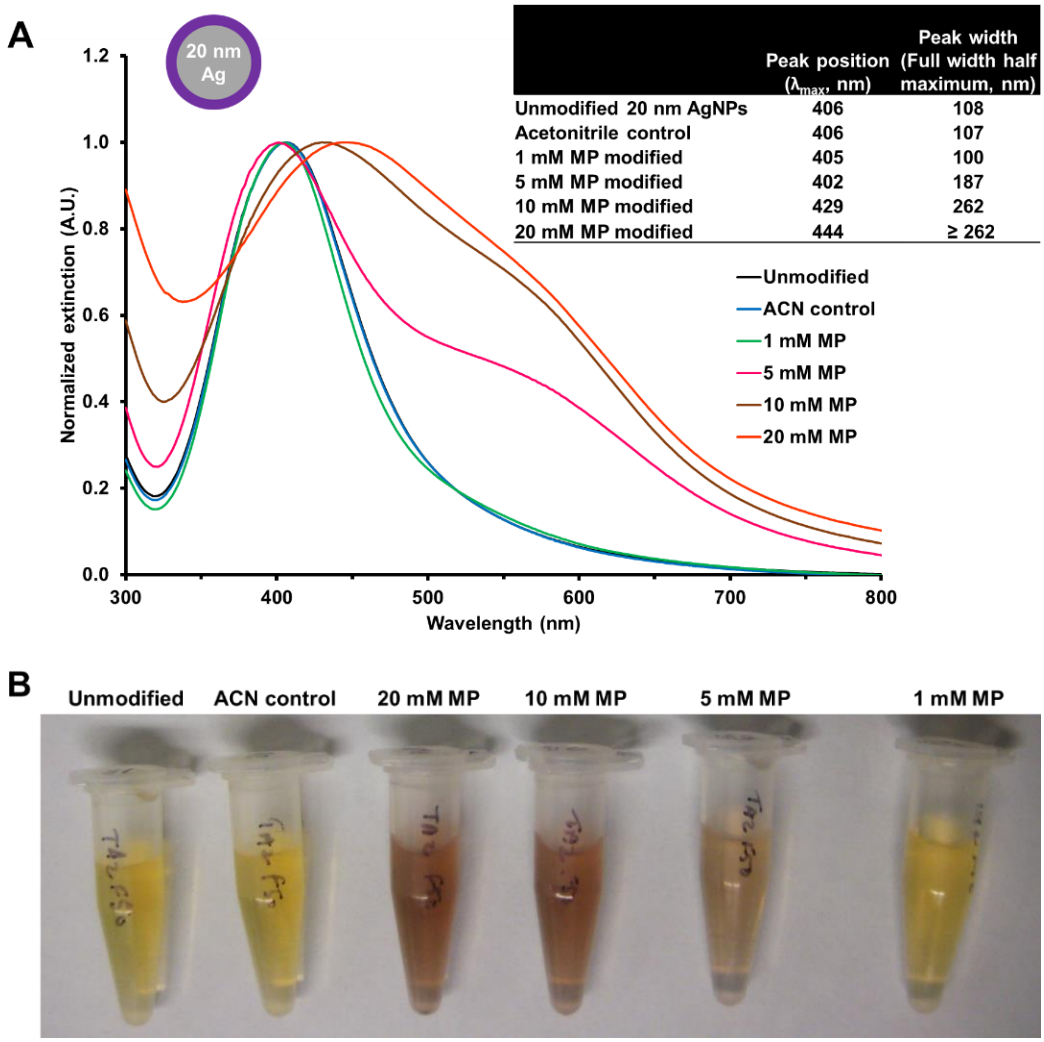

	Peak position (λ_{max}, nm)	Peak width (Full width half maximum, nm)
Unmodified 20 nm AgNPs	406	108
Acetonitrile control	406	107
1 mM MP modified	405	100
5 mM MP modified	402	187
10 mM MP modified	429	262
20 mM MP modified	444	≥ 262

Figure 4–12. Normalized UV-visible extinction spectra collected for ø20 nm biogenic silver nanoparticles before and after modification with 4-mercaptophenol (MP) dissolved in 100% acetonitrile at four different solution concentrations: 1 mM, 5 mM, 10 mM, and 20 mM. (A) Inset shows LSPR peak position, denoted by λ_{max} and peak width, denoted by full width at half maximum. (B) Photograph of ø20 nm biogenic silver nanoparticles with no treatment (unmodified), or treated with 100% acetonitrile (ACN) or a solution concentration of NT dissolved in 100% acetonitrile for 60 min.

In further testing our hypothesis of electrostatic disruption of the biocorona, we performed a single experiment to modify the surface of ø20 nm B-AgNPs with 4-mercaptobenzoic acid (MBA) at a solution concentration of 5 mM for 60 min. As seen in Figure 4–13, our UV-visible extinction plot shows the peak position blue shifted as previous modifications; however, the band width dramatically expands with a secondary absorbance band seen between 550 nm to 600 nm indicative of destabilized NPs. Our extinction results of MBA supports the notion that biocorona is sensitive to electronic disruption resulting in destabilization.

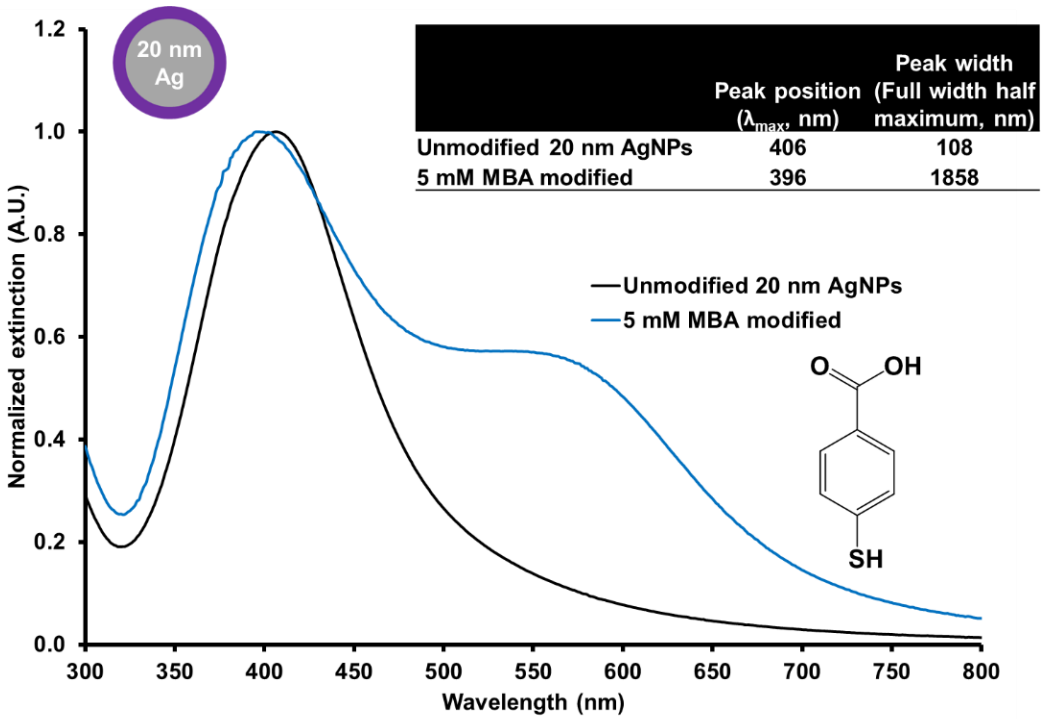

Figure 4–13. Normalized UV-visible extinction spectra collected for ø20 nm biogenic silver nanoparticles before and after modification with 4-mercaptobenzoic acid (MBA) dissolved in 100% acetonitrile. Inset shows LSPR peak position, denoted by λ_{max} and peak width, denoted by full width at half maximum.

The last Raman reporter molecule evaluated is 4-mercaptobenzonitrile (MBN). A major impetus for selecting this Raman reporter is the ν_s(C≡N) at 2225 cm^{-1}. This particular vibrational mode is in a relative quiet region (2000 cm^{-1} – 2500 cm^{-1}) of the Raman spectrum, where few organic molecules have characteristic frequency modes.[269] As our aim is designing a SERS-immunoassay for bio-specimens (e.g., serum, plasma, urine) that are rich in organic biomolecules, measuring a vibrational feature in an uncrowded region would be ideal. Thus, we start by presenting a powder spectrum of MBN shown in Figure 4– 14 to identify prominent vibrational bands.

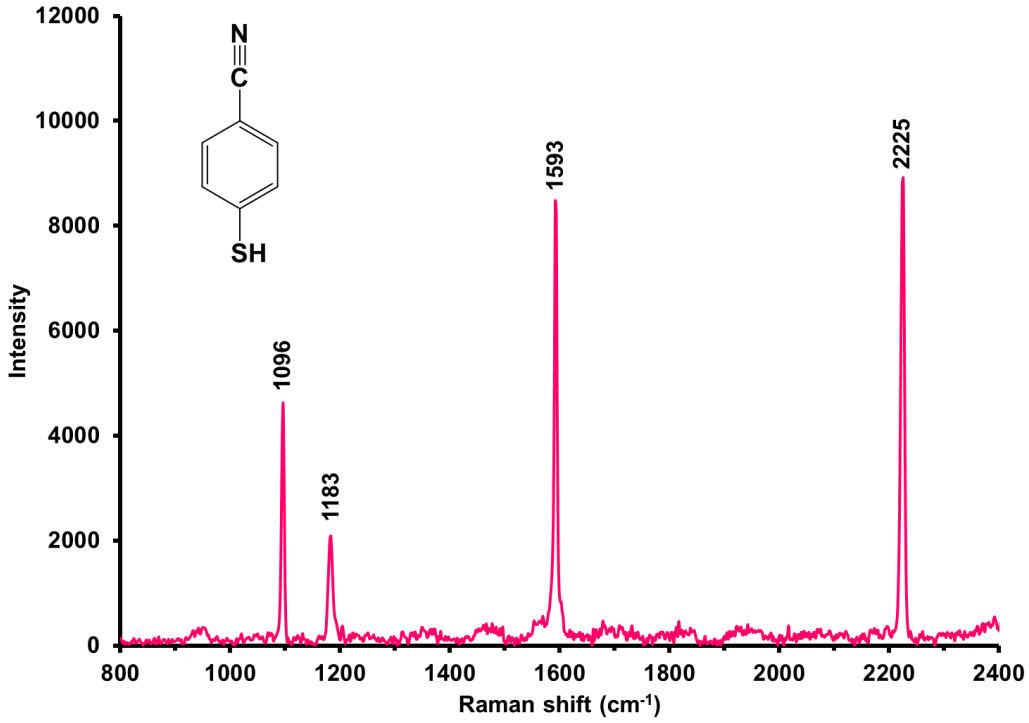

Figure 4–14. Raman spectrum of 4-mercaptobenzonitrile (inset) powder on 300 nm Au substrate. A 514.5 nm laser was used to collect the spectrum at 0.93 ± 0.01 mW laser power and an integration time of 10 sec. Spectra averaged from three different locations. Major bands are labelled.

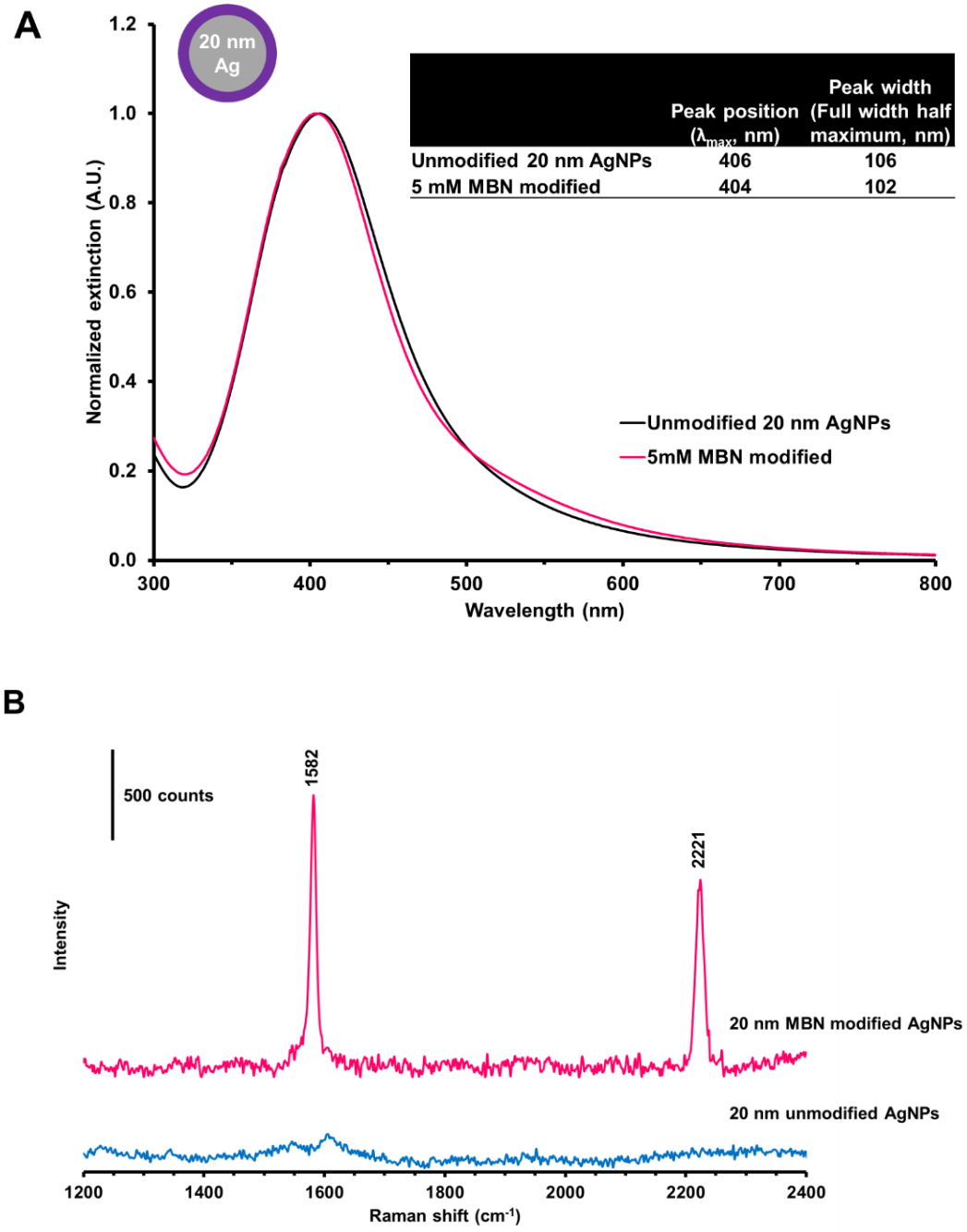

Figure 4–15. ø20 nm biogenic AgNPs before and after modification with 5 mM 4-mercaptobenzonitrile (MBN) dissolved in 100% acetonitrile for 60 min in the dark. (A) Normalized extinction plot before and after modification. Inset shows peak position, denoted by λ_{max} and peak width, denoted by full width half maximum. (B) Raman spectra collected using a 514.5 nm laser at 70 µW ± 3 µW laser power and an integration time of 10 sec. In the unmodified spectrum, a weak peak ~ 1640 cm^{-1} is consistent with Amide I band. Spectra averaged from three different locations of visually equal amounts of AgNPs and offset for clarity.

Figure 4–15 contains UV-visible extinction and Raman results to demonstrate modification of ø20 nm B-AgNPs. Consistent with previous extinction results, a blue shift in the extinction plot and a decrease in peak width is observed (Figure 4–15A). No secondary absorbance is evident, suggesting a very low level of NP aggregation. Thus, changes in the peak position and peak width suggest modification of the surface layer. Confirmation of the MBN on or near the surface is confirmed by Raman spectroscopy shown in Figure 4–15B. Table 4–4 summarizes the assigned peak frequencies collected from MBN powder and MBN adsorbed on ø30 nm B-AgNPs. The peak frequency positions are in agreement with previously published Raman spectra for 4-mercaptobenzonitrile.[276-279] The peak frequencies recorded with MBN adsorbed on B-AgNPs are similar with those of MBN powder.

Table 4–4. Peak frequencies and assignments for the Raman spectrum of solid 4-mercaptobenzonitrile and the SERS spectrum of MBN on the surface of 30 nm biogenic silver nanoparticles.[269]

	Raman shift (peak frequency, cm^{-1})	
Assignment	Powder	Adsorbed on B-AgNPs
C-H bend	1096	-
C-H bend	1183	-
Ring stretch	1593	1582
C≡N stretch	2225	2221

In summarizing up to this point, we have established that B-AgNPs can be controllably modified with different Raman reporter molecules. Ideal conditions consist of a 5 mM stock solution concentration, 60 min incubation time for surface modification, and neutral molecules with minimal secondary intermolecular interactions is desired. Among the five Raman reporter chemicals evaluated, we selected MBN for all subsequent experiments. In moving forward in context of a SERS-based bioassay platform, we decided a larger size diameter would benefit to a higher SERS signal intensity. We chose ~ ø30 nm AgNPs based on our previous work with AuNPs for SERS-based immunoassays[30] and considerations for B-AgNPs production with relatively uniform characteristics and maintaining a relatively narrow size distribution. Prior to presenting our UV-visible extinction and Raman spectroscopy results of modifying 30 nm AgNPs, we present our characterization results after biosynthesis. Figure 4–16 contains our transmission electron micrographs and our size distribution results represented by an average shifted histogram.[280] Consistent with our previous report[183] and in chapter 2, the nanoparticles produced are predominately spherical in morphology (Figure 4–16A and 4–16C) and have an average size of 27 nm and a standard deviation of 5 nm (~ 18.5% relative standard deviation) based on 320 nanoparticles.[281] Using dynamic light scattering (DLS), we also report an average hydrodynamic diameter of 57 nm ± 1 nm (based on intensity, n = 3) and a polydispersity index value of 0.4 ± 0.04. Consistent with our previous work, ~2X difference between our TEM diameter and our solution based hydrodynamic diameter is largely due to the biomolecular surface layer around B-AgNPs. Our zeta potential (ZP) measured −23 mV ± 1 mV at pH ~ 7 (n = 3) indicative of acceptable colloidal stability.[169]

Both DLS and ZP measurements are consistent with our previous report with ø10 nm and ø20 nm B-AgNPs.[183]

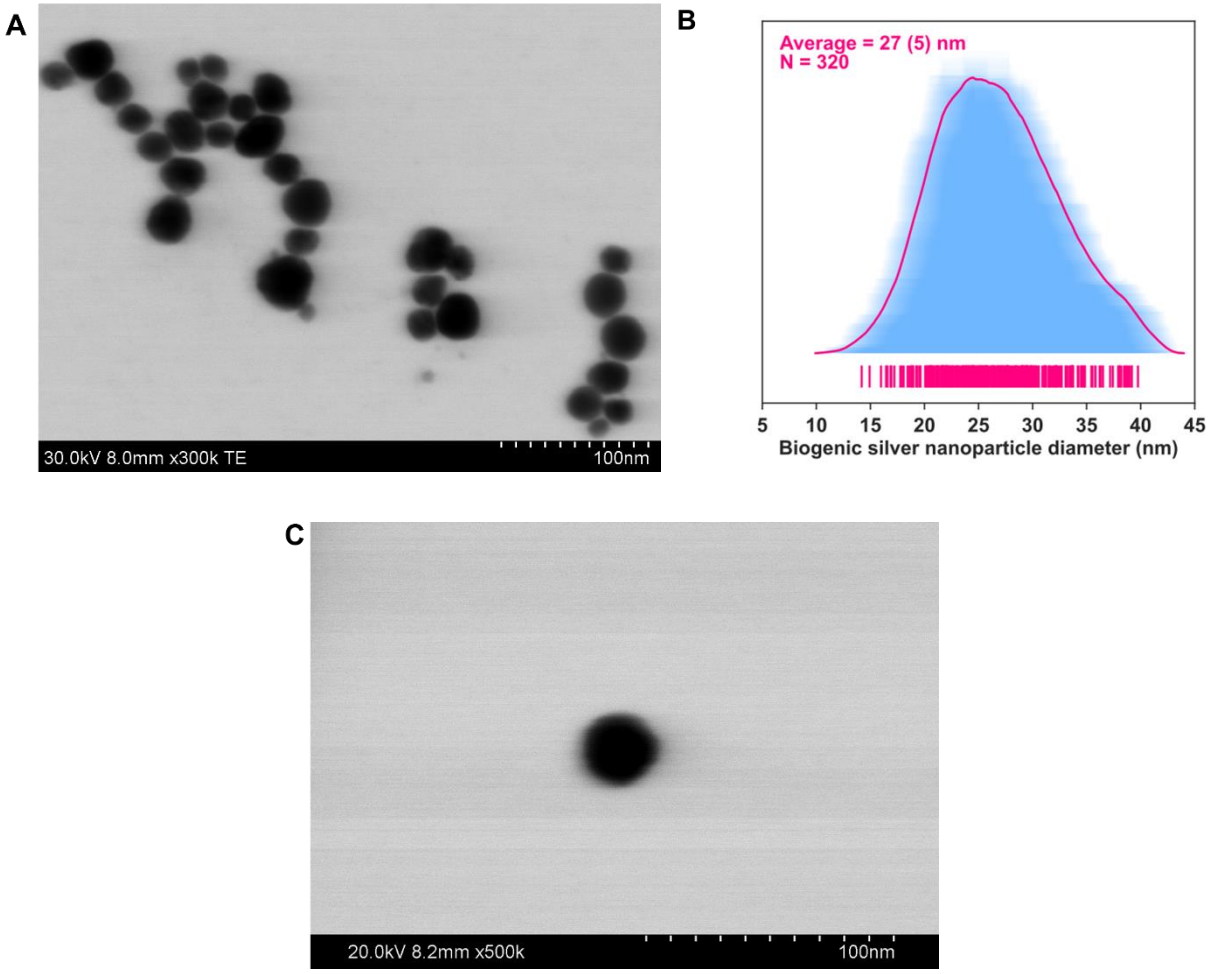

Figure 4–16. Transmission electron microscopy characterization of ~ ø30 nm biogenic silver nanoparticles produced by *Fusarium oxysporum* at 45°C ± 0.3°C shaking at 100 rpm in the dark for 3 days. Accelerating voltage, working distance, and magnification are shown in (A) and (C). (A) Representative TEM micrograph of primarily spherical nanoparticles. (B) Average shifted histogram[280, 282] of the size distribution of 320 nanoparticles with an average of 27 nm ± 5 nm (~ 18.5% relative standard deviation). The pink line represents the average shifts in bin origin. The blue shaded area comprises all the histograms generated with the overlapping regions shown in darker areas. The thickness of the edge gradient represents the uncertainty.[280] Scott's rule is used for optimal bin width.[283] Below the histogram is series of vertical lines that show the actual positions of each data point, known as a "rug" plot.[280] TEM images were analysed by ImageJ 1.51t[166] and histogram generation was performed using an online plotter.[280] (C) TEM micrograph of a single spherical nanoparticle at higher magnification (500k).

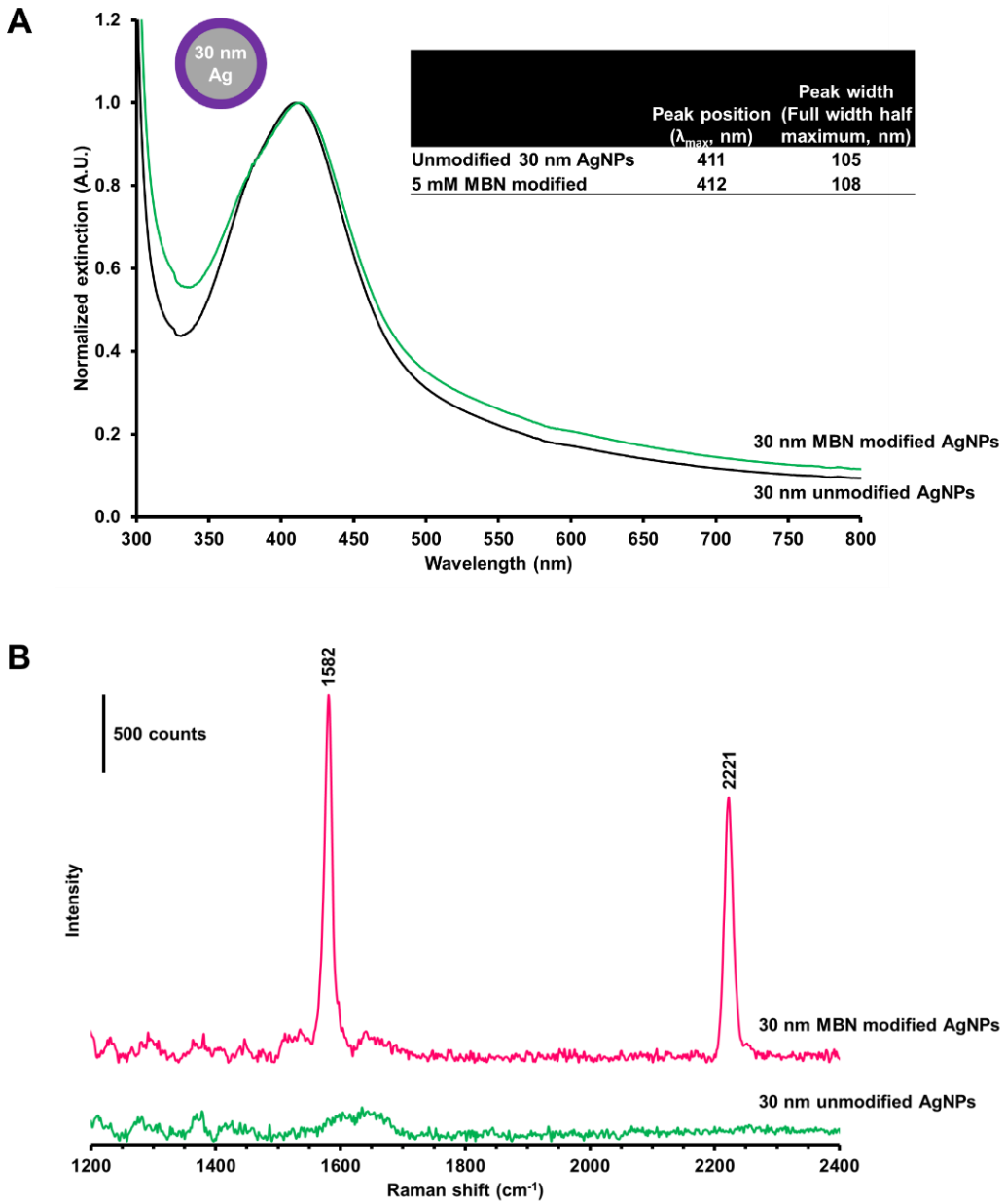

Figure 4–17. ø30 nm biogenic AgNPs before and after modification with 5 mM 4-mercaptobenzonitrile (MBN) dissolved in 100% acetonitrile for 60 min in the dark. (A) Normalized extinction plot before and after modification. Inset shows peak position, denoted by λmax and peak width, denoted by full width half maximum. (B) Raman spectra collected using a 633 nm laser at 0.7 mW ± 0.1 mW laser power and an integration time of 5 sec. A weak peak ~ 1645 cm^{-1} is consistent with Amide I band. Spectra averaged from five different locations of visually equal amounts of AgNPs and offset for clarity.

Figure 4–17 contains UV-visible extinction and Raman results to demonstrate modification of ø30 nm B-AgNPs. Contrary to our previous extinction results, we observe a red shift of 2 nm and a ~ 3 nm increase in peak width after treatment with 5 mM MBN (Figure 4–17A). This phenomenon can be explained by the larger contribution of the larger NP size (ø30 nm) resulting in a larger molar extinction or a relatively smaller contribution from the refractive index change due to the native biomolecular surface layer. Though we observe a red shift contrary to previous extinction results with smaller nanoparticles (10 nm and 20 nm), our results with 30 nm are consistent with extinction results generated by commercial synthetic NPs modified with Raman reporter molecules.[30] Confirmation of MBN modification was further verified by Raman spectroscopy demonstrated by our results presented in Figure 4–17B.

Thus far, we have demonstrated successful surface modification of B-AgNPs with different Raman reporter molecules post synthesis. This approach is consistent with the commonly performed modification approach of chemically produced NPs. As an alternate approach, we attempted to incorporate Raman reporter molecules *in situ* during bio-production of AgNPs. Our preliminary UV-visible extinction and Raman results are presented in Figure 4–18. Our UV-visible extinction results shown in Figure 4–18A reveals NPs are produced in both cases wherein fungal cultures were treated with $AgNO_3$ compared to the fungus control with no $AgNO_3$. The peak position of both the unmodified AgNPs and the *in situ* modified are relatively consistent (~ 410 nm). Remarkably, the NP concentration of *in situ* modified NPs is distinctly higher than that of unmodified NPs. We

are working to understand this dramatic change. Visually, the inset of Figure 4–18A shows that the NPs solution with 1 mM $AgNO_3$ and 5 mM MBN are stable in solution and that the colour is darker suggesting higher NP concentration or larger NP size diameter. Successful modification with MBN is confirmed by the Raman spectra shown in Figure 4–18B. *In situ* labelling offers to speed up producing extrinsic Raman labels by eliminating or removing preparative steps. Incorporation of Raman reporters *in situ* will be further examined as water dispersible SERS substrates.

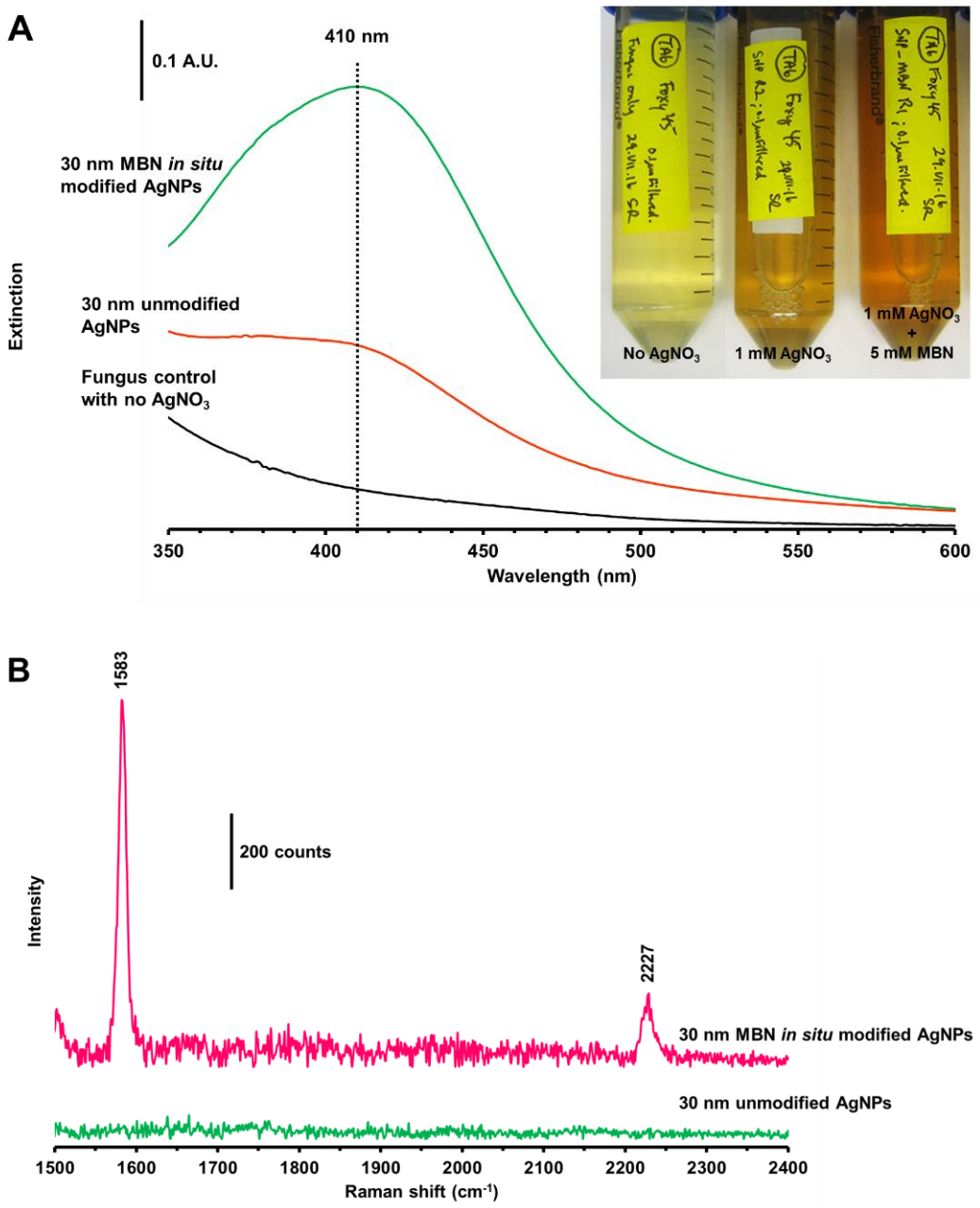

Figure 4–18. *In situ* mercaptobenzonitrile (MBN) modification of ø30 nm biogenic silver nanoparticles produced by *Fusarium oxysporum* at 45°C ± 0.3°C shaking at 100 rpm in the dark for 3 days. (A) Extinction plot before and after modification. Samples are diluted 1:4 with deionized water. Inset shows final products. Fungus control (left), unmodified silver nanoparticles (middle), and *in situ* modified silver nanoparticles (right). (B) Raman spectra collected using a 785 nm laser at 72 µW ± 3 µW laser power and an integration time of 10 sec. Spectra averaged from three different locations of visually equal amounts of AgNPs and offset for clarity.

Going back to our post synthesis modification of B-AgNPs, we now turn our attention to the incorporation of IgG antibodies. The purpose of adding antibodies is to provide biorecognition for a specific biomolecule. To demonstrate, we used anti-androgen receptor full length antibodies since we will be use these antibodies in chapter 5. Figure 4–19 presents our UV-visible extinction results tracking the sequential modification of MBN followed by the addition of antibodies. In Figure 4–19A, we recorded a red shift of 2 nm and an increase in band width (~ 3 nm) after the addition of 5 mM MBN consistent with our previous experiment shown above in Figure 4–17. Next, we recorded another red shift of 1 nm and an increase in band width (~ 8 nm) after physisorbing anti-AR-FL IgG antibodies (1 mg mL^{-1} stock concentration). The red shift in LSPR peak position and relative magnitude is consistent with a change in the dielectric constant of the medium due to changes in the mixed surface layer. The modified nanoparticles are stable evident by the absence of a secondary absorbance band. Thus, our extinction results provide evidence of successful modification of ø30 nm B-AgNPs with both Raman reporter molecules (MBN) and physisorbed antibodies.

To explain our rationale for physically adsorbing antibodies, it is important to draw attention to previous reports that have investigated the coupling chemistry using succinimidyl ester chemistry to immobilize antibodies.[151-152] Antibody coupling occurs by the primary amines from lysine residues reacting with the terminal succinimidyl ester to covalently immobilize the antibody through the formation of an amide bond.[151] Lim and co-workers suggest that succinimidyl coupling is inefficient based on their work with DTSP,

i.e., Lomant's reagent.[251] The authors report that the reaction kinetics of heterogeneous hydrolysis of the succinimidyl ester is three orders of magnitude greater than that of the heterogeneous aminolysis rate.[152] Thus, we compared immobilizing antibodies different methods, i.e., physically adsorbed, EDC-NHS chemistry, and succinimidyl ester (DTSP) chemistry by UV-visible extinction spectroscopy shown in Figure 4–19. Figure 4–19B reveals antibodies that are physically adsorbed are comparable to antibodies that have been immobilized using DTSP based on consistent peak position (413 nm) and similar peak width (~ 112 – 115 nm). Our extinction results agree with Filbrun and Driskell's report investigating ø60 nm AuNPs and antibody surface coverage using a fluorescence-based method.[151] The authors report that the surface coverage of antibody immobilized via DTSP (or DTSSP) corresponds to 298 ± 46 antibodies per AuNP compared to 309 ± 93 antibodies per AuNP via direct adsorption.[151] The authors infer that the hydrolysis of DTSP-modified AuNPs results in surface-bound carboxylates giving the AuNPs a negative surface potential similar to that of unconjugated citrate-capped AuNPs. This explanation can be extend to B-AgNPs since our native B-AgNPs also have a negative zeta potential of −23 mV ± 1 mV. For our EDC-NHS modified B-AgNPs, we observe a slightly greater red shift in peak position (414 nm), however the peak width is dramatically broader (~ 140 nm) compared to DTSP modified (~ 112 nm) (Figure 4–19B). We suspect the broader peak width is caused by the inefficiencies of each reaction step i.e., EDC activation of the carboxylic acid groups found within the biocorona followed by the addition NHS to o-acylisourea intermediate[149] resulting in heterogeneous reaction outcomes. Though our results with EDC-NHS coupling following a method described by Hermanson[149] were variable, other researchers[284] have reported success with EDC-NHS chemistry with higher concentrations of EDC (350 mM)

and NHS (110 mM) in a 1:1 ratio.[285-286] As an alternate approach, we also attempted to couple antibodies using cysteine residues via maleimide conjugation, however this approach was unsuccessful due to low abundance of cysteine residues (XPS data not shown). Thus, to simplify our process towards for an extrinsic Raman label and minimize modification variability, we proceeded with physically adsorbing antibodies to the surface of B-AgNPs.

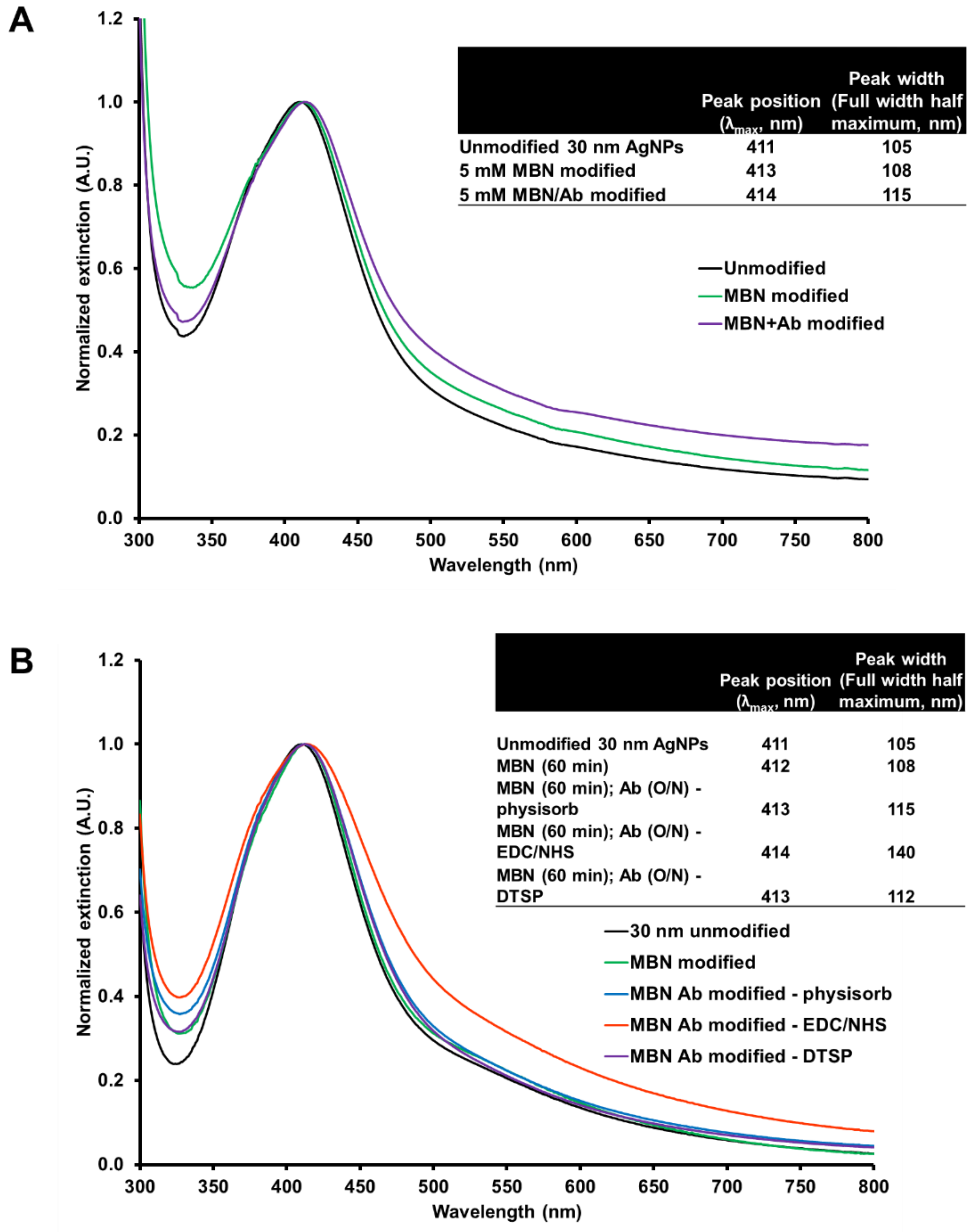

Figure 4–19. Normalized UV-visible extinction plot before and after modification with mercaptobenzonitrile (MBN) followed by IgG antibodies (Ab) of ø30 nm biogenic AgNPs. All nanoparticle dispersions are washed once and resuspended in 2 mM borate buffer with 1% bovine serum albumin. (A) Extinction curves of unmodified nanoparticles (black), nanoparticles modified with 5 mM MBN for 60 min (green), and nanoparticles modified with MBN and physisorbed antibodies incubated overnight (~ 18 h) (purple). Inset shows the LSPR peak position and peak width. (B) Extinction curves of unmodified nanoparticles (black), nanoparticles with 5 mM MBN for 60 min (green), nanoparticles with MBN and physisorbed Ab (blue), nanoparticles with MBN and Ab attached through EDC/NHS chemistry (red), and nanoparticles with MBN and Ab attached through DTSP chemistry (purple). Incubation with antibodies was overnight (~ 18 h). O/N = overnight.

We now turn our attention towards optimizing the capture substrate, which consists of a standard microscope slide with multiple metal film spots (Figure 4–1B). To produce the metal film spots, a custom aluminium mask shown in Figure 4–20 was designed and fabricated. In selecting a metal film to generate high SERS intensity, we tested 300 nm Au and 300 Ag films for enhanced plasmonic coupling.[287] We selected 300 nm thick films to ensure bulk Au and to avoid the possibility of signal attenuation due to electron tunnelling[279, 288] observed in thinner films. Figure 4–21 shows our Raman results using ø20 nm B-AgNPs modified with 5 mM NBT on both Au and Ag films. Analysis of the spectra reveal consistent vibrational features of NBT. In comparing the two films by examining the $\nu_s(NO_2)$ stretch at 1333 cm^{-1}, we observe ~ 3X increase in signal intensity and higher background signals (not shown due to background subtraction). Though results with Ag are encouraging, a magnitude within one order did not give us a compelling reason to select Ag films over Au films considering the drawbacks of Ag (e.g., oxidation and film robustness). We further investigated bare Au and Ag films by AFM presented in Figure 4–22 to explain our SERS signal differences. In analysing our AFM images of 300 nm Au and 300 Ag films, we measured the root mean square (RMS) corresponding to the surface roughness to be 3.3 nm ± 0.1 nm and 2.9 nm ± 0.1 nm, respectively. Though high SERS signal intensities can be achieved by using roughened silver surfaces,[66, 68, 289] our Raman results did not provide compelling evidence of this compared to Au (Figure 4–21). Thus, considering our experimental results in concert with ease of deposition, film robustness, and film oxidation we proceeded with Au films typically used in SERS immunoassays.[28, 75, 84, 290-291]

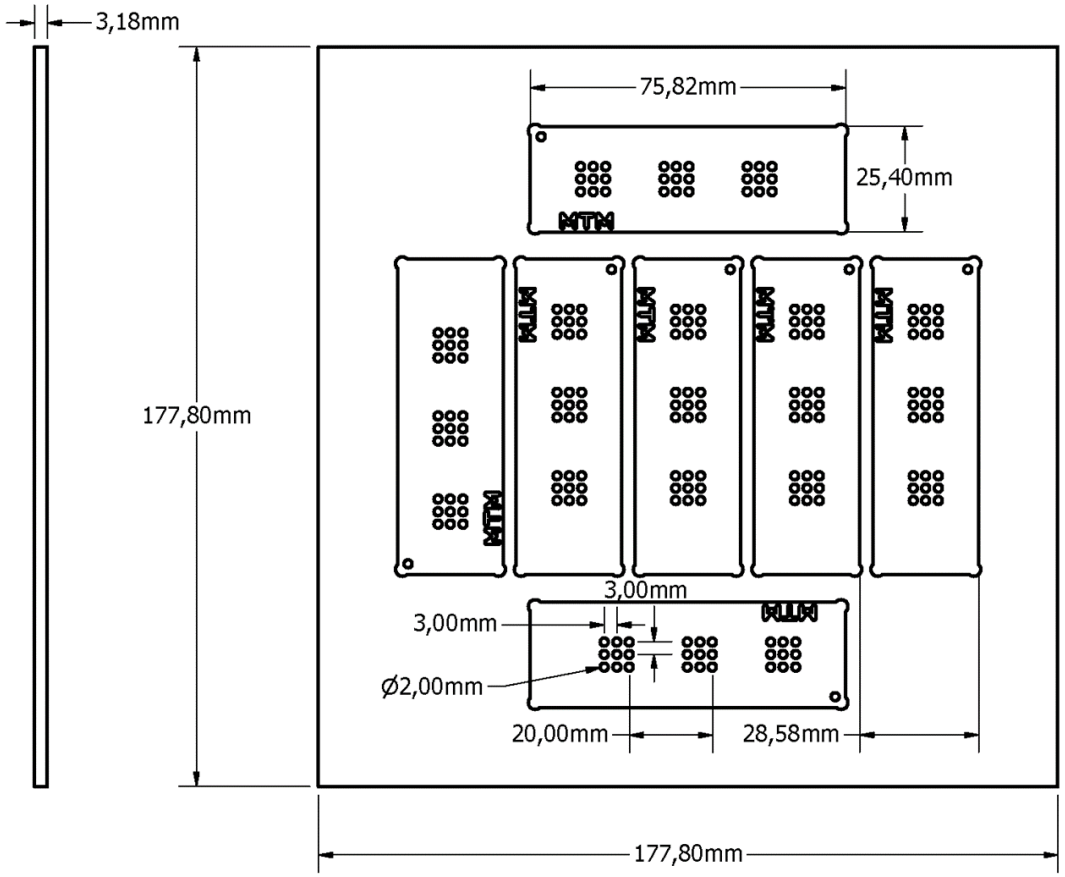

Figure 4–20. Fabricated mask for the deposition of plasmonic metal films for SERS-based substrates designed for clinical use. The mask is designed to use standard microscope slides. Each slide consists of three 3 x 3 array of ø2 mm test spots. One spot in the top left corner is designed for slide orientation. MTM represents the McDermott Research Laboratory and exemplifies substrate branding. All measurements are in mm. Left shows side view. Mask material is 6061 aluminium. Design drawing provided by Vincent Bizon (University of Alberta, Department of Chemistry, machine shop).

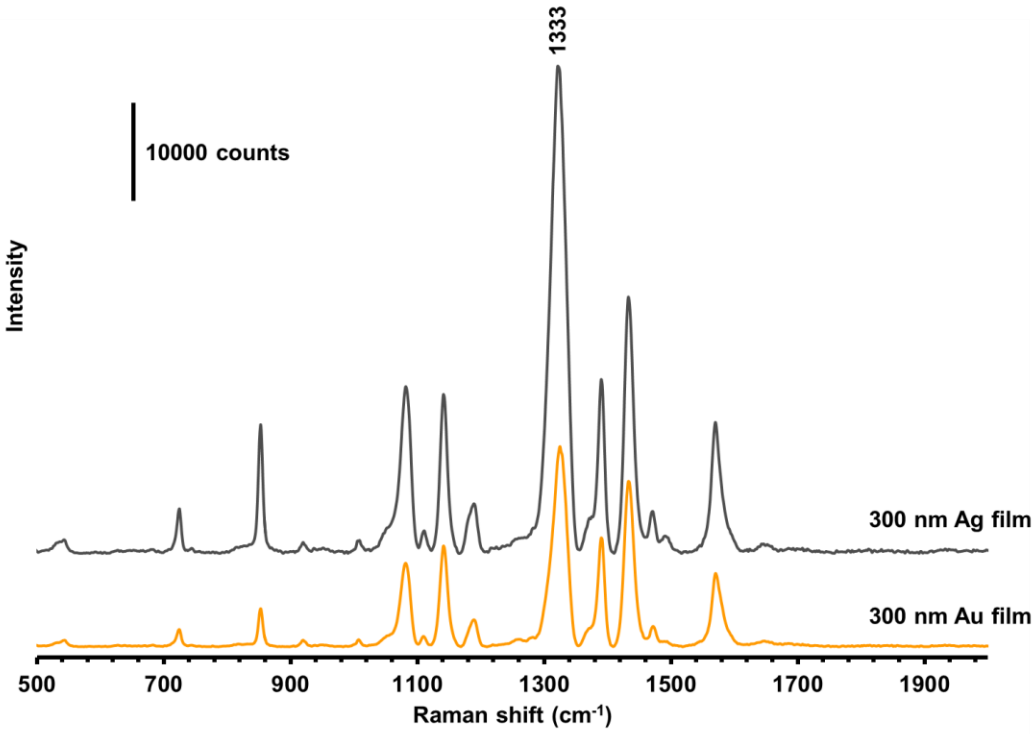

Figure 4–21. Raman spectra of ø20 nm biogenic silver nanoparticles modified with 5 mM nitrobenzene thiol on either 300 nm thickness Au or 300 nm thickness Ag film. A 514.5 nm laser was used to collect each spectrum at 70 ± 3 μW laser power and an integration time of 10 sec. Spectra averaged from three different locations of visually equal amounts of AgNPs and offset for clarity. The $\nu_s(NO_2)$ is labelled at 1333 cm^{-1}.

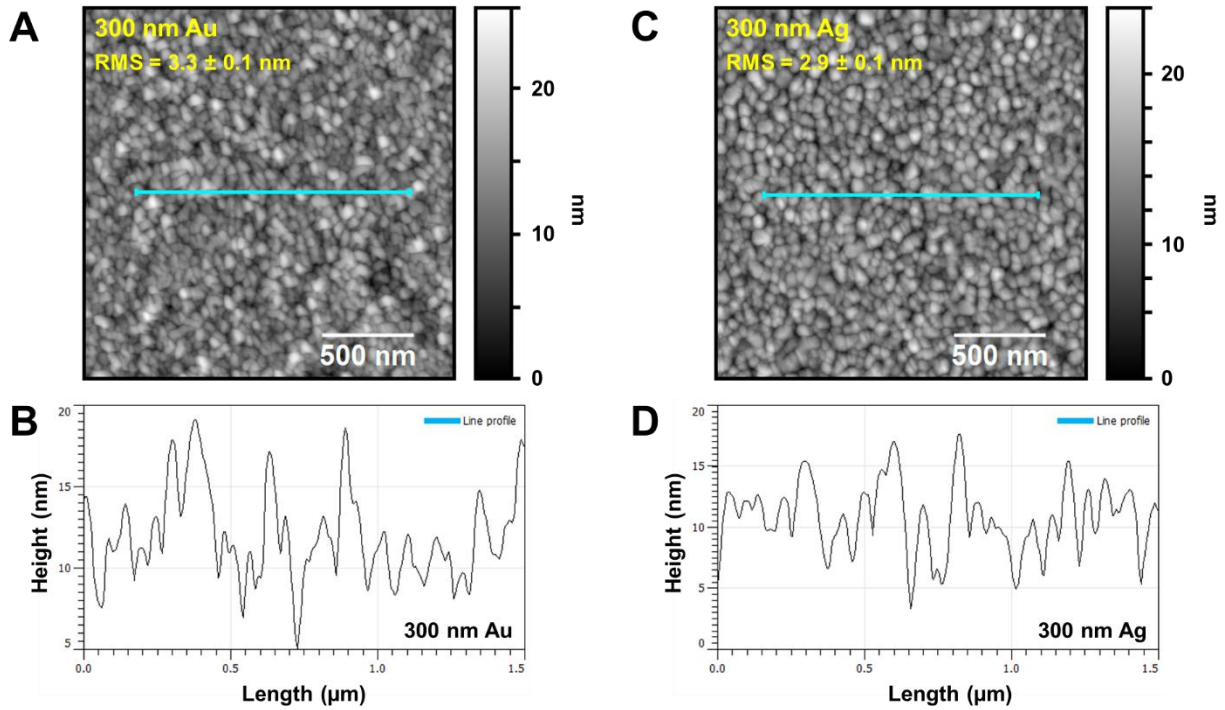

Figure 4–22. Tapping mode atomic force 2 x 2 μm micrographs of bare 300 nm thickness Au and Ag films. (A and B) Au film. Surface roughness (root mean square, RMS) measures 3.3 ± 0.1 nm. 1.5 μm blue line corresponds to the height profile in (B). (C and D) Ag film. Surface roughness (root mean square, RMS) measures 2.9 ± 0.1 nm. 1.5 μm blue line corresponds to the height profile in (C). Scale bar = 500 nm.

In establishing Au films as our plasmonic substrate, it is important to consider the remaining glass surface of the microscope slide. To use the Au spots effectively, the liquid volume deposited at each address is required to exhibit minimal spreading. Fluid spreading (low contact angle) is expected due to clean surfaces (i.e., absence of contaminating hydrocarbons). One way is minimize spreading is to increase the hydrophobic background of the glass. A common approach is to use silanating reagents and covalently linking fluorine groups. Thus, we exposed our substrates after Au deposition to a vapour of tridecafluoro-1,1,2,2-tetrahydrooctyl dimethylchlorosilane (DMS) under reduced pressure (dynamic) at room temperature (22°C) for ~ 18 h to create a hydrophobic background on the glass surface. Alkyl silane reagents are known to react with silanols to form relatively ordered monolayers driven by hydrophobic interactions between the alkyl chains.[30] The DMS silane reagent with one hydrolyzable Cl group offers monolayer coverage on the glass and minimizes modification of the Au surface.[292] We found that it is important to consider the number of hydrolyzable functional group when using silane reagents. We observed silane reagents with three hydrolyzable Cl groups (e.g., tridecafluoro-1,1,2,2-tetrahydrooctyl trichlorosilane) will lead to multilayer surface coverage (data not shown). Higher number of hydrochloric acid leaving groups will etch the Au surface and foster modification.[293] Also, when using silane reagents with >1 hydrolyzable groups, vacuum condition (i.e., dynamic versus static) is important. Under dynamic vacuum, we have observed a modification gradient when using tridecafluoro-1,1,2,2-tetrahydrooctyl trichlorosilane.

We demonstrate successful silanation of the glass surface and not the Au surface by SEM/EDX and XPS analyses. Figure 4–23 shows an EDX spectra of 300 nm bare Au film and the glass substrate. In the 300 nm Au film spectrum, Au and Si are the most abundant features identified. In the glass substrate spectrum, there is a strong signal from Si and an expected absence of Au. Centring on a kinetic energy of Kα 0.677 eV, there is a small F peak height on the glass and absent on Au (Figure 4–23 inset). The other elements detected in the glass substrate are likely surface or material impurities. Our SEM/EDX results confirm that the glass surface has been selectively silanated with DMS and the Au film remains unmodified.

To further characterization the DMS modified glass surface, we conducted XPS and present our results in Figure 4–24. Figure 4–24 shows high resolution scans for Si (Figure 4–24A) to ensure beam is targeting the glass and F (Figure 4–24B). As evidenced, detection of signal ~ 102.6 eV is consistent with the Si 2p line at 99 eV (Figure 4–24A). Confirmation of the Si ensures the X-ray beam is targeting the glass. Detection of signal ~ 687.9 eV is consistent with the F 1s line at 686 eV (Figure 4–24B). The slightly higher binding energy could be due to charging effects or caused by impurities in the microscope glass slide. Our XPS results led us to conclude that the glass surface has been successfully modified with DMS. Due to the beam spot size of approximately 400 μm x 700 μm and close proximity of glass, we could not conclusively confirm absence of F 1s on a 2 mm Au spot. Thus, we confirm the absence of fluorine modification on Au by EDX (Figure 4–23) and infrared reflection absorbance spectroscopy (data not shown).

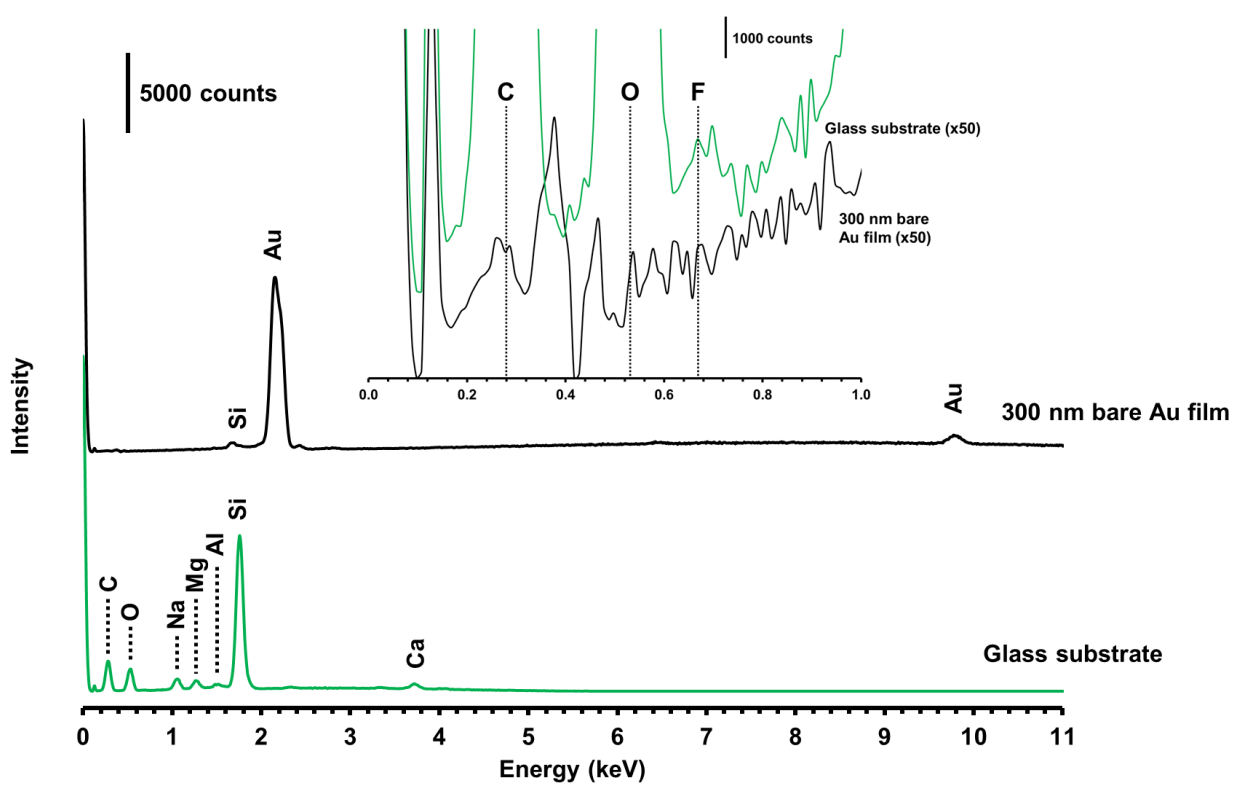

Figure 4–23. Energy dispersive X-ray spectra of fabricated glass microscope slide substrate (black spectrum) with ø2 mm Au spots (green spectrum) exposed to tridecafluoro-1,1,2,2-tetrahydrooctyl dimethylchlorosilane by vapour deposition under dynamic vacuum overnight (~ 18 h) at room temperature to confirm silane modification. Major peaks are labelled. All spectra are offset for clarity. Inset shows magnified region between 0.0 – 1.0 keV. Spectra are magnified by a factor of 50.

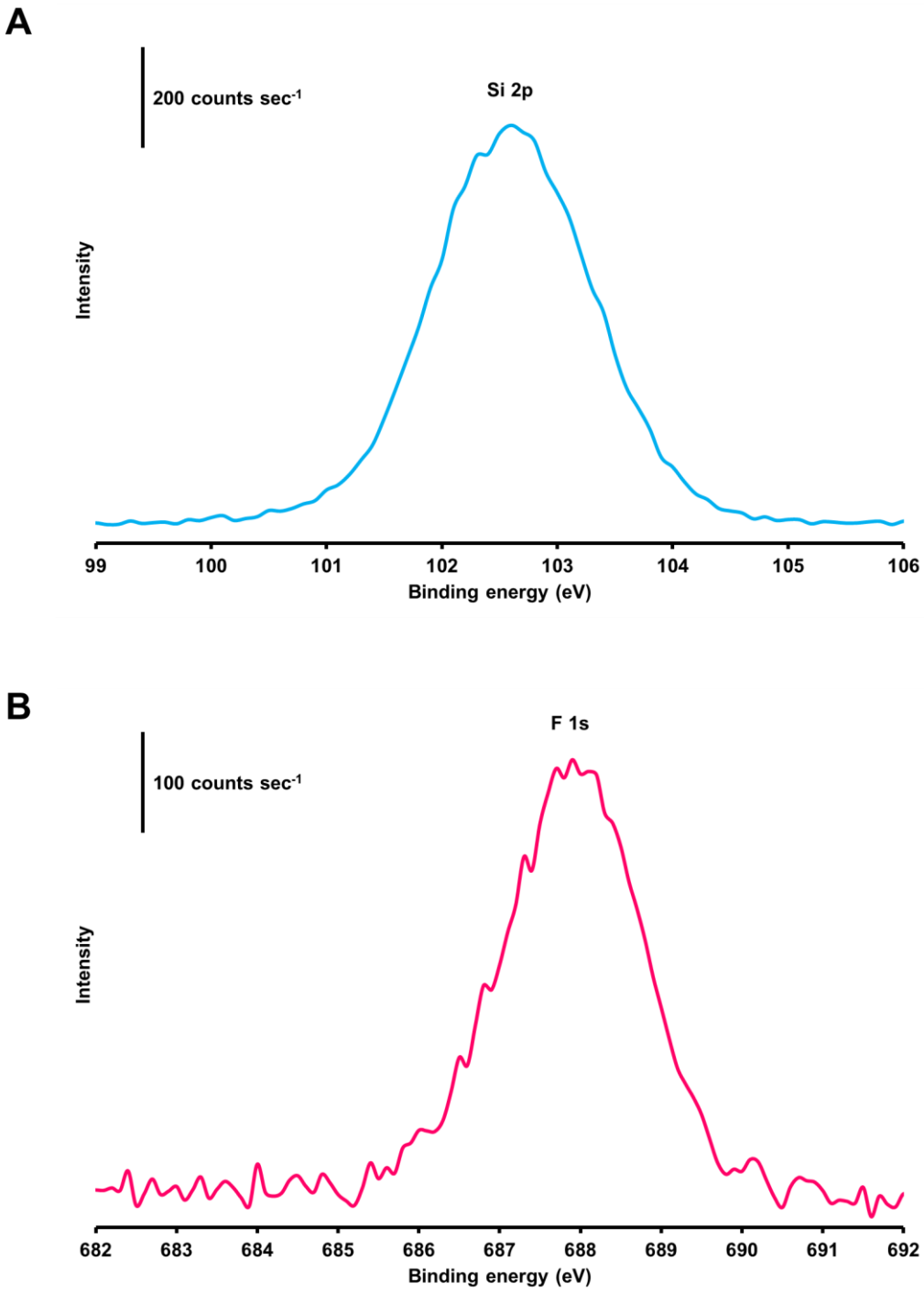

Figure 4–24. X-ray photoelectron spectra of fabricated glass microscope slide substrate exposed to tridecafluoro-1,1,2,2-tetrahydrooctyl dimethylchlorosilane by vapour deposition under dynamic vacuum overnight (~ 18 h) at room temperature to confirm silane modification. Major peaks are labelled. Spectra have been calibrated to C 1s peak. (A) High resolution scan for Si 2p. (B) High resolution scan for F 1s. Background subtracted from spectrum.

4.4. Conclusion

This chapter advances the functionality of biogenic AgNPs towards a surface-enhanced Raman scattering (SERS) sandwich immunoassay. Evidence compiled from a series of surface modification experiments demonstrates controlled modification of B-AgNPs by sequentially adding Raman reporter molecules and IgG antibodies. Modified B-AgNPs maintain colloidal stability under most conditions evaluated. Based on our results, we will proceed with ø30 nm AgNPs and mercaptobenzonitrile as our Raman reporter reagent in our SERS-based immunoassay. We also presented our results to optimize a capture substrate that will be used in a SERS immunoassay. Based on this work, we have designed and fabricated a substrate that employs a standard microscope slide with multiple Au spots to advance in our SERS-based immunoassay aimed at clinical use.

Chapter 5. Detection of the advanced prostate cancer prognostic and predictive biomarker androgen receptor V7 in serum by surface-enhanced Raman scattering

5.1. Introduction

In Chapter 4, controlled surface modification of biogenic silver nanoparticles with Raman reporter molecules and antibodies were described to establish a basis for bioanalyses (biosensing). To enhance SERS signal intensity, biogenic AgNPs were shown to be controllably modified with Raman active molecules due to weak intrinsic signal intensities. Modification with four Raman active reporters was described. Optimization of Raman reporter modification was performed through concentration dependence and time resolution studies. Among the Raman active molecules evaluated, 4-mercaptobenzonitrile was selected to advance due to its ν_s(C≡N) vibrational stretch at 2221 cm^{-1}. As metal film selection is an important contribution to SERS signal intensity, we found Au films to be superior to Ag films. Thus, we optimized critical components of a SERS-based assay to a point where it is ready for a real-world application.

Prostate cancer (PCa) is the second most common cancer in men according to the International Agency of Cancer Research.[294] In Canada and the US, PCa is the leading

cancer type in men.[295,296] The International Agency estimated that 1.1 million men worldwide were diagnosed with PCa in 2012; accounting for 15% of the cancer types diagnosed in men. According to the National Institute of Health Surveillance, Epidemiology, and End Results Program (NIH SEER)[297] and Canadian Cancer Statistics,[298] PCa ranks third both in the USA and in Canada as the leading cause of death by cancers in males. Mortality is largely attributed to the advanced metastatic context with a five-year survival rate of 29.8%.[299-300] To improve prognosis in this high risk setting, identifying treatment-specific biomarkers are needed for maximum patient benefits.

Huggins and Hodges seminal discovery in 1941 led to androgen deprivation therapy (ADT) as the standard first-line treatment for men with advanced prostate cancer (PCa).[301-303] For the past 77 years, depleting androgens or blocking the receptor's active site has been the first-line standard of care. Upon treatment, most patients with PCa initially benefit from a decline in prostate-specific antigen (PSA) levels, relief of symptoms, and disease control.[304] However, the initial clinical benefit is temporary. Most patients eventually develop resistance to ADT and present with disease progression (e.g., rising PSA levels, radiographic progression, and clinical progression) and transition to a castration-resistant state that is inevitably fatal. Androgen deprivation therapy often fails due to one or more resistance mechanisms within the androgen receptor (AR) signalling axis. On-going efforts aim to understand these mechanisms. Known mechanisms have been reviewed previously in detail.[304-305] Briefly, AR resistance mechanisms are categorised into two groups; androgen ligand–dependent and androgen ligand–independent. Androgen

ligand–dependent mechanisms reported include: AR gene amplification, autocrine androgen production, and adrenal androgen synthesis. Androgen ligand–independent mechanisms reported include: AR alternative signalling, AR mutations, AR bypass signalling, and AR splice variants.[304] Consequences of AR signalling resistance mechanisms often results in a distinctly different prognosis due to varying responses to available therapies. In our study, we focus on AR splice variant 7 (AR-V7) due to its resistance to two hormonal therapies, abiraterone and enzalutamide.[306]

Through an understanding of AR resistance mechanisms and targeting the androgen receptor signalling axis, the successful clinical development of two novel AR signalling inhibitors, abiraterone and enzalutamide, have resulted.[303, 307-308] Both agents have been approved by the United States Food and Drug Administration (FDA) to treat metastatic castration-resistant prostate cancer (CRPC) on the basis of survival improvements.[309-312] Currently, the four approved major systemic therapies for mCRPC patients are: (1) second generation AR-signalling inhibitors (abiraterone and enzalutamide); (2) taxane chemotherapy (docetaxel and cabazitaxel); (3) radiotherapy (radium-223); and (4) immunotherapy (sipuleucel-T).[304] The current Canadian guidelines for managing mCRPC recommends the use of second generation of AR signalling inhibitors, followed by taxane chemotherapy, radiotherapy, and immunotherapy in order of disease progression.[313]

An important unmet need for mCRPC patients is treatment-specific biomarkers to guide treatment selection during the course of disease with the ultimate goal of maximizing

benefits and limiting toxicity.[314] Biomarkers are defined as objective clinical or molecular characteristics that can be accurately and reproducibly measured to indicate a biological state, including normal and pathologic states, or response to a specific therapeutic intervention.[304, 315] As Terada and co-workers describe, biomarkers used for PCa are considered to be prognostic (i.e., prediction of disease progression) and / or predictive (i.e., prediction of treatment response).[314] According to Mehta and colleagues, prognostic biomarkers aim to objectively evaluate the patient's overall outcome, such as the probability of cancer recurrence after standard treatment. The presence or absence of a prognostic marker can be useful for the selection of patients for treatment but does not necessarily predict the response to treatment. Predictive biomarkers aim to objectively evaluate the likelihood of benefit from a specific clinical intervention, or the differential outcomes of two or more interventions, including toxicity.[316] Several categories of biomarkers are used for prognostic or predictive value for patients with advanced PCa. These include clinical features (e.g., pain), laboratory analytes (e.g., PSA, lactate dehydrogenase, circulating tumour cell count), imaging features (e.g., sites of metastasis), pathologic features (e.g., small cell), and molecular alterations (e.g., AR-V7+ detection, DNA damage repair gene alterations).[304] Due to the dynamic nature of PCa disease progression, active monitoring with multiple periodic measurements of biomarkers is necessary. To this end, liquid biopsies (e.g., blood, urine, semen, saliva) offer the potential for rapid, sensitive, minimally invasive, serial temporal measurements of molecular targets allowing for real-time monitoring, and early assessment of recurrence or treatment resistance.[317-318] Furthermore, liquid biopsies often result in lower morbidity compared to more invasive biopsies.

Androgen receptor splice variant 7 (AR-V7) is a biomarker that can be detected in the peripheral blood of CRPC patients. AR-V7 is the most abundant splice variant and best characterized, particularly for its potential as a prognostic and predictive character in CRPC patients among the > 20 AR splice variants reported.[319] Prior to describing the importance of AR-V7, it is important to provide a short introduction to AR splice variants. Figure 5–1 illustrates the main structural differences between full length AR (AR-FL) and AR-V7. As Luo describes, the human AR gene has eight canonical exons, including an NH_2-terminal domain (NTD) (cyan), a DNA binding domain (DBD) (yellow), a hinge region (green), and a ligand binding domain (LBD) (purple).[320] Luo further states the AR-V7 mRNA retains the first three canonical exons, followed by a variant-specific cryptic exon 3 (CE3) within intron 3.[320] Splicing of CE3 results in a LBD-truncated AR-V7 protein due to premature translation termination after 16 variant-specific amino acids.[320] These structural differences between AR-FL and AR-V7 allow for detection specificity.[320]

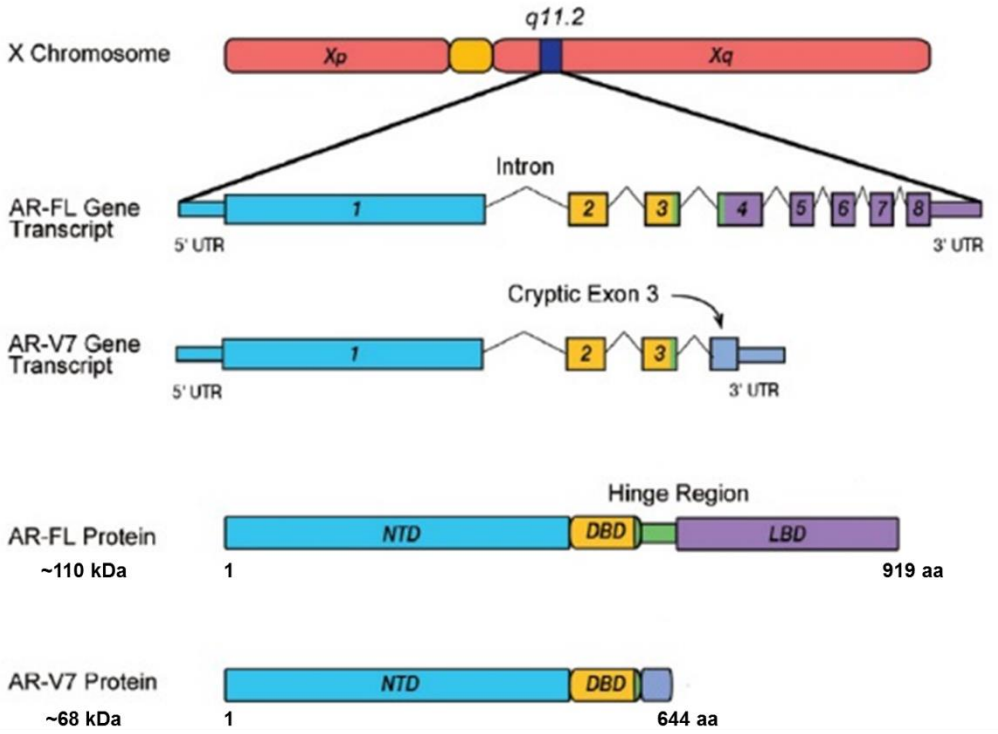

Figure 5–1. Structural illustrations of full length androgen receptor (AR-FL) and the splice variant AR-V7. Adapted and reproduced with permission from *Asian Journal of Andrology* **2016**, 18, 580-585.[320] Xp = short chromosome arm, Xq = long chromosome arm, UTR = untranslated region, NTD = NH_2-terminal domain, DBD = DNA binding domain, LBD = ligand binding domain. Copyright (2016) Asian Journal of Andrology.

Although androgen receptor splice variants lack the C-terminal ligand-binding domain, they retain the transcriptionally active N-terminal domain resulting in activation of target genes.[306] Thus, splice variants, including AR-V7, are implicated as one of the mechanisms of resistance to the currently available AR signalling inhibitors. Currently, AR-V7 is the most widely studied variant in context of AR signalling resistance and treatment selection. The first landmark study by Antonarakis and co-workers demonstrated a correlation between presence of AR-V7 mRNA in circulating tumour cells (CTCs) and worse clinical outcomes of 62 mCRPC patients treated with either abiraterone or enzalutamide.[306] Furthermore, the authors reported no PSA declines (≥ 50%) from baseline (PSA_{50}) in patients with AR-V7 positive CTCs and worse progression-free survival (PFS, radiographic and PSA), and overall survival (OS) compared to AR-V7 negative patients. The authors conclude that AR-V7 detection in CTCs from CRPC patients may be a predictive biomarker for the response to abiraterone and enzalutamide and could potentially serve as a prognostic tool.[304, 306] Since Antonarakis and co-workers initial report in 2014,[306] several studies have substantiated AR-V7 as a prognostic marker by reporting AR-V7 positive patients have inferior progression free survival and overall survival outcomes;[321-323] Previous reports have also documented that AR-V7 positive CRPC patients respond to taxane chemotherapy[322] (an alternative systemic therapy to abiraterone and enzalutamide). Therefore, men who do not respond to AR-signalling inhibitors (e.g. enzalutamide, abiraterone, apalutamide) can be treated with taxane-based chemotherapy for improved outcomes including OS.[323] A report from Scher and colleagues suggests that nuclear-localized AR-V7 protein in CTCs improves prediction of overall patient survival on taxane chemotherapy versus AR-signalling inhibitors compared to cytoplasmic (nuclear-

agonist) AR-V7.[324] In both independent reports, the investigators report AR-V7 detection justifies taxane chemotherapy to improve overall survival. To this end, analytically-validated assays for AR-V7 (mRNA or protein) that include prospective patient evaluation with specific demonstration of an outcome benefit by treatment selection depending on AR-V7 status are urgently needed for clinical validation.[325-326]

Current blood-based AR-V7 detection platforms predominantly rely on mRNA detection[306, 327-331] with only one assay reported for protein level expression.[323] Among the assays documented in the scientific literature, two have been clinically certified through the United States Clinical Laboratory Improvements Amendments (CLIA). One assay detects AR-V7 mRNA by reverse-transcription PCR in CTCs[332-333] and the other assay detects AR-V7 protein by immunofluorescence in CTCs.[323, 334] Three main drawbacks to CTC-based analysis are: (1) CTC enrichment can be difficult due to low levels of abundance and specificity. Currently, two commercial CTC isolations kits (CellSearch, Janssen Diagnostics, FDA-approved and AdnaTest ProstateCancerSelect, Qiagen) are available, but require investment of resources (labour, time, funds) for optimization; (2) CTC capture methods that rely on epithelial cell adhesion molecules or other epithelial cell-surface markers may miss mesenchymal cells undergoing epithelial-mesenchymal transition;[314] and (3) optimal mRNA detection requires that blood samples be processed for nucleic acid extraction within 24 h of collection.[335] Longer times up to 72 h[336] can decrease nucleic acid recovery and can lead to a false negative result. As an alternative approach, this chapter reports the successful development of a sandwich immunoassay for AR-V7 protein with

surface-enhanced Raman scattering (SERS) readout. In addition, the first measurements of AR-V7 protein compared with mRNA expression in CRPC patients are reported.

Surface-enhanced Raman scattering immunoassays have been widely used as a quantitative assay in various fields including human disease diagnostics.[1, 37, 75, 89, 92, 290-291, 337-339] In a recent review highlighting the wide use of SERS-based immunoassays, Wang and co-workers have covered a range of human disease biomarkers (e.g., proteins), detailing assays with broad dynamic ranges and low detection limits.[340] Figure 5–2 shows the key features of our SERS-based immunoassay. There are three main components: (1) a capture substrate to specifically bind and enrich antigens from a sample solution (Figure 5–2A); (2) surface functionalized silver nanoparticles to specifically bind captured antigens and generate intense SERS signals (Figure 5–2B); and (3) SERS readout (Figure 5–2C).[75, 145, 337] As described by Wang and co-workers, this approach exploits the strong SERS signal for organic molecules (i.e., Raman reporter molecules, RRM) that are immobilized on B-AgNPs along with the appropriate detection antibody. In our assay, we are using biogenic silver nanoparticles produced by a fungus, *Fusarium oxysporum*, for their enhanced colloidal stability compared to chemical counterparts.[183] Nanoparticles modified with RRMs are often referred to as extrinsic Raman labels or ERLs. Using a sandwich immunosorbent assay format, each antigen is identified by a characteristic SERS spectrum resulting from immobilized RRM and quantified by the corresponding SERS signal intensity. As described by Wang and colleagues, advantages of this strategy reflect three unique features of SERS: (1) Raman spectral bandwidths are typically 10-100 times

narrower than those of fluorescence, minimizing spectral overlap in the response from different RRMs and thus facilitating the detection of different ERLs at a single biochip address in multiplexed assays; (2) SERS intensities for RRMs can rival those of fluorescent dyes, which has enabled the detection of a single ERL nanoparticle using only a few seconds of signal acquisition; (3) one excitation wavelength is needed to produce SERS from different RRMs, which simplifies the instrument hardware required for signal generation and acquisition.[337]

This chapter reports the successful detection of AR-V7 protein at low levels in cultured prostate cancer cells and in human serum using a SERS-based sandwich immunoassay. We also report calibration of AR-V7 protein and AR-V7 mRNA expression levels. Herein, we show enhanced expression of AR-V7 in cultured prostate cancer cells to verify presence of AR-V7 protein. To establish a calibration curve and a linear range, we show detection of AR-V7 protein and compare our results to AR-V7 mRNA from cultured prostate cancer cells. Next, we carried out a prospective pilot scale study to investigate the clinical utility of a SERS-based immunoassay by using a retrospective cohort of seven CRPC patients pre / post treatment with enzalutamide and / or abiraterone. As detailed, our results demonstrate the ability to identify AR-V7 status (positive or negative) in CRPC patients and provide quantitative measurements to enhance prognostic and predictive value. Furthermore, our results begin to demonstrate the potential of a SERS-based immunoassay to serve in AR-V7 prognostic/predictive toolkit. Advancing this approach to the clinic and further enhancing the prognostic and predictive potential is also briefly

discussed. This approach builds on our previous work[30-31, 341] and other laboratories[1, 37, 75, 89-90, 291, 342-346] exploiting the strength of SERS for low level analyte detection and quantification.

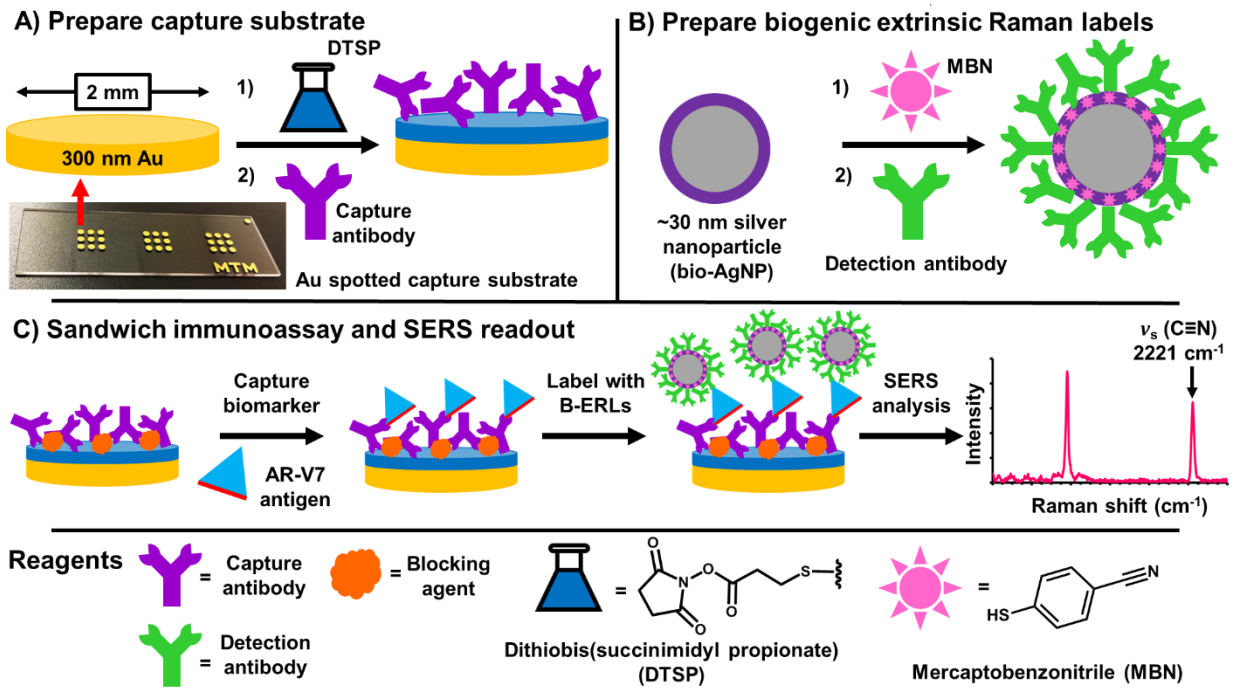

Figure 5–2. Detection scheme for AR-V7 using a sandwich immunoassay and surface-enhanced Raman scattering (SERS) immunoassay in three major components. (A) Capture substrate preparation using a standard microscope slide; (B) Biogenic extrinsic Raman labels preparation; (C) Major assay steps. Preparative steps (A) and (B) are completed prior to the assay (C). The assay is performed by spotting a sample (3.0 µL) onto the capture substrate address (2 mm) with AR-V7 binding sites active and other reactive sites are blocked followed by room temperature (22°C) incubation. Samples are rinsed, exposed to B-ERLs, rinsed again, dried, and then analysed by Raman spectroscopy and tracking the nitrile vibrational stretch at 2221 cm^{-1}. Capture antibodies = monoclonal anti-AR-V7 specific. Detection antibodies = polyclonal anti-AR-full length specific.

5.2. Experimental

5.2.1. Reagents and materials

The following reagents were used as received: acetonitrile (HPLC grade, Caledon), ethyl alcohol (anhydrous, Commercial Alcohols), H_2SO_4 (95-98%, Caledon), 4-mercaptobenzonitrile (95%, product# SS-7247, Batch# L44964, Combi-Blocks, California, USA), Tridecafluoro-1,1,2,2-tetrahydrooctyl dimethylchlorosilane (DMS, product# SIT8170.0, Gelest, USA), Enzalutamide (ENZ, MDV3100, HPLC purity: 99.51%, NMR: consistent with chemical structure, product# S1250 Batch# S125012, Selleck Chemicals, Texas, USA). The following reagents were obtained from Sigma-Aldrich and used as received: bovine serum albumin (BSA, ≥ 98%, product# A3059-50G, lot# SLBT8252, Sigma-Aldrich), H_2O_2 (30%, ACS reagent, product# 216763-500 mL, Sigma-Aldrich), dithiobis(succinimidyl propionate) (DTSP, product# D3669-500 MG, lot# BCBT0455, Sigma-Aldrich), tween 20 (Bio-Xtra, product# P7949, Sigma-Aldrich), Sodium chloride (ACS reagent, ≥ 99.0%, catalog# S9888), dimethyl sulfoxide (DMSO, Hybri-Max, ≥ 99.7%, catalog# D2650). The following reagents were obtained from Thermo Fisher Scientific and used as received: BupH borate buffer (BB) packs (catalog# 28384), Pierce 20X phosphate-buffered saline (PBS, catalog# 28348), StartingBlock PBS blocking buffer (catalog# 37578, lot# RK241503), standard microscope slides (25 mm x 75 mm x 1 mm, Fisher Scientific product# 12-550-A3). Deionized (DI) water with a resistivity of 18 MΩ·cm was used for all aqueous preparations unless otherwise noted. All buffers were prepared in deionized water. For SERS immunoassays, buffer solutions were also passed through a membrane filter with a 0.2 μm pore size.

5.2.2. Anti-androgen receptor antibodies

Antibodies against androgen receptor full length (AR-FL) and androgen receptor splice variant 7 (AR-V7) were obtained from Abcam (Ontario, Canada). Anti-AR-V7 or isoform AR3 antibodies (ab198394, lot#GR312057-5) are monoclonal raised in rabbits. Specificity to AR-V7 comes from the 16 amino acid sequence within the region of C-terminus that is only present in isoform 3.[347-349] This sequence of isoform 3 differs from the canonical sequence due to alternative splicing. Isoform 3 contains amino acids 1-629 of the canonical sequence and includes an additional amino acid sequence that is not present in the full length protein. This additional sequence is unique only to isoform 3 as shown below:[347-349]

- Amino acids 629-644 is changed from ARKLKKLGNLKLQEEG → EKFRVGNCKHLKMTRP in isoform 3.[347-350] This unique sequence for ab198394 present only in isoform 3 is the immunogen used by Abcam.[351]
- Amino acids 645-919 are missing in isoform 3.

Anti-AR-FL antibodies (ab74272, lot# GR315793-3) are polyclonal raised in rabbits. These antibodies bind to region within amino acids 290-340 of the N-terminus. Though polyclonal antibodies, the immunogen used is a short (14-16 amino acids) synthetic peptide.[352] As such, we expect the antibodies to behave as monoclonal antibodies mapping to a specific epitope.

For SERS immunoassays, both anti-androgen receptor antibodies were diluted to 1 mg mL^{-1} (if stocks received were >1 mg mL^{-1}) with 0.2 μm filtered 1X PBS.

5.2.3. Immunoassay format

Figure 5–2 overviews the details of our SERS-based immunoassay.[75] The prostate cancer biomarker, AR-V7, is sandwiched between the capture substrate and a biogenic extrinsic Raman label (B-ERL). Biogenic ERLs are prepared by modifying ~ ø30 nm biogenic AgNPs with a thiolate monolayer that forms by spontaneous adsorption of the sulfur containing Raman reporter molecule (RRM) 4-mercaptobenzonitrile (MBN). This step is followed by the adsorption of a layer of AR-FL pAbs on the RRM. This configuration allows for maximum SERS signal intensity by positioning the Raman scattering centres of the RRM monolayer in close proximity to the AgNP surface. The smooth, glass-supported gold (300 nm thick) capture substrate is coated with AR-V7 mAbs adsorbed to the thiolate monolayer formed by the spontaneous adsorption of dithiobis(succinimidyl propionate) (DTSP).[152] Measurement of captured AR-V7 is indirectly signalled by the characteristic Raman spectrum of the RRMs. Amount of AR-V7 is indirectly quantified by the strength of an intense spectral feature (i.e., the nitrile stretch, ν_s(C≡N), centred at 2221 cm^{-1} of the MBN monolayer).[290, 339] Selection of antibodies was based on four main criteria: (1) commercially available at a reasonable cost; (2) matching antibodies that would map to epitopes that are spaced apart and would prompt favourable AR-V7 orientation in a sandwich assay; (3) buffer composition; (4) level of vendor technical service support. Specific detection of AR-V7 is discussed below in our results in context of clinical serum specimens.

5.2.4. Biogenic extrinsic Raman labels (B-ERLs)

The assay is underpinned by the plasmonic enhancement that occurs when the MBN molecule is close proximity to the AgNP surface.[272, 339] As such, this interaction forms the basis of an extrinsic Raman label (ERL), which consists of 30 nm biogenic AgNP modified with Raman-active MBN molecules and anti-ARFL pAbs. Biogenic ERLs were prepared in batches using 0.96 mL suspension of 30 nm AgNPs at 9.0 x 10^9 AgNPs mL^{-1} (estimated by extinction spectroscopy[165]) and adding 40 µL of 50 mM BB (pH 8.5, 0.2 µm filtered). Buffered AgNPs in 2 mM BB (final concentration) were then modified by the addition of 10 µL of 5 mM MBN in 100% acetonitrile (fresh) for 1 h at room temperature (22°C) in the dark. After 1 h, 20 µL of anti-human ARFL pAb (1 mg mL^{-1} stock solution) was added and incubated overnight (~ 18 h) at room temperature (22°C) in the dark. After the addition of antibodies, we did not add BSA that is often used for blocking and colloidal stabilization of chemically produced nanoparticles.[152, 290] Use of biogenic AgNPs with a native biomolecular layer imparts enhanced colloidal stability and eliminates one preparative step. After ~ 18 h incubation, excess reactants were removed by centrifugation (Eppendorf 5417R microcentrifuge) at 5000 rpm for 10 min. The resulting supernatant was carefully removed and the ERL pellet was resuspended in 1.0 mL of 1% BSA in 2.0 mM BB. This process was repeated one more time with the last step resuspending the pellet in 200 µL of 1% BSA in 2.0 mM BB containing 150 mM NaCl. The final ERL concentration is estimated at 2.2 x 10^{10} AgNPs mL^{-1} using the UV-visible spectrophotometric method of Paramelle and co-workers.[165]

5.2.5. Fabrication of SERS capture substrates with multiple gold (Au) spots

Standard microscope slides (25 mm x 75 mm x 1 mm) was purchased from Fisher Scientific and used as the capture substrate base. The capture substrates were cleaned using hot piranha solution (4:1, H_2SO_4: 30% H_2O_2) for 30 min followed by thorough rinsing with DI water and blown dry using Ar gas. [*Warning: Piranha solution should be handled with extreme care; it is a strong oxidant and reacts violently with many organic materials. When mixed with incompatible chemicals, this solution presents an explosion hazard. All work should be performed in an appropriate chemical fume hood with appropriate personal protective equipment.*] The cleaned and dried substrates were mounted on a mask that exposed twenty-eight 2 mm diameter round spots (three x three arrays and one spot for slide orientation) as seen in Figure 5−2A and placed into the chamber of a thermal evaporator (Torr International Incorporated, New York). Metal films of 10 nm chromium (5N purity) and 300 nm gold (4N purity) were sequentially coated on the glass substrate through the mask under vacuum (≤ 10^{-6} mbar). After removal from the evaporator, the substrates were then exposed to a vapour of tridecafluoro-1,1,2,2-tetrahydrooctyl) dimethylchlorosilane (DMS) under reduced pressure (dynamic) at room temperature (22°C) for ~ 18 h to create a hydrophobic background on the glass surface. Alkyl silane reagents are known to react with silanols to form relatively ordered monolayers driven by hydrophobic interactions between the alkyl chains.[30] The DMS silane reagent with one hydrolyzable Cl group offers monolayer coverage on the glass and minimizes modification of the Au surface.[353] We found that it is important to consider the number of hydrolyzable

functional group when using silane reagents. We observed silane reagents with three hydrolyzable Cl groups (e.g., tridecafluoro-1,1,2,2-tetrahydrooctyl trichlorosilane) will lead to multilayer surface coverage. Higher number of hydrochloric acid leaving groups will etch the Au surface and foster modification.[354] Also, when using silane reagents with >1 hydrolyzable groups, vacuum condition (i.e., dynamic versus static) is important. Under dynamic vacuum, we have observed a modification gradient when using tridecafluoro-1,1,2,2-tetrahydrooctyl trichlorosilane. After silanization, the prepared SERS substrates were stored in a desiccator under dynamic (continuous) vacuum at room temperature until use.

5.2.6. Preparation of SERS capture substrates

SERS captures substrates were prepared by immersing the slides in an ethanolic solution of 0.1 mM DTSP at room temperature (22°C) for ~ 18 h in the dark. After incubation, the SERS capture substrates were rinsed with ethanol and dried with gentle stream of high purity nitrogen. Next, the DTSP-derived monolayer was reacted with a 3.0 μL drop of capture antibody (1 mg mL^{-1} anti-human AR-V7 mAbs) for 3 h at room temperature in a dark humidity chamber to form a layer of AR-V7 mAbs on the hydrolyzed surface.[152] As overviewed in Figure 5−2, the substrate was then rinsed three times with 20 mL of phosphate-buffered saline containing 0.1% Tween 20 (PBST, pH 7.4) and dried with gentle stream of nitrogen. Next, substrate was blocked with 6 μL of freshly prepared 3% BSA in 1X PBS (0.2 μm filtered) with 0.05% Tween 20 for 2 h; rinsed three more times with PBST and dried; and exposed to 3 μL of undiluted serum sample for 1 h. After 1 h, the sample

was rinsed three times with 20 mL of 2.0 BB containing 10 mM NaCl and 0.1% Tween 20 (BBT), dried with nitrogen, and exposed to 3 μL of the B-ERL suspension and incubated for ~ 18 h. Finally, the sample was rinsed two times with 20 mL of 2.0 BB containing 10 mM NaCl and 0.1% Tween 20, rinsed once with DI water, and then dried with a gentle stream of high purity nitrogen prior to SERS interrogation. We found that a final rinse with DI water dramatically reduces excess buffer salt crystals, which effects the SERS measurement and SEM imaging. We also found that drying with a gentle stream of nitrogen reduces the coffee-ring effect[355] compared to ambient drying.

5.2.7. Raman measurement of 30 nm bio-ERL binding

SERS spectra were recorded with a Renishaw inVia Raman microscope (serial# H18095) equipped with a helium neon 633 nm laser (Renishaw, 50 W, serial# H36379), 1200 lines/mm grating, and a charged coupled device (CCD) detector. Irradiation of 633 nm from an air-cooled He-Ne laser was used for excitation at 100% power. Laser power at the sample was 3 ± 0.1 mW, measured with a power meter (Coherent, Laser Check model# 54-018, California, USA). The microscope attachment was a Leica system. A 5X objective was used to first focus the light path to centre of the Au address and a 20X objective (Leica, numerical aperture 0.4, ~ 2 μm laser spot diameter[356]) was used to collect spectra. Data for Raman point maps were collected within a 300 μm x 300 μm bright-field area controlled by an automated motorized XYZ stage. All reported point collections and spectra were a result of 10 second integration time (1 sec acquisition, 10 accumulations). Each point map required approximately 12 min to collect.

All calibration data are presented as the average and standard deviation of collected spectra from 50 different locations per sample from triplicate substrates.

5.2.8. Raman data analysis

All Raman point maps were imported into Spectragryph v1.2.5[256] for baseline correction and data extraction at the peak position corresponding to the ν_s(C≡N) at 2221 cm^{-1}. For baseline correction, all 50 spectra were treated twice with individual baseline correction using the "adaptive" curve function (coarseness 10, offset 0). Subsequently, values at peak position 2221 cm^{-1} (spectral range: 2200-2250 cm^{-1}) were recorded for analysis.

Assays for each specimen were run in triplicate. The level of AR-V7 in each specimen are reported as an average and the uncertainties reflect the range of measurements from 50 locations per sample from triplicate substrates prepared from a single specimen. Control PBS blank or serum blank specimens were run on each assay chip to verify minimal non-specific binding.

The serum blank specimens had an average intensity of 87 counts, with a standard deviation of 16 counts. The limit of detection (LOD) with a confidence interval of > 99% was determined to be 135 counts. This value was defined by the signal on the calibration curve that matched the blank response (87 counts) plus three times its standard deviation

(3 x 16 counts). Patients were identified using our SERS-based assay as "AR-V7 positive" if the level of AR-V7 was statistically measureable above the LOD (i.e., the average response including the standard deviation of the patient sample is statistically different from the cut-off of 135 counts).

5.2.9. Scanning electron microscopy (SEM)

All substrates were coated with a 5 nm iridium film prior to SEM analysis to avoid sample charging. Selection of Ir was based on ultra-fine grain size, high secondary electron yield, and use in high resolution SEM imaging.[357] The Ir film was sputtered at a rate of 0.2 Å/sec by bombarding an Ir target with a 7 keV and ~ 310 μA electron beam in a Gatan precision etching coating system model 682. SEM images were collected on a Hitachi S4800 field emission electron microscope. Image acquisition was conducted with a 5.0 kV accelerating voltage, 20 μA emission current, and a working distance of approximately 8 mm.

5.2.10. Cell lines

The human Vertebral-Cancer of the Prostate (VCaP) cell line[358] was a generous gift from Dr. Jun Luo of Johns Hopkins University (Baltimore, Maryland, USA). Human Prostatic Carcinoma (PC3) cells[359] were purchased from American Type Culture Collection (ATCC). VCaP cells were cultured in Dulbecco's modified eagle medium (DMEM) with high glucose (Gibco, catalog# 12800-082) supplemented with 10% fetal bovine serum (FBS, Canadian; Gibco, catalog# 12483-020) and 1X penicillin and streptomycin (P/S; 100 IU/mL penicillin

and 100 μg/mL streptomycin; Sigma, catalog# P4333).[360] PC3 cells were grown in DMEM/F12 medium (Gibco; catalog# 12400-024) supplemented with 10% FBS and 1x P/S. Both cell lines were incubated at 37°C and 5% CO_2 atmosphere.

5.2.11. VCaP cell lysate for SERS and ddPCR

VCaP cells (~ 60% cell confluency) were seeded into sterile 6-well clear, polystyrene flat bottom tissue culture-treated plates (Greiner, catalog# 657160) and medium was replaced with DMEM-high glucose/10% FBS and phenol red-free RPMI 1640 medium (Gibco, catalog# 11835-030)/5% FBS at 1 : 1 for 24 h. This allowed for cell transition prior to treatment. At 60 – 70% cell confluency, the cell medium was switched to phenol red-free RPMI 1640 with 5% charcoal-stripped serum (androgen deprived medium; charcoal-stripped serum kindly provided by Lacey Haddon and Dr. Judith Hugh, University of Alberta) with 5 μM enzalutamide (diluted from a 10 mM stock prepared in Hybri-Max DMSO, resulting in a final DMSO concentration 0.05%) for 24 h for maximum androgen blockade following Li and co-workers.[302] For our Western blot experiments, we maintained VCaP cells with androgen deprived medium for at least 48 h and ~ 60% confluency and then treated with 5 μM enzalutamide for 24 h following a previous report from Dr. Xuesen Dong's research group.[361] DMSO-control treatments used 0.05% Hybri-Max DMSO only.

For cell lysates used in SERS experiments, whole cells were washed with 1 mL PBS and treated with 200 µL/well of RIPA lysis buffer (ThermoFisher, product# 89900) and EDTA-free proteinase and phosphatase inhibitors (Thermo Scientific Halt Protease and Phosphatase Inhibitor Cocktail, catalog# 78440) following vacuum removal of medium. Subsequently, cells were scraped and left on ice for 15 min at an angle (~ 45°) for collection. After 15 min, cells were scraped again and collected. Culture wells with same treatment were pooled in 1.5 mL micro-centrifuge tubes. Excess cellular debris was removed by centrifugation (3,000 x *g*) at 4°C (cold room) for 15 min. Cell lysate supernatant was carefully removed and stored at −80°C until use. Total protein concentration was determined by bicinchoninic acid (BCA) assay[362] (Pierce, catalog# 23225) and incubated at 37°C for 30 min.[363] Bovine serum albumin was used for calibration and absorbance was recorded at 562 nm.

For ddPCR experiments, attached cells were washed with 1 mL PBS and treated with 500 µL trypsin/well following vacuum removal of medium. Cells were resuspended in 1 mL in media, then washed with 1X PBS and centrifuged at 300 x *g* at 4°C (cold room) for 5 min to pellet cells. Supernatant was removed and discarded. Cell pellet was washed with 1X PBS and stored at −80°C until use.

5.2.12. Western blot

VCaP cell lysates prepared for SERS experiments were also used for Western blot experiments. Western blotting assays follow standard work procedures[364] using a polyvinylidene fluoride (PVDF) membrane and chemiluminescence detection for AR-V7 or infra-red fluorescence for AR-FL and actin. Briefly, membranes were blocked for 1 h at room temperature in diluted blocking buffer (50%, diluted with PBS, Rockland, catalog# MB-070) for fluorescent western blotting. Blocked membranes were incubated with primary antibodies prepared in diluted blocking buffer (50%) at concentration of 1 : 1,000 overnight at 4°C. After extensive washing, Amersham ECL anti-rabbit IgG, horseradish peroxidase-linked whole secondary antibody (GE Healthcare, catalog# NA934) was used for signal amplification of AR-V7 at a concentration of 1 : 10,000 in diluted blocking buffer (50%). Horseradish peroxidase signal was visualized with the Amersham ECL prime western blotting detection reagent (GE Healthcare, catalog# RPN2236) and hyperfilm (GE Healthcare, catalog# 4500-1508). Actin and AR-FL was visualized using the Alexa Fluor 680 (goat anti-rabbit IgG (H+L) secondary antibody Thermo Scientific, catalog# A21076) conjugated secondary antibody at 1 : 20,000 in diluted blocking buffer (50%) for 1 h at room temperature. After incubation with secondary antibodies, membrane was washed thrice with tris-buffered saline with 0.1% Tween 20 (VWR, catalog# 0777) and washed once with 1X PBS. Membranes were imaged and quantitated with Odyssey classic infrared imaging system (LI-COR).

5.2.13. Droplet digital polymerase chain reaction (ddPCR)

For VCaP cells, total RNA was isolated using the RNeasy mini kit (Qiagen, catalog# 74104), including on-column DNase treatment, and quantified with the Epoch plate reader (Biotek). Two (2) μg of total RNA was reverse transcribed using the high capacity cDNA reverse transcription kit (Thermo Fisher, catalog# 4368814). Random hexamers were used to prime synthesis by reverse transcriptase. For serum samples, total RNA was isolated using the miRNeasy mini kit (Qiagen, catalog# 217004). Half of the recovered RNA (7 μL) was reverse transcribed using the SuperScript VILO cDNA Synthesis Kit (Thermo Fisher, catalog# 11754050) at 42°C for 2 h.

Duplexed ddPCR for total AR and AR-V7 was conducted using the primers and probes below as indicated by Mah and co-workers.[327] Fluorophores, internal quenchers, and terminal quenchers are indicated by flanking forward slashes.

Total AR: Forward primer: 5'-GGAATTCCTGTGCATGAAAGC-3'

Total AR: Reverse primer: 5'-CGATCGAGTTCCTTGATGTAGTTC-3'

Total AR: HEX probe: / 5'-HEX / CTTCAGCAT / ZEN / TATTCCAGTG / IABKFQ-3'/

AR-V7: Forward primer: 5'-CGGAAATGTTATGAAGCAGGGATGA-3'

AR-V7: Reverse primer: 5'-CTGGTCATTTTGAGATGCTTGCAAT-3'

AR-V7: FAM probe: / 5'-FAM / CGGAATTTT / ZEN / TCTCCCAGA / IABKFQ-3'/

Reactions were performed in ddPCR SuperMix for probes (no dUTP) (Bio-Rad, catalog# 186-3023) with primers at a final concentration of 1 μM, probes at a final concentration of

250 nM, and an annealing temperature of 52°C. Reactions were analysed and quantified using the QX200 droplet reader and QuantaSoft software version 1.7.4 (Bio-Rad).

For VCaP cells treated with enzalutamide, 2 µL of 1/100 diluted cDNA was loaded for each ddPCR reaction. For serum samples, 2 µL of undiluted cDNA was loaded for each ddPCR reaction.

5.2.14. Control human male sera

Two human individual controls were used for assay development and for calibration blanks (i.e., serum without AR-V7). Herein referred to as negative human sera S and D. Blood samples were collected in Alberta, Canada on 30 June 2017. Blood was collected into BD Vacutainer serum tubes (Becton Dickinson, product# B367820), clotted (30 min), centrifuged (~ 2000 X *g* for 10 min), and then serum supernatant was drawn off. Measured total protein concentration ranged from 59 – 66 mg mL^{-1} determined by absorbance at 280 nm using NanoDrop 2000 (internally calibrated with a standard solution of concentrated aqueous potassium dichromate, ThermoFisher). Sera was stored at –80°C within 2 h of collection. Aliquots were thawed to ambient temperature (21°C) prior to use. Undiluted samples were used for SERS analyses.

5.2.15. Patient sera

Serum specimens were prospectively collected for AR-V7 status from a retrospective patient cohort. Patient sample selection was based on pre or post anti-androgen treatment of abiraterone and / or enzalutamide. All sera were collected from Alberta patients from June 2014 to December 2016 according to Standard Operating Procedures (SOP) for serum collection.[365-366] Blood was collected, processed for serum, and stored at –80°C within 2 h of collection. Measured total protein concentration ranged from 51 – 65 mg mL^{-1} determined by absorbance at 280 nm using NanoDrop 2000 (internally calibrated with a standard solution of concentrated aqueous potassium dichromate, ThermoFisher). Aliquots were thawed to ambient temperature (21°C) prior to use. Undiluted serum samples were used in SERS immunoassays.

5.2.16. Ethical statement

Anonymized archived prostate cancer patient specimens used in this study were provided by the Canadian Biosample Repository (Alberta, Canada). All prostate cancer patient specimens and normal healthy control specimens were collected as part of the Alberta Prostate Cancer Research Initiate (APCaRI) in accordance with Canadian and United States best practices for biospecimen collection.[365-368] All patients provide written informed consent and the study was approved by the scientific ethics committee in each of the following collection sites: Prostate Cancer Centre (Calgary, Alberta, Canada), Northern Alberta Urology Centre (Edmonton, Alberta, Canada), and Cross Cancer Institute (Edmonton, Alberta, Canada). Prostate cancer patient inclusion criteria were: (1) Adult

men without prior prostate cancer diagnosis who are referred to urology clinics in Alberta prostate concerns and are being scheduled for a prostate biopsy; and (2) Adult men with prior prostate cancer diagnosis who visited any of the above mentioned clinics for treatment of prostate cancer.

5.3. Results and discussion

5.3.1. Detection of AR-V7 in VCaP cell lysates by western blot and antibody validation

Currently, a source for purified AR-V7 protein is practically not available. As our ultimate goal is to detect AR-V7 in serum specimens, we surmised that AR-V7 levels in sera may vary due to various pre-analytical factors (e.g., specimen quality and specimen variability resulting from prior drug treatments, tumour heterogeneity, or disease duration) and analytical factors.[365] Thus, calibrating with sera may prove to be difficult considering variable AR-V7 expression. As an alternate approach, we started with a commonly used prostate cancer line, VCaP, which is known to express AR-V7. This approach enables more consistent expression of AR-V7 in higher abundance and with less complex matrix (i.e., lower background signals) than that of serum samples. Thus, VCaP cell lysates were used as a source of AR-V7 for our calibration experiments. To upregulate AR-V7 expression, we followed the work of Dong and co-workers wherein a combination of charcoal-stripped serum (for androgen deprivation) and enzalutamide (i.e., androgen antagonist) was administered to VCaP cells for maximum androgen blockage.[302, 361]

Maximizing AR-V7 protein expression is important for creating a broad calibration curve for our SERS-based immunoassay. For AR-V7-negative cell lysates, another well-established prostate cancer cell line (i.e., PC3) was used.

Figure 5–3 presents our Western blots using two different cell lines, VCaP and PC3 to show AR full length (AR-FL) and AR-V7 expression levels. Beta-actin protein (~ 42 kDa predicted) was used as a loading control to normalize protein expression levels (Figure 5–3). As evident in Figure 5–3A, the blot shows strong signal intensity (i.e., high abundance) for AR-FL at the predicted molecular weight of ~ 110 kDa[369] in VCaP cells for both DMSO control and enzalutamide treatments. High protein loading (70 μg well^{-1}) was necessary to reach the limit of detection for AR-V7 in Figure 5–3B, therefore the likely cause of band distortion (Figure 5–3A). PC3 cells are known to be androgen insensitive; thus we do not expect AR-FL or AR-V7 expression. Results shown in Figure 5–3A allow us to conclude that AR-FL is present in high abundance in VCaP cell lysates, our anti-AR-FL polyclonal antibodies appear to be localizing to their target, and DMSO or enzalutamide treatments are not effecting AR-FL or actin expression. The blot shown in Figure 5–3B provides evidence of AR-V7. Faint signal intensities, indicative of low protein abundance, are visible for AR-V7 in VCaP cell lysate at the predicted molecular weight of ~ 68 kDa[370] for both DMSO and enzalutamide treatments. Despite high protein loading (70 μg well^{-1}), the observed faint signal intensities suggests that AR-V7 abundance is near the limit of detection for Amersham ECL prime detection reagent (1 pg – 50 pg; depending on antibodies and image detection technique).[371] Despite low levels, we can conclude that AR-

V7 is present in our VCaP cell lysates, our anti-AR-V7 monoclonal antibodies appear to be localizing to their target, and DMSO or enzalutamide treatments appear to have an indiscernible effect on AR-V7 expression. We confirm AR-V7 quantities using more sensitive techniques described below in our ddPCR and SERS experiments. The Western blot results establish that AR-FL and AR-V7 are present in VCaP cell lysates at different levels of expression (i.e. higher AR-FL abundance than AR-V7 abundance). Confirmation of AR-FL and AR-V7 expression and relative amounts are important considerations for our SERS-based sandwich immunoassay.

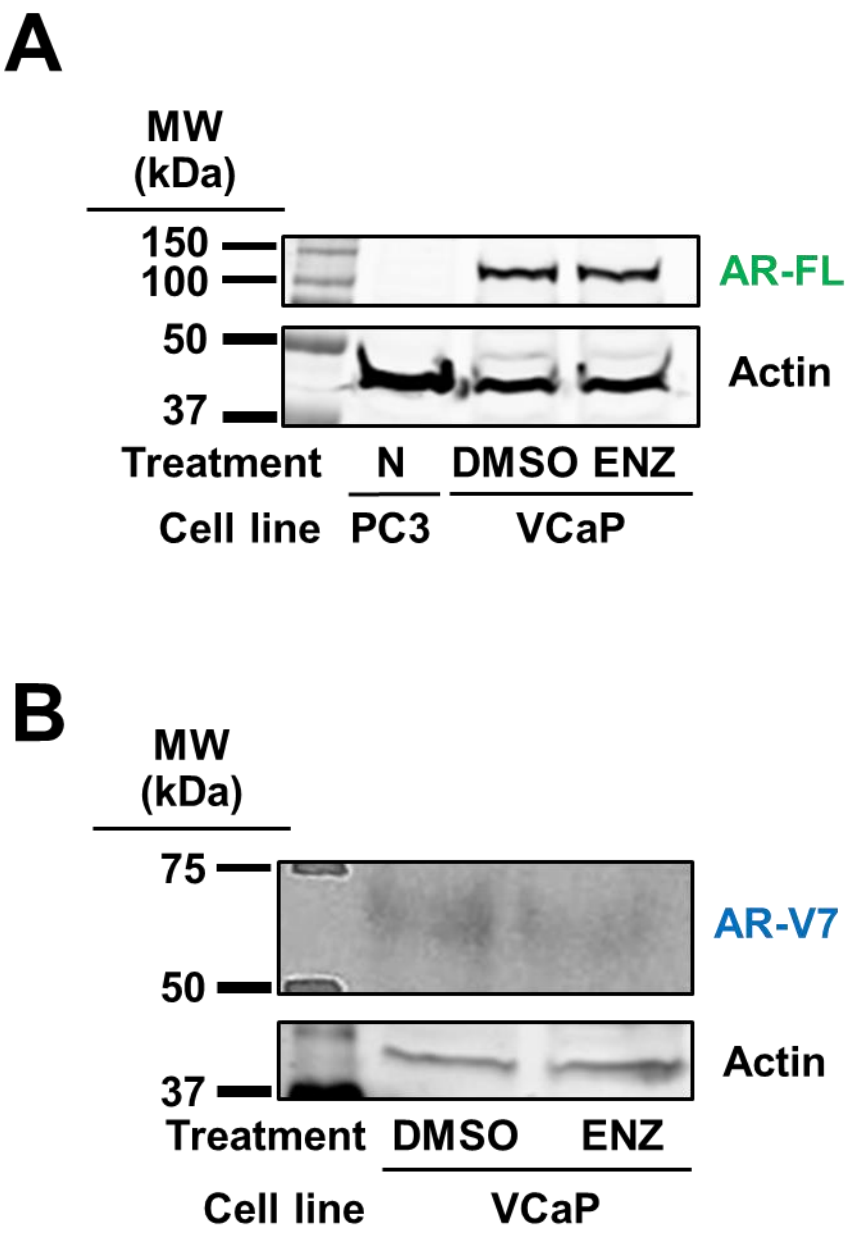

Figure 5–3. Representative Western blots of VCaP and PC3 cell lysates. VCaP cells were treated with either 0.05% DMSO or 5 μM enzalutamide (ENZ) in 0.05% DMSO for 24 h under androgen deprivation conditions. PC3 cells received no treatment (N). Beta actin used as loading control to normalize protein expression levels. (A) Blot probing for AR-FL. (B) Blot probing for AR-V7.

5.3.2. Detection of AR-V7 in VCaP cell lysates by droplet digital PCR (ddPCR)

Building on the work of Mah et al. wherein the researchers developed a ddPCR method for AR-V7 detection in circulating tumour cells of PCa patients.[327] Figure 5–4 presents our results using Mah and co-workers technique to absolutely quantify AR-V7 in VCaP and PC3 cells. We postulate correlating ddPCR results to our SERS-based immunoassay results would be beneficial in a clinical setting considering current blood-based AR-V7 detection methods rely on RNA expression.[304] Thus, to establish AR-V7 and total AR RNA expression levels in VCaP and PC3 cell lysates, we began with validating the primers, probes, and conditions described by Mah et al.[327] As evidenced in Figure 5–4, we tested the assay specificity by determining AR-V7 and total AR expression in VCaP and PC3 cells. Figure 5–4A shows ddPCR results of total AR and AR-V7 amplicon containing events (i.e., droplets) with clear separation from no target baseline events and strong PCR amplification signals specific for each probe. This establishes that our PCR probes are valid and that our amplification conditions are suitable for subsequent experiments using VCaP and PC3 cells. Figure 5–4B shows the number of transcripts detected per ng of RNA loaded that correspond to AR-V7 or total AR for VCaP and PC3 cells. For naïve VCaP cells, our results show both AR-V7 and total AR expression with a higher AR expression level relative to AR-V7 (Figure 5–4B). These results are consistent with previous reports showing VCaP cells have higher AR expression compared to AR-V7.[361, 372] PC3 cells are androgen insensitive and are not expected to express either AR-V7 or AR.[347] Figure 5–4B confirms that no signal is detected from PC3 cells. This result further supports that our PCR probes

are valid for AR-V7 and AR. Next, we analysed VCaP cells treated with DMSO control or enzalutamide (diluted in DMSO) for enhanced AR-V7 expression. Figures 5–4C and 5–4D show our results for VCaP cells and PC3 cells. For both DMSO control and enzalutamide treated cells, AR and AR-V7 are detected with similar profiles as naïve cells (Figure 5–4B). No signal was detected for PC3 cells as expected. The ratio of AR-V7 : total AR ranged from 3.1% – 3.5% for DMSO treated or enzalutamide treated, respectively. Enzalutamide-treated cells yielded slightly more AR-V7. Higher levels of AR-V7 can be achieved with longer incubation in androgen deprived media and / or longer enzalutamide exposure. As evidenced in Figures 5–4B and 5–4D, the ratio of AR-V7 : AR is higher compared to naïve cells ranging from 0.8% – 1.2%. These results are consistent with previous reports that have documented the fluctuations of AR-V7:AR depending on active AR transcription under androgen level control.[361, 372] As VCaP cells treated with enzalutamide yielded the highest ratio of AR-V7 : AR (~ 3.5%), we proceeded with this approach for the source of AR-V7 for our SERS-based immunoassay.

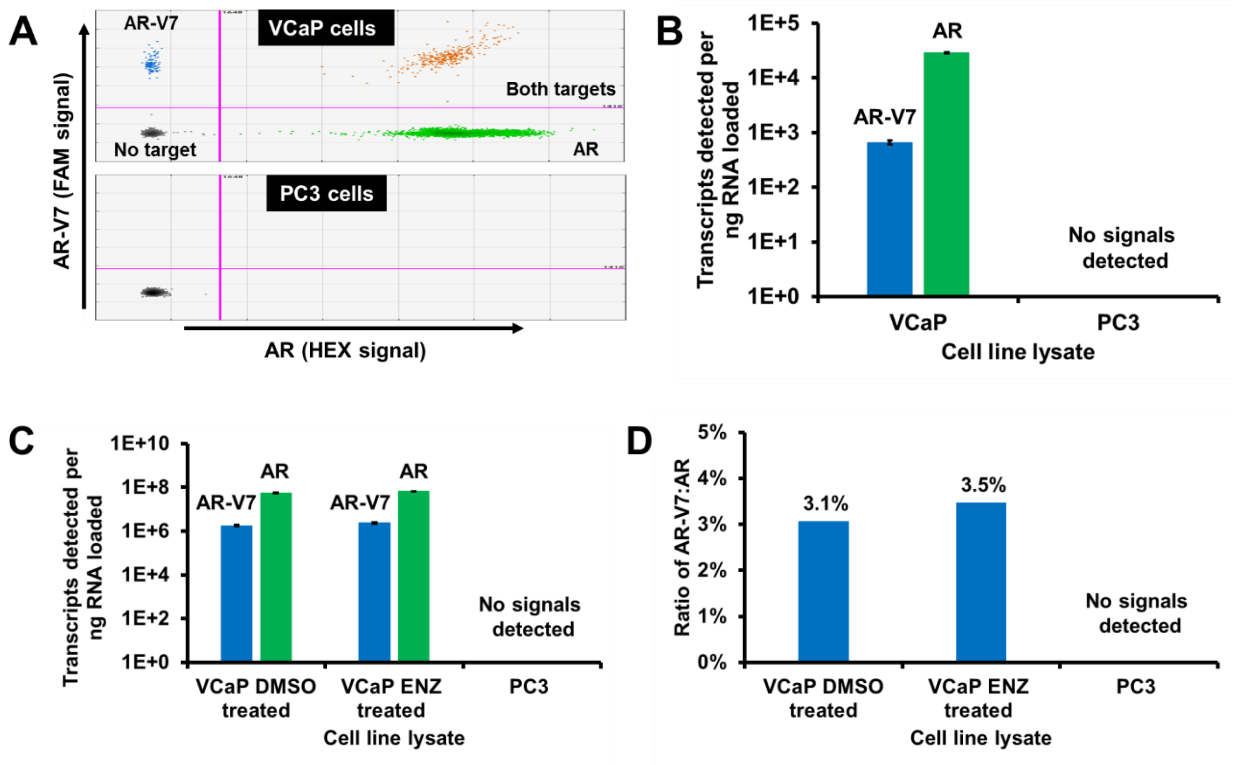

Figure 5–4. Detection of AR-V7 and total AR transcripts in VCaP and PC3 cells. (A) Two dimensional duplexed ddPCR droplet plots for AR-V7 (FAM signal) and total AR (HEX signal) in VCaP and PC3 cells. Blue dots are positive for AR-V7, green dots are positive for AR, orange dots are positive for both AR-V7 and AR, and black dots are negative (i.e., contain no target). Pink line indicates amplitude threshold set for positivity. Heat map droplet view shown. (B) Validation of AR-V7 and total AR mRNA expression. Error bars indicate 95% confidence interval for Poisson-calculated copies of transcript detected. (C) Detection of AR-V7 and total AR mRNA expression in VCaP cells treated with either 5 µM enzalutamide or 0.05% DMSO for 24 h. PC3 cells were used as a negative control for mRNA expression. Error bars indicate 95% confidence interval for Poisson-calculated copies of transcript detected. (D) AR-V7 to total AR ratio for VCaP cells treated with either 5 µM enzalutamide in 0.05% DMSO or 0.05% DMSO only for 24 h. PC3 cells were used as negative control for AR-V7 and AR.

5.3.3. Detection of AR-V7 in VCaP cell lysates by surface-enhanced Raman scattering

VCaP cell lysates collected under maximum androgen blockade conditions (i.e., charcoal-stripped serum and enzalutamide) were used as a source of AR-V7 for our SERS experiments. To generate a calibration curve for AR-V7 using SERS-based immunoassay, we measured the SERS responses of a dilution series of VCaP cell lysates. The Raman spectra and dose response plots are shown in Figure 5–5. These samples included VCaP cell lysates with total protein up to 1.6 mg mL^{-1} and a 1X PBS blank (0 mg mL^{-1}). Our Raman plot presented in Figure 5–5A highlights two important points. First, all observable spectral features are assigned to the chemical groups of the mixed monolayer of Raman active MBN molecules on B-ERLs (i.e., ν_s(C≡N) at 2221 cm^{-1} and aromatic ring breathing mode ν_s(C–C) at 1582 cm^{-1}).[75] None of the vibrational modes of the bioconjugation reagent (DTSP), the capture antibodies, or other lysate components on the capture substrate are detectably enhanced. Second, there is no measureable evidence of B-ERL adsorption in the spectrum for the blank (negative) control (64 ± 3 counts; n = 3). This value for B-ERL adsorption is consistent with the instrument noise level of 59 ± 3 counts (n = 3) and therefore can be considered negligible.

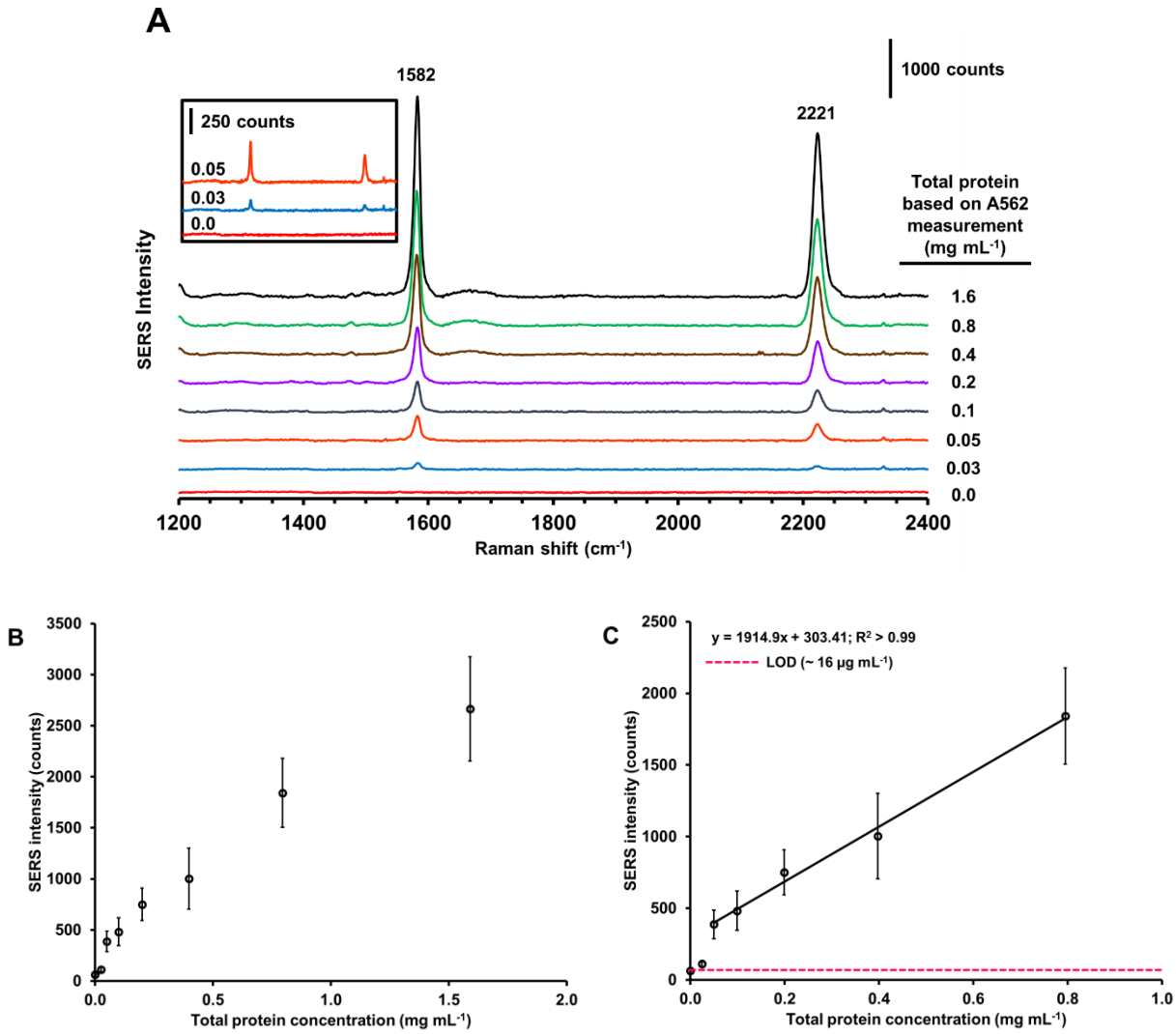

Figure 5–5. SERS-based immunoassay results of AR-V7 detection in VCaP cell lysates treated with 5 µM enzalutamide in 0.05% DMSO for 24 h. (A) Raman spectra resulting from VCaP cell lysates (0.0 – 1.6 mg mL^{-1} total protein concentration). Spectra are offset vertically for visualization. Each spectrum represents an average of 50 spectra collected from a sample concentration. (B) Dose–response plot from triplicate calibration assays for AR-V7 from 0.02 mg mL^{-1} to 1.6 mg mL^{-1} and a negative control (1X PBS buffer). (C) Lower range of the calibration curve showing the linear fit from 0.05 mg mL^{-1} to 0.8 mg mL^{-1} (y = 1914.9x + 303.41; R^2 = 0.9935). The LOD is estimated to be ~ 16 µg mL^{-1} determined by the signal of the blank sample plus three times its standard deviation. The signal at the cut-off for the LOD is indicated by the dashed pink line. Data points in (B) and (C) represent an average and standard deviation of the peak height of the ν_s(C≡N) at 2221 cm^{-1} resulting from the measurement of 50 different locations for each sample of triplicate substrates.

The dose-response plots for AR-V7 in VCaP cell lysates under maximum androgen blockade are shown in Figures 5−5B and 5−5C. These results were generated by plotting the intensity of ν_s(C≡N) at 2221 cm^{-1} as a function of total protein concentration (0.02 – 1.6 mg mL^{-1}). We present AR-V7 content as total protein concentration in cell lysates since the level of AR-V7 in cell lysates was not known. However, we address this issue further below in context of ddPCR analysis. Each calibration point represents an average signal from 50 different locations per sample in triplicate. We tracked the nitrile ν_s(C≡N) stretch at 2221 cm^{-1} for two major reasons: (1) in Chapter 4 we demonstrated that $\nu_s(NO_2)$ based Raman reporters (e.g., 4-Nitrobenzene thiol) are not suitable with AgNPs due to photocatalytic effects;[263, 265] (2) the ν_s(C≡N) is strong, sharp, and easily identifiable in a relatively quiet region of the spectrum.[276] Tracking a vibrational feature in a quiet region (i.e., few molecules with vibrational modes between 2000 cm^{-1} and 2400 cm^{-1}), reduces other organic constituents of the colloidal nanoparticle suspension to mask Raman reporter molecules.[276, 278] Moreover, previous reports have described spectral interferents between 300 cm^{-1} – 1700 cm^{-1} such as hypoxanthine (product of purine degradation from blood cellular components)[81] and anti-coagulants (i.e., Li-heparin, EDTA, and citrate) used in blood collection.[373] Thus, when selecting Raman reporters, we suggest to consider vibrational features, chemical interaction with nanomaterials, and sample matrix. We found using MBN for serum to be advantageous.

At low levels of AR-V7 (0.05 mg mL^{-1} – 0.8 mg mL^{-1}), the SERS response follows a linear dependence and then begins to level off at a high concentration (1.6 mg mL^{-1}) as

shown in Figure 5–5B. At higher concentrations, levelling off is attributed to binding sites on the capture substrate approaching saturation (Figure 5–5B). The linearity ($R^2 > 0.99$) from 0.02 mg mL^{-1} – 0.8 mg mL^{-1} range is evident in Figure 5–5C. The limit of detection (LOD) is defined as the analyte concentration that produces a signal corresponding to the blank sample signal plus three times its standard deviation.[290, 337] We report the LOD of AR-V7 to be 72 counts, which would translate to ~ 16 μg mL^{-1} total protein in VCaP cell lysates.

The standard deviation shown by uncertainty bars in Figure 5–5C were calculated from the average intensities of three separate assays (50 locations per solution concentration per assay). Measurement uncertainty provides an indication of reproducibility and variability across the capture surface. We report an inter-assay relative standard deviation (RSD) of ~ 23% (n = 3), with lower %RSD values at higher concentrations (≥ 0.8 mg mL^{-1}) and higher %RSD values at lower concentrations (≤ 0.1 mg mL^{-1}). This trend is consistent with previous reports that described the variability of SERS signal in context of statistical sampling, wherein the RSD value decreases as the number of counts increases.[34, 337] We report our intra-assay precision to be ~ 10% (n = 2) accounting for all solution concentrations. An important aspect to consider is the stochastic distribution of AR-V7 molecules on the capture substrate. As a result, depending on the relative abundance within a sample, the capture surface is expected to be inherently heterogeneous. Our assertion is consistent with previous SERS-based surface immunoassays targeting a pancreatic marker MUC4[337] and a tuberculosis marker

mannose-capped lipoarabinomannan,[290, 339] both typically in native low abundance (ng – μg mL^{-1} quantities).

An indirect approach to investigate AR-V7 abundance and distribution on the capture substrate is to observe B-ERL binding density and distribution by SEM. Figure 5–6 shows a representative image for the highest solution concentration of VCaP cell lysate tested (1.6 mg mL^{-1}). In contrast, Figure 5–7 shows a representative image our blank sample (1X PBS buffer). Figure 5–6 shows several individual ~ ø30 nm spherical AgNPs along with some noticeably aggregated nanoparticles. One important aspect to consider when examining SEM images is that the samples were imaged after drying. As such, a previous report described that aggregation may be induced by solvent evaporation.[374] This may explain the presence of some dimers, trimers, or more seen in the SEM image (Figure 5–6). The large clusters in Figure 5–6 are unidentified, however we suspect they may be cellular debris, salt crystals, or dust particles. Density of B-ERLs will be governed by the number of analyte (e.g., AR-V7) molecules captured, which depends on the binding strength between the immobilized capture agent and analyte.[30] Though density of B-ERLs seen in Figure 5–6 may appear low, we observe an appreciable signal to noise SERS intensity (~ 2600 counts) (Figure 5–5). Though data are not shown for other solution concentrations, our results were consistent with previous reports showing surface coverage of nanoparticles on SERS capture substrate is proportional to analyte abundance.[30, 337] Figure 5–7 shows a representative SEM of our blank sample for our VCaP

cell lysate experiments. Absence of B-ERLs binding observed indicate a low level of non-specific binding between the capture antibodies and detection antibodies.

Considering disease biomarkers can be in low abundance and spatial orientation of immobilized capture antibodies, we found sampling a larger surface area to be beneficial for greater accuracy and precision.[152] We used a ~ 2 μm diameter circular laser spot size and sampled 50 different locations in triplicate. The random distribution of B-ERLs on the capture surface seen in Figure 5–6 can also be explained by the spatial orientation of the immobilized antibodies. Dong and Shannon previously demonstrated ~ 23% of immobilized antibodies on a capture substrate were effective in target binding.[375] This level of activity was attributed to the steric effect with respect to the spatial orientation of the capture antibodies and / or to denaturation due to interactions with the surface substrate.[375-376] Moreover, distribution of accessible lysine residues on the antibody surface indicates that an immobilized antibody can have a distribution of orientations.[376]

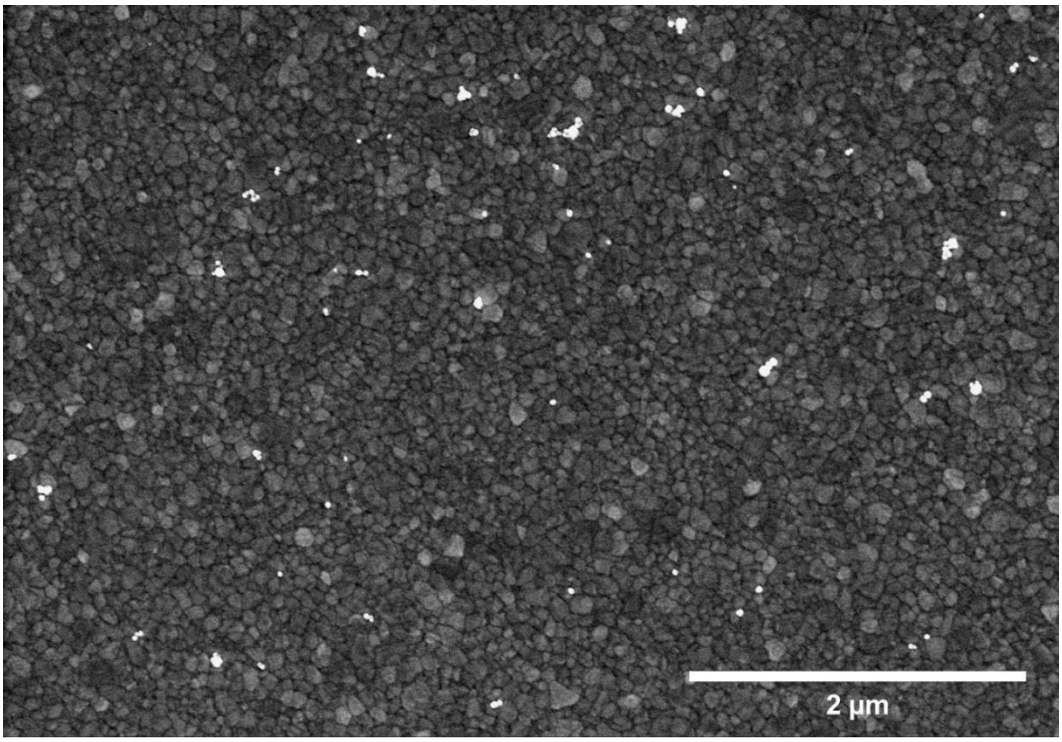

Figure 5–6. Representative scanning electron micrograph of a SERS immunoassay substrate for AR-V7 at a high concentration of VCaP cell lysate (1.6 mg mL^{-1} total protein concentration). Bright white circular features in the micrograph are consistent with ~ ø30 nm AgNP to produce biogenic ERLs. For Raman spectroscopy, 2 µm laser spot size used for interrogation.

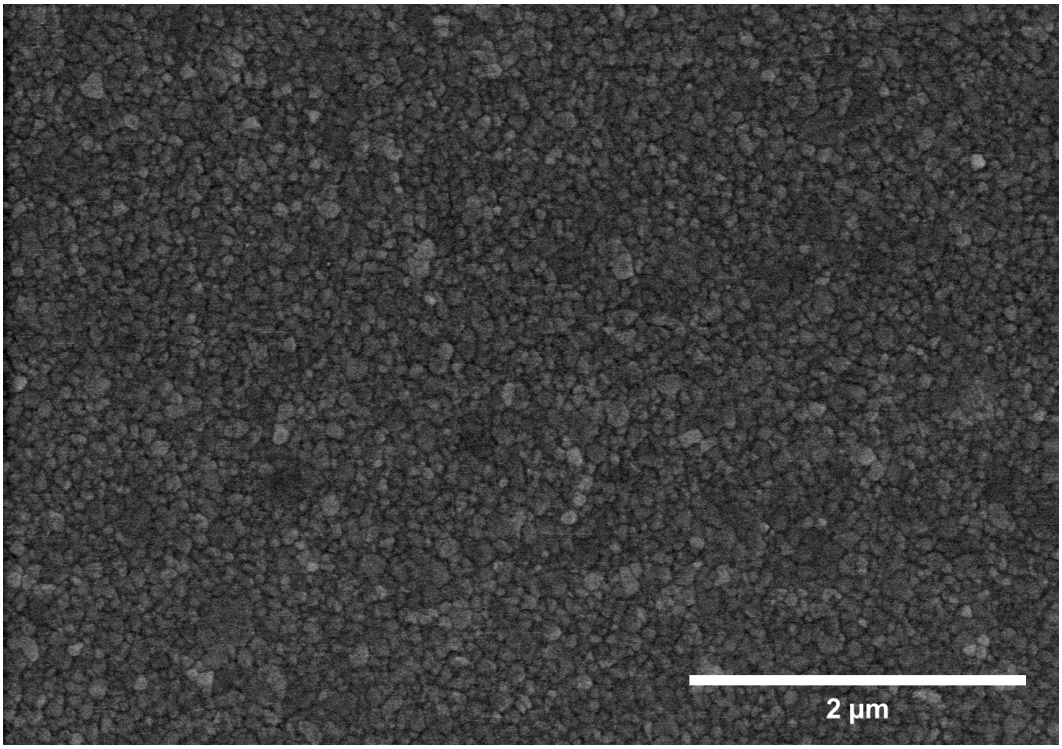

Figure 5–7. Representative scanning electron micrograph of a SERS immunoassay substrate for a blank sample (PBS buffer, 0 mg mL^{-1} total protein concentration). For Raman spectroscopy, 2 µm laser spot size used for interrogation.

Currently, there is no AR-V7 standard reference material for determining the concentration of AR-V7 in cell lysates. Furthermore, a clinical reference range for AR-V7 is unknown. In Figure 5–8, we address the issue of quantifying AR-V7 expression with greater accuracy and propose a reference for clinical application by correlating our SERS-based protein measurements with our ddPCR-based RNA measurements. The plot shown in Figure 5–8 was generated by starting with a culture of VCaP cells under androgen deprived conditions and treated with enzalutamide (Figure 5–8 inset). Known proportions of cells were used for RNA determination (ddPCR) and for protein determination (SERS) followed by separate cell lysis. This allowed for relative comparison of SERS and ddPCR

results. Based on our SERS response for each solution concentration from 0.0 mg mL^{-1} – 0.8 mg mL^{-1}, we calculated the amount of RNA present in the volume of solution delivered to the capture surface (3 μL spot volume; 1% of total lysate volume). RNA content was derived by interpolating a single RNA measurement representing the total cell input (~ 4.7 x 10^6 transcripts/ng RNA). In Figure 5–8, our results show a linear dependence ($R^2 > 0.99$) between 1.0 x 10^3 transcripts/ng RNA – 1.6 x 10^4 transcripts/ng RNA based on 90 ng – 2400 ng total protein deposited on the substrate. We calculated total protein deposited on the substrate by taking the protein solution concentration and multiplying by the spot volume (3 μL). As expected, we observe an increase in AR-V7 signal intensity with increasing protein solution concentrations of VCaP cell lysate. Thus, our results offer a method to calibrate AR-V7 expression at both RNA and protein levels within linear range between 1.0 x 10^3 transcripts/ng RNA (90 ng total protein deposited) – 1.6 x 10^4 transcripts/ng RNA (2400 ng total protein deposited). A closer examination of amount of RNA analysed (1 ng), reveals an important point that considers the inherent tumour cell heterogeneity that exists within prostate cancer cells. Based on a commonly used estimate of one mammalian cell contains approximately 10 – 30 pg of total RNA,[327] our approach takes into account cellular heterogeneity by analyzing 10,000 – 30,000 cells. Thus, measuring AR-V7 in a patient with a heterogeneous tumour background may account for inherent fluctuations in the biological disease state. Thus, our SERS-based detection assay has high specificity, sensitivity, and is reliable for advanced PCa patient samples.

Selection of biomarker expression level (e.g., nucleic acid versus protein) have trade-offs such as abundance, disease specificity, detection challenges, and clinical relevance.[315] More details on analytical biomarker selection can be found in Byrnes and Weigl's review.[315] Although eight blood-based AR-V7 detection methods are currently documented with most (seven) relying on RNA expression,[304] we agree with Byrnes and Weigl that protein levels of AR-V7 are a closer reflection of the disease state and provides higher specificity for disease activity.[315] Hence, detection of AR-V7 protein would be impactful in a clinical setting.

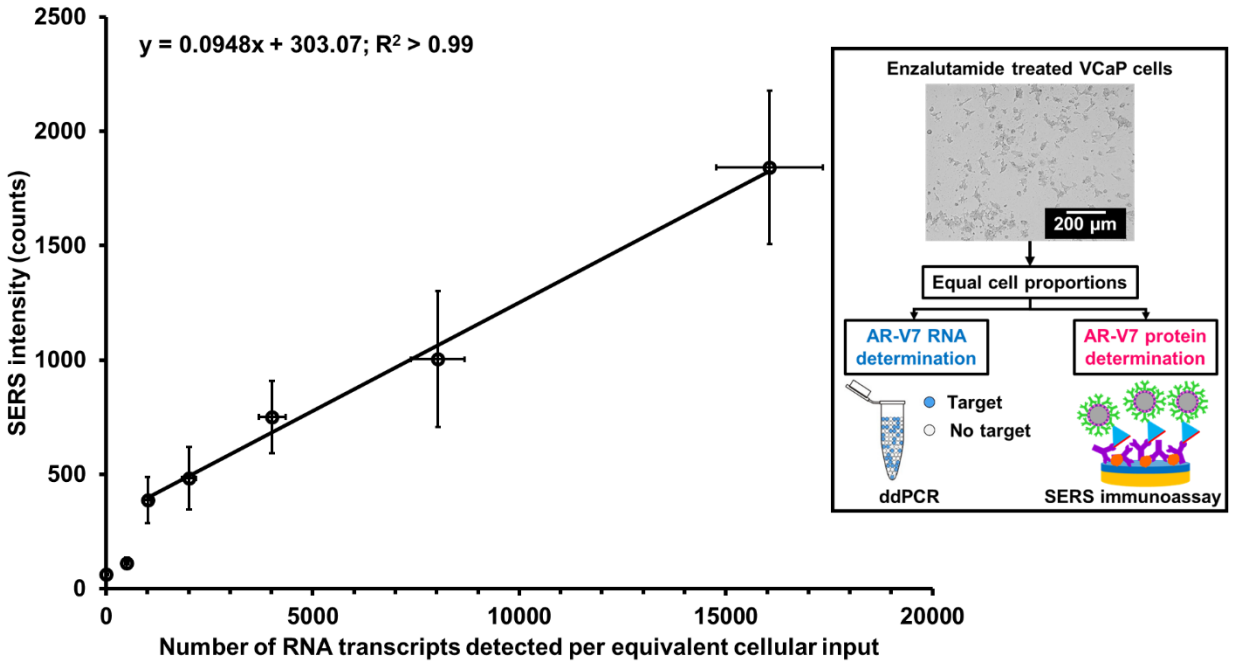

Figure 5–8. Calibration plot correlating SERS-based immunoassay results for AR-V7 protein and ddPCR results for AR-V7 mRNA expression from VCaP cells treated with enzalutamide shown in the inset scheme. mRNA expression level was calculated by interpolating the total AR-V7 mRNA expression level for the equivalent cell proportion and calculating the mRNA content with the sample spot volume (3.0 µL) delivered to the SERS capture substrate. The linear fit is for between 1004 – 16,058 transcripts loaded ($y = 0.0948x + 303.07$; $R^2 = 0.9935$). X-axis error bars indicate 95% confidence interval for Poisson-calculated copies of transcript detected. Data points represent the average and standard deviation (Y-axis) of the peak height of the ν_s(C≡N) resulting from the measurement of 50 different locations on each sample of triplicate substrates.

5.3.4. Detection of AR-V7 in clinical serum specimens

Our encouraging VCaP cell lysate results led us to prospectively pilot our SERS-based sandwich immunoassay using sera collected from a retrospective cohort of mCRPC patients. We analysed seven mCRPC patients (identifiers #46, #102, #112, #123, #1667, #2825, and #2848) and two healthy male controls (identifiers S and D). Selection of mCRPC patients were principally based on anti-androgen therapy with serum samples

collected either pre or post anti-androgen therapy. Our study includes patients treated with either enzalutamide, abiraterone, or both therapies. Table 5–1 provides a short clinical history of each patient at diagnosis and provides a prognostic overview to assess clinical risk level.[300] As Table 5–1 lists, age at diagnosis ranges from 55 – 87 years, with broad PSA levels ranging from 2.4 ng mL^{-1} – 135.5 ng mL^{-1}, and Gleason scores at diagnosis ≥ 7 indicative of poor prognosis.[377-378] Clinical staging reveals two patients (#112 and #123) had more severe metastasis (i.e., bone(s)), whereas others (e.g., #46) had less severe spread among the patients sampled (Table 5–1). Two patients (#112 and 123) were exposed to chemotherapy. All other patients were chemotherapy-naïve.

Figures 5–9 to 5–11 presents our SERS immunoassay results for seven CRPC patients and the two healthy male controls. Figure 5–9 summarizes our SERS measurements for all CRPC patients by using a histogram to represent the average signal intensity at ν_s(C≡N) at 2221 cm^{-1} for each specimen, and includes a threshold marker (dashed pink line) for the LOD (135 counts) for the SERS assay. Figure 5–10 shows the corresponding Raman spectra for all CRPC patients before and after anti-androgen treatment and the two control males. Figure 5–11 shows a histogram representing the two control males with a threshold marker (dashed pink line) for the LOD.

Table 5–1. Characteristics of prostate cancer cases at diagnosis, anti-androgen therapy, and blood sample collection

Patient ID	Age @ diagnosis	Prostate specific antigen level @ diagnosis (ng mL^{-1})	Gleason score @ biopsy[a]	Clinical stage @ diagnosis[b]	Anti-androgen type	Pre or post anti-androgen	Anti-androgen start date	Blood sample collected on
46	58	2.4	9	T2b, N0, MX	Abiraterone	Post-abiraterone (23 months)	8/27/2014	7/24/2016
102	87	19.8	9	N/A[d]	Abiraterone	Post-abiraterone (<1 month)	10/27/2014	11/12/2014
112	58	135.5	9	T2a, N1, M1b	1) Abiraterone; 2) Enzalutamide	Post-abiraterone and pre-enzalutamide	1) 8/28/2014; 2) 3/10/2016	1) 11/18/2014; 2) 11/17/2015
123	63	14.8	7	T2c, NX, M1b	Enzalutamide	Pre- and post-enzalutamide	10/2/2015	1) 1/5/2015; 2) 1/15/2016
1667	87	13.8	9	N/A[c]	Abiraterone	Pre- and post-abiraterone	6/28/2016	1) 11/17/2015; 2) 2/16/2017
2825	65	26.4	9	T2c, NX, M1	Enzalutamide	Pre-enzalutamide	3/8/2017	9/14/2016
2848	55	36.8	8	T3, N1, M0	1) Enzalutamide; 2) Abiraterone	Pre- and post-enzalutamide/ abiraterone	1) 4/13/2017; 2) 6/14/2017	1) 10/4/2016; 2) 10/10/2017

[a] Gleason values reported are sum total.
[b] Based on American Joint Committee on Cancer TNM classification to provide prognostic value.[379] T = extent of the primary tumour, N = extent of spread to lymph nodes, M = presence of distant metastasis. X = not assessed; 0 = not detected.
[c] Not applicable. Prostate cancer diagnosis confirmed after transurethral resection of the prostate (TURP) examination.

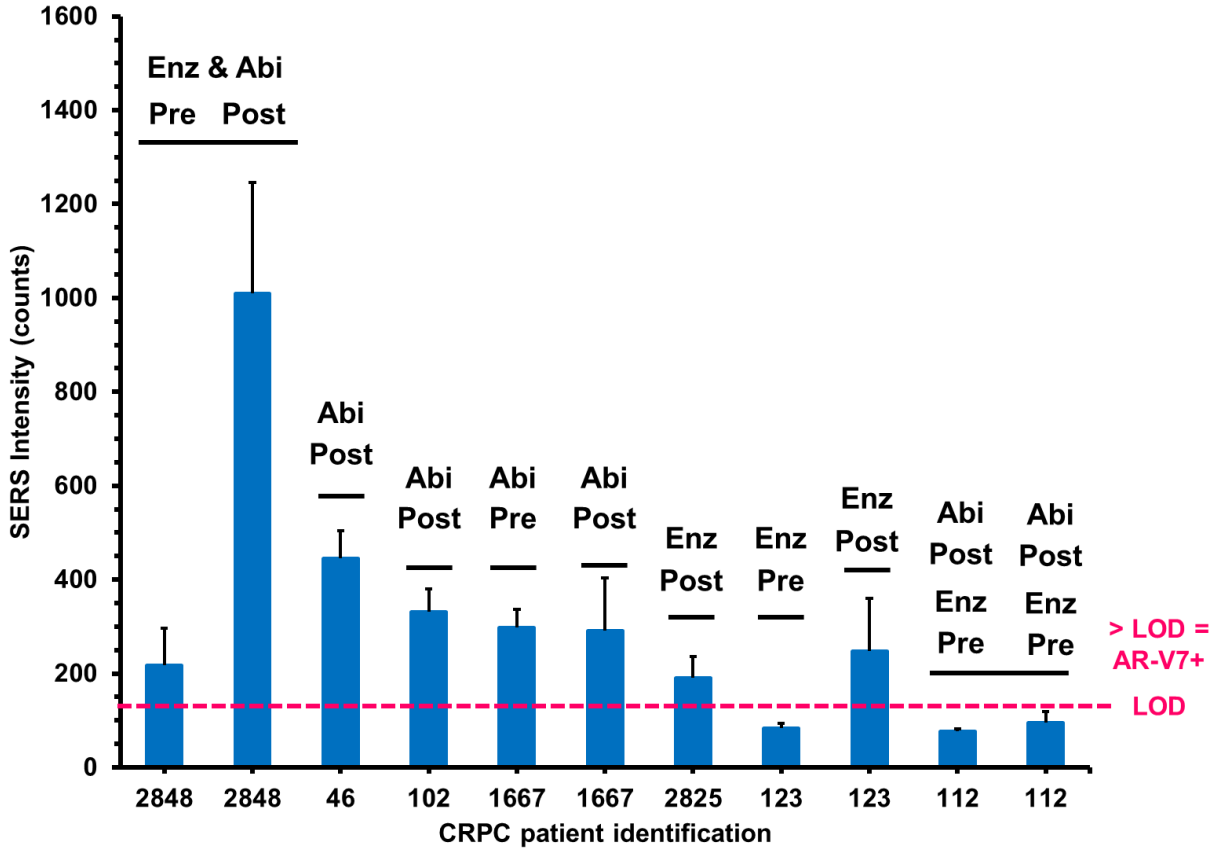

Figure 5–9. Results of SERS analyses of castration-resistant prostate cancer patient sera for the quantitation of AR-V7. The pink dashed line represents the SERS LOD of 135 counts. The average SERS signal intensity is calculated from the peak height of the ν_s(C≡N) at 2221 cm^{-1} from baseline-corrected SERS spectra collected from 50 different locations for each specimen in triplicate. All error bars represent the standard deviation of triplicate measurements. Enz = enzalutamide; Abi = abiraterone; pre = pre therapy; post = post therapy. Above LOD (> LOD) indicates positive AR-V7 status.

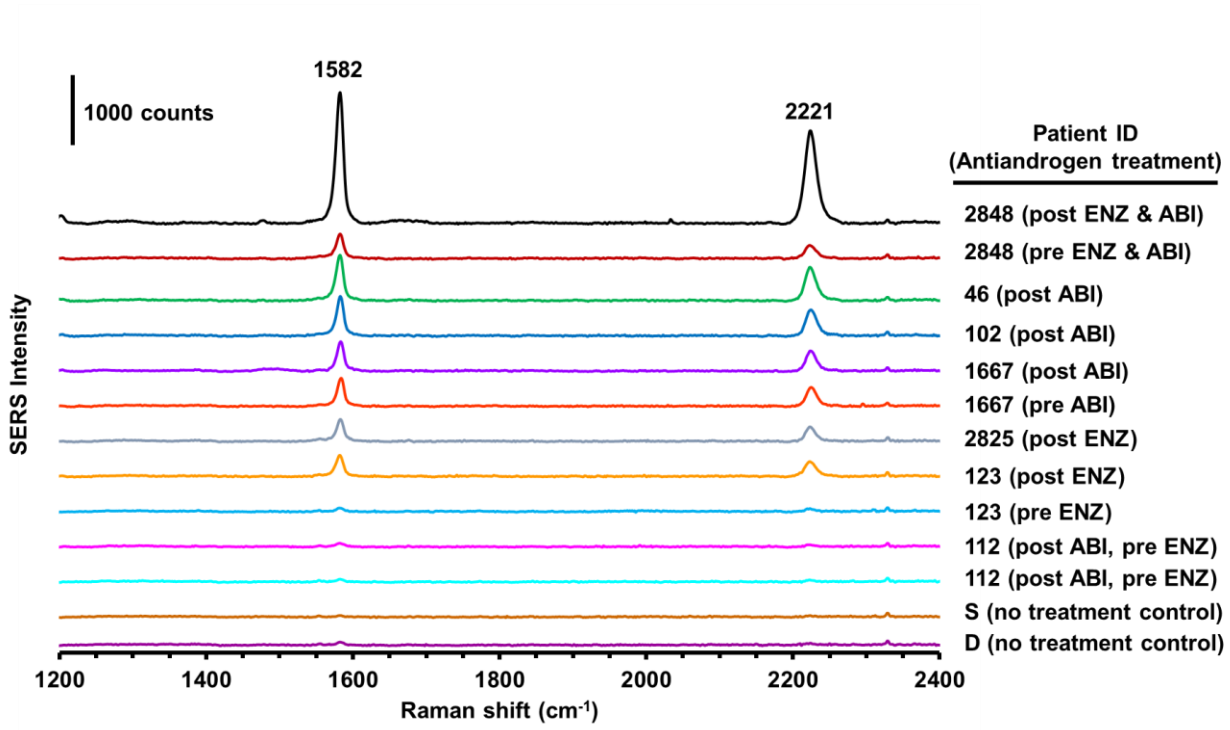

Figure 5–10. Representative Raman spectra from metastatic castration-resistant prostate cancer and healthy male patient sera. Specimens S and D are control healthy male serum specimens with no treatments. All other specimens are mCRPC patients. Specimens #112 and #123 (pre ENZ) are below the LOD. Two spectral features assigned represent the characteristic ν_s(C=C) ring breathing mode at 1582 cm^{-1} and the ν_s(C≡N) at 2221 cm^{-1} for the Raman active molecule mercaptobenzonitrile. ENZ = enzalutamide; ABI = abiraterone; pre = pre therapy; post = post therapy.

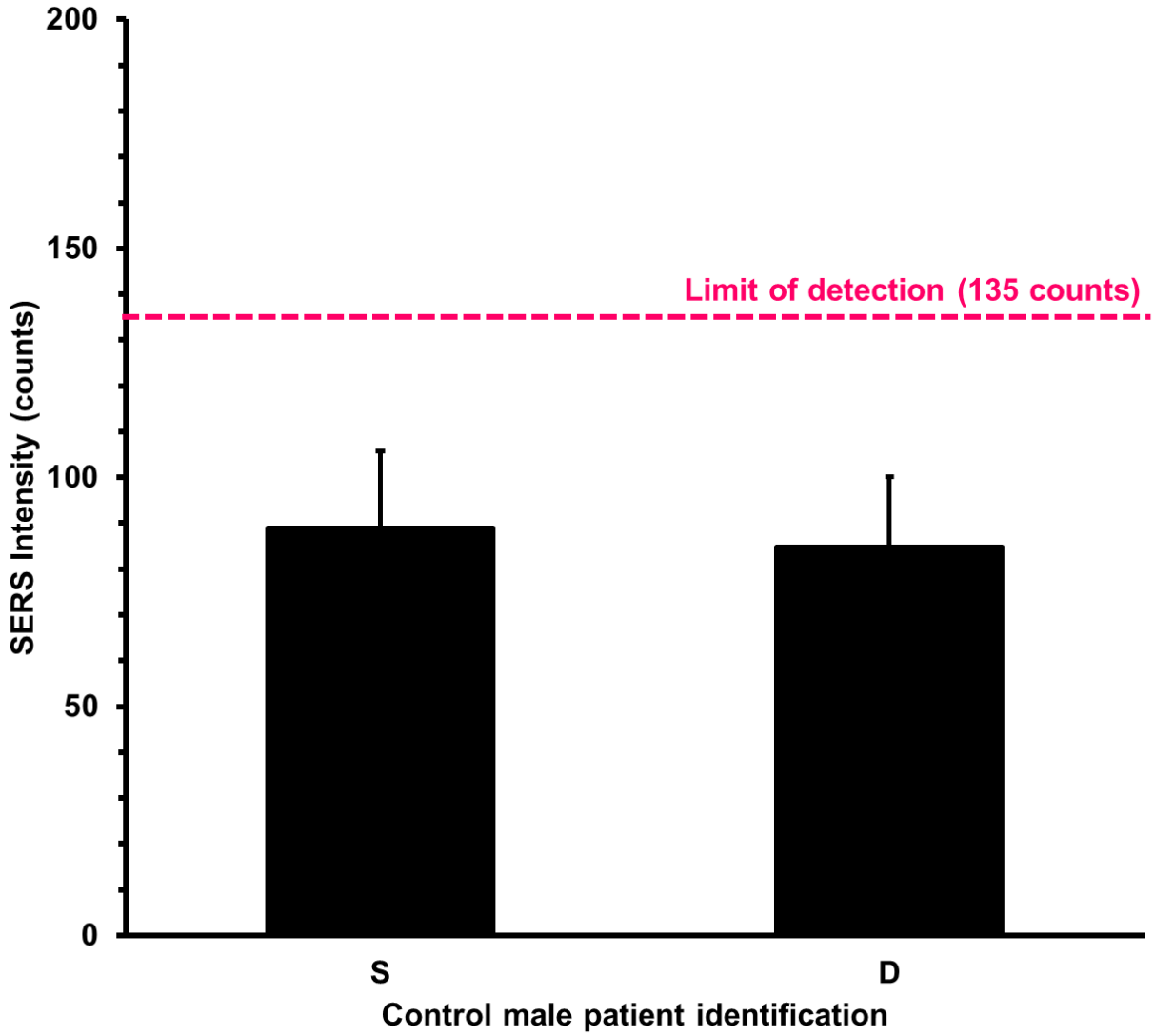

Figure 5–11. Results of SERS-based immunoassays of control healthy male serum for quantitation of AR-V7. The pink dashed line represents the SERS LOD of 135 counts. The average SERS signal is calculated from the peak height of the ν_s(C≡N) at 2221 cm^{-1} from baseline-corrected SERS spectra collected from 50 different locations for each specimen in triplicate samples. All error bars represent the standard deviation of triplicate measurements.

As seen in Figure 5–9, AR-V7 was detectable in six out of seven CRPC patients. AR-V7 was not detectable for one CRPC patient (#112) or in the two control specimens (Figure 5–11). One patient (#123) had an undetectable level of AR-V7 prior to enzalutamide therapy and then detectable levels post therapy. As such, we included patient (#123) has having a detectable level of AR-V7 post-enzalutamide treatment. An interesting finding with this patient (#123) is that our assay is able detect AR-V7+ conversion[380] (AR-V7- → AR-V7+) ~ 3 months after enzalutamide treatment (Table 5–1).

Further analysis of Figure 5–9, AR-V7 detection ranges from 191 ± 45 counts (#2825, post-enzalutamide) to 1009 ± 237 counts (#2848, post-enzalutamide and abiraterone). Only two specimens (#2848 and #46) fall within our linear range (Figure 5–8). Thus, we report 7448 ± 2503 copies of RNA/ng for specimen #2848 post-enzalutamide / -abiraterone (SERS intensity 1009 ± 237 counts) and 1509 ± 605 copies of RNA/ng for specimen #46 (SERS intensity 446 ± 57 counts) by using our linear regression equation. As a separate experiment, we attempted to quantify AR-V7 mRNA expression using ddPCR directly from patient sera. This approach failed due to RNA degradation likely due to endogenous RNAases seen in Figure 5–12. Detection of AR-V7 in blood specimens using ddPCR is possible, however specialised collection tubes (e.g. PAXgene[381] or Streck cell-free BCT tubes[382]) are necessary to stabilise RNA or maintain cellular integrity prior to processing. We found our preliminary negative ddPCR results of sera adds support to the utility of a SERS-based immunoassay.

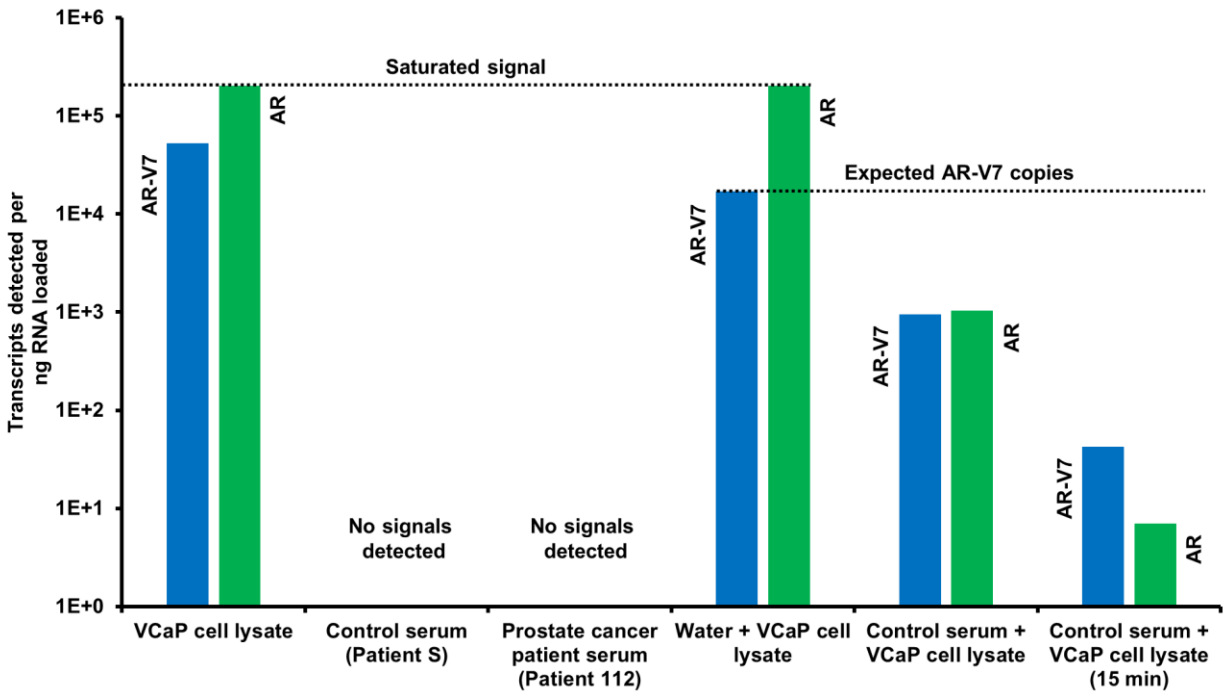

Figure 5–12. Effect of serum samples spiked with VCaP cell lysate on AR-V7 and total AR mRNA expression levels.

In analysing our SERS immunoassay results, many of our serum specimens are below our linear range, yet they are above our detection limit. Hence, AR-V7 status would be positive above the LOD. Positive or negative status reporting is consistent with the current two clinically approved assays that rely on AR-V7 mRNA or AR-V7 protein detection that report the status of AR-V7 as either positive or negative.[323, 332-333] As no clinical reference ranges are presently defined, a binary AR-V7 status report aims to provide prognostic information and to guide treatment selection. The Canadian Urologic Association and American Society of Clinical Oncology guidelines for management of mCRPC patients indicates four systemic therapies: enzalutamide, abiraterone, docetaxel, and cabazitaxel until disease progression to bone(s).[313, 383] Optimal sequencing of these systemic therapies is unknown and remains a major challenge.[332] Thus, our SERS-based approach will be useful to guide treatment selection by predicting a treatment response in the clinic. A blood-based AR-V7 immunoassay will allow rapid triaging to determine treatment course with either androgen signaling inhibitors (e.g., abiraterone or enzalutamide) or taxane-based chemotherapy (e.g., docetaxel, cabazitaxel) for mCRPC patients. As AR-V7 protein expression has been correlated with poor patient prognosis,[323] our approach to detect AR-V7 and relate to RNA expression with provide enhanced prognostic value and improve overall survival by bypassing AR-directed agents and proceeding directly to other systemic therapies (e.g., docetaxel, cabazitaxel, radium 223, sipuleucel-T). Antonarakis and co-workers have documented that taxane-treated AR-V7+ patients had improved overall survival that AR-V7+ patients treated with AR-directed therapies; no difference was observed for AR-V7- patients.[322] Recently, National Comprehensive Cancer Network (NCCN) prostate cancer guidelines[384] now suggests that

AR-V7 testing can be considered and may play a role in guiding therapy selection in for (metastatic) CRPC patients. At this time, the NCCN guidelines suggests AR-V7 testing and has not established a recommendation.[332]

Our results show a trend that AR-V7 signal increases post-enzalutamide and / or abiraterone therapy consistent with a previous study.[323] In two patients (#1667 and #112), the change in signal is indistinguishable post anti-androgen therapy. For this patient, another mechanism for AR-directed therapeutic resistance is likely responsible. Examples of other mechanisms include, AR overexpression, AR mutation, AR activation by other signals, and non-AR pathways.[314] The highest signal change is evident from a patient treated with both abiraterone and enzalutamide (#2848). As PSA level is often used an intermediate end point, we found an interesting correlation. Patient #112 had the highest PSA level at diagnosis (135 ng mL^{-1}), yet had an undetectable level of AR-V7 despite abiraterone treatment. Patient #46 had the lowest PSA level at diagnosis (2.4 ng mL^{-1}) and had a higher level of AR-V7 within our cohort. Though this finding is retrospective, it suggests that PSA levels may not be positively correlated with AR-V7 expression. This observation is consistent with Qu and co-workers report stating that AR-V7 expression is inversely associated with serum PSA level at diagnosis.[319] Though PSA level is a relatively simple and a low cost measurement, we suggest PSA levels should not be a primary intermediate end point to assess enzalutamide or abiraterone effectiveness. Other intermediate endpoint measures used in conjunction with PSA tests to monitor progression-free survival are imaging diagnostics such as computerized tomography using

X-rays,[385] radionuclide bone imaging with bone indexing,[386] or multi-parametric magnetic resonance imaging.[387] We conclude that our results demonstrate the ability to detect and quantify AR-V7 levels in castration-resistant prostate cancer patient sera. Furthermore, we provide a calibration results to correlate protein and RNA levels of expression.

Our conclusion is supported by the results of our blank sera or normal healthy male control specimens shown in Figure 5–11. For our SERS experiments using clinical specimens, we used undiluted, non-sterile, normal male sera (specimens S and D) as our blank specimens. These specimens are not expected to contain AR-V7, however AR expression is expected, so effective blocking is crucial. Figure 5–11 shows SERS measurements by using a histogram to represent the average signal intensity at ν_s(C≡N) at 2221 cm^{-1} for each specimen, and includes a threshold marker (dashed pink line) for the LOD (135 counts). As the LOD is calculated as the signal response for the blank sample plus three times its standard deviation, we took the average of the two specimens for the resulting LOD value to account for biological variability. For example, amount of large globular proteins, lipids, carbohydrates, or microbial attributes can influence non-specific binding of the B-ERLs. Based on our results, we conclude the capture substrate has a low degree of non-specific binding, relative signal intensities for both control serum specimens are indistinguishable (89 ± 17 counts for control S and 85 ± 15 counts for control D), and are 1.5X – 1.6X lower than the LOD. Our conclusion is further supported by our SEM images shown in Figure 5–13. For both healthy control patients, negligible B-ERLs binding observed indicates the effectiveness of the blocking agent (3% BSA/0.05% Tween 20).

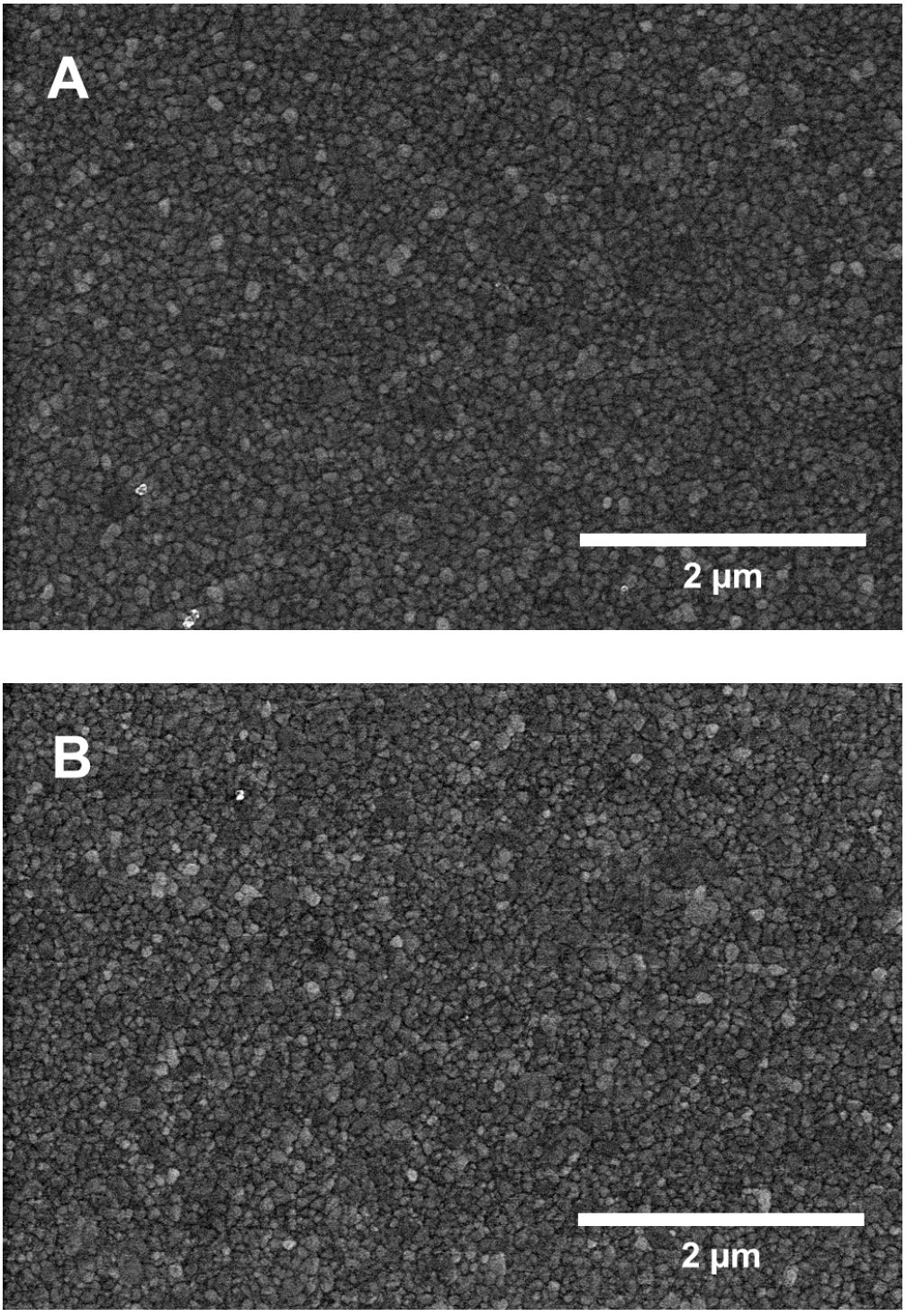

Figure 5–13. Representative scanning electron micrographs of SERS-based immunoassays of undiluted healthy normal male (serum blank) specimens. (A) Patient S (B) Patient D. For Raman spectroscopy, 2 µm laser spot size used for interrogation.

A crucial component of any SERS immunoassay is the blocking agent used to minimize non-specific binding of non-target molecules. The importance of this aspect is strongly emphasized when working with bio-specimens with a complex background matrix (e.g., blood serum). To further challenge, most clinically relevant biomarkers are in substantially lower abundance than other normal physiological proteins (e.g., albumin). In our assay design, we use anti-AR-V7 specific mAbs for our capture substrate and anti-AR-FL pAbs for detection due to a limited commercial supply of anti-AR-V7 antibodies available. Consequently, it is important to be aware of AR-FL expression in normal male serum specimens (i.e., blank control). Based on our ddPCR experiments using VCaP cells, the ratio of AR-V7 : total AR is 3.5%. Mah and co-workers report an AR-V7 : total AR range of 0.6% – 2.5% in blood samples of CRPC patients analysed with ddPCR.[327] Thus, accurate determination of AR-V7 is largely dependent on effective blocking when working biomarkers in low abundance. To optimize blocking, we evaluated several different blocking reagents and exposure times. We present our SERS immunoassay results in Figure 5–14 showing two reagents, starting block (ThermoFisher, commonly used for SERS-based immunoassays) and 3% BSA/0.05% Tween 20 for both control specimens. For both specimens, 3% BSA/0.05% Tween 20 resulted in very low levels of non-specific adsorption in contrast with starting block showing spectral features of mercaptobenzonitrile (ring breathing, ν_s(C–C), 1582 cm^{-1} and ν_s(C≡N), 2221 cm^{-1}). No spectral features from the blocking agent are observed. Typically, we found 5X – 6X reduction in SERS intensity resulting from non-specific binding, which translated to a 2X – 3X improvement in LOD compared to starting block. Thus, we proceeded with 3%

BSA/0.05% Tween 20 for all our SERS assays and recommend this blocking reagent when working with blood sera.

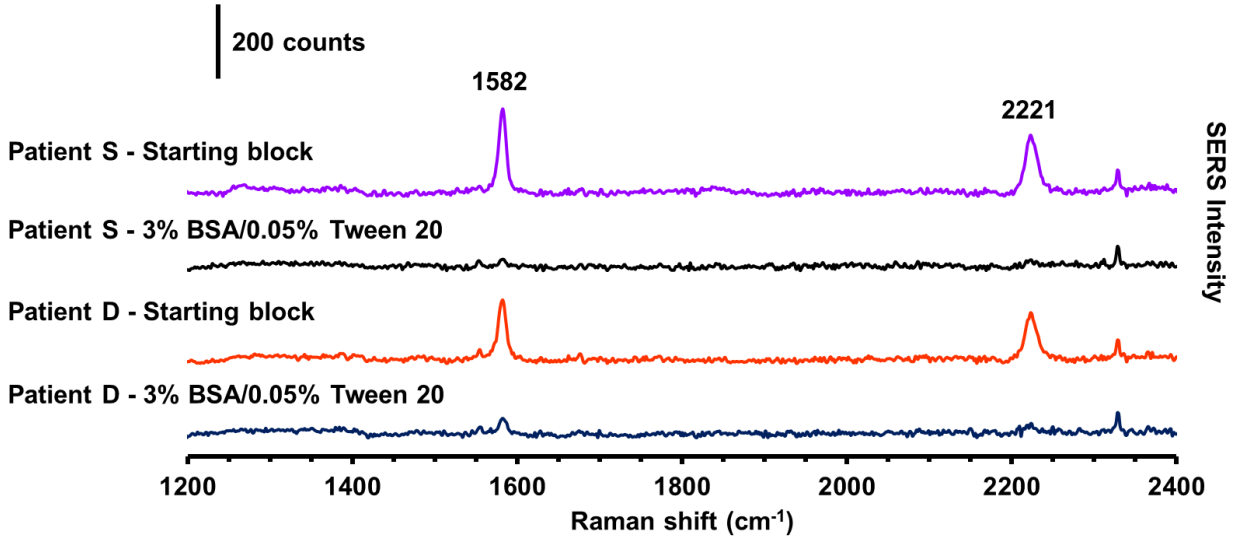

Figure 5–14. Raman spectra demonstrating the effect of two different blocking reagents in a SERS-based immunoassay using two different healthy control male (blank serum) specimens. Spectra are offset vertically for visualization. Each spectrum represents an average of 50 spectra collected from a specimen. Dominant spectral features at 1582 cm^{-1} and 2221 cm^{-1} are consistent with the ν_s(C–C) ring breathing mode and the ν_s(C≡N), respectively. The two blocking reagents evaluated are: commercial Starting Block (used as received) and 3% bovine serum albumin dissolved in 1X PBS with 0.05% Tween 20.

Considering the high relative abundance of AR-FL to AR-V7 (~ 32X more abundant), specific detection of AR-V7 is largely established by the results of our undiluted healthy normal male controls. To explain, we begin by addressing the antibodies used in the sandwich immunoassay. The antibodies on the capture substrate are specific to AR-V7. These antibodies bind to a unique epitope at the C-terminus of the AR-V7. Considering our VCaP cell lysate blank control (PBS buffer), we do not expect AR-V7 (or AR-FL) proteins. Our SERS immunoassay results show a low signal intensity (64 ± 3 counts; n = 3), slightly above the instrument noise level (59 ± 3 counts; n = 3) (Figure 5–4). This establishes a low level of cross-reactivity. The detection antibodies are specific to AR-FL. Thus, in normal male specimens we can expect AR-FL expression and no AR-V7 expression. Our SERS immunoassay results show that both normal males have low SERS signal intensities (87 ± 16 counts; n = 3) and are below the LOD (135 counts) (Figure 5–10). Our SEM results supports our SERS immunoassay results showing virtually nil AgNP binding. If AR-FL proteins were being detected, then signal intensities generated from the normal males would be substantially higher. Hence, our emphasis on highly effective blocking reagents for low abundance analytes in complex matrices.

Our SERS immunoassay results suggest a clinical specificity of ~ 100% (2 / 2 control cases considered as true negatives) for this limited data set. A first approximation of clinical sensitivity suggests that our assay shows ~ 86% (6 / 7 patient cases considered as true positives). In these preliminary assertions on clinical specificity and sensitivity, we acknowledge that we have not shown evidence using other methods to confirm AR-V7 status to substantiate our claims. Thus, future work aim to rule out the possibility of false negatives by tissue immunohistochemistry and false positives by examine specimens using other detection methods (e.g., Johns Hopkins University CTC-mRNA assay or Genomic Health Oncotype Dx AR-V7 Nucleus Detect).

Another limitation with our pilot study is the small sample size. We address this point two ways by considering the endpoint of the assay. First, we considered a positive endpoint (i.e., AR-V7+). In this case, the ratio of patient cases to controls is 6 : 0 or 85.6% (6 CRPC patients / 7 total CRPC patients) : 0% (0 controls / 2 total controls). Based on a large difference between patient cases and the controls, a large sample size is not required for statistical validation at a threshold of 95% confidence level ($\alpha = 0.05$) and 80% power ($\beta = 0.80$).[388] Though our small sample size in context of a positive endpoint is statistically encouraging, it would not be representative of the biological variation that exists within a CRPC population. Hence, our limited data set would not make a strong argument for clinical validation. This led us to consider a negative endpoint (i.e., AR-V7–). We postulate that a negative endpoint would better inform a sample size needed for statistical validation. In this case, we can also account for the possibility of a false positive result. Though we can

expect the control arm to be all biologically negative, there is a chance that the SERS-based assay reveals a false positive. We calculated sample sizes needed for statistical validation ($\alpha = 0.05$, $\beta = 0.80$) for clinical studies[389-390] based on liberal differences between patient cases and controls. We set these percent differences at 25%, 30%, and 35% to allow for analytical optimization of accuracy and precision. Based on our results showing ~ 30% negative status (3 AR-V7- patients / 9 total patients), the number of patients required for the next pilot study are: 60 (25% difference), 41 (30% difference), and 31 (35% difference) in each experimental arm (i.e., patient cases : controls).[391] Our initial pilot study was useful in allowing us to test our prospective hypothesis, demonstrate the effectiveness of our SERS-based assay, and inform us of logistical challenges that require consideration moving forward towards internal and external prospective validation of a SERS-based assay for AR-V7 detection. Plans to expand our pilot study to strengthen our efforts in prospective validation are underway.

Our SERS-based immunoassay platform for AR-V7 protein detection in a liquid biopsy (serum) is the first of its kind. Tsaur et al. describe the two main current approaches for AR-V7 detection in liquid biopsies that rely on circulating tumour cells. In these assays, AR-V7 detection is based on mRNA (Qiagen AdnaTest) and protein (EPIC Sciences now part of Genomic Health) expression. Tsaur and co-workers further describe advantages and limitations of these assay in terms of clinical feasibility and reflection of disease state.[326] The authors discuss quantifying AR-V7 mRNA with reverse transcriptase-PCR may is clinically more feasible, however mRNA expression is less direct measure of the

disease state than protein expression. Whereas, AR-V7 protein detection is more precise and can provide enhanced prognostic information based on nuclear localization,[324] CTC-based immunohistochemistry may not be clinically feasible. Drawbacks of CTC-based analyses that need consideration are the inherent difficulty in cell isolation, very short timeframe (< 24 h) to process blood samples for mRNA isolation, and the potential to miss mesenchymal cells undergoing epithelial-mesenchymal transition due to CTC capture methods relying on cell surface markers.[314]

Highlights of our SERS-based platform are that it does not require specialized specimen collection tubes with nucleic acid stabilizing reagents, CTC enrichment, or mRNA isolation. Prior to ruling out any detection platform, we should place greater emphasis on clinical application and CRPC patients that can benefit from an AR-V7 detection platform. Markowski and colleagues estimated 30% of mCRPC patients may have detectable AR-V7 in CTCs. Assessing AR-V7 status this population prior to starting enzalutamide or abiraterone treatment would result in a cost savings of $150 Million per year in the United States.[332] Markowski and colleagues further report that more than 50% prostate cancer specialists stated that an AR-V7 test changed their treatment decision. The specialists polled reported that men with AR-V7+ results (62%) had the most treatment changes, with preferentially managed with taxane therapy or offered a clinical trial, which may have improved outcomes.[332] We propose that a SERS-based platform can be positioned for rapid (≤ 24 h) determination of AR-V7 status to guide treatment selection. To further enhance prognostic value of our approach, experiments to include biomarkers specific for PCa

aggressiveness are underway. We aim to propose a risk scoring system to stratify patients and determine an effective treatment strategy.

An urgent need remains for prospective validation studies for AR-V7 as a predictive and prognostic biomarker in patients with CRPC. Presently, a multi-centre clinical trial examining AR-V7 using three different liquid biopsy assays (two rely on mRNA detection using PCR and one relies on protein detection using immunofluorescence) is underway (PROPHECY, NCT02269982).[392] As Bastos and Antonarakis state in their recent review,[304] 120 mCRPC patients at the outset of next-generation androgen receptor signaling inhibitors (enzalutamide / abiraterone / taxanes) will be prospectively sampled at baseline using three different AR-V7 detection assays, and then monitored prospectively until clinical or radiographic disease progression. At the time of progression, patients will be resampled using the three platform assays and then offered a taxane chemotherapy. At the time of progression on taxane, a third set of liquid biopsies will be collected for analyses. A unique advantage of this study is the ability to assess the prognostic value of each the three AR-V7 assays and to indirectly compare the analytical and clinical characteristics of each test against the others. Preliminary communication of results are expected in the 2nd quarter of 2018.[304]

5.4. Conclusion

Prostate cancer continues to be a global health priority. Though survivorship rates are high for localized PCa, these rates drop dramatically in a metastatic context. Disease-related mortality is inevitable in this setting. Patients with metastatic disease are strongly dependent on treatment selection to maximize overall survival. First line androgen deprivation therapies result in initial benefit, however eventually become ineffective due to resistance mechanisms associated with the androgen receptor signalling axis resulting in a castration-resistant state. An important unmet need for mCRPC patients is treatment-specific biomarkers to guide treatment selection during the course of disease. Androgen receptor V7 is a biomarker that has received the most attention to date for its role as a predictive and prognostic biomarker for advanced PCa patients. As liquid biopsies offer several advantages, including serial measurements to monitor treatment progress, there are only two CLIA-approved blood-based assays for the detection of AR-V7 in circulating tumour cells; one for mRNA detection and one for protein detection.

Our study reports the successful detection of AR-V7 protein at low levels in cultured prostate cancer cells and in human serum using a SERS-based sandwich immunoassay. We also provide calibration results for AR-V7 protein and AR-V7 mRNA expression levels. To assess clinical utility of a SERS-based immunoassay, we carried out a prospective pilot scale using a retrospective cohort of seven mCRPC patients pre / post treatment with enzalutamide and / or abiraterone. Our results demonstrate the ability to identify AR-V7 status (positive or negative) in mCRPC patients and provide quantitative measurements to

enhance prognostic and predictive value. Future studies to expand our pilot scale for prospective validation and to enhance the prognostic value of our assay by integrating markers for aggressiveness are currently underway and will be reported separately.

Chapter 6. Conclusion and future directions

6.1. Conclusion

Motivation for the work presented in this thesis converged from three points: (1) deep curiosity and ambition to discover unique attributes of biogenic nanoparticles; (2) to address the health sector by delivering on an unmet clinical need for a major disease impacting a global population level, and (3) to tap into the growing market segments of diagnostics/biosensors and liquid biopsies.[180, 393-394] This thesis presents both scientific advances focused on biogenic silver nanoparticles and a value proposition for a target-agnostic platform technology with a SERS readout. One notable advance is the enhanced colloidal stability of biogenic AgNPs attributed to the biomolecular surface layer or biocorona. Detailed investigation of this thin layer revealed a composition of peptides and carbohydrates that originates from the fungal organism in response to stress. These peptides and carbohydrates are believed to protect a fungal organism or adapt it to its environment. From another perspective, the biocorona can be a considered a native scaffold for expanding functions. Successful modifications included Raman reporter molecules and antibodies resulting in Raman active labels that are stable and selective for SERS-based immunoassays. Another notable advance is a successful prospective pilot scale investigation of clinical utility demonstrating the ability to quantitatively measure AR-V7 in serum of a blinded retrospective cohort of seven advanced PCa patients pre / post treatment with enzalutamide and / or abiraterone. Presence and amount of AR-V7 in

serum offers predictive and prognostic value to inform selection between two classes of systemic treatments (i.e., hormones or taxanes) outlined in the Canadian and American clinical guidelines for managing castration-resistant PCa. Contributions of this work paves the way for a sensitive, rapid, and minimally-invasive SERS-based tool for detection of AR-V7 in serum. The body of work in this thesis aims to benefit advanced PCa patients by optimizing the treatment algorithm, providing an indication of enzalutamide / abiraterone resistance, and improving quality of life.

Above serves to highlight major contributions presented within the body of work contained in this thesis. Since each chapter contains its own conclusion of the specific work done, this conclusion offers three points of advice for next generation of analytical chemists.

1. **When working in a sparely populated research area or on a new technological innovation, do not be discouraged by opposition.** Claims against can vary; however be vigilant that such claims may be unsubstantiated, may serve to stall, or derail advances. As Professor Calestous Juma concludes from nearly 600 years of technology history, the two fundamental drivers of concern over new technologies or innovation: (1) *a fear that the innovation may lead to a loss or change with consequences to either economics or cultural identities* or (2) *the perception that the benefits of the new area or technology will accrue to a small population while the risks will be more widely distributed*.[395] Consider such

opposition or resistance as opportunities to be bold, creative, and resilient. To help build one's own resilience, *seek and engage mentors* who show strong support, leadership, and are willing to challenge status quo. Through diligence, hard work, and good mentorship; one can make scientific discoveries and become an authority on the subject,[396] which global society desperately needs.

2. When selecting analytical biomarkers for diagnostic, predictive, or prognostic applications; obtain current clinical guidelines used for patient/disease management. Clinical guidelines for patient/disease management informs clinicians on how to consistently manage patient care supported by evidence. Early acquisition of guidelines from a clinician aims to position the measurement science in-step with clinical practice with a greater effectiveness. This approach also sheds light on competing assays and workflow for an end user. Understanding the clinical setting and unmet need will enhance an assay designer's confidence and increase the value of the assay.

3. When designing an assay with commercial potential, aim to build your interpersonal network in context of the supply chain. A simple example of a supply chain is a system of interconnected links assembled to transition raw input materials through to end use. Seek insights and feedback from diverse members within the supply chain throughout the design process. This approach enables an assay designer to stay nimble and consider important factors while prototyping with an enhanced success rate.

6.2. Future directions

6.2.1. Enhancing our understanding of biogenic nanoparticles and the biocorona.

Though the biocorona is composed of abundant peptides identified with extensive homology to stress or adaptive proteins, we do not know if fungi originally synthesize short peptides (for perhaps quicker response) or if proteins are originally synthesized and degraded leaving peptide fragments on the NP surface. Other questions include: (1) Are there correlations with other fungi in producing peptides/proteins consistent with stress or adaptive proteins? (2) Can the stress/adaptive protein genes be cloned and expressed in another host for a source of stabilizing biomolecules for nanoparticles? (3) Can fungi be engineered to be more efficient at producing nanoparticles (e.g., quantity, physical characteristics) at ambient conditions? Further work to enhance our understanding in these areas would benefit the field of biogenic nanoparticles.

6.2.2. AR-V7 SERS immunoassay validation – need more patients.

As discussed in chapter 5, one limitation with our pilot study is the small sample size. In advancing towards internal validation and external validation, I propose another pilot study with 30 – 60 patient specimens in each experimental arm (patient cases : controls). These numbers are based on our results showing ~ 30% negative status and a statistical basis of $\alpha = 0.05$ and $\beta = 0.80$. Also, it would be beneficial to use freshly collected specimens of a prospective cohort, rather than previously frozen specimens. This approach

will provide a more accurate measure of AR-V7 levels. Another point to consider is validating laboratory assay/technologies in a commercial diagnostic laboratory. This effort will contribute to greater exposure and de-risking investments. At the time of writing this, DynaLIFE Accelerator program has been initiated to validate laboratory technologies in a real-world diagnostic laboratory. [397] Lastly, parallel studies with other competing technologies (e.g., CTC-based, mRNA detection) would complement a SERS-based approach presented in this thesis.

6.2.3. AR-V7 SERS immunoassay 2.0

As discussed in chapter 5, an unmet need for patients with advanced prostate cancer is the determination of prostate cancer aggressiveness.[304] In advancing our AR-V7 assay, I propose to extend the detection panel to include two aggressive biomarkers with the aim of scoring index and to enhance treatment selection. Two aggressive biomarkers are proposed for greater confidence in predictive value. Figure 6–1 shows a proposed plan to extend the biomarker panel for CRPC patients with the outcomes of risk stratification and enhanced treatment selection. Proposed ideas in selecting aggressive biomarkers are a combination of: (1) membrane scaffolding proteins (e.g., tetraspanins, prostate-specific membrane antigen);[398-401] (2) sirtuins;[402-403] and (3) other androgen splice variants (e.g., AR-v5,6,7).[350, 404]

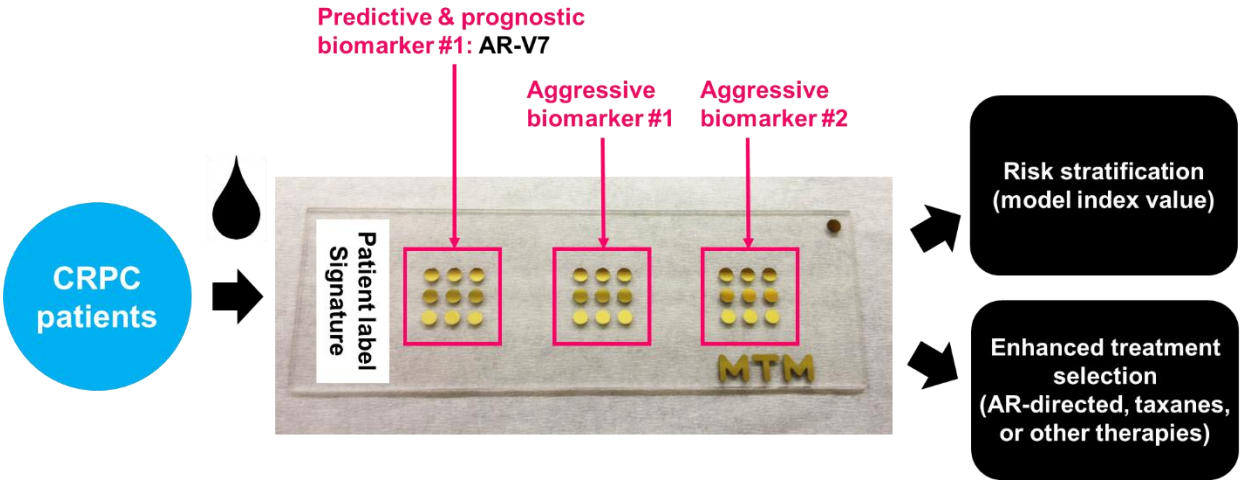

Figure 6–1. Blood-based AR-V7 SERS immunoassay 2.0 for enhanced prediction and prognosis. Patient label consists of two rows, one for a human signature (if required). CRPC = castration-resistant prostate cancer. AR = androgen receptor.

Other ways to potentially improve the SERS-based assay are:

a) Increase nanoparticle diameter (e.g., ø40 nm – ø80nm)[75, 260, 290, 405-406] or use anisotropic shapes (e.g., silver rods)[52, 94, 96, 407] for higher extinction coefficients with 633 nm or 785 nm excitation. Larger sizes will result in greater overlap between the plasmon band and the excitation wavelength, enhance the scattering cross section, and will permit greater coverage of Raman reporter molecules. Collectively, this approach aims to increase Raman cross section; thus, increasing signal intensity and improving the limit of detection.

b) For surface-based assays, it would be beneficial to map the entire address[34] with shorter integration times and collect each point in focus. New advances in 'digital' Raman may help in data processing when analysing analytes in ultra-low concentration (≤ 1 nM).[345] Combining digitized Raman maps with the predictive

capability of artificial intelligence (machine learning or deep learning algorithms) may reveal new interpretations in sample analyses.

c) Solution-based SERS would be beneficial to reduce sample processing, data collection, and analyses represented as an average. As a preliminary approach, my colleague (Casey Rusin) and I attempted to use cellulose nanofibres and attach biorecognition agents (e.g., antibodies) to serve as a bio-analyte capture mesh. Our early results appear encouraging.

6.2.4. Partner with artificial intelligence to enhance bioassays

Over the last five or so years, artificial intelligence (AI) is increasing its ubiquity among society. For example, if you use or have used an Apple product equipped with Siri or a modern iPhone (iPhone 4S or higher) for photos, then you have held AI in your hand. Beyond Apple, other tech giants such as Google, Microsoft, Facebook, Baidu, and Amazon all use AI to enhance business. Artificial intelligence is a broad term that applies to a computer system that mimics human intelligence such as solving problems, making decisions, processing language, and recognizing images.[408] Machine learning, a subcategory of AI, is a set of algorithms that can be designed to analyse large and complex data sets (also known as 'big data') and learn to identify statistical patterns or trends that can scale our expertise to unprecedented levels. Analytical chemists who are designing assays with real-world applications are strongly encouraged to collaborate with computer/data scientists. Such efforts will lead to a strong potential for discovery and higher value for the assay.

In medicine, the role of AI is to enhance assays used for biological measurements. Ultimately, AI-enhanced bioassays serve as a tool to enhance the physician's expertise. For example, results of an AI-enhanced bioassay could also include patient characteristics, symptoms, drug indications/contra-indications, and active clinical trials. This would enable physicians (e.g., medical oncologists) to predict patient outcomes or treat patients more effectively. For example, IBM is developing an AI-based tool (Watson Health for oncology) to provide clinicians with evidence-based treatment options based on expertise of the Memorial Sloan Kettering institute.[409] To realize the impact of AI-enhancement, big data is needed. To this end, Alberta's population base of 4.3 billion[410] and health system provides a unique big data advantage for researchers. The system is organised with a single payer (i.e., public health care) and a single care provider (i.e., Alberta Health Services) allows researchers to link clinical data in an unparalleled fashion.[411] Alberta's new impending system, Connect Care, will further enhance links to centralized patient information, clinical standards, and best healthcare practices.[412,413] Collectively, AI-enhanced bioanalysis aims to scale a human's expertise in advancing research and delivering patient care to unprecedented levels.

References

1. Laurentius, L. B.; Owens, N. A.; Park, J.; Crawford, A. C.; Porter, M. D., Advantages and limitations of nanoparticle labeling for early diagnosis of infection. *Expert Review of Molecular Diagnostics* **2016,** *16* (8), 883-895.

2. Boverhof, D. R.; Bramante, C. M.; Butala, J. H.; Clancy, S. F.; Lafranconi, M.; West, J.; Gordon, S. C., Comparative assessment of nanomaterial definitions and safety evaluation considerations. *Regul. Toxicol. Pharm.* **2015,** *73* (1), 137-150.

3. Daniel, M.-C.; Astruc, D., Gold Nanoparticles: Assembly, Supramolecular Chemistry, Quantum-Size-Related Properties, and Applications toward Biology, Catalysis, and Nanotechnology. *Chem. Rev.* **2004,** *104* (1), 293-346.

4. Eustis, S.; El-Sayed, M. A., Why gold nanoparticles are more precious than pretty gold: Noble metal surface plasmon resonance and its enhancement of the radiative and nonradiative properties of nanocrystals of different shapes. *Chem. Soc. Rev.* **2006,** *35* (3), 209-217.

5. Faraday, M., Experimental relations of gold (and other metals) to light. *Philosophical Transactions of the Royal Society of London* **1857,** *147*, 145-181.

6. Mie, G., [Beiträge zur Optik trüber Medien, speziell kolloidaler Metallösungen] Contributions to the optics of turbid media, particularly of colloidal metal solutions. *Annalen der Physik* **1908,** *330* (3), 377-445.

7. Hulst, H. C. v. d., Light scattering by small particles. Rev. ed ed.; Wiley: New York: 1957.

8. Bohren, C. F.; Huffman, D. R., *Absorption and Scattering of Light by Small Particles*. Wiley: New York: 1983.

9. Willets, K. A.; Duyne, R. P. V., Localized Surface Plasmon Resonance Spectroscopy and Sensing. *Annu. Rev. Phys. Chem.* **2007,** *58* (1), 267-297.

10. Saha, K.; Agasti, S. S.; Kim, C.; Li, X.; Rotello, V. M., Gold Nanoparticles in Chemical and Biological Sensing. *Chem. Rev.* **2012,** *112* (5), 2739-2779.

11. Kreibig, U., *Optical properties of metal clusters*. Springer:: Berlin, Germany, 1995; p 532.

12. Murphy, C. J.; Gole, A. M.; Hunyadi, S. E.; Stone, J. W.; Sisco, P. N.; Alkilany, A.; Kinard, B. E.; Hankins, P., Chemical sensing and imaging with metallic nanorods. *Chem. Commun.* **2008,** (5), 544-557.

13. Link, S.; Wang, Z. L.; El-Sayed, M. A., Alloy Formation of Gold−Silver Nanoparticles and the Dependence of the Plasmon Absorption on Their Composition. *The Journal of Physical Chemistry B* **1999,** *103* (18), 3529-3533.

14. Mock, J. J.; Smith, D. R.; Schultz, S., Local Refractive Index Dependence of Plasmon Resonance Spectra from Individual Nanoparticles. *Nano Lett.* **2003,** *3* (4), 485-491.

15. Hao, E.; Schatz, G. C.; Hupp, J. T., Synthesis and Optical Properties of Anisotropic Metal Nanoparticles. *Journal of Fluorescence* **2004,** *14* (4), 331-341.

16. Evanoff, D. D.; Chumanov, G., Size-Controlled Synthesis of Nanoparticles. 2. Measurement of Extinction, Scattering, and Absorption Cross Sections. *The Journal of Physical Chemistry B* **2004,** *108* (37), 13957-13962.

17. nanoComposix. https://nanocomposix.com/. Permission granted by Amanda Madsen (personal communication, 2018).

18. nanoComposix. https://nanocomposix.com/. Permission granted by Amanda Madsen (personal communication, 2018).

19. Dreaden, E. C.; Alkilany, A. M.; Huang, X.; Murphy, C. J.; El-Sayed, M. A., The golden age: gold nanoparticles for biomedicine. *Chem. Soc. Rev.* **2012,** *41* (7), 2740-2779.

20. Burrows, N. D.; Lin, W.; Hinman, J. G.; Dennison, J. M.; Vartanian, A. M.; Abadeer, N. S.; Grzincic, E. M.; Jacob, L. M.; Li, J.; Murphy, C. J., Surface Chemistry of Gold Nanorods. *Langmuir* **2016,** *32* (39), 9905-9921.

21. Chang, H.-H.; Murphy, C. J., Mini Gold Nanorods with Tunable Plasmonic Peaks beyond 1000 nm. *Chem. Mater.* **2018,** *30* (4), 1427-1435.

22. Doria, G.; Conde, J.; Veigas, B.; Giestas, L.; Almeida, C.; Assunção, M.; Rosa, J.; Baptista, P. V., Noble Metal Nanoparticles for Biosensing Applications. *Sensors* **2012,** *12* (2), 1657.

23. Arvizo, R. R.; Bhattacharyya, S.; Kudgus, R. A.; Giri, K.; Bhattacharya, R.; Mukherjee, P., Intrinsic therapeutic applications of noble metal nanoparticles: past, present and future. *Chem. Soc. Rev.* **2012,** *41* (7), 2943-2970.

24. Zhou, W.; Gao, X.; Liu, D.; Chen, X., Gold Nanoparticles for In Vitro Diagnostics. *Chem. Rev.* **2015,** *115* (19), 10575-10636.

25. Li, J.; Zhao, T.; Chen, T.; Liu, Y.; Ong, C. N.; Xie, J., Engineering noble metal nanomaterials for environmental applications. *Nanoscale* **2015,** *7* (17), 7502-7519.

26. Freeman, R. G.; Grabar, K. C.; Allison, K. J.; Bright, R. M.; Davis, J. A.; Guthrie, A. P.; Hommer, M. B.; Jackson, M. A.; Smith, P. C.; Walter, D. G.; Natan, M. J., Self-Assembled Metal Colloid Monolayers: An Approach to SERS Substrates. *Science* **1995,** *267* (5204), 1629-1632.

27. Le Ru, E. C.; Etchegoin, P. G., *Principles of surface-enhanced Raman spectroscopy : and related plasmonic effects*. Amsterdam : Elsevier, 2009 (Norwood, Mass.)

1st ed.: 2009.

28. Driskell, J. D.; Lipert, R. J.; Porter, M. D., Labeled Gold Nanoparticles Immobilized at Smooth Metallic Substrates: Systematic Investigation of Surface Plasmon Resonance and Surface-Enhanced Raman Scattering. *The Journal of Physical Chemistry B* **2006,** *110* (35), 17444-17451.

29. Jain, K. K., Applications of Nanobiotechnology in Clinical Diagnostics. *Clin. Chem.* **2007,** *53* (11), 2002.

30. Laurentius, L. B. Modification and Application of Gold Nanoparticles in Surface-Based Immunoassays. Thesis, University of Alberta, 2012.

31. Elbayomy, S. A. T. Modification and application of gold nanorods in surface enhanced Raman scattering based assays. University of Alberta, 2015.

32. Graham, D.; Faulds, K.; Smith, W. E., Biosensing using silver nanoparticles and surface enhanced resonance Raman scattering. *Chem. Commun.* **2006,** (42), 4363-4371.

33. Abalde-Cela, S.; Aldeanueva-Potel, P.; Mateo-Mateo, C.; Rodríguez-Lorenzo, L.; Alvarez-Puebla, R. A.; Liz-Marzán, L. M., Surface-enhanced Raman scattering biomedical applications of plasmonic colloidal particles. *Journal of The Royal Society Interface* **2010**.

34. Crawford, A. C.; Skuratovsky, A.; Porter, M. D., Sampling Error: Impact on the Quantitative Analysis of Nanoparticle-Based Surface-Enhanced Raman Scattering Immunoassays. *Anal. Chem.* **2016,** *88* (12), 6515-6522.

35. Orendorff, C. J.; Gole, A.; Sau, T. K.; Murphy, C. J., Surface-Enhanced Raman Spectroscopy of Self-Assembled Monolayers: Sandwich Architecture and Nanoparticle Shape Dependence. *Anal. Chem.* **2005,** *77* (10), 3261-3266.

36. Sharma, B.; Fernanda Cardinal, M.; Kleinman, S. L.; Greeneltch, N. G.; Frontiera, R. R.; Blaber, M. G.; Schatz, G. C.; Van Duyne, R. P., High-performance SERS substrates: Advances and challenges. *MRS Bull.* **2013,** *38* (8), 615-624.

37. Driskell, J. D.; Kwarta, K. M.; Lipert, R. J.; Porter, M. D.; Neill, J. D.; Ridpath, J. F., Low-Level Detection of Viral Pathogens by a Surface-Enhanced Raman Scattering Based Immunoassay. *Anal. Chem.* **2005,** *77* (19), 6147-6154.

38. Larmour, I. A.; Faulds, K.; Graham, D., SERS activity and stability of the most frequently used silver colloids. *Journal of Raman Spectroscopy* **2012,** *43* (2), 202-206.

39. Fan, M.; Thompson, M.; Andrade, M. L.; Brolo, A. G., Silver Nanoparticles on a Plastic Platform for Localized Surface Plasmon Resonance Biosensing. *Anal. Chem.* **2010,** *82* (15), 6350-6352.

40. Wiley, B. J.; Im, S. H.; Li, Z.-Y.; McLellan, J.; Siekkinen, A.; Xia, Y., Maneuvering the Surface Plasmon Resonance of Silver Nanostructures through Shape-Controlled Synthesis. *The Journal of Physical Chemistry B* **2006,** *110* (32), 15666-15675.

41. Lee, P. C.; Meisel, D., Adsorption and surface-enhanced Raman of dyes on silver and gold sols. *The Journal of Physical Chemistry* **1982,** *86* (17), 3391-3395.

42. Wang, L.; Bai, J.; Huang, P.; Wang, H.; Zhang, L.; Zhao, Y., *Self-assembly of gold nanoparticles for the voltammetric sensing of epinephrine*. 2006; Vol. 8, p 1035-1040.

43. Pinijsuwan, S.; Rijiravanich, P.; Somasundrum, M.; Surareungchai, W., Sub-Femtomolar Electrochemical Detection of DNA Hybridization Based on Latex/Gold Nanoparticle-Assisted Signal Amplification. *Anal. Chem.* **2008,** *80* (17), 6779-6784.

44. Wang, Q.; Yang, L.; Yang, X.; Wang, K.; He, L.; Zhu, J., Electrochemical biosensors for detection of point mutation based on surface ligation reaction and oligonucleotides modified gold nanoparticles. *Anal. Chim. Acta* **2011,** *688* (2), 163-167.

45. Maxwell, D. J.; Taylor, J. R.; Nie, S., Self-Assembled Nanoparticle Probes for Recognition and Detection of Biomolecules. *J. Am. Chem. Soc.* **2002,** *124* (32), 9606-9612.

46. Shan, W.; Pan, Y.; Fang, H.; Guo, M.; Nie, Z.; Huang, Y.; Yao, S., An aptamer-based quartz crystal microbalance biosensor for sensitive and selective detection of leukemia cells using silver-enhanced gold nanoparticle label. *Talanta* **2014,** *126*, 130-135.

47. Ly, T. N.; Park, S.; Park, S. J., Detection of HIV-1 antigen by quartz crystal microbalance using gold nanoparticles. *Sensors and Actuators B: Chemical* **2016,** *237*, 452-458.

48. Nelson, B. P.; Grimsrud, T. E.; Liles, M. R.; Goodman, R. M.; Corn, R. M., Surface Plasmon Resonance Imaging Measurements of DNA and RNA Hybridization Adsorption onto DNA Microarrays. *Anal. Chem.* **2001,** *73* (1), 1-7.

49. Masson, J.-F., Surface Plasmon Resonance Clinical Biosensors for Medical Diagnostics. *ACS Sensors* **2017,** *2* (1), 16-30.

50. Cao, Y.; Griffith, B.; Bhomkar, P.; Wishart, D. S.; McDermott, M. T., Functionalized gold nanoparticle-enhanced competitive assay for sensitive small-molecule metabolite detection using surface plasmon resonance. *Analyst* **2018,** *143* (1), 289-296.

51. Lopatynskyi, A. M.; Lopatynska, O. G.; Guo, L. J.; Chegel, V. I., Localized Surface Plasmon Resonance Biosensor 2014;Part I: Theoretical Study of Sensitivity 2014; Extended Mie Approach. *IEEE Sens. J.* **2011,** *11* (2), 361-369.

52. Lee, K.-S.; El-Sayed, M. A., Gold and Silver Nanoparticles in Sensing and Imaging: Sensitivity of Plasmon Response to Size, Shape, and Metal Composition. *The Journal of Physical Chemistry B* **2006,** *110* (39), 19220-19225.

53. Haynes, C. L.; Frontiera, R. R.; Willets, K., Preface of Richard P. Van Duyne Festschrift. *The Journal of Physical Chemistry C* **2016,** *120* (37), 20483-20485.

54. Roldán, M. V.; Pellegri, N. S.; de Sanctis, O. A., Optical Response of Silver Nanoparticles Stabilized by Amines to LSPR based Sensors. *Procedia Materials Science* **2012,** *1*, 594-600.

55. Malinsky, M. D.; Kelly, K. L.; Schatz, G. C.; Van Duyne, R. P., Chain Length Dependence and Sensing Capabilities of the Localized Surface Plasmon Resonance of Silver

Nanoparticles Chemically Modified with Alkanethiol Self-Assembled Monolayers. *J. Am. Chem. Soc.* **2001,** *123* (7), 1471-1482.

56. Guo, L.; Jackman, J. A.; Yang, H.-H.; Chen, P.; Cho, N.-J.; Kim, D.-H., Strategies for enhancing the sensitivity of plasmonic nanosensors. *Nano Today* **2015,** *10* (2), 213-239.

57. Mirkin, C. A.; Letsinger, R. L.; Mucic, R. C.; Storhoff, J. J., A DNA-based method for rationally assembling nanoparticles into macroscopic materials. *Nature* **1996,** *382*, 607.

58. Elghanian, R.; Storhoff, J. J.; Mucic, R. C.; Letsinger, R. L.; Mirkin, C. A., Selective Colorimetric Detection of Polynucleotides Based on the Distance-Dependent Optical Properties of Gold Nanoparticles. *Science* **1997,** *277* (5329), 1078.

59. Storhoff, J. J.; Elghanian, R.; Mucic, R. C.; Mirkin, C. A.; Letsinger, R. L., One-Pot Colorimetric Differentiation of Polynucleotides with Single Base Imperfections Using Gold Nanoparticle Probes. *J. Am. Chem. Soc.* **1998,** *120* (9), 1959-1964.

60. Nath, N.; Chilkoti, A., A Colorimetric Gold Nanoparticle Sensor To Interrogate Biomolecular Interactions in Real Time on a Surface. *Anal. Chem.* **2002,** *74* (3), 504-509.

61. Sepúlveda, B.; Angelomé, P. C.; Lechuga, L. M.; Liz-Marzán, L. M., LSPR-based nanobiosensors. *Nano Today* **2009,** *4* (3), 244-251.

62. Stiles, P. L.; Dieringer, J. A.; Shah, N. C.; Van Duyne, R. P., Surface-enhanced Raman spectroscopy. *Annu Rev Anal Chem* **2008,** *1*, 601-26.

63. Raman, C. V.; Krishnan, K. S., A New Type of Secondary Radiation. *Nature* **1928,** *121*, 501.

64. Schlucker, S., SERS microscopy: nanoparticle probes and biomedical applications. *Chemphyschem* **2009,** *10* (9-10), 1344-54.

65. Goodacre, R.; Graham, D.; Faulds, K., Recent developments in quantitative SERS: Moving towards absolute quantification. *TrAC, Trends Anal. Chem.* **2018,** *102*, 359-368.

66. Fleischmann, M.; Hendra, P. J.; McQuillan, A. J., Raman spectra of pyridine adsorbed at a silver electrode. *Chem. Phys. Lett.* **1974,** *26* (2), 163-166.

67. Jeanmaire, D. L.; Van Duyne, R. P., Surface raman spectroelectrochemistry. *Journal of Electroanalytical Chemistry and Interfacial Electrochemistry* **1977,** *84* (1), 1-20.

68. Albrecht, M. G.; Creighton, J. A., Anomalously intense Raman spectra of pyridine at a silver electrode. *J. Am. Chem. Soc.* **1977,** *99* (15), 5215-5217.

69. Jamieson, L. E.; Asiala, S. M.; Gracie, K.; Faulds, K.; Graham, D., Bioanalytical Measurements Enabled by Surface-Enhanced Raman Scattering (SERS) Probes. *Annual Review of Analytical Chemistry* **2017,** *10* (1), 415-437.

70. Howard, R. E.; Liao, P. F.; Skocpol, W. J.; Jackel, L. D.; Craighead, H. G., Microfabrication as a Scientific Tool. *Science* **1983,** *221* (4606), 117.

71. Le Ru, E. C.; Blackie, E.; Meyer, M.; Etchegoin, P. G., Surface Enhanced Raman Scattering Enhancement Factors: A Comprehensive Study. *The Journal of Physical Chemistry C* **2007,** *111* (37), 13794-13803.

72. Asiala, S. M.; Schultz, Z. D., Characterization of hotspots in a highly enhancing SERS substrate. *Analyst* **2011,** *136* (21), 4472-4479.

73. Nie, S.; Emory, S. R., Probing Single Molecules and Single Nanoparticles by Surface-Enhanced Raman Scattering. *Science* **1997,** *275* (5303), 1102-1106.

74. Kneipp, K.; Kneipp, H.; Itzkan, I.; Dasari, R. R.; Feld, M. S., Ultrasensitive Chemical Analysis by Raman Spectroscopy. *Chem. Rev.* **1999,** *99* (10), 2957-2976.

75. Porter, M. D.; Lipert, R. J.; Siperko, L. M.; Wang, G.; Narayanan, R., SERS as a bioassay platform: fundamentals, design, and applications. *Chem. Soc. Rev.* **2008,** *37* (5), 1001-1011.

76. Ding, S.-Y.; You, E.-M.; Tian, Z.-Q.; Moskovits, M., Electromagnetic theories of surface-enhanced Raman spectroscopy. *Chem. Soc. Rev.* **2017,** *46* (13), 4042-4076.

77. Haes, A. J.; Zou, S.; Schatz, G. C.; Van Duyne, R. P., A Nanoscale Optical Biosensor: The Long Range Distance Dependence of the Localized Surface Plasmon Resonance of Noble Metal Nanoparticles. *The Journal of Physical Chemistry B* **2004,** *108* (1), 109-116.

78. Porter, M. D.; Granger, J. H., Surface-enhanced Raman scattering II: concluding remarks. *Faraday Discuss.* **2017,** *205*, 601-613.

79. Zhang, Y.; Hong, H.; Myklejord, D. V.; Cai, W., Molecular imaging with SERS-active nanoparticles. *Small* **2011,** *7* (23), 3261-9.

80. Rodriguez-Lorenzo, L.; Fabris, L.; Alvarez-Puebla, R. A., Multiplex optical sensing with surface-enhanced Raman scattering: a critical review. *Anal. Chim. Acta* **2012,** *745*, 10-23.

81. Premasiri, W. R.; Lee, J. C.; Ziegler, L. D., Surface-Enhanced Raman Scattering of Whole Human Blood, Blood Plasma, and Red Blood Cells: Cellular Processes and Bioanalytical Sensing. *The Journal of Physical Chemistry B* **2012,** *116* (31), 9376-9386.

82. Driscoll, A. J.; Harpster, M. H.; Johnson, P. A., The development of surface-enhanced Raman scattering as a detection modality for portable in vitro diagnostics: progress and challenges. *Phys. Chem. Chem. Phys.* **2013,** *15* (47), 20415-33.

83. Vendrell, M.; Maiti, K. K.; Dhaliwal, K.; Chang, Y. T., Surface-enhanced Raman scattering in cancer detection and imaging. *Trends Biotechnol.* **2013,** *31* (4), 249-57.

84. Wang, Y.; Schlucker, S., Rational design and synthesis of SERS labels. *Analyst* **2013,** *138* (8), 2224-38.

85. Wang, Y.; Yan, B.; Chen, L., SERS tags: novel optical nanoprobes for bioanalysis. *Chem. Rev.* **2013,** *113* (3), 1391-428.

86. Harper, M. M.; McKeating, K. S.; Faulds, K., Recent developments and future directions in SERS for bioanalysis. *PCCP* **2013,** *15* (15), 5312-5328.

87. Schlücker, S., Surface-Enhanced Raman Spectroscopy: Concepts and Chemical Applications. *Angew. Chem. Int. Ed.* **2014,** *53* (19), 4756-4795.

88. Lane, L. A.; Qian, X.; Nie, S., SERS Nanoparticles in Medicine: From Label-Free Detection to Spectroscopic Tagging. *Chem. Rev.* **2015,** *115* (19), 10489-10529.

89. Granger, J. H.; Schlotter, N. E.; Crawford, A. C.; Porter, M. D., Prospects for point-of-care pathogen diagnostics using surface-enhanced Raman scattering (SERS). *Chem. Soc. Rev.* **2016,** *45* (14), 3865-3882.

90. Laing, S.; Gracie, K.; Faulds, K., Multiplex in vitro detection using SERS. *Chem. Soc. Rev.* **2016,** *45* (7), 1901-1918.

91. Cialla-May, D.; Zheng, X. S.; Weber, K.; Popp, J., Recent progress in surface-enhanced Raman spectroscopy for biological and biomedical applications: from cells to clinics. *Chem. Soc. Rev.* **2017,** *46* (13), 3945-3961.

92. Wang, Z.; Zong, S.; Wu, L.; Zhu, D.; Cui, Y., SERS-Activated Platforms for Immunoassay: Probes, Encoding Methods, and Applications. *Chem. Rev.* **2017,** *117* (12), 7910-7963.

93. Seney, C. S.; Gutzman, B. M.; Goddard, R. H., Correlation of Size and Surface-Enhanced Raman Scattering Activity of Optical and Spectroscopic Properties for Silver Nanoparticles. *The Journal of Physical Chemistry C* **2009,** *113* (1), 74-80.

94. Emory, S. R.; Haskins, W. E.; Nie, S., Direct Observation of Size-Dependent Optical Enhancement in Single Metal Nanoparticles. *J. Am. Chem. Soc.* **1998,** *120* (31), 8009-8010.

95. Moskovits, M., Surface-enhanced Raman spectroscopy: a brief retrospective. *Journal of Raman Spectroscopy* **2005,** *36* (6-7), 485-496.

96. Jana, N. R.; Pal, T., Anisotropic Metal Nanoparticles for Use as Surface-Enhanced Raman Substrates. *Adv. Mater.* **2007,** *19* (13), 1761-1765.

97. Petryayeva, E.; Krull, U. J., Localized surface plasmon resonance: Nanostructures, bioassays and biosensing—A review. *Anal. Chim. Acta* **2011,** *706* (1), 8-24.

98. Potara, M.; Bawaskar, M.; Simon, T.; Gaikwad, S.; Licarete, E.; Ingle, A.; Banciu, M.; Vulpoi, A.; Astilean, S.; Rai, M., Biosynthesized silver nanoparticles performing as biogenic SERS-nanotags for investigation of C26 colon carcinoma cells. *Colloids and Surfaces B: Biointerfaces* **2015,** *133*, 296-303.

99. Haefeli, C.; Franklin, C.; Hardy, K., Plasmid-determined silver resistance in Pseudomonas stutzeri isolated from a silver mine. *J. Bacteriol.* **1984,** *158* (1), 389-392.

100. Klaus, T.; Joerger, R.; Olsson, E.; Granqvist, C.-G., Silver-based crystalline nanoparticles, microbially fabricated. *Proceedings of the National Academy of Sciences* **1999,** *96* (24), 13611-13614.

101. Li, X.; Xu, H.; Chen, Z.-S.; Chen, G., Biosynthesis of Nanoparticles by Microorganisms and Their Applications. *Journal of Nanomaterials* **2011,** *2011*, 1-16.

102. Dhillon, G. S.; Brar, S. K.; Kaur, S.; Verma, M., Green approach for nanoparticle biosynthesis by fungi: current trends and applications. *Crit. Rev. Biotechnol.* **2012,** *32* (1), 49-73.

103. Rai, M.; Birla, S.; Ingle Avinash, P.; Gupta, I.; Gade, A.; Abd-Elsalam, K.; Marcato Priscyla, D.; Duran, N., Nanosilver: an inorganic nanoparticle with myriad potential applications. In *Nanotechnology Reviews*, 2014; Vol. 3, p 281.

104. Birla, S. S.; Gaikwad, S. C.; Gade, A. K.; Rai, M. K., Rapid Synthesis of Silver Nanoparticles from Fusarium oxysporum by Optimizing Physicocultural Conditions. *The Scientific World Journal* **2013,** *2013*, 12.

105. Duran, N.; Marcato, P. D.; Alves, O. L.; Souza, G. I.; Esposito, E., Mechanistic aspects of biosynthesis of silver nanoparticles by several Fusarium oxysporum strains. *J Nanobiotechnology* **2005,** *3*.

106. Kimber Richard, L.; Lewis Edward, A.; Parmeggiani, F.; Smith, K.; Bagshaw, H.; Starborg, T.; Joshi, N.; Figueroa Adriana, I.; van der Laan, G.; Cibin, G.; Gianolio, D.; Haigh

Sarah, J.; Pattrick Richard, A. D.; Turner Nicholas, J.; Lloyd Jonathan, R., Biosynthesis and Characterization of Copper Nanoparticles Using Shewanella oneidensis: Application for Click Chemistry. *Small* **2018,** *14* (10), 1703145.

107. Bhainsa, K. C.; D'Souza, S. F., Extracellular biosynthesis of silver nanoparticles using the fungus Aspergillus fumigatus. *Colloids and Surfaces B: Biointerfaces* **2006,** *47* (2), 160-164.

108. Vigneshwaran, N.; Ashtaputre, N. M.; Varadarajan, P. V.; Nachane, R. P.; Paralikar, K. M.; Balasubramanya, R. H., Biological synthesis of silver nanoparticles using the fungus Aspergillus flavus. *Mater. Lett.* **2007,** *61* (6), 1413-1418.

109. Basavaraja, S.; Balaji, S. D.; Lagashetty, A.; Rajasab, A. H.; Venkataraman, A., Extracellular biosynthesis of silver nanoparticles using the fungus Fusarium semitectum. *Mater. Res. Bull.* **2008,** *43* (5), 1164-1170.

110. Kathiresan, K.; Manivannan, S.; Nabeel, M. A.; Dhivya, B., Studies on silver nanoparticles synthesized by a marine fungus, Penicillium fellutanum isolated from coastal mangrove sediment. *Colloids and Surfaces B: Biointerfaces* **2009,** *71* (1), 133-137.

111. Mukherjee, P.; Senapati, S.; Mandal, D.; Ahmad, A.; Khan, M. I.; Kumar, R.; Sastry, M., Extracellular Synthesis of Gold Nanoparticles by the Fungus Fusarium oxysporum. *ChemBioChem* **2002,** *3* (5), 461.

112. Ahmad, A.; Mukherjee, P.; Mandal, D.; Senapati, S.; Khan, M. I.; Kumar, R.; Sastry, M., Enzyme Mediated Extracellular Synthesis of CdS Nanoparticles by the Fungus, Fusarium oxysporum. *J. Am. Chem. Soc.* **2002,** *124* (41), 12108-12109.

113. Ahmad, A.; Mukherjee, P.; Senapati, S.; Mandal, D.; Khan, M. I.; Kumar, R.; Sastry, M., Extracellular biosynthesis of silver nanoparticles using the fungus Fusarium oxysporum. *Colloids and Surfaces B: Biointerfaces* **2003,** *28* (4), 313-318.

114. Longhi, C.; Santos, J. P.; Morey, A. T.; Marcato, P. D.; Duran, N.; Pinge-Filho, P.; Nakazato, G.; Yamada-Ogatta, S. F.; Yamauchi, L. M., Combination of fluconazole with silver nanoparticles produced by Fusarium oxysporum improves antifungal effect against planktonic cells and biofilm of drug-resistant Candida albicans. *Med Mycol* **2015**.

115. Ke, P. C.; Lin, S.; Parak, W. J.; Davis, T. P.; Caruso, F., A Decade of the Protein Corona. *ACS Nano* **2017**.

116. Forest, V.; Pourchez, J., The nanoparticle protein corona: The myth of average. *Nano Today* **2016**.

117. Delpino, P.; Pelaz, B.; Zhang, Q.; Maffre, P.; Nienhaus, G. U.; Parak, W. J., Protein corona formation around nanoparticles—from the past to the future. *Mater Horiz* **2014,** *1*.

118. Monopoli, M. P.; Pitek, A. S.; Lynch, I.; Dawson, K. A., Formation and Characterization of the Nanoparticle–Protein Corona. In *Nanomaterial Interfaces in Biology: Methods and Protocols*, Bergese, P.; Hamad-Schifferli, K., Eds. Humana Press: Totowa, NJ, 2013; pp 137-155.

119. Monopoli, M. P.; Åberg, C.; Salvati, A.; Dawson, K. A., Biomolecular coronas provide the biological identity of nanosized materials. *Nat Nanotechnol* **2012,** *7*.

120. Monopoli, M. P.; Bombelli, F. B.; Dawson, K. A., Nanobiotechnology: Nanoparticle coronas take shape. *Nature Nanotechnology* **2011,** *6* (1), 11-12.

121. Monopoli, M. P.; Walczyk, D.; Campbell, A.; Elia, G.; Lynch, I.; Baldelli Bombelli, F.; Dawson, K. A., Physical–Chemical Aspects of Protein Corona: Relevance to in Vitro and in Vivo Biological Impacts of Nanoparticles. *J. Am. Chem. Soc.* **2011,** *133* (8), 2525-2534.

122. Monopoli, M. P.; Baldelli Bombelli, F.; Dawson, K. A., Nanobiotechnology: nanoparticle coronas take shape. *Nat Nanotechnol* **2011,** *6*.

123. Cedervall, T.; Lynch, I.; Lindman, S.; Berggard, T.; Thulin, E.; Nilsson, H.; Dawson, K. A.; Linse, S., Understanding the nanoparticle-protein corona using methods to quantify exchange rates and affinities of proteins for nanoparticles. *Proc Natl Acad Sci USA* **2007,** *104*.

124. Zanganeh, S.; Spitler, R.; Erfanzadeh, M.; Alkilany, A. M.; Mahmoudi, M., Protein corona: Opportunities and challenges. *The International Journal of Biochemistry & Cell Biology* **2016,** *75*, 143-147.

125. Docter, D.; Westmeier, D.; Markiewicz, M.; Stolte, S.; Knauer, S. K.; Stauber, R. H., The nanoparticle biomolecule corona: lessons learned - challenge accepted? *Chem. Soc. Rev.* **2015,** *44* (17), 6094-6121.

126. Cedervall, T.; Lynch, I.; Lindman, S.; Berggård, T.; Thulin, E.; Nilsson, H.; Dawson, K. A.; Linse, S., Understanding the nanoparticle–protein corona using methods to quantify exchange rates and affinities of proteins for nanoparticles. *Proceedings of the National Academy of Sciences* **2007,** *104* (7), 2050-2055.

127. Monopoli, M. P.; Aberg, C.; Salvati, A.; Dawson, K. A., Biomolecular coronas provide the biological identity of nanosized materials. *Nat Nanotechnol* **2012,** *7* (12), 779-86.

128. Durán, N.; Silveira, C. P.; Durán, M.; Martinez, D. S. T., Silver nanoparticle protein corona and toxicity: a mini-review. *Journal of Nanobiotechnology* **2015,** *13* (1), 55.

129. Lee, Y. K.; Choi, E.-J.; Webster, T. J.; Kim, S.-H.; Khang, D., Effect of the protein corona on nanoparticles for modulating cytotoxicity and immunotoxicity. *International Journal of Nanomedicine* **2015,** *10*, 97-113.

130. Wen, Y.; Geitner, N. K.; Chen, R.; Ding, F.; Chen, P.; Andorfer, R. E.; Govindan, P. N.; Ke, P. C., Binding of cytoskeletal proteins with silver nanoparticles. *RSC Advances* **2013,** *3* (44), 22002-22007.

131. Monopoli, M. P.; Walczyk, D.; Campbell, A.; Elia, G.; Lynch, I.; Bombelli, F. B.; Dawson, K. A., Physical–chemical aspects of protein corona: relevance to in vitro and in vivo biological impacts of nanoparticles. *J. Am. Chem. Soc.* **2011,** *133*.

132. Saha, K.; Rahimi, M.; Yazdani, M.; Kim, S. T.; Moyano, D. F.; Hou, S.; Das, R.; Mout, R.; Rezaee, F.; Mahmoudi, M.; Rotello, V. M., Regulation of Macrophage Recognition through the Interplay of Nanoparticle Surface Functionality and Protein Corona. *ACS Nano* **2016,** *10* (4), 4421-4430.

133. Mukherjee, P.; Roy, M.; Mandal, B. P.; Dey, G. K.; Mukherjee, P. K.; Ghatak, J.; Tyagi, A. K.; Kale, S. P., Green synthesis of highly stabilized nanocrystalline silver particles by a non-pathogenic and agriculturally important fungus T. asperellum. *Nanotechnology* **2008,** *19* (7), 075103.

134. Sanghi, R.; Verma, P., Biomimetic synthesis and characterisation of protein capped silver nanoparticles. *Bioresour. Technol.* **2009,** *100* (1), 501-504.

135. Kneipp, K.; Haka, A. S.; Kneipp, H.; Badizadegan, K.; Yoshizawa, N.; Boone, C.; Shafer-Peltier, K. E.; Motz, J. T.; Dasari, R. R.; Feld, M. S., Surface-Enhanced Raman Spectroscopy in Single Living Cells Using Gold Nanoparticles. *Appl. Spectrosc.* **2002,** *56* (2), 150-154.

136. Kneipp, K.; Flemming, J., Surface enhanced Raman scattering (SERS) of nucleic acids adsrobed on colloidal silver particles. *J. Mol. Struct.* **1986,** *145* (1), 173-179.

137. Love, J. C.; Estroff, L. A.; Kriebel, J. K.; Nuzzo, R. G.; Whitesides, G. M., Self-Assembled Monolayers of Thiolates on Metals as a Form of Nanotechnology. *Chem. Rev.* **2005,** *105* (4), 1103-1170.

138. Nuzzo, R. G.; Allara, D. L., Adsorption of bifunctional organic disulfides on gold surfaces. *J. Am. Chem. Soc.* **1983,** *105* (13), 4481-4483.

139. Bumm, L. A.; Arnold, J. J.; Cygan, M. T.; Dunbar, T. D.; Burgin, T. P.; Jones, L.; Allara, D. L.; Tour, J. M.; Weiss, P. S., Are Single Molecular Wires Conducting? *Science* **1996,** *271* (5256), 1705.

140. Tour, J. M., Molecular Electronics. Synthesis and Testing of Components. *Acc. Chem. Res.* **2000,** *33* (11), 791-804.

141. Vericat, C.; Vela, M. E.; Benitez, G.; Carro, P.; Salvarezza, R. C., Self-assembled monolayers of thiols and dithiols on gold: new challenges for a well-known system. *Chem. Soc. Rev.* **2010,** *39* (5), 1805-1834.

142. Bonanni, B.; Bizzarri, A. R.; Cannistraro, S., Optimized Biorecognition of Cytochrome c 551 and Azurin Immobilized on Thiol-Terminated Monolayers Assembled on Au(111) Substrates. *The Journal of Physical Chemistry B* **2006,** *110* (30), 14574-14580.

143. Laibinis, P. E.; Whitesides, G. M.; Allara, D. L.; Tao, Y. T.; Parikh, A. N.; Nuzzo, R. G., Comparison of the structures and wetting properties of self-assembled monolayers of n-alkanethiols on the coinage metal surfaces, copper, silver, and gold. *J. Am. Chem. Soc.* **1991,** *113* (19), 7152-7167.

144. Walczak, M. M.; Chung, C.; Stole, S. M.; Widrig, C. A.; Porter, M. D., Structure and interfacial properties of spontaneously adsorbed n-alkanethiolate monolayers on evaporated silver surfaces. *J. Am. Chem. Soc.* **1991,** *113* (7), 2370-2378.

145. Ni, J.; Lipert, R. J.; Dawson, G. B.; Porter, M. D., Immunoassay Readout Method Using Extrinsic Raman Labels Adsorbed on Immunogold Colloids. *Anal. Chem.* **1999,** *71* (21), 4903-4908.

146. Weisbecker, C. S.; Merritt, M. V.; Whitesides, G. M., Molecular Self-Assembly of Aliphatic Thiols on Gold Colloids. *Langmuir* **1996,** *12* (16), 3763-3772.

147. Porter, M. D.; Bright, T. B.; Allara, D. L.; Chidsey, C. E. D., Spontaneously organized molecular assemblies. 4. Structural characterization of n-alkyl thiol monolayers on gold by optical ellipsometry, infrared spectroscopy, and electrochemistry. *J. Am. Chem. Soc.* **1987,** *109* (12), 3559-3568.

148. Frey, S.; Stadler, V.; Heister, K.; Eck, W.; Zharnikov, M.; Grunze, M.; Zeysing, B.; Terfort, A., Structure of Thioaromatic Self-Assembled Monolayers on Gold and Silver. *Langmuir* **2001,** *17* (8), 2408-2415.

149. Hermanson, G. T., *Bioconjugate Techniques*. Academic Press: London, 2013; Vol. Third edition.

150. Bartczak, D.; Kanaras, A. G., Preparation of Peptide-Functionalized Gold Nanoparticles Using One Pot EDC/Sulfo-NHS Coupling. *Langmuir* **2011,** *27* (16), 10119-10123.

151. Filbrun, S. L.; Driskell, J. D., A fluorescence-based method to directly quantify antibodies immobilized on gold nanoparticles. *Analyst* **2016,** *141* (12), 3851-3857.

152. Lim, C. Y.; Owens, N. A.; Wampler, R. D.; Ying, Y.; Granger, J. H.; Porter, M. D.; Takahashi, M.; Shimazu, K., Succinimidyl Ester Surface Chemistry: Implications of the Competition between Aminolysis and Hydrolysis on Covalent Protein Immobilization. *Langmuir* **2014,** *30* (43), 12868-12878.

153. Sapsford, K. E.; Algar, W. R.; Berti, L.; Gemmill, K. B.; Casey, B. J.; Oh, E.; Stewart, M. H.; Medintz, I. L., Functionalizing Nanoparticles with Biological Molecules: Developing Chemistries that Facilitate Nanotechnology. *Chem. Rev.* **2013,** *113* (3), 1904-2074.

154. Quaroni, L.; Chumanov, G., Preparation of Polymer-Coated Functionalized Silver Nanoparticles. *J. Am. Chem. Soc.* **1999,** *121* (45), 10642-10643.

155. Evanoff, D. D.; Chumanov, G., Synthesis and Optical Properties of Silver Nanoparticles and Arrays. *ChemPhysChem* **2005,** *6* (7), 1221-1231.

156. Grzelczak, M.; Perez-Juste, J.; Mulvaney, P.; Liz-Marzan, L. M., Shape control in gold nanoparticle synthesis. *Chem. Soc. Rev.* **2008,** *37* (9), 1783-1791.

157. Zhao, P.; Li, N.; Astruc, D., State of the art in gold nanoparticle synthesis. *Coord. Chem. Rev.* **2013,** *257* (3–4), 638-665.

158. Thanh, N. T. K.; Maclean, N.; Mahiddine, S., Mechanisms of Nucleation and Growth of Nanoparticles in Solution. *Chem. Rev.* **2014,** *114* (15), 7610-7630.

159. Thakkar, K. N.; Mhatre, S. S.; Parikh, R. Y., Biological synthesis of metallic nanoparticles. *Nanomedicine : nanotechnology, biology, and medicine* **2010,** *6* (2), 257-62.

160. Ahmed, S.; Ahmad, M.; Swami, B. L.; Ikram, S., A review on plants extract mediated synthesis of silver nanoparticles for antimicrobial applications: A green expertise. *Journal of Advanced Research* **2016,** *7* (1), 17-28.

161. Ahmad, A.; Senapati, S.; Khan, M. I.; Kumar, R.; Sastry, M., Extra-/Intracellular Biosynthesis of Gold Nanoparticles by an Alkalotolerant Fungus, Trichothecium sp. *Journal of Biomedical Nanotechnology* **2005,** *1* (1), 47-53.

162. Mukherjee, P.; Senapati, S.; Mandal, D.; Ahmad, A.; Khan, M.; Kumar, R.; Sastry, M., Extracellular synthesis of gold nanoparticles by the fungus Fusarium oxysporum. *ChemBioChem* **2002,** *3*, 461 - 463.

163. Song, J. Y.; Kim, B. S., Rapid biological synthesis of silver nanoparticles using plant leaf extracts. *Bioprocess and Biosystems Engineering* **2009,** *32* (1), 79-84.

164. Gericke, M.; Pinches, A., Biological synthesis of metal nanoparticles. *Hydrometallurgy* **2006,** *83* (1-4), 132-140.

165. Paramelle, D.; Sadovoy, A.; Gorelik, S.; Free, P.; Hobley, J.; Fernig, D. G., A rapid method to estimate the concentration of citrate capped silver nanoparticles from UV-visible light spectra. *Analyst* **2014,** *139* (19), 4855-4861.

166. Rasband, W. S. *ImageJ*, U. S. National Institutes of Health, Bethesda, MD. http://imagej.nih.gov/ij/.

167. Nayak, R. R.; Pradhan, N.; Behera, D.; Pradhan, K. M.; Mishra, S.; Sukla, L. B.; Mishra, B. K., Green synthesis of silver nanoparticle by Penicillium purpurogenum NPMF: the process and optimization. *J. Nanopart. Res.* **2011,** *13* (8), 3129-3137.

168. Alarcon, E. I.; Griffith, M.; Udekwu, K. I., Silver Nanoparticle Applications : In the Fabrication and Design of Medical and Biosensing Devices. Springer International Publishing: 2015.

169. Hirtzel, C. S.; Rajagopalan, R., *Colloidal Phenomena: Advanced Topics*. Noyes Publications Park Ridge, N.J., 1985.

170. Gunawan, C.; Lim, M.; Marquis, C. P.; Amal, R., Nanoparticle-protein corona complexes govern the biological fates and functions of nanoparticles. *Journal of Materials Chemistry B* **2014,** *2* (15), 2060-2083.

171. Jain, N.; Bhargava, A.; Majumdar, S.; Tarafdar, J. C.; Panwar, J., Extracellular biosynthesis and characterization of silver nanoparticles using Aspergillus flavus NJP08: A mechanism perspective. *Nanoscale* **2011,** *3* (2), 635-641.

172. Zhang, X.; He, X.; Wang, K.; Yang, X., Different Active Biomolecules Involved in Biosynthesis of Gold Nanoparticles by Three Fungus Species. *Journal of Biomedical Nanotechnology* **2011,** *7* (2), 245-254.

173. Ingle, A.; Gade, A.; Pierrat, P.; Sonnichsen, C.; Rai, M., Mycosynthesis of Silver Nanoparticles Using the Fungus Fusarium acuminatum and its Activity Against Some Human Pathogenic Bacteria. *Current Nanoscience* **2008,** *4* (2), 141-144.

174. Chowdhury, S.; Basu, A.; Kundu, S., Green synthesis of protein capped silver nanoparticles from phytopathogenic fungus Macrophomina phaseolina (Tassi) Goid with antimicrobial properties against multidrug-resistant bacteria. *Nanoscale Research Letters* **2014,** *9* (1), 365.

175. Stoscheck, C. M., Quantitation of Protein. In *Methods Enzymol.*, Murray, P. D., Ed. Academic Press: San Diego: 1990; Vol. 182, pp 50-68.

176. Layne, E., Spectrophotometric and turbidimetric methods for measuring proteins. *Methods Enzymol.* **1957,** *3*, 447-454.

177. Alarcon, E. I.; Udekwu, K.; Skog, M.; Pacioni, N. L.; Stamplecoskie, K. G.; González-Béjar, M.; Polisetti, N.; Wickham, A.; Richter-Dahlfors, A.; Griffith, M.; Scaiano, J. C., The biocompatibility and antibacterial properties of collagen-stabilized, photochemically prepared silver nanoparticles. *Biomaterials* **2012,** *33* (19), 4947-4956.

178. Alarcon, E. I.; Vulesevic, B.; Argawal, A.; Ross, A.; Bejjani, P.; Podrebarac, J.; Ravichandran, R.; Phopase, J.; Suuronen, E. J.; Griffith, M., Coloured cornea replacements with anti-infective properties: expanding the safe use of silver nanoparticles in regenerative medicine. *Nanoscale* **2016,** *8* (12), 6484-6489.

179. Alarcon, E. I.; Bueno-Alejo, C. J.; Noel, C. W.; Stamplecoskie, K. G.; Pacioni, N. L.; Poblete, H.; Scaiano, J. C., Human serum albumin as protecting agent of silver nanoparticles:

role of the protein conformation and amine groups in the nanoparticle stabilization. *J. Nanopart. Res.* **2013,** *15* (1), 1-14.

180. Turner, A. P. F., Biosensors: sense and sensibility. *Chem. Soc. Rev.* **2013,** *42* (8), 3184-3196.

181. Stark, W. J.; Stoessel, P. R.; Wohlleben, W.; Hafner, A., Industrial applications of nanoparticles. *Chem. Soc. Rev.* **2015,** *44* (16), 5793-5805.

182. Rai, M.; Ingle, A. P.; Birla, S.; Yadav, A.; Santos, C. A. D., Strategic role of selected noble metal nanoparticles in medicine. *Critical Reviews in Microbiology* **2016,** *42* (5), 696-719.

183. Rajput, S.; Werezuk, R.; Lange, R. M.; McDermott, M. T., Fungal Isolate Optimized for Biogenesis of Silver Nanoparticles with Enhanced Colloidal Stability. *Langmuir* **2016,** *32* (34), 8688-8697.

184. Cedervall, T.; Lynch, I.; Foy, M.; Berggard, T.; Donnelly, S. C.; Cagney, G.; Linse, S.; Dawson, K. A., Detailed identification of plasma proteins adsorbed on copolymer nanoparticles. *Angew. Chem. Int. Ed. Engl.* **2007,** *46* (30), 5754-6.

185. Colangelo, E.; Comenge, J.; Paramelle, D.; Volk, M.; Chen, Q.; Lévy, R., Characterizing Self-Assembled Monolayers on Gold Nanoparticles. *Bioconjugate Chem.* **2017,** *28* (1), 11-22.

186. Duran, N.; Marcato, P. D.; De Souza, G. I. H.; Alves, O. L.; Esposito, E., Antibacterial Effect of Silver Nanoparticles Produced by Fungal Process on Textile Fabrics and Their Effluent Treatment. *JOURNAL OF BIOMEDICAL NANOTECHNOLOGY* **2007,** *3* (2), 203-208.

187. Bansal, V.; Rautaray, D.; Ahmad, A.; Sastry, M., Biosynthesis of zirconia nanoparticles using the fungus Fusarium oxysporum. *J. Mater. Chem.* **2004,** *14* (22), 3303-3305.

188. Marcato, P. D.; Nakasato, G.; Brocchi, M.; Melo, P. S.; Huber, S. C.; Ferreira, I. R.; Alves, O. L.; Duran, N., Biogenic silver nanoparticles: Antibacterial and cytotoxicity applied to textile fabrics. **2012,** *20*, 69-76.

189. Qian, H.; Laurentius, L.; Egerton, R. F., Artefacts Induced on Soft Layer of Hybrid Metallic Nanoparticles in TEM. *Microsc. Microanal.* **2015,** *21* (S3), 1551-1552.

190. Reference equation for laser spot diameter: https://www.olympus-ims.com/en/microscope/terms/luminous_flux/ [Accessed 30 March 2018].

191. Green, M. R., Molecular cloning : a laboratory manual. 4th ed. ed.; Sambrook, J., Ed. Cold Spring Harbor Laboratory Press: Cold Spring Harbor, N.Y. :, 2012.

192. Bollag, D. M.; Edelstein, S. J., Protein methods / Daniel M. Bollag, Stuart J. Edelstein. New York : Wiley-Liss, c1991.: 1991.

193. Schagger, H., Tricine-SDS-PAGE. *Nat. Protocols* **2006,** *1* (1), 16-22.

194. Neuhoff, V.; Arold, N.; Taube, D.; Ehrhardt, W., Improved staining of proteins in polyacrylamide gels including isoelectric focusing gels with clear background at nanogram sensitivity using Coomassie Brilliant Blue G-250 and R-250. *Electrophoresis* **1988,** *9* (6), 255-262.

195. Shevchenko, A.; Wilm, M.; Vorm, O.; Mann, M., Mass Spectrometric Sequencing of Proteins from Silver-Stained Polyacrylamide Gels. *Anal. Chem.* **1996,** *68* (5), 850-858.

196. Perkins, D. N.; Pappin, D. J. C.; Creasy, D. M.; Cottrell, J. S., Probability-based protein identification by searching sequence databases using mass spectrometry data. *Electrophoresis* **1999,** *20* (18), 3551-3567.

197. Hwang, T. L.; Shaka, A. J., Water Suppression That Works. Excitation Sculpting Using Arbitrary Wave-Forms and Pulsed-Field Gradients. *Journal of Magnetic Resonance, Series A* **1995,** *112* (2), 275-279.

198. Dalvit, C., Efficient multiple-solvent suppression for the study of the interactions of organic solvents with biomolecules. *J. Biomol. NMR* **1998,** *11* (4), 437-444.

199. Harris, R. B. B., E.D.; Cabral De Menezes, S.M.; Goodfellow, R.; and Granger, P., NMR Nomenclature. Nuclear Spin Properties and Conventions for Chemical Shifts. IUPAC Recommendations 2001. . *Pure Appl. Chem.* **2001,** *73* (11), 1795-1818.

200. Vroman, L.; Adams, A.; Fischer, G.; Munoz, P., Interaction of high molecular weight kininogen, factor XII, and fibrinogen in plasma at interfaces. *Blood* **1980,** *55* (1), 156-159.

201. Hirsh, S. L.; McKenzie, D. R.; Nosworthy, N. J.; Denman, J. A.; Sezerman, O. U.; Bilek, M. M. M., The Vroman effect: Competitive protein exchange with dynamic multilayer protein aggregates. *Colloids and Surfaces B: Biointerfaces* **2013,** *103*, 395-404.

202. Mabuchi, M.; Takenaka, T.; Fujiyoshi, Y.; Uyeda, N., Surface enhanced Raman scattering of citrate ions adsorbed on gold sol particles. *Surf. Sci.* **1982,** *119* (2–3), 150-158.

203. Fernandez-Iglesias, N.; Bettmer, J., Complementary mass spectrometric techniques for the quantification of the protein corona: a case study on gold nanoparticles and human serum proteins. *Nanoscale* **2015,** *7* (34), 14324-14331.

204. Horvath, H., Gustav Mie and the scattering and absorption of light by particles: Historic developments and basics. *J. Quant. Spectrosc. Radiat. Transfer* **2009,** *110* (11), 787-799.

205. Jain, N.; Bhargava, A.; Rathi, M.; Dilip, R. V.; Panwar, J., Removal of Protein Capping Enhances the Antibacterial Efficiency of Biosynthesized Silver Nanoparticles. *PLOS ONE* **2015,** *10* (7), e0134337.

206. McQuillan, A. J., The discovery of surface-enhanced Raman scattering. *Notes and Records of the Royal Society* **2009,** *63* (1), 105-109.

207. Guerrini, L.; Graham, D., Molecularly-mediated assemblies of plasmonic nanoparticles for Surface-Enhanced Raman Spectroscopy applications. *Chem. Soc. Rev.* **2012,** *41* (21), 7085-7107.

208. Laemmli, U. K., Cleavage of Structural Proteins during the Assembly of the Head of Bacteriophage T4. *Nature* **1970,** *227* (5259), 680-685.

209. Weber, K.; Osborn, M., The Reliability of Molecular Weight Determinations by Dodecyl Sulfate-Polyacrylamide Gel Electrophoresis. *J. Biol. Chem.* **1969,** *244* (16), 4406-4412.

210. Biosciences, B. D., BD Bionutrients Technical Manual In *Advanced Bioprocessing* [Online] Fourth ed.; Becton Dickinson and Company: Sparks, MD, 2015. https://www.bd.com/ds/technicalCenter/misc/lcn01558-bionutrients-manual.pdf.

211. Anil Kumar, S.; Abyaneh, M. K.; Gosavi, S. W.; Kulkarni, S. K.; Pasricha, R.; Ahmad, A.; Khan, M. I., Nitrate reductase-mediated synthesis of silver nanoparticles from AgNO3. *Biotechnol. Lett* **2007,** *29* (3), 439-445.

212. Gessler, N. N.; Aver'yanov, A. A.; Belozerskaya, T. A., Reactive oxygen species in regulation of fungal development. *Biochemistry (Moscow)* **2007,** *72* (10), 1091-1109.

213. Sun, Y.; Yi, X.; Peng, M.; Zeng, H.; Wang, D.; Li, B.; Tong, Z.; Chang, L.; Jin, X.; Wang, X., Proteomics of Fusarium oxysporum Race 1 and Race 4 Reveals Enzymes Involved in Carbohydrate Metabolism and Ion Transport That Might Play Important Roles in Banana Fusarium Wilt. *PLOS ONE* **2014,** *9* (12), e113818.

214. Aguirre, J.; Hansberg, W.; Navarro, R., Fungal responses to reactive oxygen species. *Medical Mycology* **2006,** *44* (Supplement_1), S101-S107.

215. Sharma, P.; Jha, A. B.; Dubey, R. S.; Pessarakli, M., Reactive Oxygen Species, Oxidative Damage, and Antioxidative Defense Mechanism in Plants under Stressful Conditions. *Journal of Botany* **2012,** *2012*, 26.

216. Gough, D. R.; Cotter, T. G., Hydrogen peroxide: a Jekyll and Hyde signalling molecule. *Cell Death and Dis* **2011,** *2*, e213.

217. Lamb, C.; Dixon, R. A., THE OXIDATIVE BURST IN PLANT DISEASE RESISTANCE. *Annual Review of Plant Physiology and Plant Molecular Biology* **1997,** *48* (1), 251-275.

218. Hamel, L.-P.; Nicole, M.-C.; Duplessis, S.; Ellis, B. E., Mitogen-Activated Protein Kinase Signaling in Plant-Interacting Fungi: Distinct Messages from Conserved Messengers. *The Plant Cell* **2012,** *24* (4), 1327-1351.

219. Gavanji, S.; Abdul Aziz, H.; Larki, B.; Mojiri, A., Bioinformatics prediction of interaction of silver nitrate and nano silver on catalase and nitrat reductase. *International Journal of Scientific Research in Environmental Sciences* **2013,** *1* (2), 26-35.

220. Ding, Z.; Li, M.; Sun, F.; Xi, P.; Sun, L.; Zhang, L.; Jiang, Z., Mitogen-Activated Protein Kinases Are Associated with the Regulation of Physiological Traits and Virulence in *Fusarium oxysporum* f. sp. *cubense*. *PLoS ONE* **2015,** *10* (4), e0122634.

221. Xu, J.-R., MAP Kinases in Fungal Pathogens. *Fungal Genetics and Biology* **2000,** *31* (3), 137-152.

222. Bailey, B. A.; Jennings, J. C.; Anderson, J. D., The 24-kDa protein from Fusarium oxysporum f.sp. erythroxyli: occurrence in related fungi and the effect of growth medium on its production. *Can. J. Microbiol.* **1997,** *43* (1), 45-55.

223. Radici, L.; Bianchi, M.; Crinelli, R.; Magnani, M., Ubiquitin C gene: Structure, function, and transcriptional regulation. *Advances in Bioscience and Biotechnology* **2013,** *4*, 1057-1062.

224. Hershko, A.; Ciechanover, A., THE UBIQUITIN SYSTEM. *Annu. Rev. Biochem* **1998,** *67* (1), 425-479.

225. Goldstein, G.; Scheid, M.; Hammerling, U.; Schlesinger, D. H.; Niall, H. D.; Boyse, E. A., Isolation of a polypeptide that has lymphocyte-differentiating properties and is probably represented universally in living cells. *Proceedings of the National Academy of Sciences* **1975,** *72* (1), 11-15.

226. Calzolai, L.; Franchini, F.; Gilliland, D.; Rossi, F., Protein−Nanoparticle Interaction: Identification of the Ubiquitin−Gold Nanoparticle Interaction Site. *Nano Lett.* **2010,** *10* (8), 3101-3105.

227. Jha, A. K.; Prasad, K.; Prasad, K.; Kulkarni, A. R., Plant system: Nature's nanofactory. *Colloids and Surfaces B: Biointerfaces* **2009,** *73* (2), 219-223.

228. Segorbe, D.; Di Pietro, A.; Pérez-Nadales, E.; Turrà, D., Three Fusarium oxysporum mitogen-activated protein kinases (MAPKs) have distinct and complementary roles in stress adaptation and cross-kingdom pathogenicity. *Molecular Plant Pathology* **2016**, n/a-n/a.

229. Gustin, M. C.; Albertyn, J.; Alexander, M.; Davenport, K., MAP Kinase Pathways in the Yeast Saccharomyces cerevisiae. *Microbiology and Molecular Biology Reviews* **1998,** *62* (4), 1264-1300.

230. Pitzschke, A.; Schikora, A.; Hirt, H., MAPK cascade signalling networks in plant defence. *Current Opinion in Plant Biology* **2009,** *12* (4), 421-426.

231. Schaeffer, H. J.; Weber, M. J., Mitogen-Activated Protein Kinases: Specific Messages from Ubiquitous Messengers. *Molecular and Cellular Biology* **1999,** *19* (4), 2435-2444.

232. Li, M.; Liu, J.; Zhang, C., Evolutionary History of the Vertebrate Mitogen Activated Protein Kinases Family. *PLoS ONE* **2011,** *6* (10), e26999.

233. Segorbe, D.; Di Pietro, A.; Perez-Nadales, E.; Turra, D., Three Fusarium oxysporum mitogen-activated protein kinases (MAPKs) have distinct and complementary roles in stress adaptation and cross-kingdom pathogenicity. *Mol Plant Pathol* **2017,** *18* (7), 912-924.

234. Kracht, S.; Messerer, M.; Lang, M.; Eckhardt, S.; Lauz, M.; Grobéty, B.; Fromm, K. M.; Giese, B., Electron Transfer in Peptides: On the Formation of Silver Nanoparticles. *Angew. Chem. Int. Ed.* **2015,** *54* (10), 2912-2916.

235. Ballottin, D.; Fulaz, S.; Souza, M. L.; Corio, P.; Rodrigues, A. G.; Souza, A. O.; Gaspari, P. M.; Gomes, A. F.; Gozzo, F.; Tasic, L., Elucidating Protein Involvement in the Stabilization of the Biogenic Silver Nanoparticles. *Nanoscale Research Letters* **2016,** *11* (1), 1-9.

236. Swiss Prot Database. 5933 active entries. Accessed 15 March 2017.

237. Swiss Prot Database. 5933 active entries. Accessed 15 March 2017.

238. Swiss Prot Database. 5933 active entries. Accessed 15 March 2017.

239. Wan, S.; Kelly, P. M.; Mahon, E.; Stöckmann, H.; Rudd, P. M.; Caruso, F.; Dawson, K. A.; Yan, Y.; Monopoli, M. P., The "Sweet" Side of the Protein Corona: Effects of Glycosylation on Nanoparticle–Cell Interactions. *ACS Nano* **2015,** *9* (2), 2157-2166.

240. Bubb, W. A., NMR spectroscopy in the study of carbohydrates: Characterizing the structural complexity. *Concepts in Magnetic Resonance Part A* **2003,** *19A* (1), 1-19.

241. Wüthrich, K., NMR of proteins and nucleic acids. Wiley: New York :, 1986.

242. Masjedi-Arani, M.; Salavati-Niasari, M., Effect of carbohydrate sugars as a capping agent on the size and morphology of pure Zn2SnO4 nanostructures and their optical properties. *Mater. Lett.* **2016,** *174*, 71-74.

243. de la Fuente, J. M.; Penadés, S., Glyconanoparticles: Types, synthesis and applications in glycoscience, biomedicine and material science. *Biochimica et Biophysica Acta (BBA) - General Subjects* **2006,** *1760* (4), 636-651.

244. Suvarna, S.; Das, U.; Kc, S.; Mishra, S.; Sudarshan, M.; Saha, K. D.; Dey, S.; Chakraborty, A.; Narayana, Y., Synthesis of a novel glucose capped gold nanoparticle as a better theranostic candidate. *PLOS ONE* **2017,** *12* (6), e0178202.

245. Alocilja, E. C.; Anderson, M. J.; Torres-Chavolla, E. Metallic Nanoparticle Synthesis with Carbohydrate Capping Agent. Feb. 28, 2017 2017.

246. Fulmer, G. R.; Miller, A. J. M.; Sherden, N. H.; Gottlieb, H. E.; Nudelman, A.; Stoltz, B. M.; Bercaw, J. E.; Goldberg, K. I., NMR Chemical Shifts of Trace Impurities: Common Laboratory Solvents, Organics, and Gases in Deuterated Solvents Relevant to the Organometallic Chemist. *Organometallics* **2010,** *29* (9), 2176-2179.

247. Naik, R. R.; Stringer, S. J.; Agarwal, G.; Jones, S. E.; Stone, M. O., Biomimetic synthesis and patterning of silver nanoparticles. *Nat Mater* **2002,** *1* (3), 169-172.

248. Kelly, P. M.; Åberg, C.; Polo, E.; O'Connell, A.; Cookman, J.; Fallon, J.; KrpetićŽeljka; Dawson, K. A., Mapping protein binding sites on the biomolecular corona of nanoparticles. *Nat Nano* **2015,** *10* (5), 472-479.

249. Clem Gruen, L., Interaction of amino acids with silver(I) ions. *Biochimica et Biophysica Acta (BBA) - Protein Structure* **1975,** *386* (1), 270-274.

250. Poblete, H.; Agarwal, A.; Thomas, S. S.; Bohne, C.; Ravichandran, R.; Phospase, J.; Comer, J.; Alarcon, E. I., New Insights into Peptide-Silver Nanoparticle Interaction:

Deciphering the Role of Cysteine and Lysine in the Peptide Sequence. *Langmuir* **2016,** *32* (1), 265-73.

251. Lomant, A. J.; Fairbanks, G., Chemical probes of extended biological structures: Synthesis and properties of the cleavable protein cross-linking reagent [35S]dithiobis(succinimidyl propionate). *J. Mol. Biol.* **1976,** *104* (1), 243-261.

252. Gelest Techical Document - Coupling Agents. https://www.gelest.com/wp-content/uploads/Goods-PDF-brochures-couplingagents.pdf [Accessed 1 April 2018].

253. Susan Tilford, Gelest, personal communication, 2017.

254. Reference equation for laser spot diameter: https://www.olympus-ims.com/en/microscope/terms/luminous_flux/ [Accessed 30 March 2018].

255. Reference equation for laser spot diameter: https://www.olympus-ims.com/en/microscope/terms/luminous_flux/ [Accessed 30 March 2018].

256. Friedrich, M. Spectragryph - optical spectroscopy software, Version 1.2.5, 2016-2017, http://www.effemm2.de/spectragryph/.

257. Paul Concepcion, personal communication, 2017.

258. Nečas, D.; Klapetek, P., Gwyddion: an open-source software for SPM data analysis. *Central European Journal of Physics* **2012,** *10* (1), 181-188.

259. Anker, J. N.; Hall, W. P.; Lyandres, O.; Shah, N. C.; Zhao, J.; Van Duyne, R. P., Biosensing with plasmonic nanosensors. *Nature Materials* **2008,** *7*, 442.

260. Jain, P. K.; Lee, K. S.; El-Sayed, I. H.; El-Sayed, M. A., Calculated Absorption and Scattering Properties of Gold Nanoparticles of Different Size, Shape, and Composition: Applications in Biological Imaging and Biomedicine. *The Journal of Physical Chemistry B* **2006,** *110* (14), 7238-7248.

261. Lee, K.-S.; El-Sayed, M. A., Dependence of the Enhanced Optical Scattering Efficiency Relative to That of Absorption for Gold Metal Nanorods on Aspect Ratio, Size, End-Cap Shape, and Medium Refractive Index. *The Journal of Physical Chemistry B* **2005,** *109* (43), 20331-20338.

262. Jakubowicz, A.; Jia, H.; Wallace, R. M.; Gnade, B. E., Adsorption Kinetics of p-Nitrobenzenethiol Self-Assembled Monolayers on a Gold Surface. *Langmuir* **2005,** *21* (3), 950-955.

263. Kim, K.; Lee, I.; Lee, S. J., Photolytic reduction of 4-nitrobenzenethiol on Au mediated via Ag nanoparticles. *Chem. Phys. Lett.* **2003,** *377* (1–2), 201-204.

264. van Schrojenstein Lantman, E. M.; Deckert-Gaudig, T.; Mank, A. J. G.; Deckert, V.; Weckhuysen, B. M., Catalytic processes monitored at the nanoscale with tip-enhanced Raman spectroscopy. *Nat Nano* **2012,** *7* (9), 583-586.

265. Sun, M.; Zhang, Z.; Zheng, H.; Xu, H., In-situ plasmon-driven chemical reactions revealed by high vacuum tip-enhanced Raman spectroscopy. *Scientific Reports* **2012,** *2*, 647.

266. Futamata, M., Surface-Plasmon-Polariton-Enhanced Raman Scattering from Self-Assembled Monolayers of p-Nitrothiophenol and p-Aminothiophenol on Silver. *The Journal of Physical Chemistry* **1995,** *99* (31), 11901-11908.

267. Skadtchenko, B. O.; Aroca, R., Surface-enhanced Raman scattering of p-nitrothiophenol: Molecular vibrations of its silver salt and the surface complex formed on silver islands and colloids. *Spectrochimica Acta Part A: Molecular and Biomolecular Spectroscopy* **2001,** *57* (5), 1009-1016.

268. Shin, K. S.; Lee, H. S.; Joo, S. W.; Kim, K., Surface-Induced Photoreduction of 4-Nitrobenzenethiol on Cu Revealed by Surface-Enhanced Raman Scattering Spectroscopy. *The Journal of Physical Chemistry C* **2007,** *111* (42), 15223-15227.

269. Lambert, J. B.; Shurvell, H. F.; Lightner, D.; Cooks, R. G., *Introduction to organic spectroscopy*. New York : Macmillan, c1987.: 1987.

270. Nsiah, F. Surface spectroscopies for evaluating protein binding. University of Alberta, 2007.

271. Alvarez-Puebla, R. A.; Dos Santos Jr, D. S.; Aroca, R. F., Surface-enhanced Raman scattering for ultrasensitive chemical analysis of 1 and 2-naphthalenethiols. *Analyst* **2004,** *129* (12), 1251-1256.

272. McCreery, R. L., *Raman spectroscopy for chemical analysis*. New York : John Wiley & Sons, c2000.: 2000.

273. Li, R.; Ji, W.; Chen, L.; Lv, H.; Cheng, J.; Zhao, B., Vibrational spectroscopy and density functional theory study of 4-mercaptophenol. *Spectrochimica Acta Part A: Molecular and Biomolecular Spectroscopy* **2014,** *122*, 698-703.

274. Liptak, M. D.; Gross, K. C.; Seybold, P. G.; Feldgus, S.; Shields, G. C., Absolute pKa Determinations for Substituted Phenols. *J. Am. Chem. Soc.* **2002,** *124* (22), 6421-6427.

275. Weller, C. E.; Dhall, A.; Ding, F.; Linares, E.; Whedon, S. D.; Senger, N. A.; Tyson, E. L.; Bagert, J. D.; Li, X.; Augusto, O.; Chatterjee, C., Aromatic thiol-mediated cleavage of N–O bonds enables chemical ubiquitylation of folded proteins. *Nature Communications* **2016,** *7*, 12979.

276. Tay, L.-L.; Hulse, J., Surface-enhanced Raman and optical scattering in coupled plasmonic nanoclusters. *Journal of Modern Optics* **2013,** *60* (14), 1107-1114.

277. Kwasnieski, D. T.; Wang, H.; Schultz, Z. D., Alkyl-nitrile adlayers as probes of plasmonically induced electric fields. *Chemical Science* **2015,** *6* (8), 4484-4494.

278. Wang, S.; Tay, L. L.; Liu, H., A SERS and electrical sensor from gas-phase generated Ag nanoparticles self-assembled on planar substrates. *Analyst* **2016,** *141* (5), 1721-1733.

279. Wang, H.; Yao, K.; Parkhill, J. A.; Schultz, Z. D., Detection of electron tunneling across plasmonic nanoparticle-film junctions using nitrile vibrations. *PCCP* **2017,** *19* (8), 5786-5796.

280. Anderson, S. L.; Luber, E. J.; Olsen, B. C.; Buriak, J. M., Substance over Subjectivity: Moving beyond the Histogram. *Chem. Mater.* **2016,** *28* (17), 5973-5975.

281. Murphy, C. J.; Buriak, J. M., Best Practices for the Reporting of Colloidal Inorganic Nanomaterials. *Chem. Mater.* **2015,** *27* (14), 4911-4913.

282. Scott, D., *Averaged Shifted Histogram*. 2009; Vol. 2, p 160-164.

283. Scott, D. W., On optimal and data-based histograms. *Biometrika* **1979,** *66* (3), 605-610.

284. Dr. Jean-Francois Masson, 2017, personal communication.

285. Ratel, M.; Provencher-Girard, A.; Zhao, S. S.; Breault-Turcot, J.; Labrecque-Carbonneau, J.; Branca, M.; Pelletier, J. N.; Schmitzer, A. R.; Masson, J.-F., Imidazolium-Based Ionic Liquid Surfaces for Biosensing. *Anal. Chem.* **2013,** *85* (12), 5770-5777.

286. Breault-Turcot, J.; Poirier-Richard, H. P.; Couture, M.; Pelechacz, D.; Masson, J. F., Single chip SPR and fluorescent ELISA assay of prostate specific antigen. *Lab on a Chip* **2015,** *15* (23), 4433-4440.

287. Hill, R. T.; Mock, J. J.; Urzhumov, Y.; Sebba, D. S.; Oldenburg, S. J.; Chen, S.-Y.; Lazarides, A. A.; Chilkoti, A.; Smith, D. R., Leveraging Nanoscale Plasmonic Modes to Achieve Reproducible Enhancement of Light. *Nano Lett.* **2010,** *10* (10), 4150-4154.

288. Marinica, D. C.; Kazansky, A. K.; Nordlander, P.; Aizpurua, J.; Borisov, A. G., Quantum Plasmonics: Nonlinear Effects in the Field Enhancement of a Plasmonic Nanoparticle Dimer. *Nano Lett.* **2012,** *12* (3), 1333-1339.

289. Rohr, T. E.; Cotton, T.; Fan, N.; Tarcha, P. J., Immunoassay employing surface-enhanced Raman spectroscopy. *Anal. Biochem.* **1989,** *182* (2), 388-398.

290. Crawford, A. C.; Laurentius, L. B.; Mulvihill, T. S.; Granger, J. H.; Spencer, J. S.; Chatterjee, D.; Hanson, K. E.; Porter, M. D., Detection of the tuberculosis antigenic marker mannose-capped lipoarabinomannan in pretreated serum by surface-enhanced Raman scattering. *Analyst* **2017,** *142* (1), 186-196.

291. Grubisha, D. S.; Lipert, R. J.; Park, H.-Y.; Driskell, J.; Porter, M. D., Femtomolar Detection of Prostate-Specific Antigen: An Immunoassay Based on Surface-Enhanced Raman Scattering and Immunogold Labels. *Anal. Chem.* **2003,** *75* (21), 5936-5943.

292. Gelest Techical Document - Coupling Agents. https://www.gelest.com/wp-content/uploads/Goods-PDF-brochures-couplingagents.pdf [Accessed 1 April 2018].

293. Susan Tilford, Gelest, personal communication, 2017.

294. M. Ervik, F. Lam, J. Ferlay, L. Mery, I. Soerjomataram, F. Bray (2016). Cancer Today. Lyon, France: International Agency for Research on Cancer. Cancer Today. Available from: http://gco.iarc.fr/today. [Accessed 19 March 2018].

295. Canadian Cancer Society's Advisory Committee on Cancer

Statistics. Canadian Cancer Statistics 2017. Toronto, ON: Canadian Cancer Society; 2017. Available at: cancer.ca/Canadian-Cancer-Statistics-2017-EN.pdf [Accessed 30 March 2018].

296. SEER Cancer Statistics Factsheets: Common Cancer Sites. National Cancer Institute. Bethesda, MD, https://seer.cancer.gov/statfacts/html/common.html [Accessed 20 March 2018].

297. SEER Cancer Stat Facts: Prostate Cancer. National Cancer Institute. Bethesda, MD, http://seer.cancer.gov/statfacts/html/prost.html. [Accessed 19 March 2018].

298. Canadian Cancer Statistics Advisory Committee. Canadian Cancer Statistics 2017. Toronto, ON: Canadian Cancer Society; 2017. Available at: cancer.ca/Canadian-Cancer-Statistics-2017-EN.pdf. [Accessed 18 March 2018].

299. SEER Cancer Stat Facts: Prostate Cancer. National Cancer Institute. Bethesda, MD, http://seer.cancer.gov/statfacts/html/prost.html. [Accessed 19 March 2018].

300. Gaudreau, P.-O.; Stagg, J.; Soulières, D.; Saad, F., The Present and Future of Biomarkers in Prostate Cancer: Proteomics, Genomics, and Immunology Advancements:Supplementary Issue: Biomarkers and their Essential Role in the Development of Personalised Therapies (A). B*iomarkers in Cancer 2***016,** 8*s2,* BIC.S31802.

301. Huggins, C.; Hodges, C. V., Studies on Prostatic Cancer. I. The Effect of Castration, of Estrogen and of Androgen Injection on Serum Phosphatases in Metastatic Carcinoma of the Prostate. C*ancer Research 1***941,** 1 (4), 293-297.

302. Li, Y.; Xie, N.; Gleave, M. E.; Rennie, P. S.; Dong, X., AR-v7 protein expression is regulated by protein kinase and phosphatase. O*ncotarget 2***015,** 6 (32), 33743-33754.

303. Antonarakis, E. S.; Armstrong, A. J.; Dehm, S. M.; Luo, J., Androgen receptor variant-driven prostate cancer: clinical implications and therapeutic targeting. P*rostate Cancer And Prostatic Disease 2***016,** 1*9,* 231.

304. Bastos, D. A.; Antonarakis, E. S., CTC-derived AR-V7 detection as a prognostic and predictive biomarker in advanced prostate cancer. E*xpert Review of Molecular Diagnostics 2***018,** 1*8* (2), 155-163.

305. Maughan, B. L.; Antonarakis, E. S., Androgen pathway resistance in prostate cancer and therapeutic implications. E*xpert Opinion on Pharmacotherapy 2***015,** 1*6* (10), 1521-1537.

306. Antonarakis, E. S.; Lu, C.; Wang, H.; Luber, B.; Nakazawa, M.; Roeser, J. C.; Chen, Y.; Mohammad, T. A.; Chen, Y.; Fedor, H. L.; Lotan, T. L.; Zheng, Q.; De Marzo, A. M.; Isaacs, J. T.; Isaacs, W. B.; Nadal, R.; Paller, C. J.; Denmeade, S. R.; Carducci, M. A.; Eisenberger, M. A.; Luo, J., AR-V7 and Resistance to Enzalutamide and Abiraterone in Prostate Cancer. N*ew England Journal of Medicine 2***014,** 3*71* (11), 1028-1038.

307. Attard, G.; Cooper, C. S.; de Bono, J. S., Steroid Hormone Receptors in Prostate Cancer: A Hard Habit to Break? C*ancer Cell 2***009,** 1*6* (6), 458-462.

308. Chen, Y.; Sawyers, C. L.; Scher, H. I., Targeting the androgen receptor pathway in prostate cancer. C*urr. Opin. Pharmacol. 2***008,** 8 (4), 440-448.

309. de Bono , J. S.; Logothetis , C. J.; Molina , A.; Fizazi , K.; North , S.; Chu , L.; Chi , K. N.; Jones , R. J.; Goodman , O. B. J.; Saad , F.; Staffurth , J. N.; Mainwaring , P.; Harland , S.; Flaig , T. W.; Hutson , T. E.; Cheng , T.; Patterson , H.; Hainsworth , J. D.; Ryan , C. J.; Sternberg , C. N.; Ellard , S. L.; Fléchon , A.; Saleh , M.; Scholz , M.; Efstathiou , E.; Zivi , A.; Bianchini , D.; Loriot , Y.; Chieffo , N.; Kheoh , T.; Haqq , C. M.; Scher , H. I., Abiraterone and Increased Survival in Metastatic Prostate Cancer. N*ew England Journal of Medicine 2***011,** 3*64* (21), 1995-2005.

310. Scher , H. I.; Fizazi , K.; Saad , F.; Taplin , M.-E.; Sternberg , C. N.; Miller , K.; de Wit , R.; Mulders , P.; Chi , K. N.; Shore , N. D.; Armstrong , A. J.; Flaig , T. W.; Fléchon , A.; Mainwaring , P.; Fleming , M.; Hainsworth , J. D.; Hirmand , M.; Selby , B.; Seely , L.; de Bono , J. S.,

Increased Survival with Enzalutamide in Prostate Cancer after Chemotherapy. N*ew England Journal of Medicine 2***012,** 3*67* (13), 1187-1197.

311. Ryan , C. J.; Smith , M. R.; de Bono , J. S.; Molina , A.; Logothetis , C. J.; de Souza , P.; Fizazi , K.; Mainwaring , P.; Piulats , J. M.; Ng , S.; Carles , J.; Mulders , P. F. A.; Basch , E.; Small , E. J.; Saad , F.; Schrijvers , D.; Van Poppel , H.; Mukherjee , S. D.; Suttmann , H.; Gerritsen , W. R.; Flaig , T. W.; George , D. J.; Yu , E. Y.; Efstathiou , E.; Pantuck , A.; Winquist , E.; Higano , C. S.; Taplin , M.-E.; Park , Y.; Kheoh , T.; Griffin , T.; Scher , H. I.; Rathkopf , D. E., Abiraterone in Metastatic Prostate Cancer without Previous Chemotherapy. N*ew England Journal of Medicine 2***013,** 3*68* (2), 138-148.

312. Beer , T. M.; Armstrong , A. J.; Rathkopf , D. E.; Loriot , Y.; Sternberg , C. N.; Higano , C. S.; Iversen , P.; Bhattacharya , S.; Carles , J.; Chowdhury , S.; Davis , I. D.; de Bono , J. S.; Evans , C. P.; Fizazi , K.; Joshua , A. M.; Kim , C.-S.; Kimura , G.; Mainwaring , P.; Mansbach , H.; Miller , K.; Noonberg , S. B.; Perabo , F.; Phung , D.; Saad , F.; Scher , H. I.; Taplin , M.-E.; Venner , P. M.; Tombal , B., Enzalutamide in Metastatic Prostate Cancer before Chemotherapy. N*ew England Journal of Medicine 2***014,** 3*71* (5), 424-433.

313. Saad, F.; Chi, K. N.; Finelli, A.; Hotte, S. J.; Izawa, J.; Kapoor, A.; Kassouf, W.; Loblaw, A.; North, S.; Rendon, R.; So, A.; Usmani, N.; Vigneault, E.; Fleshner, N. E., The 2015 CUA-CUOG Guidelines for the management of castration-resistant prostate cancer (CRPC). C*anadian Urological Association Journal 2***015,** 9 (3-4), 90-96.

314. Terada, N.; Akamatsu, S.; Kobayashi, T.; Inoue, T.; Ogawa, O.; Antonarakis, E. S., Prognostic and predictive biomarkers in prostate cancer: latest evidence and clinical implications. T*herapeutic Advances in Medical Oncology 2***017,** 9 (8), 565-573.

315. Byrnes, S. A.; Weigl, B. H., Selecting analytical biomarkers for diagnostic applications: a first principles approach. E*xpert Review of Molecular Diagnostics 2***018,** 1*8* (1), 19-26.

316. Mehta, S.; Shelling, A.; Muthukaruppan, A.; Lasham, A.; Blenkiron, C.; Laking, G.; Print, C., Predictive and prognostic molecular markers for cancer medicine. T*herapeutic Advances in Medical Oncology 2***010,** 2 (2), 125-148.

317. Di Meo, A.; Bartlett, J.; Cheng, Y.; Pasic, M. D.; Yousef, G. M., Liquid biopsy: a step forward towards precision medicine in urologic malignancies. M*olecular Cancer 2***017,** 1*6* (1), 80.

318. Fletcher, C., AR-v7 liquid biopsy for treatment stratification in prostate cancer: how close are we? C*urrent Opinion in Urology 2***017,** 2*7* (5), 500-509.

319. Qu, Y.; Dai, B.; Ye, D.; Kong, Y.; Chang, K.; Jia, Z.; Yang, X.; Zhang, H.; Zhu, Y.; Shi, G., Constitutively Active AR-V7 Plays an Essential Role in the Development and Progression of Castration-Resistant Prostate Cancer. S*ci. Rep. 2***015,** 5*.*

320. Luo, J., Development of AR-V7 as a putative treatment selection marker for metastatic castration-resistant prostate cancer. A*sian Journal of Andrology 2***016,** 1*8* (4), 580-585.

321. Antonarakis, E. S.; Lu, C.; Luber, B.; Wang, H.; Chen, Y.; Zhu, Y.; Silberstein, J. L.; Taylor, M. N.; Maughan, B. L.; Denmeade, S. R.; Pienta, K. J.; Paller, C. J.; Carducci, M. A.; Eisenberger, M. A.; Luo, J., Clinical Significance of Androgen Receptor Splice Variant-7 mRNA Detection in Circulating Tumor Cells of Men With Metastatic Castration-Resistant

Prostate Cancer Treated With First- and Second-Line Abiraterone and Enzalutamide. J*ournal of Clinical Oncology 2***017,** 3*5* (19), 2149-2156.

322. Antonarakis, E. S.; Lu, C.; Luber, B.; Wang, H.; Chen, Y.; Nakazawa, M.; Nadal, R.; Paller, C. J.; Denmeade, S. R.; Carducci, M. A., Androgen Receptor Splice Variant 7 and Efficacy of Taxane Chemotherapy in Patients With Metastatic Castration-Resistant Prostate Cancer. J*AMA Oncol 2***015,** 1.

323. Scher, H. I.; Lu, D.; Schreiber, N. A.; et al., Association of ar-v7 on circulating tumor cells as a treatment-specific biomarker with outcomes and survival in castration-resistant prostate cancer. J*AMA Oncology 2***016,** 2 (11), 1441-1449.

324. Scher, H. I.; Graf, R. P.; Schreiber, N. A.; McLaughlin, B.; Lu, D.; Louw, J.; Danila, D. C.; Dugan, L.; Johnson, A.; Heller, G.; Fleisher, M.; Dittamore, R., Nuclear-specific AR-V7 Protein Localization is Necessary to Guide Treatment Selection in Metastatic Castration-resistant Prostate Cancer. E*uropean Urology 2***017,** 7*1* (6), 874-882.

325. Antonarakis, E. S.; Scher, H. I., Do Patients With AR-V7–Positive Prostate Cancer Benefit from Novel Hormonal Therapies? It All Depends on Definitions. E*uropean Urology 2***017,** 7*1* (1), 4-6.

326. Tsaur, I.; Borgmann, H.; Surcel, C. I.; Ost, P.; Ploussard, G., AR-V7 predicting treatment response in metastasized prostate cancer: has it peaked? W*orld Journal of Urology 2***018,** 3*6* (1), 149-151.

327. Ma, Y.; Luk, A.; Young, F. P.; Lynch, D.; Chua, W.; Balakrishnar, B.; de Souza, P.; Becker, T. M., Droplet Digital PCR Based Androgen Receptor Variant 7 (AR-V7) Detection

from Prostate Cancer Patient Blood Biopsies. I*nternational Journal of Molecular Sciences 2***016,** 1*7* (8), 1264.

328. Miyamoto, D. T.; Zheng, Y.; Wittner, B. S.; Lee, R. J.; Zhu, H.; Broderick, K. T.; Desai, R.; Fox, D. B.; Brannigan, B. W.; Trautwein, J.; Arora, K. S.; Desai, N.; Dahl, D. M.; Sequist, L. V.; Smith, M. R.; Kapur, R.; Wu, C.-L.; Shioda, T.; Ramaswamy, S.; Ting, D. T.; Toner, M.; Maheswaran, S.; Haber, D. A., RNA-Seq of single prostate CTCs implicates noncanonical Wnt signaling in antiandrogen resistance. S*cience 2***015,** 3*49* (6254), 1351-1356.

329. Seitz, A. K.; Thoene, S.; Bietenbeck, A.; Nawroth, R.; Tauber, R.; Thalgott, M.; Schmid, S.; Secci, R.; Retz, M.; Gschwend, J. E.; Ruland, J.; Winter, C.; Heck, M. M., AR-V7 in Peripheral Whole Blood of Patients with Castration-resistant Prostate Cancer: Association with Treatment-specific Outcome Under Abiraterone and Enzalutamide. E*uropean Urology 2***017,** 7*2* (5), 828-834.

330. Qu, F.; Xie, W.; Nakabayashi, M.; Zhang, H.; Jeong, S. H.; Wang, X.; Komura, K.; Sweeney, C. J.; Sartor, O.; Lee, G.-S. M.; Kantoff, P. W., Association of AR-V7 and Prostate-Specific Antigen RNA Levels in Blood with Efficacy of Abiraterone Acetate and Enzalutamide Treatment in Men with Prostate Cancer. C*linical Cancer Research 2***017,** 2*3* (3), 726-734.

331. Del Re, M.; Biasco, E.; Crucitta, S.; Derosa, L.; Rofi, E.; Orlandini, C.; Miccoli, M.; Galli, L.; Falcone, A.; Jenster, G. W.; van Schaik, R. H.; Danesi, R., The Detection of Androgen Receptor Splice Variant 7 in Plasma-derived Exosomal RNA Strongly Predicts Resistance to Hormonal Therapy in Metastatic Prostate Cancer Patients. E*uropean Urology 2***017,** 7*1* (4), 680-687.

332. Markowski, M. C.; Silberstein, J. L.; Eshleman, J. R.; Eisenberger, M. A.; Luo, J.; Antonarakis, E. S., Clinical Utility of CLIA-Grade AR-V7 Testing in Patients With Metastatic Castration-Resistant Prostate Cancer. J*CO Precision Oncology 2***017,** - (1), 1-9.

333. Lokhandwala, P. M.; Riel, S. L.; Haley, L.; Lu, C.; Chen, Y.; Silberstein, J.; Zhu, Y.; Zheng, G.; Lin, M.-T.; Gocke, C. D.; Partin, A. W.; Antonarakis, E. S.; Luo, J.; Eshleman, J. R., Analytical Validation of Androgen Receptor Splice Variant 7 Detection in a Clinical Laboratory Improvement Amendments (CLIA) Laboratory Setting. T*he Journal of Molecular Diagnostics 2***017,** 1*9* (1), 115-125.

334. Werner, S. L.; Graf, R. P.; Landers, M.; Valenta, D. T.; Schroeder, M.; Greene, S. B.; Bales, N.; Dittamore, R.; Marrinucci, D., Analytical Validation and Capabilities of the Epic CTC Platform: Enrichment-Free Circulating Tumour Cell Detection and Characterization. J*ournal of Circulating Biomarkers 2***015,** 4*,* 3.

335. John Hopkins Molecular Diagnostic Laboratory. http://pathology.jhu.edu/MolecularDiagnostics/tests.cfm [Accessed 1 April 2018].

336. Genomic Health [Personal Communication, 1 Feb 2018].

337. Wang, G.; Lipert, R. J.; Jain, M.; Kaur, S.; Chakraboty, S.; Torres, M. P.; Batra, S. K.; Brand, R. E.; Porter, M. D., Detection of the Potential Pancreatic Cancer Marker MUC4 in Serum Using Surface-Enhanced Raman Scattering. A*nal. Chem. 2***011,** 8*3* (7), 2554-2561.

338. Granger, J. H.; Granger, M. C.; Firpo, M. A.; Mulvihill, S. J.; Porter, M. D., Toward development of a surface-enhanced Raman scattering (SERS)-based cancer diagnostic immunoassay panel. A*nalyst 2***013,** 1*38* (2), 410-416.

339. Laurentius, L. B.; Crawford, A. C.; Mulvihill, T. S.; Granger, J. H.; Robinson, R.; Spencer, J. S.; Chatterjee, D.; Hanson, K. E.; Porter, M. D., Importance of specimen pretreatment for the low-level detection of mycobacterial lipoarabinomannan in human serum. A*nalyst 2***017,** 1*42* (1), 177-185.

340. Wu, Y.; Wang, Y. Q.; Weng, W. W.; Zhang, Q. Y.; Yang, X. Q.; Gan, H. L.; Yang, Y. S.; Zhang, P. P.; Sun, M. H.; Xu, M. D.; Wang, C. F., A serum-circulating long noncoding RNA signature can discriminate between patients with clear cell renal cell carcinoma and healthy controls. O*ncogenesis 2***016,** 5*.*

341. Laurentius, L.; Stoyanov, S. R.; Gusarov, S.; Kovalenko, A.; Du, R.; Lopinski, G. P.; McDermott, M. T., Diazonium-Derived Aryl Films on Gold Nanoparticles: Evidence for a Carbon–Gold Covalent Bond. A*CS Nano 2***011,** 5 (5), 4219-4227.

342. Fisk, H.; Westley, C.; Turner, N. J.; Goodacre, R., Achieving optimal SERS through enhanced experimental design. J*ournal of Raman Spectroscopy 2***016,** 4*7* (1), 59-66.

343. Henry, A.-I.; Sharma, B.; Cardinal, M. F.; Kurouski, D.; Van Duyne, R. P., Surface-Enhanced Raman Spectroscopy Biosensing: In Vivo Diagnostics and Multimodal Imaging. A*nal. Chem. 2***016,** 8*8* (13), 6638-6647.

344. McAughtrie, S.; Faulds, K.; Graham, D., Surface enhanced Raman spectroscopy (SERS): Potential applications for disease detection and treatment. J*ournal of Photochemistry and Photobiology C: Photochemistry Reviews 2***014,** 2*1* (0), 40-53.

345. de Albuquerque, C. D. L.; Sobral-Filho, R. G.; Poppi, R. J.; Brolo, A. G., Digital Protocol for Chemical Analysis at Ultralow Concentrations by Surface-Enhanced Raman Scattering. A*nal. Chem. 2***018,** 9*0* (2), 1248-1254.

346. Cao, Y. C.; Jin, R.; Mirkin, C. A., Nanoparticles with Raman Spectroscopic Fingerprints for DNA and RNA Detection. S*cience 2***002,** 2*97* (5586), 1536-1540.

347. Guo, Z.; Yang, X.; Sun, F.; Jiang, R.; Linn, D. E.; Chen, H.; Chen, H.; Kong, X.; Melamed, J.; Tepper, C. G.; Kung, H.-J.; Brodie, A. M. H.; Edwards, J.; Qiu, Y., A Novel Androgen Receptor Splice Variant Is Up-regulated during Prostate Cancer Progression and Promotes Androgen Depletion–Resistant Growth. C*ancer Research 2***009,** 6*9* (6), 2305-2313.

348. Hu, R.; Dunn, T. A.; Wei, S.; Isharwal, S.; Veltri, R. W.; Humphreys, E.; Han, M.; Partin, A. W.; Vessella, R. L.; Isaacs, W. B.; Bova, G. S.; Luo, J., Ligand-independent androgen receptor variants derived from splicing of cryptic exons signify hormone-refractory prostate cancer. C*ancer Res 2***009,** 6*9* (1), 16-22.

349. Dehm, S. M.; Tindall, D. J., Alternatively spliced androgen receptor variants. E*ndocrine-Related Cancer 2***011,** 1*8* (5), 183-196.

350. Thadani-Mulero, M.; Portella, L.; Sun, S.; Sung, M.; Matov, A.; Vessella, R. L.; Corey, E.; Nanus, D. M.; Plymate, S. R.; Giannakakou, P., Androgen Receptor Splice Variants Determine Taxane Sensitivity in Prostate Cancer. C*ancer Research 2***014,** 7*4* (8), 2270.

351. Lisa Saccomano, Abcam, personal communication, 2017.

352. Lisa Saccomano, Abcam, personal communication, 2017.

353. Gelest Techical Document - Coupling Agents. https://www.gelest.com/wp-content/uploads/Goods-PDF-brochures-couplingagents.pdf [Accessed 1 April 2018].

354. Susan Tilford, Gelest, personal communication, 2017.

355. Deegan, R. D.; Bakajin, O.; Dupont, T. F.; Huber, G.; Nagel, S. R.; Witten, T. A., Capillary flow as the cause of ring stains from dried liquid drops. N*ature 1***997,** 3*89,* 827.

356. Reference equation for laser spot diameter: https://www.olympus-ims.com/en/microscope/terms/luminous_flux/ [Accessed 30 March 2018].

357. Paul Concepcion, Technical Officer - Electron Microscopy, National Research Council Canada [personal communication, 2017].

358. Korenchuk, S.; Lehr, J. E.; McLean, L.; Lee, Y. G.; Whitney, S.; Vessella, R.; Lin, D. L.; Pienta, K. J., VCaP, a cell-based model system of human prostate cancer. I*n Vivo 2***001,** 1*5* (2), 163-168.

359. Kaighn, M. E.; Narayan, K. S.; Ohnuki, Y.; Lechner, J. F.; Jones, L. W., Establishment and characterization of a human prostatic carcinoma cell line (PC-3). I*nvestigative Urology 1***979,** 1*7* (1), 16-23.

360. Eskra, J., Culture methods for VCaP prostate cancer cells. 2**015.**

361. Liu, L. L.; Xie, N.; Sun, S.; Plymate, S.; Mostaghel, E.; Dong, X., Mechanisms of the androgen receptor splicing in prostate cancer cells. O*ncogene 2***014,** 3*3* (24), 3140-3150.

362. Smith, P. K.; Krohn, R. I.; Hermanson, G. T.; Mallia, A. K.; Gartner, F. H.; Provenzano, M. D.; Fujimoto, E. K.; Goeke, N. M.; Olson, B. J.; Klenk, D. C., Measurement of protein using bicinchoninic acid. A*nal. Biochem. 1***985,** 1*50* (1), 76-85.

363. Olson, B. J. S. C.; Markwell, J., Assays for Determination of Protein Concentration. In C*urrent Protocols in Protein Science,* John Wiley & Sons, Inc.: 2007.

364. Green, M. R.; Sambrook, J., M*olecular cloning : a laboratory manual.* Cold Spring Harbor, N.Y. : Cold Spring Harbor Laboratory Press, ©2012.

4th ed.: 2012.

365. Health, N. I. o.; Institute, N. C., National Cancer Institute Best Practices for Biospecimen Resources. Services, U. S. D. o. H. a. H., Ed. 2016.

366. Research, C. I. o. H.; Canada, N. S. a. E. R. C. o.; Canada, S. S. a. H. R. C. o., Tri-Council Policy Statement: Ethical Conduct for Research Involving Humans. Ethics, P. o. R., Ed. 2014.

367. Networks, N. o. Biospecimen related SOPs. http://n2canada.ca/resources/ (accessed 28 February 2018).

368. Network, C. C. C. T. Biospecimen Standard Operating Procedures. http://3ctn.ca/page/biospecimen-standard-operating-procedures-and-quiz (accessed 28 February 2018).

369. http://www.abcam.com/androgen-receptor-antibody-chip-grade-ab74272.html [accessed 26 February 2018].

370. http://www.abcam.com/androgen-receptor-ar-v7-specific-antibody-epr15656-ab198394.html [accessed 26 February 2018].

371. Courtney Mankus, GE Healthcare Life Sciences support scientist, personal communication, 2018.

372. Watson, P. A.; Chen, Y. F.; Balbas, M. D.; Wongvipat, J.; Socci, N. D.; Viale, A.; Kim, K.; Sawyers, C. L., Constitutively active androgen receptor splice variants expressed in castration-resistant prostate cancer require full-length androgen receptor. P*roceedings of the National Academy of Sciences 2***010,** 1*07* (39), 16759-16765.

373. Bonifacio, A.; Dalla Marta, S.; Spizzo, R.; Cervo, S.; Steffan, A.; Colombatti, A.; Sergo, V., Surface-enhanced Raman spectroscopy of blood plasma and serum using Ag and Au nanoparticles: a systematic study. A*nalytical and Bioanalytical Chemistry 2***014,** 4*06* (9), 2355-2365.

374. Li, L.; Tsung, C.-K.; Ming, T.; Sun, Z.; Ni, W.; Shi, Q.; Stucky, G. D.; Wang, J., Multifunctional Mesostructured Silica Microspheres from an Ultrasonic Aerosol Spray. A*dv. Funct. Mater. 2***008,** 1*8* (19), 2956-2962.

375. Dong, Y.; Shannon, C., Heterogeneous Immunosensing Using Antigen and Antibody Monolayers on Gold Surfaces with Electrochemical and Scanning Probe Detection. A*nal. Chem. 2***000,** 7*2* (11), 2371-2376.

376. Lu, B.; Smyth, M. R.; O'Kennedy, R., Tutorial review. Oriented immobilization of antibodies and its applications in immunoassays and immunosensors. A*nalyst 1***996,** 1*21* (3), 29R-32R.

377. Rusthoven, C. G.; Carlson, J. A.; Waxweiler, T. V.; Yeh, N.; Raben, D.; Flaig, T. W.; Kavanagh, B. D., The prognostic significance of Gleason scores in metastatic prostate cancer. U*rologic Oncology: Seminars and Original Investigations 2***014,** 3*2* (5), 707-713.

378. D'Amico, A. V.; Whittington, R.; Malkowicz, S.; et al., Biochemical outcome after radical prostatectomy, external beam radiation therapy, or interstitial radiation therapy for clinically localized prostate cancer. J*AMA 1***998,** 2*80* (11), 969-974.

379. Amin, M.; Edge, S.; Greene, F.; Byrd, D.; Brookland, R.; Washington, M.; Gershenwald, J.; Compton, C.; Hess, K.; Sullivan, D.; Jessup, J.; Brierley, J.; Gaspar, L.; Schilsky, R.; Balch, C.; Winchester, D.; Asare, E.; Madera, M.; Gress, D.; Meyer, L., A*JCC Cancer Staging Manual 8th Edition.* Springer: New York, 2017.

380. Nakazawa, M.; Lu, C.; Chen, Y.; Paller, C. J.; Carducci, M. A.; Eisenberger, M. A.; Luo, J.; Antonarakis, E. S., Serial blood-based analysis of AR-V7 in men with advanced prostate cancer. A*nnals of Oncology 2***015,** 2*6* (9), 1859-1865.

381. https://www.preanalytix.com/products/blood/RNA/paxgene-blood-rna-tube [accessed 14 March 2018]. Product available through Qiagen.

382. https://www.streck.com/collection/cell-free-rna-bct/ [accessed 14 March 2018].

383. Basch, E.; Loblaw, D. A.; Oliver, T. K.; Carducci, M.; Chen, R. C.; Frame, J. N.; Garrels, K.; Hotte, S.; Kattan, M. W.; Raghavan, D.; Saad, F.; Taplin, M. E.; Walker-Dilks, C.; Williams, J.; Winquist, E.; Bennett, C. L.; Wootton, T.; Rumble, R. B.; Dusetzina, S. B.; Virgo, K. S., Systemic therapy in men with metastatic castration-resistant prostate cancer:American

Society of Clinical Oncology and Cancer Care Ontario clinical practice guideline. J *Clin Oncol 2***014,** 3*2* (30), 3436-48.

384. https://www.nccn.org/professionals/physician_gls/default.aspx [Accessed 15 March 2018].

385. Morris, M. J.; Molina, A.; Small, E. J.; Bono, J. S. d.; Logothetis, C. J.; Fizazi, K.; Souza, P. d.; Kantoff, P. W.; Higano, C. S.; Li, J.; Kheoh, T.; Larson, S. M.; Matheny, S. L.; Naini, V.; Burzykowski, T.; Griffin, T. W.; Scher, H. I.; Ryan, C. J., Radiographic Progression-Free Survival As a Response Biomarker in Metastatic Castration-Resistant Prostate Cancer: COU-AA-302 Results. J*ournal of Clinical Oncology 2***015,** 3*3* (12), 1356-1363.

386. Imbriaco, M.; Larson, S. M.; Yeung, H. W.; Mawlawi, O. R.; Erdi, Y.; Venkatraman, E. S.; Scher, H. I., A new parameter for measuring metastatic bone involvement by prostate cancer: the Bone Scan Index. C*linical Cancer Research 1***998,** 4 (7), 1765-1772.

387. Ahmed, H. U.; El-Shater Bosaily, A.; Brown, L. C.; Gabe, R.; Kaplan, R.; Parmar, M. K.; Collaco-Moraes, Y.; Ward, K.; Hindley, R. G.; Freeman, A.; Kirkham, A. P.; Oldroyd, R.; Parker, C.; Emberton, M., Diagnostic accuracy of multi-parametric MRI and TRUS biopsy in prostate cancer (PROMIS): a paired validating confirmatory study. T*he Lancet 2***017,** *389* (10071), 815-822.

388. Sunita Ghosh, personal communication, 2018. Dr. Ghosh is an Assistant Clinical Professor at the University of Alberta and a Research Scientist for Alberta Health Services - Cancer Control.

389. Chow, S.-C.; Shao, J.; Wang, H., S*ample size calculations in clinical research.* Boca Raton : Chapman & Hall/CRC, c2008.

2nd ed.: 2008.

390. Machin, D.; Campbell, M.; Tan, S. B.; Tan, S. H., S*ample size tables for clinical studies.* Chichester, UK ; Hoboken, NJ : Wiley-Blackwell, 2009.

3rd ed.: 2009.

391. Sunita Ghosh, personal communication, 2018. Dr. Ghosh is an Assistant Clinical Professor at the University of Alberta and a Research Scientist for Alberta Health Services - Cancer Control.

392. Prospective CiRculating prOstate Cancer Predictors in HighEr Risk mCRPC studY (PROPHECY). ClinicalTrials.gov Identifier: NCT02269982 [accessed 9 March 2018].

393. Tothill, I. E., Biosensors for cancer markers diagnosis. S*emin Cell Dev Biol 2***009,** 2*0* (1), 55-62.

394. Frost; Sullivan A*nalytical review of world biosensors market 2*010.

395. Juma, C., I*nnovation and its enemies : why people resist new technologies.* Oxford University: New York, NY, 2016.

396. Wilson, E. O., L*etters to a young scientist.* Liveright Publishing Corporation, a Division of W. W. Norton & Company New York, NY, 2014.

397. https://www.tecedmonton.com/dynalifeaccelerator/ [Accessed 4 May 2018].

398. Palmer, T. D.; Ashby, W. J.; Lewis, J. D.; Zijlstra, A., Targeting tumor cell motility to prevent metastasis. A*dvanced Drug Delivery Reviews 2***011,** 6*3* (8), 568-581.

399. Palmer, T. D.; Martínez, C. H.; Vasquez, C.; Hebron, K. E.; Jones-Paris, C.; Arnold, S. A.; Chan, S. M.; Chalasani, V.; Gomez-Lemus, J. A.; Williams, A. K.; Chin, J. L.; Giannico, G. A.; Ketova, T.; Lewis, J. D.; Zijlstra, A., Integrin-Free Tetraspanin CD151 Can Inhibit Tumor Cell Motility upon Clustering and Is a Clinical Indicator of Prostate Cancer Progression. C*ancer Research 2***014,** 7*4* (1), 173.

400. Tagawa, S. T.; Milowsky, M. I.; Morris, M.; Vallabhajosula, S.; Christos, P.; Akhtar, N. H.; Osborne, J.; Goldsmith, S. J.; Larson, S.; Taskar, N. P.; Scher, H. I.; Bander, N. H.; Nanus, D. M., Phase II Study of Lutetium-177–Labeled Anti-Prostate-Specific Membrane Antigen Monoclonal Antibody J591 for Metastatic Castration-Resistant Prostate Cancer. C*linical Cancer Research 2***013,** 1*9* (18), 5182.

401. Haberkorn, U.; Eder, M.; Kopka, K.; Babich, J. W.; Eisenhut, M., New Strategies in Prostate Cancer: Prostate-Specific Membrane Antigen (PSMA) Ligands for Diagnosis and Therapy. C*linical Cancer Research 2***016,** 2*2* (1), 9.

402. Chalkiadaki, A.; Guarente, L., The multifaceted functions of sirtuins in cancer. N*ature Reviews Cancer 2***015,** 1*5,* 608.

403. Haider, R.; Massa, F.; Kaminski, L.; Clavel, S.; Djabari, Z.; Robert, G.; Laurent, K.; Michiels, J.-F.; Durand, M.; Ricci, J.-E.; Tanti, J.-F.; Bost, F.; Ambrosetti, D., Sirtuin 7: a new marker of aggressiveness in prostate cancer. O*ncotarget 2***017,** 8 (44), 77309-77316.

404. Giannakakou, P.; Plymate, S. R. Identifying taxane sensitivity in prostate cancer patients US patent 2015/0233927 A1. 2017.

405. Njoki, P. N.; Lim, I. I. S.; Mott, D.; Park, H.-Y.; Khan, B.; Mishra, S.; Sujakumar, R.; Luo, J.; Zhong, C.-J., Size Correlation of Optical and Spectroscopic Properties for Gold Nanoparticles. T*he Journal of Physical Chemistry C 2***007,** 1*11* (40), 14664-14669.

406. Stamplecoskie, K. G.; Scaiano, J. C.; Tiwari, V. S.; Anis, H., Optimal Size of Silver Nanoparticles for Surface-Enhanced Raman Spectroscopy. T*he Journal of Physical Chemistry C 2***011,** 1*15* (5), 1403-1409.

407. Orendorff, C. J.; Gearheart, L.; Jana, N. R.; Murphy, C. J., Aspect ratio dependence on surface enhanced Raman scattering using silver and gold nanorod substrates. P*CCP 2***006,** 8 (1), 165-170.

408. Time magazine. Artifical intelligence: The future of humankind. September 2017.

409. https://www.ibm.com/watson/health/oncology-and-genomics/ [accessed 10 May 2018].

410. Alberta's population statistic. http://economicdashboard.alberta.ca/Population [accessed 16 May 2018].

411. https://www.folio.ca/big-data-opens-door-to-big-possibilities-in-health-care/ [Accessed 9 May 2018].

412. Alberta Health Services - Connect Care. https://www.albertahealthservices.ca/info/cis.aspx [Accessed 9 May 2018].

413. Alberta Health Services - Connect Care.

https://www.albertahealthservices.ca/info/cis.aspx [Accessed 9 May 2018].